Numerical Studies of Heavy-Fermion Systems and Correlated Topological Insulators

Dissertation zur Erlangung des naturwissenschaftlichen Doktorgrades der
Julius-Maximilians-Universität Würzburg

vorgelegt von

Martin Helmut Bercx

aus Tettnang

Würzburg 2014

Eingereicht am 19.12.2014
bei der Fakultät für Physik und Astronomie.
1. Gutachter: Prof. Dr. Fakher F. Assaad
2. Gutachter: Prof. Dr. Björn Trauzettel
der Dissertation.
Vorsitzender: Prof. Dr. Sven Höfling
1. Prüfer: Prof. Dr. Fakher F. Assaad
2. Prüfer: Prof. Dr. Björn Trauzettel
3. Prüfer: Prof. Dr. Friedrich Reinert
des Promotionskolloquiums.
Tag des Promotionskolloquiums: 13.05.2015
Doktorurkunde ausgehändigt am: . . . .

Abstract

In this thesis, we investigate aspects of the physics of heavy-fermion systems and correlated topological insulators. We numerically solve the interacting Hamiltonians that model the physical systems using quantum Monte Carlo algorithms to access both ground-state and finite-temperature observables. Initially, we focus on the metamagnetic transition in the Kondo lattice model for heavy fermions. On the basis of the dynamical mean-field theory and the dynamical cluster approximation, our calculations point towards a continuous transition, where the signatures of metamagnetism are linked to a Lifshitz transition of heavy-fermion bands.

In the second part of the thesis, we study various aspects of magnetic π fluxes in the Kane-Mele-Hubbard model of a correlated topological insulator. We describe a numerical measurement of the topological index, based on the localized mid-gap states that are provided by π flux insertions. Furthermore, we take advantage of the intrinsic spin degree of freedom of a π flux to devise instances of interacting quantum spin systems.

In the third part of the thesis, we introduce and characterize the Kane-Mele-Hubbard model on the π flux honeycomb lattice. We place particular emphasis on the correlations effects along the one-dimensional boundary of the lattice and compare results from a bosonization study with finite-size quantum Monte Carlo simulations.

Zusammenfassung

Gegenstand der vorliegenden Arbeit ist die Untersuchung von Aspekten der Physik schwerer Fermionen und korrelierter topologischer Isolatoren. Wir lösen den wechselwirkenden Hamiltonoperator, der das jeweilige System modelliert, mithilfe von Quanten-Monte-Carlo-Algorithmen, um Erwartungswerte sowohl im Grundzustand als auch im thermisch angeregten Zustand zu erhalten. Zunächst richten wir das Augenmerk auf den metamagnetischen Übergang im Kondo-Gitter-Model für schwere Fermionen. Unsere Rechnungen basieren auf der dynamischen Mean-Field-Theorie und der dynamischen Cluster-Näherung. Sie weisen auf einen kontinuierlichen Übergang hin, der die metamagnetischen Merkmale mit einem Lifshitz-Übergang in der Bandstruktur der schweren Fermionen verbindet.

Im zweiten Teil der Arbeit untersuchen wir verschiedene Facetten von magnetischen π-Flüssen im Kane-Mele-Hubbard-Modell des korrelierten topologischen Isolators. Wir beschreiben eine numerische Messung der topologischen Invariante. Diese Messung beruht auf der Tatsache, dass das Einfügen von π-Flüssen lokalisierte Zustände in der Mitte der Bandlücke des Isolators erzeugt. Darüberhinaus verwenden wir den intrinsischen Spinfreiheitsgrad eines π-Flusses, um wechselwirkende Spinmodelle zu realisieren.

Im dritten Teil der Arbeit stellen wir das Kane-Mele-Modell auf dem hexagonalen π-Fluss-Gitter vor und charakterisieren es. Wir legen besonderen Schwerpunkt auf Wechselwirkungseffekte entlang des eindimensionalen Randes des Gitters und vergleichen die Ergebnisse einer Bosonisierungsstudie mit Quanten-Monte-Carlo-Simulationen auf endlichen Gittern.

Contents

1

Introduction

In this thesis, we consider instances of correlation induced phenomena in condensed matter physics. The notion of correlations describes the effect of the interactions between the constituent particles of a many-body system. Solving an interacting model is in general a formidable task. Since analytical solutions are often only known in well-defined limits, numerical methods come into play. To simulate the electron-electron interactions, we use quantum Monte Carlo methods. In the following, we introduce the two main subjects of this thesis, namely heavy-fermion systems and topological insulators.

1.1 Heavy-fermion systems

The physics of local moments is a prime example of correlation induced behavior in condensed matter. A key insight in this field has been the understanding of the anomalous temperature dependence of many physical observables when magnetic impurities are dispersed in metals [1; 2]. Both the experimental observation and its theoretical modelling in terms of coupled spin and fermionic degrees of freedom are summarized under the term Kondo effect [3].

The lattice analog to the Kondo effect can be observed in metallic crystals containing selected elements that provide the additional spin and in general also charge degrees of freedom. Whereas at high temperature the spin of the ions and the itinerant electrons of the metal are nearly independent, they strongly interact at low temperatures, eventually resulting in a system of fermionic quasiparticles with masses that are orders of magnitude larger than the bare electron mass. Consequently, these compounds are called heavy-fermion systems [4].

The ground-state of heavy-fermion systems and therefore the low-temperature, macroscopic properties are a result of the strong hybridization between local spin moments and Bloch fermion states. The presence of various competing phases makes heavy-fermion systems susceptible to external tuning parameters, like electromagnetic field, pressure or chemical doping [5; 6; 7]. One focus of this work are heavy-fermion metamagnets (Ch. 3). Theses are paramagnetic Kondo lattice systems that show an unexpected nonlinear behavior of the magnetization at a sharply defined value of an external magnetic field.

Materials that exhibit heavy-fermion phases are usually intermetallic compounds where ions from rare-earth elements (for example, cerium or ytterbium) or from actinide elements contribute the localized spin degrees of freedom. These ions have electrons in the atomic 4f orbitals. Considering the ionic configurations only, we may discriminate two different situations [4]. In the mixed valence regime, there are ionic configurations that are close in energy and consequently the kinetic energy of the f-electrons is enhanced. On the other hand, one may find the Kondo regime where there is a single ionic configuration which is well separated from configurations at higher energies. In the Kondo regime, the charge fluctuations of the f-electrons are suppressed and the occupancy of the f-level is close to unity and therefore fulfills the prerequisite for heavy-fermion physics.

Among the canonical heavy-fermion compounds are those that contain trivalent cerium or ytterbium ions. The Ce^{3+} (Yb^{3+}) ion has the configuration $[\mathrm{Xe}]4\mathrm{f}^1$ ($[\mathrm{Xe}]4\mathrm{f}^{13}$), i.e. one remaining electron (hole) in the 4f shell. To obtain the ground-state of the ion, one has to consider its multiplet structure characterized by the quantum numbers $|l, s, j, m_j\rangle$ (denoting angular momentum, spin, total angular momentum and its magnetic quantum number). In the 4f systems, the multiplet structure essentially results from the competition between a spin-orbit coupling term $\mathcal{H}_{\mathrm{so}}$ and a term $\mathcal{H}_{\mathrm{cf}}$ describing the action of the crystal field, where $\mathcal{H}_{\mathrm{so}} \gg \mathcal{H}_{\mathrm{cf}}$ [8]. The crystal field is the effective static electric field from the surrounding charge distribution. The multiplet structure of Ce^{3+} yields a ground-state doublet with $m_j = \pm 5/2$ (Fig. 1.1). It is important to note that the remaining two-fold degeneracy of the ground-state is a consequence of the Kramers theorem for half-integer (effective) spins and it cannot be lifted unless time-reversal symmetry is broken [8]. A comprehensive experimental review of heavy-fermion materials is presented in [9].

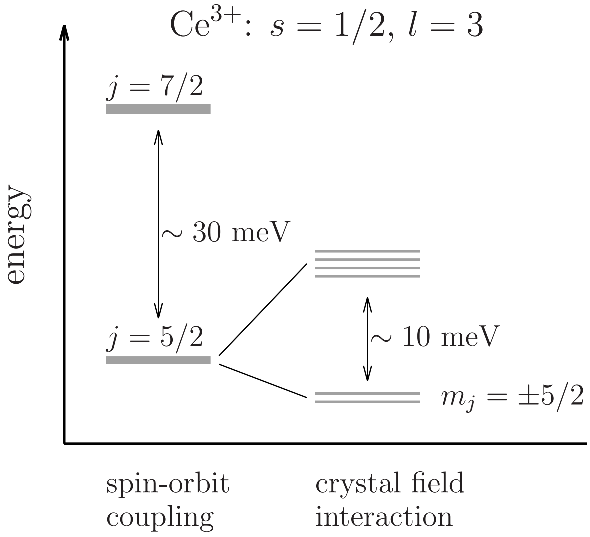

Figure 1.1: Multiplet structure of Ce^{3+} and typical energy scales, for the case of $\mathcal{H}_{\mathrm{so}} \gg \mathcal{H}_{\mathrm{cf}}$. Since the 4f shell is less than half-filled, the application of Hund's rule yield a degenerate spin-orbit ground-state with $j = 5/2$. The crystal field interaction partially lifts this degeneracy, resulting in a $|l = 3, s = 1/2, j = 5/2, m_j = \pm 5/2\rangle$ ground-state doublet. (The figure has been reproduced from Ref. [8].)

1.1.1 The Kondo lattice model

The minimal model for heavy-fermions has to include both a conduction (c) band and dispersionless, localized (f) orbitals. This is accomplished by the periodic Anderson model (PAM) [3; 4]:

$$\mathcal{H} = -t \sum_{\langle \boldsymbol{i},\boldsymbol{j}\rangle,\sigma=\uparrow,\downarrow} (\hat{c}^{\dagger}_{\boldsymbol{i}\sigma}\hat{c}_{\boldsymbol{j}\sigma} + \text{H.c.}) + \epsilon_f \sum_{\boldsymbol{i}\sigma} \hat{n}^{f}_{\boldsymbol{i}\sigma} + V \sum_{\boldsymbol{i},\sigma} (\hat{c}^{\dagger}_{\boldsymbol{i}\sigma}\hat{f}_{\boldsymbol{i}\sigma} + \text{H.c.}) + U \sum_{\boldsymbol{i}} \hat{n}^{f}_{\boldsymbol{i}\uparrow}\hat{n}^{f}_{\boldsymbol{i}\downarrow} \; . \tag{1.1}$$

Here, $\langle \boldsymbol{i}, \boldsymbol{j}\rangle$ denotes hopping between nearest neighbors, σ is the spin projection, ϵ_f is a chemical potential, V is the matrix element describing the overlap between the c- and f-orbitals and U denotes the Coulomb interaction. The density is $\hat{n}^{f}_{\boldsymbol{i}\sigma} = \hat{f}^{\dagger}_{\boldsymbol{i}\sigma}\hat{f}_{\boldsymbol{i}\sigma}$. The PAM has an $SU(2)$ spin symmetry and, similar to the Hubbard model, an additional $SU(2)$ charge symmetry for $U > 0$ and under the particle-hole symmetry condition $\epsilon_f = -U/2$ [4].

At low-energies, the PAM is the parent model of the Kondo lattice model. It describes the Kondo regime where the f-orbitals are represented by spin degrees of freedom and it is formally obtained by integrating out the valence fluctuations of the f-orbitals in the PAM [10]. The Kondo lattice model (KLM) is given by

$$\mathcal{H} = -t \sum_{\langle \boldsymbol{i},\boldsymbol{j}\rangle,\sigma} (\hat{c}^{\dagger}_{\boldsymbol{i}\sigma}\hat{c}_{\boldsymbol{j}\sigma} + \text{H.c.}) + J \sum_{i} \hat{\boldsymbol{S}}^{c}_{\boldsymbol{i}} \cdot \hat{\boldsymbol{S}}^{f}_{\boldsymbol{i}} \; . \tag{1.2}$$

The local spin-operators $\hat{\boldsymbol{S}}^{f}_{\boldsymbol{i}}$ in the Heisenberg term are expressed using auxiliary lattice fermions, $\hat{\boldsymbol{S}}^{f}_{\boldsymbol{i}} = (1/2)\sum_{\alpha,\beta} \hat{f}^{\dagger}_{\boldsymbol{i},\alpha}\boldsymbol{\sigma}_{\alpha\beta}\hat{f}_{\boldsymbol{i},\beta}$, where $\boldsymbol{\sigma}$ is the vector of Pauli matrices and one has to impose the constraint of single occupancy, $\hat{f}^{\dagger}_{\boldsymbol{i},\uparrow}\hat{f}_{\boldsymbol{i},\uparrow} + \hat{f}^{\dagger}_{\boldsymbol{i},\downarrow}\hat{f}_{\boldsymbol{i},\downarrow} = 1$.

The KLM has the same spin and charge symmetries as the PAM, but is also has additional, local $U(1)$ charge symmetries,

$$\hat{f}_{\boldsymbol{i}\sigma} \rightarrow e^{i\theta_{\boldsymbol{i}}}\hat{f}_{\boldsymbol{i}\sigma} \; , \tag{1.3}$$

that correspond to the absence of charge fluctuations at the f-orbitals [4]. The exchange interaction of the Heisenberg term can be written as $J = 8V^2/U$ (for $\epsilon_f = -U/2$) and therefore the limit of strong Coulomb interaction in the PAM maps to a small exchange interaction in the KLM [3].

In the case of half-filling (one conduction electron per lattice site), it has been rigorously shown that both the PAM and the KLM have a unique, spin-singlet ground-state [4; 11]. This statement has been proven to hold in any spatial dimension for bipartite lattices and, for the KLM, both for antiferromagnetic ($J > 0$) and ferromagnetic ($J < 0$) coupling. The KLM away from half-filling is obtained by adding a chemical potential term of the form $-\mu \sum_{\boldsymbol{i},\sigma} \hat{n}^{c}_{\boldsymbol{i}\sigma}$ to the Hamiltonian (1.2). It has been shown that the weakly doped KLM exhibits a Fermi-liquid ground-state [12].

Phenomenologically, the single-impurity Kondo problem introduces an energy scale T_{K}. The Kondo temperature T_{K} is the scale for the formation of a local singlet between the f-orbital spin and the spin polarization of the surrounding conduction electrons. Looking at the Kondo system for decreasing temperature, the local spin moment gets quenched below

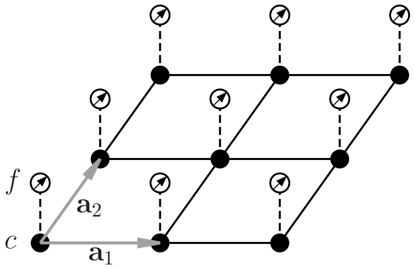

Figure 1.2: Sketch of the Kondo lattice model on the square lattice, where the basis vectors are $\boldsymbol{a}_1 = (1, 0)$ and $\boldsymbol{a}_2 = (0, 1)$.

T_K when the screening of the local moment by the conduction electrons occurs. In the Kondo lattice, a similar crossover from the local moment phase to the Kondo phase happens. The natural energy scale on the lattice is the coherence temperature T_coh. It determines the formation of coherent quasiparticles, consisting of f-spins and c-fermions, that constitute the low-temperature Fermi liquid state. In a very simplified picture, the heavy-fermion phase can be thought of a coherent superposition of individual Kondo screening clouds. More accurately, the heavy-fermion phase is characterized by a large length scale over which a conduction electron spin is coherent with a local moment.

On the lattice, the formation of a many-body Kondo singlet state generally is in competition with mechanisms that favor magnetic ordering. One important mechanism is given by the Rudermann-Kittel-Kasuya-Yosida (RKKY) interaction [4]. It describes an effective f-spin – f-spin interaction which is mediated by the polarization of the conduction electrons. The RKKY scale is set by $T_\mathrm{RKKY} \propto J^2 \chi_c(\boldsymbol{q}, \omega = 0)$ where $\chi_c(\boldsymbol{q}, \omega)$ is the conduction electron spin susceptibility [13].

Guidelines for the scales T_K and T_coh are given by $SU(N)$ mean-field calculations [14] which however neglect spatial fluctuations and therefore the effect of the RKKY interaction. At low conduction electron density, which marks the so-called exhaustion limit, the ratio $T_\mathrm{coh}/T_\mathrm{K} \ll 1$ and therefore two separate energy scales are present. In the weak-coupling limit however, characterized by $J/W \ll 1$ (W is the bandwidth), and at small deviations from half-filling, $1 - n_c \ll 1$, this approach gives the same scaling for both temperatures,

$$T_\mathrm{K,coh} \propto W e^{-1/[J\rho(\epsilon_\mathrm{F})]} \ , \tag{1.4}$$

where $\rho(\epsilon_\mathrm{F})$ is the conduction electron density of states. Importantly, quantum Monte Carlo simulations of the two-dimensional, half-filled KLM capturing the RKKY interaction have been shown to be consistent with the relation (1.4) [15].

Whereas the ground-state phase diagram of the one-dimensional KLM is well understood [4], the study of the KLM in two dimensions (Fig. 1.2) is an active area of research [12; 16; 17].

In Ref. [17], we report the results of a large scale dynamical cluster approximation (DCA+HF-QMC) study aimed at the investigation of the KLM ground-state. The details of the numerical method are given in Sec. 2.3. The obtained phase diagram, as a function of exchange coupling J and conduction electron density n_c is shown in Fig. 1.3.

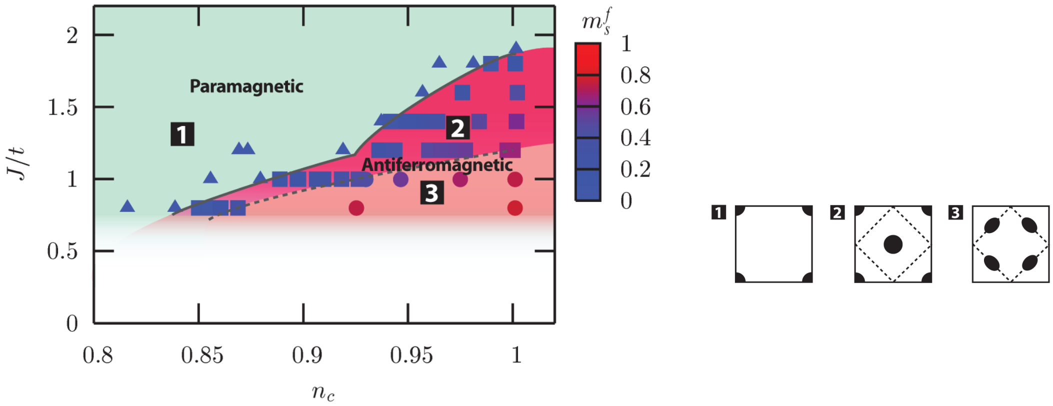

Figure 1.3: Ground-state magnetic phase diagram of the Kondo lattice model, as a function of the coupling J/t and the conduction electron occupancy, obtained from DCA+HF-QMC simulations [17]. When J/t is small, the RKKY scale T_{RKKY} dominates over the Kondo scale T_{K}, leading to a continuous order-disorder transition. The color-coding indicates the value of the staggered magnetization $m_s^f = (1/2N_p)\sum_{\boldsymbol{i}}\langle \hat{n}^f_{\boldsymbol{i}\uparrow} - \hat{n}^f_{\boldsymbol{i}\downarrow}\rangle \exp(-i\boldsymbol{Q}\boldsymbol{i})$, where $\boldsymbol{Q} = (\pi, \pi)$ and $\boldsymbol{i}$ points to the f-orbitals of a cluster of N_p magnetic unit cells that contains two original unit cells. The results are obtained for a weak value of next-nearest neighbor hopping, $t'/t = -0.3$, to suppress the magnetic order which stems from the nesting of the conduction electron Fermi surface. The results have been obtained at finite temperatures $1/\beta$ (up to $\beta t = 100$) and have been checked to stay invariant at lower temperatures. The right panel shows the Fermi surface topologies of the paramagnetic (1, triangles) and the antiferromagnetic [2 (squares) and 3 (circles)] phase.

The particle-hole symmetric KLM at half-filling shows a magnetic order-disorder transition from an antiferromagnetic insulator to the paramagnetic Kondo insulator and numerical exact QMC simulations give a critical coupling of $J_c/t = 1.45$ [18; 19]. Hole-doping drives the system away from half-filing and the antiferromagnetic order gradually decreases. Away from half-filling, the RKKY scale T_{RKKY} dominates over the Kondo scale T_{K} and therefore stabilizes the magnetic order.

The evolution of the Fermi surface topology from the disordered to the ordered phase has been obtained by computing the single-particle spectral function [17]. In the paramagnetic phase, the Fermi surface consists of closed loops that enclose empty states (hole pockets) around $\boldsymbol{k} = (\pm\pi, \pm\pi)$ in the Brillouin zone (Fig. 1.3,1). This corresponds to a large Fermi surface which accounts both for the conduction electrons and the impurity spins (see the discussion of the Luttinger sum rule in Sec. 3.4). In the antiferromagnetic phase, the Fermi surface corresponds to a backfolding of the paramagnetic Fermi surface, similar to a spin-density wave transition. Accordingly, the Fermi surface has an additional shadow feature at $\boldsymbol{k} = (0, 0)$ (Fig. 1.3,2). Deep in the antiferromagnetically ordered phase, the Fermi surface topology changes and is given by hole pockets centered around $\boldsymbol{k} = (\pm\pi/2, \pm\pi/2)$ in the Brillouin zone (Fig. 1.3,3). This topology can be adiabatically linked to a Fermi surface where the f-spins are frozen and Kondo screening is absent [20]. In this sense, it is a small Fermi surface.

Importantly, besides the three different Fermi surface topologies, our results for the hole-doped KLM show evidence of the absence of the breakdown of Kondo screening, even deep in the antiferromagnetic phase. In this context, it is interesting to consider scenarios where the Kondo breakdown can be deliberately induced. One possibility is to include a Heisenberg interaction term in the Hamiltonian (1.2), which couples neighboring f-spins. When this term becomes dominant, the f-spin can decouple from the conduction electrons and form valence-bond solid or spin-liquid phases [7].

1.2 Topological insulators

The classification of insulating states of matter has been refined recently in terms of generic quantum mechanical symmetries that protect certain classes of insulating states [21]. The theoretical [22; 23; 24] and experimental [25] discovery of topological insulators has triggered the renewed interest in classifying non-interacting insulators. A key insight has been the characterization of two-dimensional insulators by an integer, two-valued (Z_2) invariant when time-reversal symmetry is preserved [22]. Accordingly, the insulator can be either a topologically trivial band insulator or a topologically nontrivial, so-called quantum spin Hall insulator. The first material in which the topologically nontrivial state was measured has been a $2d$ semiconductor structure consisting of a mercury telluride quantum well sandwiched between cadmium telluride barriers [25]. The theoretical description of this material rests on spin-orbit coupled electronic orbitals [24].

The Z_2 topological index may be regarded as the time-reversal symmetric counterpart of the integer Chern number. The Chern number characterizes the integer quantum Hall effect occurring in two-dimensional systems at strong external magnetic fields. The Z_2 topological insulator in two-dimensions is one instance in the exhaustive classification of all topological insulators (and topological superconductors) in d-dimensional systems. This classification has been achieved by investigating the Anderson localization problem at the $d-1$-dimensional boundary of the system [21].

Phenomenologically, the two-dimensional topological insulator has robust one-dimensional edge states when it shares a boundary with the topologically trivial vacuum state. The edge states consist of an odd number of Kramers doublets, i.e. pairs of fermionic modes that are connected by time-reversal. The Z_2 index is equal to the number of these edge state pairs modulo two, i.e. the parity of this number [23]. In case one additionally has a spin-rotation symmetry, the edge states can be labelled by the spin projection and electrons with opposite spin propagate on the edge in opposite directions, i.e. the edge states are helical.

Importantly, the robustness of the edge state with respect to random potential disorder is due to time-reversal symmetry which prohibits elastic single-particle backscattering, as shown below. Similar to Ref. [26], we consider the anti-unitary time-reversal operator θ and the overlap $\langle\phi_\mathrm{L}|\mathcal{H}|\phi_\mathrm{R}\rangle$, where $\mathcal{H}$ is the time-reversal invariant Hamiltonian which induces scattering on the one-dimensional edge, $[\mathcal{H}, \theta] = 0$, and $|\phi_{\mathrm{L(R)}}\rangle$ refers to a set of chiral modes consisting of n left (right) movers. These states are connected by time-reversal, i.e. $|\phi_{\mathrm{L}}\rangle = \theta|\phi_{\mathrm{R}}\rangle$. The time-reversal operator fulfills

$$\theta|j, m_j\rangle = i^{2m_j}|j, -m_j\rangle \ , \tag{1.5}$$

where j is the angular momentum, using the convention of Ref. [27]. The case of j being half-integer (integer) represents a system with an odd (even) number n of fermions of the same chirality and we then have $\theta^2 = -1$ ($\theta^2 = +1$). Elastic single-particle backscattering is described by the matrix elements

$$\langle\phi_{\mathrm{L}}|\mathcal{H}|\phi_{\mathrm{R}}\rangle = \langle\theta\phi_{\mathrm{R}}|\mathcal{H}|\phi_{\mathrm{R}}\rangle = \langle\theta\mathcal{H}\phi_{\mathrm{R}}|\theta^2\phi_{\mathrm{R}}\rangle = (-1)^n\langle\theta\mathcal{H}\phi_{\mathrm{R}}|\phi_{\mathrm{R}}\rangle = (-1)^n\langle\phi_{\mathrm{L}}|\mathcal{H}|\phi_{\mathrm{R}}\rangle \ . \tag{1.6}$$

To obtain the third expression, we used that $\langle\alpha|\beta\rangle = \langle\theta\beta|\theta\alpha\rangle$ holds for anti-unitary transformations θ. Therefore, the overlap $\langle\phi_{\mathrm{L}}|\mathcal{H}|\phi_{\mathrm{R}}\rangle$ (1.6) is zero for an odd number n of Kramers pairs on the edge.

The effect of electronic interactions on the stability of the quantum spin Hall effect can be analyzed using the low-energy theory of the edge states [26; 28]. Time-reversal invariant interactions that do not lead to a spontaneous symmetry breaking of the ground state leave the edge state intact, at least when they are weak [26].

A central problem in the context of topological insulators is the question of how to detect the topologically nontrivial state, i.e. how to determine the topological index for a given system. In very general terms, the topological index is a label for the topological properties of the electronic ground state wave function.

For non-interacting systems, there are a number of ways to represent the topological Z_2 index. Naturally, one could just determine the parity of the Kramers pairs on the edge which however requires to abandon periodic boundary conditions. In case of translation symmetry and a $U(1)$ spin symmetry, one may calculate the spin-resolved first Chern number, also known as TKKN (Thouless, Kohmoto, Nightingale, den Nijs) invariant [29; 30] as an integral over momentum space and define a spin Chern number [23]. The first Chern number can be directly obtained from the zero-frequency limit of the transverse quantum Hall conductivity (see Sec. 6.2.2). In case of translation symmetry and inversion symmetry, one can use the method of Fu and Kane [31] which expresses the Z_2 invariant as the product of the parity eigenvalues at the time-reversal invariant momenta in the Brillouin zone. Recently, a manifestly gauge-invariant formulation of the Z_2 invariant has been proposed [32] which only relies on time-reversal symmetry (see Sec. 6.2.3).

For interacting systems, the identification of a topological state is in general much more difficult. One can define a generalized Chern number for interacting systems in terms of an integral over single-particle Green functions in the space of momentum and frequency which makes it however often impractical to implement in numerical algorithms [33]. In the presence of inversion symmetry, one can use a generalization of the method of Fu and Kane in terms of the parity eigenvalues of the interacting single-particle Green function [34]. An overview on the computation of topological invariants can be found in Refs. [35] and [36].

We have studied an alternative way to determine the topological invariant in two dimensions, by measuring the response to a topological defect in form of a magnetic π flux (Ch. 4). A π flux on a two-dimensional lattice results from a magnetic vector potential which leads to the well-known Aharonov-Bohm effect, i.e. electrons that encircle the origin pick up a phase (of π). The idea of inserting a π flux into a quantum spin Hall insulator to define a measurement for the Z_2 index has been first discussed in Refs. [37] and [38]. In general, topological defects like π fluxes [37; 38; 39], dislocations [39] or lattice disclinations [40] lead to a unique spectral response when inserted in a topological insulator. In Ch. 4, we discuss the topological signatures of π fluxes and their application for studying interacting topological insulators in combination with quantum Monte Carlo methods.

Apart from detecting topologically nontrivial states, the degrees of freedom that are provided by π fluxes in topological insulators can be exploited to construct interacting quantum spin models. On a two-dimensional lattice, π fluxes can be arranged in almost arbitrary geometries and they experience an effective interaction which is mediated by the magnetic excitations of the topological insulator. In Ch. 5, we present a detailed study of various quantum spin models based on π flux insertions.

The classification of topological insulators in terms of the most generic quantum mechanical symmetries, time-reversal symmetry and charge conjugation symmetry [21], as outlined above, has been further refined by the theoretical prediction [41; 42; 43] and the experimental realization [44; 45; 46] of topological crystalline insulators in three dimensions. In this case, in addition to time-reversal symmetry, the two-dimensional surface has crystal symmetries that protect the topological state against perturbations. Naturally, this definition of topological crystalline insulators requires a three-dimensional bulk and a two-dimensional surface, since crystal symmetries (point group symmetries) are not defined in one dimension.

In Ch. 6, we introduce a two-dimensional counterpart to the topological crystalline insulator. In addition to time-reversal symmetry, the model we consider preserves translation symmetry along the one-dimensional edge. Despite a topologically trivial Z_2 invariant, this leads to protection of the edge states at the single-particle level. Our model is based on the Kane-Mele model [22] [see Eq. (1.13)] for quantum spin Hall insulators on the honeycomb lattice. We obtain a new model, the π *Kane-Mele model*, by threading each honeycomb plaquette with a magnetic flux of $\pm\pi$. Already for the non-interacting case, the π Kane-Mele model shows rich physics which we characterize in Secs. 6.2 and 6.4. We address the effect of correlations in the bulk as well as on the edge, using a combination of mean-field approximation, bosonization and quantum Monte Carlo methods (Secs. 6.3, 6.5, 6.6).

1.2.1 The Kane-Mele-Hubbard model

The non-interacting Kane-Mele model for the Z_2 topological insulator [22] originates from the earlier Haldane model [47] for a quantum Hall insulator. The Haldane model is characterized by a nonzero, quantized Hall conductance, without an external magnetic field. The Haldane model is formulated on the two-dimensional honeycomb lattice. The energy spectrum of

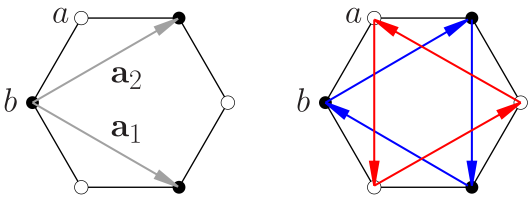

Figure 1.4: Hexagonal unit cell of the Haldane and the Kane-Mele model. The the unit vectors are $\boldsymbol{a}_{1,2} = (3/2, \mp\sqrt{3}/2)$ and the reciprocal lattice vectors are $\boldsymbol{k}_{1,2} = 2\pi(1/3, \mp 1/\sqrt{3})$. The right panel shows the sign convention we use to define the Haldane and Kane-Mele model. The second-neighbor hopping process which includes a right turn (blue) for the electron is $t_2\exp(+i\phi)$ in the Haldane model and $i\sigma\lambda$ in the Kane-Mele model.

a tight-binding Hamiltonian on the honeycomb lattice, which is realized in the material graphene, shows a linear dispersion relation at the corners of the Brillouin zone. Therefore, its low-energy behavior is similar to that of relativistic fermions which are described by the massless Dirac equation (see Ref. [48] for a review on graphene).

The Haldane model involves spinless electrons and therefore does not contain spin-orbit coupling. It includes two real hopping parameters t_1 and t_2, describing nearest-neighbor and second-neighbor hopping processes. Furthermore, a local vector potential is assumed which respects the full symmetry of the lattice and has the property of creating zero total flux through the unit cell. This leads to a constant Peierls phase factor for the second-neighbor hopping process [47], i.e. $t_2\exp(+i\phi)$, which breaks time-reversal invariance. The Haldane model is given by

$$\begin{aligned} \mathcal{H} &= t_1 \sum_{\boldsymbol{i},\boldsymbol{s}} \left[\hat{b}^\dagger_{\boldsymbol{i}+\boldsymbol{s}} \hat{a}_{\boldsymbol{i}} + \text{H.c.} \right] + t_2 \sum_{\boldsymbol{i},\boldsymbol{t}} \left[\hat{a}^\dagger_{\boldsymbol{i}+\boldsymbol{t}} \hat{a}_{\boldsymbol{i}} e^{-i\phi} + \hat{b}^\dagger_{\boldsymbol{i}+\boldsymbol{t}} \hat{b}_{\boldsymbol{i}} e^{+i\phi} + \text{H.c.} \right] \\ &= \sum_{\boldsymbol{k}} \left(\hat{b}^\dagger_{\boldsymbol{k}}, \hat{a}^\dagger_{\boldsymbol{k}} \right) H(t_1, t_2, \phi) \begin{pmatrix} \hat{b}_{\boldsymbol{k}} \\ \hat{a}_{\boldsymbol{k}} \end{pmatrix} , \end{aligned} \tag{1.7}$$

where $\boldsymbol{s} = \{\boldsymbol{0}, -\boldsymbol{a}_2, \boldsymbol{a}_1 - \boldsymbol{a}_2\}$ and $\boldsymbol{t} = \{\boldsymbol{a}_2, -\boldsymbol{a}_1, \boldsymbol{a}_1 - \boldsymbol{a}_2\}$. The Hamilton matrix is

$$H(t_1, t_2, \phi) = 2t_2 \cos(\phi)\alpha(\boldsymbol{k})\mathbf{1} + \boldsymbol{h}(t_1, t_2, \phi) \cdot \boldsymbol{\sigma} \ , \tag{1.8}$$

where $\boldsymbol{\sigma}$ is the vector of Pauli matrices and

$$\begin{aligned} \alpha(\boldsymbol{k}) &= \cos(\boldsymbol{k}\boldsymbol{a}_2) + \cos(\boldsymbol{k}\boldsymbol{a}_1) + \cos[\boldsymbol{k}(\boldsymbol{a}_2 - \boldsymbol{a}_1)] \ , \\ \beta(\boldsymbol{k}) &= \sin(\boldsymbol{k}\boldsymbol{a}_2) - \sin(\boldsymbol{k}\boldsymbol{a}_1) - \sin[\boldsymbol{k}(\boldsymbol{a}_2 - \boldsymbol{a}_1)] \ , \\ \boldsymbol{h}(t_1, t_2, \phi) &= \left(t_1 \sum_{\boldsymbol{s}} \cos(\boldsymbol{k}\boldsymbol{s}), t_1 \sum_{\boldsymbol{s}} \sin(\boldsymbol{k}\boldsymbol{s}), 2t_2 \sin(\phi)\beta(\boldsymbol{k}) \right) \ . \end{aligned} \tag{1.9}$$

In the following, we focus on the case of $\phi = \pm\pi/2$, introduce a spin index $\sigma = \pm 1$ and relabel $t_1 = -t$ and $t_2 = \lambda$. We then obtain a spinful version of the Haldane model:

$$
\begin{aligned}
\mathcal{H}^{\sigma} &= -t\sum_{\boldsymbol{i},\boldsymbol{s}}\left[\hat{b}^{\dagger}_{\boldsymbol{i}+\boldsymbol{s},\sigma}\hat{a}_{\boldsymbol{i}\sigma}+\text{H.c.}\right]+\sigma\lambda\sum_{\boldsymbol{i},\boldsymbol{t}}\left[\hat{a}^{\dagger}_{\boldsymbol{i}+\boldsymbol{t},\sigma}\hat{a}_{\boldsymbol{i}\sigma}(\mp i)+\hat{b}^{\dagger}_{\boldsymbol{i}+\boldsymbol{t},\sigma}\hat{b}_{\boldsymbol{i}\sigma}(\pm i)+\text{H.c.}\right]\\
&= \sum_{\boldsymbol{k}}\left(\hat{b}^{\dagger}_{\boldsymbol{k}\sigma},\hat{a}^{\dagger}_{\boldsymbol{k}\sigma}\right)H(-t,\sigma\lambda,\pm\pi/2)\begin{pmatrix}\hat{b}_{\boldsymbol{k}\sigma}\\ \hat{a}_{\boldsymbol{k}\sigma}\end{pmatrix}\,,
\end{aligned}
\tag{1.10}
$$

where $H(-t,\sigma\lambda,\pm\pi/2)=\boldsymbol{h}(-t,\sigma\lambda,\pm\pi/2)\cdot\boldsymbol{\sigma}$. The Kane-Mele (KM) model is essentially obtained by summing Eq. (1.10) over the spins. The KM model is usually written as

$$
\mathcal{H}=-t\sum_{\langle\boldsymbol{i},\boldsymbol{j}\rangle,\sigma}\hat{c}^{\dagger}_{\boldsymbol{i}\sigma}\hat{c}_{\boldsymbol{j}\sigma}+i\lambda\sum_{\langle\langle\boldsymbol{i},\boldsymbol{j}\rangle\rangle,\sigma}\sigma\hat{c}^{\dagger}_{\boldsymbol{i}\sigma}\nu_{\boldsymbol{i}\boldsymbol{j}}\hat{c}_{\boldsymbol{j}\sigma}\,. \tag{1.11}
$$

In this notation, $\hat{c}_{\boldsymbol{i}\sigma}=\{\hat{b}_{\boldsymbol{i}\sigma},\hat{a}_{\boldsymbol{i}\sigma}\}$, and the index $\boldsymbol{i}$ is a combined lattice site and orbital index. The sum labelled $\langle\boldsymbol{i},\boldsymbol{j}\rangle$ includes all nearest-neighbor bonds while the sum labelled $\langle\langle\boldsymbol{i},\boldsymbol{j}\rangle\rangle$ includes all next-nearest-neighbor bonds.

The phase factor $\nu_{\boldsymbol{i}\boldsymbol{j}}=\pm1$ defines the phase, the electron gets in the hopping process from $\boldsymbol{j}$ to $\boldsymbol{i}$. From the condition $\nu_{\boldsymbol{j}\boldsymbol{i}}=-\nu_{\boldsymbol{i}\boldsymbol{j}}$ it follows that left- and right-turning hopping processes have the opposite sign. By comparing the Hamiltonians (1.10) and (1.11), we observe that $\phi=+\pi/2(-\pi/2)$ corresponds to $\nu_{\boldsymbol{i}\boldsymbol{j}}=-1(+1)$ for a left turn. In the following, we choose the convention that a left turn gets a phase of minus one, i.e. $\hat{a}^{\dagger}_{\boldsymbol{i}+\boldsymbol{a}_2}\nu_{\boldsymbol{i}\boldsymbol{j}}\hat{a}_{\boldsymbol{i}}=-\hat{a}^{\dagger}_{\boldsymbol{i}+\boldsymbol{a}_2}\hat{a}_{\boldsymbol{i}}$. The KM model (1.11) restores the broken time-reversal symmetry since it combines two copies of the (spinful) Haldane model (1.10). The λ-term takes the role of an intrinsic spin-orbit coupling [23].

To allow mixing between the two spin projections, we consider a Rashba term:

$$
\begin{aligned}
\mathcal{H}_{\text{R}} &= i\frac{\lambda_{\text{R}}}{2}\sum_{\langle\boldsymbol{i},\boldsymbol{j}\rangle}c^{\dagger}_{\boldsymbol{i}}\left[\boldsymbol{e}_z(\boldsymbol{\sigma}\times\boldsymbol{d}_{\boldsymbol{i}\boldsymbol{j}})\right]c_{\boldsymbol{j}}\\
&= i\frac{\lambda_{\text{R}}}{2}\sum_{\boldsymbol{i},\boldsymbol{d}}\left[b^{\dagger}_{\boldsymbol{i}}\left[\boldsymbol{e}_z(\boldsymbol{\sigma}\times\boldsymbol{d})\right]a_{\boldsymbol{i}+\boldsymbol{f}(\boldsymbol{d})}-\text{H.c.}\right]\\
&= i\frac{\lambda_{\text{R}}}{2}\sum_{\boldsymbol{k},\boldsymbol{d}}\left[b^{\dagger}_{\boldsymbol{k}}\left(d_y\sigma_x-d_x\sigma_y\right)a_{\boldsymbol{k}}e^{i\boldsymbol{k}\boldsymbol{f}(\boldsymbol{d})}-\text{H.c.}\right]\,.
\end{aligned}
\tag{1.12}
$$

We have defined $c^{\dagger}_{\boldsymbol{i}}=(\hat{c}^{\dagger}_{\boldsymbol{i}\uparrow},\hat{c}^{\dagger}_{\boldsymbol{i}\downarrow})$ and the sum extends over $\boldsymbol{d}=\{\boldsymbol{d}^{(1)},\boldsymbol{d}^{(2)},\boldsymbol{d}^{(3)}\}$. We have $\boldsymbol{d}^{(1,2)}=(1/2,\pm\sqrt{3}/2)$, $\boldsymbol{d}^{(3)}=(-1,0)$, $\boldsymbol{f}(\boldsymbol{d}_1)=\boldsymbol{0}$, $\boldsymbol{f}(\boldsymbol{d}_2)=\boldsymbol{a}_1-\boldsymbol{a}_2$ and $\boldsymbol{f}(\boldsymbol{d}_3)=-\boldsymbol{a}_2$. The complete non-interacting KM model is then given by

$$
\begin{aligned}
\mathcal{H}_0 &= -t\sum_{\langle\boldsymbol{i},\boldsymbol{j}\rangle}c^{\dagger}_{\boldsymbol{i}}c_{\boldsymbol{j}}-\mu\sum_{\boldsymbol{i}}c^{\dagger}_{\boldsymbol{i}}c_{\boldsymbol{i}}+i\lambda\sum_{\langle\langle\boldsymbol{i},\boldsymbol{j}\rangle\rangle}c^{\dagger}_{\boldsymbol{i}}\nu_{\boldsymbol{i}\boldsymbol{j}}\sigma_z c_{\boldsymbol{j}}+i\frac{\lambda_{\text{R}}}{2}\sum_{\langle\boldsymbol{i},\boldsymbol{j}\rangle}c^{\dagger}_{\boldsymbol{i}}\left[\boldsymbol{e}_z(\boldsymbol{\sigma}\times\boldsymbol{d}_{\boldsymbol{i}\boldsymbol{j}})\right]c_{\boldsymbol{j}}\\
&= \sum_{\boldsymbol{k}}\Psi^{\dagger}_{\boldsymbol{k}}\begin{pmatrix}H(-t,+\lambda)-\mu\boldsymbol{1} & R\\ \overline{R}^{T} & H(-t,-\lambda)-\mu\boldsymbol{1}\end{pmatrix}\Psi_{\boldsymbol{k}}\\
&= \sum_{\boldsymbol{k}}\Psi^{\dagger}_{\boldsymbol{k}}M(\boldsymbol{k})\Psi_{\boldsymbol{k}}\,,
\end{aligned}
\tag{1.13}
$$

using the basis $\Psi^\dagger_{\boldsymbol{k}} = (\hat{b}^\dagger_{\boldsymbol{k}\uparrow}, \hat{a}^\dagger_{\boldsymbol{k}\uparrow}, \hat{b}^\dagger_{\boldsymbol{k}\downarrow}, \hat{a}^\dagger_{\boldsymbol{k}\downarrow})$ and the matrix

$$R = \frac{\lambda_{\mathrm{R}}}{2} \begin{pmatrix} 0 & \sum\limits_{\boldsymbol{d}} e^{i\boldsymbol{k}\boldsymbol{f}(\boldsymbol{k})}(id_y - d_x) \\ \sum\limits_{\boldsymbol{d}} e^{-i\boldsymbol{k}\boldsymbol{f}(\boldsymbol{k})}(-id_y + d_x) & 0 \end{pmatrix} . \tag{1.14}$$

An example of the eigenvalue spectrum of the Kane-Mele model is shown in Fig. 1.5.

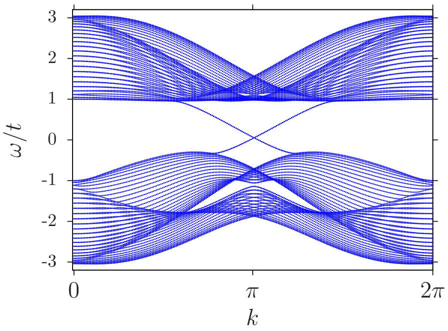

Figure 1.5: Eigenvalue spectrum of the Kane-Mele model on a ribbon geometry with zigzag edges [open (periodic) boundary conditions in the $\boldsymbol{a}_1$ ($\boldsymbol{a}_2$)-direction], showing the bulk insulating gap and the two degenerate Kramers pairs corresponding to counter-propagating states on the top and on the bottom of the ribbon. Here, $\lambda/t = 0.2$ and $\lambda_{\mathrm{R}}/t = 0.5$.

The anti-unitary time-reversal operator is given by $\theta = UK$, where K denotes complex conjugation. For the Kane-Mele model (1.13) in the given basis we may represent the unitary operator by $U = (i\sigma_y \otimes \mathbf{1}_{2\times 2})$ The condition of symmetry with respect to θ reads

$$\theta M(\boldsymbol{k})\theta^{-1} = \overline{UM(\boldsymbol{k})U^{-1}} = M(-\boldsymbol{k}) \ , \tag{1.15}$$

which is fulfilled by Kane-Mele Hamilton matrix $M(\boldsymbol{k})$.

The intrinsic spin-orbit coupling breaks the $SU(2)$ spin symmetry to a $U(1)$ spin symmetry, corresponding to conservation of the z-component of spin. The Rashba term $\mathcal{H}_{\mathrm{R}}$ further reduces the symmetry to a Z_2 spin symmetry. Naturally, we also have a $U(1)$ charge symmetry, corresponding to the conservation of charge, and a particle-hole symmetry.

The Kane-Mele-Hubbard (KMH) model is obtained by adding a Hubbard term $\mathcal{H}_U$,

$$\mathcal{H} = \mathcal{H}_0 + \mathcal{H}_U \ , \tag{1.16}$$

which inherits the symmetries of the non-interacting Hamiltonian. Written explicitly in aa $SU(2)$ invariant form, the Hubbard interaction is

$$\mathcal{H}_U = U \sum_{\boldsymbol{i}} \left(\hat{n}_{\boldsymbol{i}\uparrow} - \frac{1}{2}\right)\left(\hat{n}_{\boldsymbol{i}\downarrow} - \frac{1}{2}\right) = \frac{U}{2} \sum_{\boldsymbol{i}} (\hat{n}_{\boldsymbol{i}\uparrow} + \hat{n}_{\boldsymbol{i}\uparrow} - 1)^2 + \frac{U}{4} \ . \tag{1.17}$$

For the KMH model, the case of half-filled bands corresponds to $\mu = 0$. The bulk phase

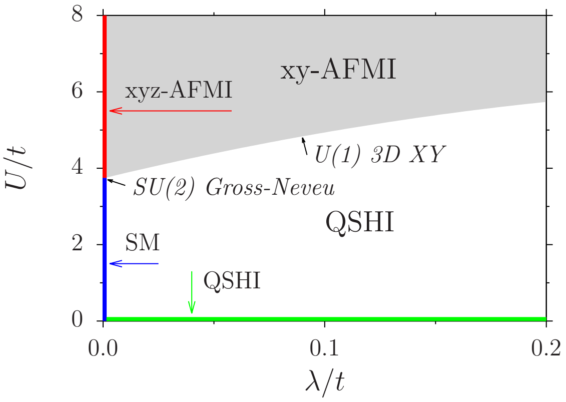

Figure 1.6: The bulk phase diagram of the KMH model (for $\lambda_{\mathrm{R}} = 0$), adapted from Refs. [49] and [50]. At $\lambda = 0$, the model reduces to the Hubbard model on the honeycomb lattice. the semi-metallic phase (SM) is separated from an isotropic antiferromagnetic Mott insulating phase (xyz-AFMI) by a continuous phase transition which falls into the $SU(2)$ Gross-Neveu universality class. At $\lambda \neq 0$, the quantum spin Hall insulating phase (QSHI) at $U = 0$ is a topological band insulator which adiabatically connects to the interacting quantum spin Hall insulator. This phase is separated from an easy-plane antiferromagnetic Mott insulator (xy-AFMI) by a continuous phase transition of the $U(1)$ 3D XY universality class.

diagram of the KMH model (Fig. 1.6, without the Rasbha term) can be calculated using numerically exact QMC simulations, since its symmetries guarantee the absence of the negative sign problem [49]. The phase boundaries and the critical exponents have been obtained using finite-size scaling analysis of the QMC data (see Refs. [49; 50]). Analytical field-theoretical calculations of the phase diagram have been performed in Refs. [51] and [17].

In the following, we concentrate on the case $\lambda/t \neq 0$. The topological band insulator at $U = 0$ is characterized by a non-trivial Z_2 index [22]. Since its protecting symmetry, the time-reversal symmetry, is not spontaneously broken at $U > 0$ and since the system stays an insulator (the single-particle gap does not close immediately at $U > 0$, see Fig. 1.7), the phase at non-zero values of the Hubbard interaction is adiabatically connected to the non-interacting phase, i.e. it is an interacting QSHI. At large values of the Hubbard interaction, a magnetic phase with transverse antiferromagnetic order is realized. This is in contrast to the isotropic antiferromagnetic order which occurs at $\lambda = 0$. The transverse antiferromagnetic order can be deduced from the behavior of the spin-orbit term in the strong-coupling limit, $U/t \to \infty$. Using second-order perturbation theory, it has been shown that in this limit an effective spin-model holds, which consists of the following terms [52],

$$\frac{4\lambda^2}{U}\left(-\hat{S}^x_{\boldsymbol{i}}\hat{S}^x_{\boldsymbol{j}} - \hat{S}^y_{\boldsymbol{i}}\hat{S}^y_{\boldsymbol{j}} + \hat{S}^z_{\boldsymbol{i}}\hat{S}^z_{\boldsymbol{j}}\right), \tag{1.18}$$

where $\boldsymbol{i}, \boldsymbol{j}$ indicate neighboring sites on the same sublattice only. This model favors second-neighbor ferromagnetic order in the XY plane and second-neighbor antiferromagnetic order in the longitudinal (z) direction. However, at $\lambda = 0$, the Hubbard model maps to an isotropic

Heisenberg model of the form $(4t^2/U)\hat{\boldsymbol{S}}_{\boldsymbol{i}} \cdot \hat{\boldsymbol{S}}_{\boldsymbol{j}}$, where $\boldsymbol{i}, \boldsymbol{j}$ indicate neighboring sites on different sublattices, leading to isotropic next-neighbor antiferromagnetic order. By taking both models together, the longitudinal direction becomes frustrated whereas XY next-neighbor antiferromagnetic order is stabilized in the strong-coupling limit.

Phenomenologically, the transition from the interacting QSHI to the xyAFMI is induced by the condensation of magnetic excitons that are the lowest-energy magnetic excitations of the correlated QSHI [53]. At the transition, the spin gap vanishes (Fig. 1.7) and the magnetic excitations are the massless Goldstone modes of the antiferromagnet since the continuous spin symmetry has been broken.

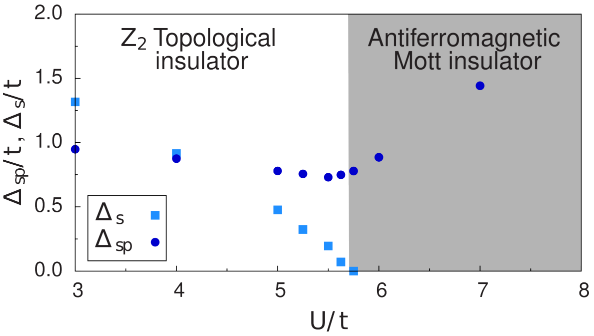

Figure 1.7: The QSHI-xyAFMI phase transition in the Kane-Mele-Hubbard model. The figure shows the spin gap $\Delta_s(\boldsymbol{k} = \boldsymbol{0})$ and the single particle gap $\Delta_{sp}(\boldsymbol{k} = \boldsymbol{K})$ as a function of the Hubbard interaction. The single-particle gap is measured at the Dirac point $\boldsymbol{K} = 2\pi(1/3, \pm 1/(3\sqrt{3}))$ and we have $\lambda/t = 0.2$ and $\lambda_{\mathrm{R}} = 0$. From a finite size scaling analysis one obtains the critical value $U_c/t = 5.70(3)$ [49].

2

Numerical Methods

This chapter begins with a review of the the auxiliary field (or determinantal) quantum Monte Carlo algorithms for the study of the many-electron problems presented in this thesis. The method is based on the path integral representation of the partition function and maps the d-dimensional quantum system to a $d+1$-dimensional classical system by introducing Euclidean (imaginary) time. The formulation of the auxiliary field QMC method we use relies on discretizing imaginary time. The auxiliary field QMC method, in its zero and finite temperature formulation, has been used to perform the finite size simulations of the Kane-Mele-Hubbard model, discussed in Chs. 4, 5, and 6.

Additionally, we briefly discuss the continuous-time quantum Monte Carlo (CT-INT) algorithm for fermions which rests on a perturbation expansion of the partition function. We have used this algorithm to study the edge states of the Kane-Mele-Hubbard model on the π flux honeycomb lattice (Ch. 6).

We also review the dynamical mean field theory (DMFT) and its momentum-space cluster extension, the dynamical cluster approximation (DCA), in combination with a finite temperature auxiliary field QMC cluster solver. We have applied this approach, which is an approximation on spatial correlations while treating temporal correlations exactly, to simulate the Kondo lattice model, see Ch. 3.

Finally, we discuss the analytic continuation of the (imaginary time dependent) QMC data to real frequencies and the calculation of dynamic correlation functions.

2.1 Auxiliary field QMC methods

The most straightforward way to solve a correlated model is to exactly diagonalize the interacting many-body Hamiltonian. Naturally, due to the exponential growth of the Hilbert space with system size this method is very limited. Currently, the best implementations of exact diagonalization are able to simulate the Heisenberg model on a square lattice of 40 spins or the half-filled Hubbard model on a 20 sites square lattice [54].

In order to solve larger systems numerically exact and without prior knowledge, one has to resort to statistical methods. Quantum Monte Carlo methods are designed to numerically solve the correlated model by sampling the most important parts of the Hilbert space. We consider the model to be solved when we have access to all possible observables and correlation functions. The QMC method can only be used efficiently in cases where the QMC sign problem does not occur, i.e. when the probability weight of a statistical configuration is strictly positive. In the auxiliary field QMC method, the absence of the sign problem can be analytically proven in a few cases using the symmetries of the Hamiltonian. The Kane-Mele-Hubbard model has no sign-problem, provided that particle-hole symmetry, time-reversal symmetry and $U(1)$ spin symmetry are present [49].

When the sign problem is too severe for a direct lattice simulation, one can turn to approximative calculations, like the DMFT for the many-electron problem at finite spatial dimensions. In the framework of DMFT and its cluster extensions, only a small number of interacting sites has to be simulated exactly which is feasible in case of a mild sign problem.

Before going into the details of the QMC algorithms, we briefly review the basic idea behind Monte Carlo sampling [55], the estimation of statistical errors, and the notion of the Green function which is the fundamental quantity in the algorithm.

2.1.1 Monte Carlo method

The task one would like to solve with Monte Carlo methods is to compute a sum over a high-dimensional configuration space Ω:

$$\langle A \rangle = \sum_{\Omega} P_{\boldsymbol{s}} A_{\boldsymbol{s}} \ , \tag{2.1}$$

where $P_{\boldsymbol{s}} = w_{\boldsymbol{s}}/Z$ is a discrete probability distribution, i.e. $\sum_{\Omega} P_{\boldsymbol{s}} = 1$ and $P_{\boldsymbol{s}} \geq 0 \ \forall \ \boldsymbol{s} \in \Omega$. Let us assume that we have a set of N_{sa} independent configurations $\{\boldsymbol{s}\}$ distributed according the probability distribution $P_{\boldsymbol{s}}$. The Monte Carlo estimator of the sum (2.1) is then given by

$$\bar{A} = \frac{1}{N_{sa}} \sum_{\{\boldsymbol{s}\}} A_{\boldsymbol{s}} \ . \tag{2.2}$$

According to the central limit theorem, the distribution function of the estimator $\bar{A}$ converges in the limit of a large number N_{sa} to a Gaussian distribution centered at $\langle A \rangle$ and with a width $\sigma = \sqrt{\operatorname{var} A / N_{\text{meas}}}$, where $\operatorname{var} A = \langle A^2 \rangle - \langle A \rangle^2$, which decays algebraically with the number of samples.

In practice, we do not have access to the normalized probability distribution $P_{\boldsymbol{s}}$. Instead, only the unnormalized probability weight $w_{\boldsymbol{s}}$ is known. However, this information is enough to devise a transition probability from one configuration to another. In order to achieve the desired set of configurations $\{\boldsymbol{s}\}$ to compute the Monte Carlo estimator (2.2), one may implement a stochastic process with importance sampling. The stochastic process is a Markov chain which depends on Monte Carlo time t and connects states in the configuration space. The transition probability connecting two subsequent states has to satisfy ergodicity and stationarity [55]. There are many possible ways to model the move from a state $\boldsymbol{s}_1$ to a state $\boldsymbol{s}_2$, for example the Metropolis algorithm or the heat bath algorithm. In the Metropolis algorithm [56], the acceptance probability $a_{2,1}$ of a transition from $\boldsymbol{s}_1$ to $\boldsymbol{s}_2$ is

$$a_{2,1} = \min\left(1, \frac{T^0_{1,2} P_{\boldsymbol{s}_2}}{T^0_{2,1} P_{\boldsymbol{s}_1}}\right) \tag{2.3}$$

where $T^0_{i,j}$ is the probability of proposing the move from $\boldsymbol{s}_j$ to $\boldsymbol{s}_i$.

In a practical implementation of the Markov process, one will always be faced with the issue of autocorrelations, i.e. measurements of $A_{\boldsymbol{s}}$ based on consecutive configurations are not truly independent. The autocorrelation function is defined as

$$c_A(t) = \frac{\sum' A_{\boldsymbol{s},i} A_{\boldsymbol{s},i+t} - \left(\sum' A_{\boldsymbol{s},i}\right)^2}{\sum' A^2_{\boldsymbol{s},i} - \left(\sum' A_{\boldsymbol{s}.i}\right)^2} \,, \tag{2.4}$$

where $\sum' = (1/N_{sa}) \sum_i^{N_{sa}}$ is the normalized sum over a sequence of measurements. One usually has $c_A(t) \sim \exp(-t/\tau_A)$. The scale τ_A is a measure of the autocorrelation time and therefore of the number of Monte Carlo steps that should lie between individual measurements. A similar scale is the equilibration time τ_{eq} which has to pass at the beginning of the simulation before the system is close to the given distribution.

2.1.2 Data analysis

The quality of the data in terms of autocorrelations can be tested by a re-binning analysis [57]. One iteratively creates a binned series of data by averaging over consecutive entries. For example, one has

$$A^{(l)}_{\boldsymbol{s},i} = \left(A^{(l-1)}_{\boldsymbol{s},2i-1} + A^{(l-1)}_{\boldsymbol{s},2i}\right)/2 \,, \tag{2.5}$$

where $i = 1, 2 \cdots N_{\text{meas}}/2^l$ and $A^{(0)}_{\boldsymbol{s},i}$ are the entries of the original, unbinned data series. Naturally, this leaves the mean value invariant but reduces the correlation between consecutive entries. Given that we have a means to calculate an estimate of the root mean square error $\Delta A^{(l)}$ for each series, the errors will converge to the correct estimate of the error ΔA for an uncorrelated data set: $\Delta A = \lim_{l \to \infty} \Delta A^{(l)}$. Furthermore, an estimate of the integrated autocorrelation time, $\tau_{A,\text{int}} = \sum_{t=1,\infty} c_A(t)$, is given by

$$\tau_{A,\text{int}} = \left[(\Delta A/\Delta A^{(0)})^2 - 1\right]/2 \,, \tag{2.6}$$

see Ref. [57].

Once we have generated sets of N_{meas} independent and identically distributed measurements of the observables $A, B, C, \cdots$, we would like to consider a generic function $\theta = \theta(\langle A \rangle, \langle B \rangle, \langle C \rangle, \cdots)$ of their expectation values and obtain an estimate $\bar{\theta}$ for its mean and an estimate $\sigma = \sqrt{\text{var}\,\theta}$ for the standard deviation of its mean. In principle, this is a difficult task, since one has to take care of error-propagation and correlations among the observables. There are non-parametric ways to obtain reliable estimates for the error and bias corrections for the mean, called re-sampling methods, notably the bootstrap and the jackknife method [58]. In the following, we concentrate on the jackknife analysis. The idea is to generate N_{meas} new sets of data samples $\{A_{\boldsymbol{s}}\}_{(i)}$, by leaving out the i-th measurement:

$$\{A_{\boldsymbol{s}}\}_{(i)} = A_{\boldsymbol{s}_1}, \cdots A_{\boldsymbol{s}_{i-1}}, A_{\boldsymbol{s}_{i+1}}, \cdots A_{\boldsymbol{s}_{N_{\text{meas}}}} \,. \tag{2.7}$$

The respective sample averages are $\bar{A}_{\boldsymbol{s}(i)} = (1/N_{\text{meas}} - 1)\sum_{j\neq i} A_{\boldsymbol{s}_j}$, and we define

$$\theta_{(i)} = \theta\left(\bar{A}_{\boldsymbol{s}(i)}, \bar{B}_{\boldsymbol{s}(i)}, \bar{C}_{\boldsymbol{s}(i)} \cdots\right) \ . \tag{2.8}$$

Using the notation $\theta_{(\cdot)} = (1/N_{\text{meas}})\sum_i \theta_{(i)}$, we obtain the estimate for the mean,

$$\bar{\theta} = \theta_{(\cdot)} \ , \tag{2.9}$$

where bias corrections to the mean are neglected (see Ref. [58]). The jackknife estimate for the error of $\bar{\theta}$ is given by

$$\begin{aligned} \Delta\theta &= \left[\frac{N_{\text{meas}}-1}{N_{\text{meas}}}\sum_{i=1}^{N_{\text{meas}}}(\theta_{(i)} - \theta_{(\cdot)})^2\right]^{1/2} \\ &= \sqrt{N_{\text{meas}}-1}\left[\left(\frac{1}{N_{\text{meas}}}\sum_{i}^{N_{\text{meas}}}\theta_{(i)}^2\right) - \theta_{(\cdot)}^2\right]^{1/2} \ . \end{aligned} \tag{2.10}$$

Note that for the limiting case of plain sample averages, $\theta = \langle A\rangle$, we have $\theta_{(\cdot)} = \bar{A}$ and $\theta_{(i)} = (N_{\text{meas}}\bar{A} - A_{\boldsymbol{s}_i})/(N_{\text{meas}} - 1)$, and Eq. (2.10) reduces to

$$\Delta A = \left[\frac{(\bar{A^2}) - (\bar{A})^2}{N_{\text{meas}}-1}\right]^{1/2} \ , \tag{2.11}$$

which is the standard (bias corrected) estimate of the error. An extension to the outlined jackknife method is the delete-k jackknife, where $\binom{N_{\text{meas}}}{k}$ samples are generated by deleting k values in the original data set.

2.1.3 Green functions

We can define a dynamic measurement as the result of a retarded correlation function $C^{\mathrm{R}}(t,t')$ which express the (linear) response of a quantum system at a time t to a perturbation at an earlier time t'. The Fourier transform of $C^{\mathrm{R}}(t,t')$ gives us information about the excitation spectrum. In the theory of many-particle systems, the most important correlation functions are Green functions. For technical reasons it is convenient to define a Green functions $\mathcal{C}(\tau,\tau')$ in imaginary time, $\tau = it$, and its discrete Fourier transform $\mathcal{C}(i\omega_n)$, in Matsubara frequencies ω_n. One can proof, for example using the Lehmann representation in the grand-canonical ensemble, that the retarded correlation function $C^{\mathrm{R}}(\omega)$ is obtained by analytical continuation: $C^{\mathrm{R}}(\omega) = \mathcal{C}(i\omega_n \to \omega + i\eta)$. This is discussed in the standard textbooks on many-particle theory, see for example Refs. [59; 60].

The central quantity is the finite-temperature single-particle Green function in imaginary time:

$$\begin{aligned} \mathcal{G}(\tau_1\nu_1;\tau_2\nu_2) &= -\langle \mathrm{T}\hat{c}_{\nu_1}(\tau_1)\hat{c}^\dagger_{\nu_2}(\tau_2)\rangle \\ &= -\mathrm{H}(\tau_1-\tau_2)\langle\hat{c}_{\nu_1}(\tau_1)\hat{c}^\dagger_{\nu_2}(\tau_2)\rangle - \zeta\mathrm{H}(\tau_2-\tau_1)\langle\hat{c}^\dagger_{\nu_2}(\tau_2)\hat{c}_{\nu_1}(\tau_1)\rangle \ , \end{aligned} \tag{2.12}$$

where T denotes time-ordering, $\mathrm{H}(\tau,\tau')$ is the Heaviside step function and $-\beta < \tau_1 - \tau_2 < \beta$. Due to translation symmetry in imaginary time, $\mathcal{G}(\tau_1\nu_1;\tau_2\nu_2) = \mathcal{G}(\tau_1-\tau_2,\nu_1;\nu_2)$. We have $\zeta = -$ ($\zeta = +$) for fermions (bosons). The brackets denote the finite-temperature expectation value.

The n-particle Green function is defined as

$$\mathcal{G}(\tau_1\nu_1,\cdots,\tau_n\nu_n;\tau_1'\nu_1',\cdots,\tau_n'\nu_n') = (-1)^n\langle \mathrm{T}\hat{c}_{\nu_1}(\tau_1)\cdots\hat{c}_{\nu_n}(\tau_n)\hat{c}^\dagger_{\nu_n'}(\tau_n')\cdots\hat{c}^\dagger_{\nu_1'}(\tau_1')\rangle \tag{2.13}$$

We proceed by stating Wick's theorem for non-interacting particles (again, for a proof, see e.g. Refs. [59; 60]). It says that the n-particle Green function can be factorized in sums of products of single-particle Green functions:

$$\mathcal{G}(\tau_1\nu_1,\cdots,\tau_n\nu_n;\tau_1'\nu_1',\cdots,\tau_n'\nu_n') = |M|_\zeta \ , \tag{2.14}$$

where the matrix M has elements $M_{ij} = \mathcal{G}(\tau_i\nu_i;\tau_j'\nu_j')$. $|M|_-$ is a determinant (fermions) and $|M|_+$ a permanent (bosons).

To simplify the notation in the following sections on QMC methods (Secs. 2.1.4 and 2.1.5), we introduce a single-particle Green function matrix $G(\tau_1,\tau_2)$, with elements

$$G(\tau_1,\tau_2)_{i,j} = -\mathcal{G}(\tau_1\nu_i;\tau_2\nu_j) \ . \tag{2.15}$$

The various Green functions in the section on the DMFT/DCA method (Sec. 2.3) are also denoted by a capital G, but they are defined as the proper thermal Green functions (2.12).

2.1.4 Projector QMC

We consider an interacting fermionic model, described by $\mathcal{H} = \mathcal{H}_\mathrm{t} + \mathcal{H}_\mathrm{U}$, where $\mathcal{H}_\mathrm{t}$ denotes the non-interacting part of the Hamiltonian and $\mathcal{H}_\mathrm{U} = U\sum_{\boldsymbol{i}}(n_{\boldsymbol{i}\uparrow}-1/2)(n_{\boldsymbol{i}\downarrow}-1/2)$ is the Hubbard interaction. At $T=0$, a very efficient method to solve the interacting model is to filter out the ground state $|\Psi_\mathrm{G}\rangle$ by repeatedly projecting the many-body Hamiltonian on a trial wave function $|\Psi_\mathrm{T}\rangle$ [61; 62],

$$|\Psi_\mathrm{G}\rangle \propto \lim_{m\to\infty}[\exp(-\Delta\tau\mathcal{H})]^m\,|\Psi_\mathrm{T}\rangle \ , \tag{2.16}$$

where $\Delta\tau > 0$ and $\langle\Psi_\mathrm{G}|\Psi_\mathrm{T}\rangle \neq 0$. The ground state is assumed to be non-degenerate. The canonical expectation value of the observable A is then given by

$$\frac{\langle\Psi_\mathrm{G}|A|\Psi_\mathrm{G}\rangle}{\langle\Psi_\mathrm{G}|\Psi_\mathrm{G}\rangle} = \frac{\langle\Psi_\mathrm{T}|e^{-(\theta/2)\mathcal{H}}Ae^{-(\theta/2)\mathcal{H}}|\Psi_\mathrm{T}\rangle}{\langle\Psi_\mathrm{T}|e^{-\theta\mathcal{H}}|\Psi_\mathrm{T}\rangle} \ , \tag{2.17}$$

where $\theta = m\Delta\tau$. The trial wave function is $|\Psi_\mathrm{T}\rangle = |\Psi_{\mathrm{T},\uparrow}\rangle\otimes|\Psi_{\mathrm{T},\downarrow}\rangle$ and it is typically written as the product wave function of the non-interacting model $\mathcal{H}_\mathrm{t}$, i.e. as a Slater determinant. In many cases it is however favorable to choose the Slater determinant to be the ground state of a trial single-particle Hamiltonian, for example to maximize the overlap with the interacting ground state. A discussion of symmetry-projected trial wave functions in projector QMC methods can be found in Ref. [63]. The trial wave function can always be written in the following form

$$|\Psi_{\mathrm{T},\sigma}\rangle = \prod_{i=1}^{N_p} \left(\boldsymbol{c}_\sigma^\dagger P_\sigma \right)_i |0\rangle \ , \tag{2.18}$$

where $\boldsymbol{c}_\sigma^\dagger = (\hat{c}_{1\sigma}^\dagger, \hat{c}_{2\sigma}^\dagger, \cdots, \hat{c}_{N_s\sigma}^\dagger)$. P_σ is a $N_s \times N_{p\sigma}$ matrix, with $N_{p\sigma} \leq N_s$. N_s denotes the number of single-particle states of the trial Hamiltonian and $N_{p\sigma}$ the number of occupied single particle-orbitals of spin σ. The matrix P contains the column eigenvectors of the trial Hamiltonian. P is referred to as a Slater determinant, although a proper determinant is only obtained in a specific representation, for example in the position representation:

$$\phi(\boldsymbol{r}_1, \cdots, \boldsymbol{r}_{N_p}) = \langle \boldsymbol{r}_1, \cdots, \boldsymbol{r}_{N_p} | \Psi_{\mathrm{T}} \rangle = \det(R^\dagger P) \ , \tag{2.19}$$

where $R_{i,j} = \chi_i(\boldsymbol{r}_j)$. Here, we already used the first of two important properties of Slater determinants: (i) the overlap of two Slater determinants is given by the determinant of the matrix product, and (ii) the evolution of a Slater determinant with a single-particle evolution operator described by a Hermitian (or anti-Hermitian) matrix is again a Slater determinant. A proof of both properties can be found in Ref. [62].

In order to obtain $|\Psi_{\mathrm{G}}\rangle$ starting from a single Slater determinant $|\Psi_{\mathrm{T}}\rangle$, we have to find a way to express the evolution operator $\exp(-\Delta\tau\mathcal{H})$ containing the quartic Hubbard interaction in terms of single-particle operators. This is essentially accomplished by the Hubbard-Stratonovich (HS) transformation [64]. It transforms the interacting evolution operator in a field-dependent single-particle evolution operator which is integrated over the configuration space of the (bosonic) field.

Prior to applying the HS transformation, we separate the non-interacting part $\mathcal{H}_{\mathrm{t}}$ from the interacting part $\mathcal{H}_{\mathrm{U}}$ via the Trotter decomposition:

$$\begin{aligned} e^{-\theta\mathcal{H}} &= \lim_{\Delta\tau\to 0} \left(e^{-\Delta\tau\mathcal{H}_{\mathrm{U}}} e^{-\Delta\tau\mathcal{H}_{\mathrm{t}}} \right)^m \\ &= \left(e^{-\Delta\tau\mathcal{H}_{\mathrm{U}}} e^{-\Delta\tau\mathcal{H}_{\mathrm{t}}} \right)^m + \frac{\Delta\tau}{2} X(\mathcal{H}_{\mathrm{t}}, \mathcal{H}_{\mathrm{U}}) + \mathcal{O}(\Delta\tau^2) \ . \end{aligned} \tag{2.20}$$

The operator $X(\mathcal{H}_{\mathrm{t}}, \mathcal{H}_{\mathrm{U}})$ can be shown [62] to be an anti-Hermitian operator, $X = -X^\dagger$. Then, and under the condition that A, $\mathcal{H}_{\mathrm{t}}$ and $\mathcal{H}_{\mathrm{U}}$ are simultaneously representable by real numbers, it follows that the term linear in $\Delta\tau$ vanishes in the expectation value for the Hermitian observable A [in terms of the ground state expectation value, Eq. (2.17), or the trace over Fock space, Eq. (2.41)]. However, the Trotter decomposition is not unique, and in some cases a symmetric decomposition or expansion to higher-order can be favorable. A discussion of systematic higher-order approximations of $\exp(-\theta\mathcal{H})$ can be found in Ref. [65].

The HS decomposition for evolution operators with four fermionic operators, like the Hubbard term, is an operator identity which originates from the Gaussian integral [64]. A general, discrete form of the transformation [66] can be written as

$$e^{-\Delta\tau\sum_{\boldsymbol{i}} O_{\boldsymbol{i}}^2} = C\sum_{\boldsymbol{s}}\left[\prod_{\boldsymbol{i}} p(s_{\boldsymbol{i}})\right] e^{\sum_{\boldsymbol{i}}\tilde{O}_{\boldsymbol{i}}} \ . \tag{2.21}$$

$O_{\boldsymbol{i}}$ and $\tilde{O}_{\boldsymbol{i}}$ are single-particle operators, $p(s_{\boldsymbol{i}})$ is a normalized probability distribution, obeying $\sum_{s_{\boldsymbol{i}}} p(s_{\boldsymbol{i}}) = 1$ and C is a constant. The sum runs over all configurations of the auxiliary field $s_{\boldsymbol{i}}$ on the lattice, which is denoted by the vector notation $\boldsymbol{s} = (s_{\boldsymbol{i}_1}, \cdots, s_{\boldsymbol{i}_N})$. This transformation therefore converts the interacting evolution operator on the lattice to many non-interacting evolution operators that live in a fluctuating external field. The implementation of continuous Hubbard-Stratonovich decompositions in the PQMC method is discussed in Ref. [66].

For the Hubbard interaction, two widely used possibilities [62; 67] involve single-particle operators $\tilde{O}_{\boldsymbol{i}}$ which are proportional to the charge density (magnetization) $n_{\boldsymbol{i}\uparrow} + (-)n_{\boldsymbol{i}\downarrow}$. In the latter case, the auxiliary field couples to the S_z component thereby breaking the $SU(2)$ spin symmetry for a given field configuration. We then have

$$e^{-\Delta\tau\mathcal{H}_{\mathrm{U}}} = \gamma^N \sum_{\boldsymbol{s}} e^{\alpha\sum_{\boldsymbol{i}} s_{\boldsymbol{i}}(n_{\boldsymbol{i}\uparrow}-n_{\boldsymbol{i}\downarrow})} \ , \tag{2.22}$$

where $s_{\boldsymbol{i}} = \pm 1$, $\gamma = \exp(-\Delta\tau U/4)/2$ and $\cosh(\alpha) = \exp(\Delta\tau U/2)$. Alternatively, one obtains an approximation to the evolution operator by the following series expansion [62]

$$e^{-\Delta\tau O_{\boldsymbol{i}}^2} = \sum_{s=\pm1,\pm2} \gamma(s) e^{i\sqrt{\Delta\tau}\eta(s)O_{\boldsymbol{i}}} + \mathcal{O}(\Delta\tau^4) \ , \tag{2.23}$$

with

$$\begin{aligned} &\gamma(\pm1) = (1+\sqrt{6}/3)/4 \ , \ \gamma(\pm2) = (1-\sqrt{6}/3)/4 \ , \\ &\eta(\pm1) = \pm\sqrt{2(3-\sqrt{6})} \ , \ \eta(\pm2) = \pm\sqrt{2(3+\sqrt{6})} \ . \end{aligned} \tag{2.24}$$

Eq. (2.23) can be easily proven by expanding its right hand side to eighth order in $O_{\boldsymbol{i}}$. The transformation introduces therefore two Ising field per lattice site $\boldsymbol{i}$, taking the values ±1 and ±2. Note that the $\Delta\tau$ error of Eq. (2.23) propagates to an error of order $\Delta\tau^3$ in the evolution operator $\exp(-\theta\mathcal{H})$ (2.20), which is however dominated by the Trotter error of order $\Delta\tau^2$. For example, in case of the Hubbard interaction, the interaction on each site is decoupled with $O_{\boldsymbol{i}} = \sqrt{U/2}(n_{\boldsymbol{i}\uparrow} + n_{\boldsymbol{i}\downarrow} - 1)$, and Eq. (2.23) becomes

$$e^{-\Delta\tau\sum_{\boldsymbol{i}}(O_{\boldsymbol{i}\uparrow}+O_{\boldsymbol{i}\downarrow})^2} = \sum_{\boldsymbol{s}}\prod_{\sigma}\left[\prod_{\boldsymbol{i}}\gamma(s_{\boldsymbol{i}})\right] e^{i\sqrt{\Delta\tau}\sum_{\boldsymbol{i}}\eta(s_{\boldsymbol{i}})O_{\boldsymbol{i}\sigma}} \ , \tag{2.25}$$

where we defined $O_{\boldsymbol{i}\sigma} = \sqrt{U/2}(n_{\boldsymbol{i}\sigma} - 1/2)$.

We now have all the ingredients to evaluate the expectation value (2.17) by rewriting the evolution operator (2.20) in single-particle notation. Following Ref. [62], we write the hopping part of the Hamiltonian in matrix form, as $H_\mathrm{t} = \sum_{x,y} \hat{c}_x^\dagger T_{xy} \hat{c}_x = \boldsymbol{c}^\dagger T \boldsymbol{c}$ where $x = (\boldsymbol{i}, \sigma)$ indexes both lattice site and spin projection. In the same manner, we write the single-particle operator in Eq. (2.21) as $\tilde{O}_{\boldsymbol{i}} = \boldsymbol{c}^\dagger V(\boldsymbol{s}) \boldsymbol{c}$ where the matrix $V(\boldsymbol{s})$ depends on the vector of the local fields $\boldsymbol{s}$. The HS transformation (2.21) accordingly becomes

$$e^{-\Delta\tau \sum_{\boldsymbol{i}} O_{\boldsymbol{i}}^2} = C \sum_{\boldsymbol{s}} \left[\prod_{\boldsymbol{i}} p(s_{\boldsymbol{i}}) \right] e^{\boldsymbol{c}^\dagger V(\boldsymbol{s}) \boldsymbol{c}} \; . \tag{2.26}$$

We proceed by defining the imaginary time propagators,

$$U_{\boldsymbol{S}}(\tau_2, \tau_1) = \prod_{n=n_1+1}^{n_2} e^{\boldsymbol{c}^\dagger V(\boldsymbol{s}_n) \boldsymbol{c}} e^{-\Delta\tau \boldsymbol{c}^\dagger T \boldsymbol{c}} \; , \; B_{\boldsymbol{S}}(\tau_2, \tau_1) = \prod_{n=n_1+1}^{n_2} e^{V(\boldsymbol{s}_n)} e^{-\Delta\tau T} \; , \tag{2.27}$$

where $n_i \Delta\tau = \tau_i$ and $\tau_2 > \tau_1$. $B_{\boldsymbol{S}}(\tau_2, \tau_1)$ is the matrix representation of $U_{\boldsymbol{S}}(\tau_2, \tau_1)$ and $U_{\boldsymbol{S}}(\tau_1, \tau_1) = 1$. The auxiliary field configuration is indexed by the $N \times m$ matrix $\boldsymbol{S} = \boldsymbol{s}_1, \cdots, \boldsymbol{s}_m)$. We can finally write

$$e^{-\theta\mathcal{H}} = C^m \sum_{\boldsymbol{S}} \left[\prod_{n=1}^{m} \prod_{\boldsymbol{i}} p[s_{\boldsymbol{i}n}] \right] U_{\boldsymbol{S}}(\theta, 0) + [\Delta\tau\text{-terms}] \; , \tag{2.28}$$

where the sum $\sum_{\boldsymbol{S}} = \sum_{\boldsymbol{s}_1} \cdots \sum_{\boldsymbol{s}_m}$ was defined. As explained above, from the $\Delta\tau$-terms only the quadratic term will survive in observables, given the Trotter decomposition in $\exp(-\theta\mathcal{H})$ (2.20). The partition function is now given by a sum of overlaps of two Slater determinants:

$$Z = \langle \Psi_\mathrm{T} | e^{-\theta\mathcal{H}} | \Psi_\mathrm{T} \rangle = C^m \sum_{\boldsymbol{S}} \left[\prod_{n=1}^{m} \prod_{\boldsymbol{i}} p[s_{\boldsymbol{i}n}] \right] \det \left[P^\dagger B_{\boldsymbol{S}}(\theta, 0) P \right] + \mathcal{O}(\Delta\tau^2) \; . \tag{2.29}$$

The expectation value (2.17) can accordingly be written as

$$\frac{\langle \Psi_\mathrm{T} | e^{-(\theta/2)\mathcal{H}} A e^{-(\theta/2)\mathcal{H}} | \Psi_\mathrm{T} \rangle}{\langle \Psi_\mathrm{T} | e^{-\theta\mathcal{H}} | \Psi_\mathrm{T} \rangle} = \sum_{\boldsymbol{S}} P_{\boldsymbol{S}} \langle A \rangle_{\boldsymbol{S}} + \mathcal{O}(\Delta\tau^2) \; , \tag{2.30}$$

using $P_{\boldsymbol{S}} = w_{\boldsymbol{S}} / Z$,

$$w_{\boldsymbol{S}} = \left[\prod_{n=1}^{m} \prod_{\boldsymbol{i}} p[s_{\boldsymbol{i}n}] \right] \det \left[P^\dagger B_{\boldsymbol{S}}(\theta, 0) P \right] \; , \tag{2.31}$$

and the non-interacting expectation value $\langle A \rangle_{\boldsymbol{S}}$ with respect to a pair of Slater determinants,

$$\langle A \rangle_{\boldsymbol{S}} = \frac{\langle \Psi_\mathrm{T} | U_{\boldsymbol{S}}(\theta, \theta/2) \; A \; U_{\boldsymbol{S}}(\theta/2, 0) | \Psi_\mathrm{T} \rangle}{\langle \Psi_\mathrm{T} | U_{\boldsymbol{S}}(\theta, 0) | \Psi_\mathrm{T} \rangle} \; . \tag{2.32}$$

Formally, Eq. (2.30) brings us back to Eq. (2.1). However, the distribution $P_{\boldsymbol{S}}$ is not necessarily positive definite (see Sec. 2.1.7).

For the Hubbard model, the phase space is the space of $\mathcal{O}(mN)$ Ising spins and, since direct summation is not feasible, has to be sampled by Monte Carlo methods.

2.1.4.1 Calculation of Green functions

In the following, we briefly review the calculation of observables [62]. According to Eq. (2.15), the fermionic single-particle imaginary-time Green function is given by

$$G_{\boldsymbol{S}}(\tau_1,\tau_2)_{x,y} = \begin{cases} \langle \hat{c}_x(\tau_1)\hat{c}^\dagger_y(\tau_2)\rangle_{\boldsymbol{S}} & \text{if} \quad \tau_1 \geq \tau_2 \\ -\langle \hat{c}^\dagger_y(\tau_2)\hat{c}_x(\tau_1)\rangle_{\boldsymbol{S}} & \text{if} \quad \tau_1 < \tau_2 \end{cases} , \tag{2.33}$$

where $\langle \bullet \rangle_{\boldsymbol{S}}$ is a ground state expectation value (or a thermal expectation value, at finite temperatures). In the PQMC algorithm, we measure symmetrically around the central time slice at $n\Delta\tau = \theta/2$. We therefore let

$$\tau_{1,2} \to \theta/2 \pm (\tau_1 - \tau_2)/2 \tag{2.34}$$

Note that we evaluate the Green function of a non-interacting model which defined by the hopping term and the auxiliary field configuration $\boldsymbol{S}$. Importantly, we know that Wick's theorem (2.14) holds, both for equal-time and time displaced multi-point correlation functions. The equal-time ground state Green function can be obtained from a generating functional of the form

$$F[\eta] = \langle \Psi_{\mathrm{T}} | U_{\boldsymbol{S}}(\theta,\tau) e^{\eta \boldsymbol{c}^\dagger A \boldsymbol{c}} \; U_{\boldsymbol{S}}(\tau,0) | \Psi_{\mathrm{T}} \rangle \; , \tag{2.35}$$

where $A_{i,j} = \delta_{i,y}\delta_{j,x}$. One obtains [62]:

$$\begin{aligned} G_{\boldsymbol{S}}(\tau,\tau)_{x,y} &= \langle \hat{c}_x(\tau)\hat{c}^\dagger_y(\tau)\rangle_{\boldsymbol{S}} = \delta_{x,y} - \frac{\partial}{\partial\eta} \ln F[\eta]\Big|_{\eta=0} \\ &= \left\{ 1 - B_{\boldsymbol{S}}(\tau,0) P \left[P^\dagger B_{\boldsymbol{S}}(\theta,0) P \right]^{-1} P^\dagger B_{\boldsymbol{S}}(\theta,\tau) \right\}_{x,y} . \end{aligned} \tag{2.36}$$

Furthermore, since

$$G_{\boldsymbol{S}}(\tau,\tau) G_{\boldsymbol{S}}(\tau,\tau) = G_{\boldsymbol{S}}(\tau,\tau) \; , \tag{2.37}$$

which follows directly from Eq. (2.36), $G_{\boldsymbol{S}}(\tau,\tau)_{x,y}$ is a projector [68]. The imaginary time displaced Green functions (2.33) are

$$\begin{aligned} G_{\boldsymbol{S}}(\tau_1,\tau_2)_{x,y} &\overset{\tau_1 \geq \tau_2}{=} \frac{\langle \Psi_{\mathrm{T}} | U_{\boldsymbol{S}}(\theta,\tau_1) \; \hat{c}_x \; U_{\boldsymbol{S}}(\tau_1,\tau_2) \; \hat{c}^\dagger_y \; U_{\boldsymbol{S}}(\tau_2,0) | \Psi_{\mathrm{T}} \rangle}{\langle \Psi_{\mathrm{T}} | U_{\boldsymbol{S}}(\theta,0) | \Psi_{\mathrm{T}} \rangle} \\ &= \left[B_{\boldsymbol{S}}(\tau_1,\tau_2) G_{\boldsymbol{S}}(\tau_2,\tau_2) \right]_{x,y} \; , \\ G_{\boldsymbol{S}}(\tau_1,\tau_2)_{x,y} &\overset{\tau_1 \leq \tau_2}{=} - \left[\left(1 - G_{\boldsymbol{S}}(\tau_1,\tau_1) \right) B^{-1}_{\boldsymbol{S}}(\tau_2,\tau_1) \right]_{x,y} . \end{aligned} \tag{2.38}$$

Note that in a measurement, we will use the rule (2.34) for the values $\tau_{1,2}$ can take. Importantly, we have the composition identity (assuming $\tau_1 > \tau_2 > \tau_1$)

$$\begin{aligned} G_{\boldsymbol{S}}(\tau_1,\tau_3) &= B_{\boldsymbol{S}}(\tau_1,\tau_3) G_{\boldsymbol{S}}(\tau_3,\tau_3) = B_{\boldsymbol{S}}(\tau_1,\tau_3) G_{\boldsymbol{S}}(\tau_3,\tau_3) B^{-1}_{\boldsymbol{S}}(\tau_1,\tau_2) B_{\boldsymbol{S}}(\tau_1,\tau_2) G_{\boldsymbol{S}}(\tau_3,\tau_3) \\ &= G_{\boldsymbol{S}}(\tau_1,\tau_2) G_{\boldsymbol{S}}(\tau_2,\tau_3) \; , \end{aligned} \tag{2.39}$$

which is readily obtained using Eq. (2.36) and (2.38). The identity (2.39) allows us to rewrite the time displaced Green function (2.38) as

$$G_{\boldsymbol{S}}(\tau_1, \tau_2) = \prod_{n=0}^{N_\tau - 1} G_{\boldsymbol{S}}\left[\tau_2 + (n+1)\tau, \tau_2 + n\tau\right] \ , \tag{2.40}$$

where the interval $\tau_1 - \tau_2$ is broken up in to $N_\tau = (\tau_1 - \tau_2)/\tau$ smaller intervals. For each $G_{\boldsymbol{S}}(\tau_2 + (n+1)\tau, \tau_2 + n\tau)$, stretching over a distance of τ, Eq. (2.38) is applied. The direct application of Eq. (2.38) is numerically instable when the distance $\tau_1 - \tau_2$ is large. In this case, $G_{\boldsymbol{S}}(\tau_1, \tau_2)$ can be calculated in a numerically stable manner using Eq. (2.40).

Prior to discussing the Monte Carlo updates, we repeat the steps leading to the partition function and the Green functions for the finite-temperature case.

2.1.5 Finite-temperature QMC methods

Two finite-temperature formulations of a QMC algorithm to solve field theories with fermionic degrees of freedom on a lattice have been introduced by Blankenbecler, Scalapino and Sugar (BSS) [69; 70] and by Hirsch and Fye (HF) [71]. Both methods, the BSS-QMC and the HF-QMC method, rely on the same path-integral formulation of the partition function.

Each algorithm, however, makes use of a different subset of the set of equations that describe the many-body problem: the BSS-QMC algorithm is formulated with matrices whose dimension depends on the lattice size N ("space formulation") and the HF-QMC algorithm is formulated with matrices whose dimension depends on the number of interacting sites N_c, where $N_c \leq N$, and the inverse temperature β ("space-time formulation").

Consequently, the computing time scales differently: we have a scaling of $\mathcal{O}[\beta N^3]$ (BSS-QMC), and a scaling with $\mathcal{O}[(\beta N_c)^3]$ (HF-QMC).

The HF-QMC method can access the thermodynamic limit, in the sense that the lattice size N drops out of the scaling. This property makes it explicitly useful for impurity problems with a small number N_c of interacting impurities.

In the end, we would like to numerically calculate the thermal expectation value of an observable A in the grand-canonical ensemble as a trace over Fock space,

$$\langle A \rangle = \frac{\mathrm{Tr}\left[e^{-\beta(\mathcal{H}-\mu\mathcal{N})}A\right]}{\mathrm{Tr}\left[e^{-\beta(\mathcal{H}-\mu\mathcal{N})}\right]} \ . \tag{2.41}$$

We can profit from the above obtained results, Eq. 2.20 and 2.28, and directly state the partition function

$$Z = C^m \sum_{\boldsymbol{S}} \left[\prod_{n=1}^{m} \prod_{\boldsymbol{i}} p[s_{\boldsymbol{i}n}]\right] \mathrm{Tr}\left[U_{\boldsymbol{s}}(\beta, 0)\right] + \mathcal{O}(\Delta\tau^2) \ . \tag{2.42}$$

Since the operator $U_{\boldsymbol{S}}(\beta, 0)$ is a product of single-particle operators, the fermionic trace can can be carried out explicitly:

$$\mathrm{Tr}\left[U_{\boldsymbol{S}}(\beta, 0)\right] = \det\left[1 + B_{\boldsymbol{S}}(\beta, 0)\right] \ . \tag{2.43}$$

Eq. (2.43) is proven using the functional integral formalism and expressing the trace with Fermion coherent states [60]. Alternative proofs are presented in Ref. [69] and Ref. [62].

Finally, one obtains

$$\frac{\mathrm{Tr}\left[e^{-\beta(\mathcal{H}-\mu\mathcal{N})}A\right]}{\mathrm{Tr}\left[e^{-\beta(\mathcal{H}-\mu\mathcal{N})}\right]} = \sum_{\boldsymbol{S}} P_{\boldsymbol{S}} A_{\boldsymbol{S}} + \mathcal{O}(\Delta\tau^2) \ , \tag{2.44}$$

using $P_{\boldsymbol{S}} = w_{\boldsymbol{S}}/Z$,

$$w_{\boldsymbol{S}} = \left[\prod_{n=1}^{m}\prod_{\boldsymbol{i}} p[s_{\boldsymbol{i}n}]\right] \det\left[1 + B_{\boldsymbol{S}}(\beta,0)\right] \ , \tag{2.45}$$

and

$$A_{\boldsymbol{S}} = \frac{\mathrm{Tr}\left[U_{\boldsymbol{S}}(\beta,\tau)\ A\ U_{\boldsymbol{S}}(\tau,0)\right]}{\mathrm{Tr}\left[U_{\boldsymbol{S}}(\beta,0)\right]} \ . \tag{2.46}$$

In order to introduce the concepts of the BSS-QMC and the HF-QMC method in parallel, it is convenient to factorize the partition function (2.42) in spin components. In doing that, we assume that the many-body Hamiltonian has a $U(1)$ spin symmetry. We define the sum

$${\sum_{\boldsymbol{S}}}' = C^m \sum_{\boldsymbol{S}} \left[\prod_{n=1}^{m}\prod_{\boldsymbol{i}} p[s_{\boldsymbol{i}n}]\right] \ , \tag{2.47}$$

and the spin-dependent evolution matrix $B^{\sigma}_{\boldsymbol{S}}(\beta,0)$,

$$B^{\sigma}_{\boldsymbol{S}}(\beta,0) = \prod_{n=1}^{m} e^{V_\sigma(\boldsymbol{s}_n)} e^{-\Delta\tau T_\sigma} = \prod_{n=1}^{m} B^{\sigma}_{\boldsymbol{s}_n} \ . \tag{2.48}$$

The partition function then is, omitting the $\Delta\tau$-correction,

$$\begin{aligned} Z &= C^m \sum_{\boldsymbol{S}} \left[\prod_{n=1}^{m}\prod_{\boldsymbol{i}} p[s_{\boldsymbol{i}n}]\right] \mathrm{Tr}\left[U_{\boldsymbol{s}}(\beta,0)\right] \\ &= {\sum_{\boldsymbol{S}}}' \mathrm{Tr}\left[\prod_{n=1}^{m}\prod_{\sigma} e^{\boldsymbol{c}_\sigma^\dagger V_\sigma(\boldsymbol{s}_n)\boldsymbol{c}_\sigma} e^{-\Delta\tau \boldsymbol{c}_\sigma^\dagger T_\sigma \boldsymbol{c}_\sigma}\right] \\ &= {\sum_{\boldsymbol{S}}}' \prod_{\sigma} \det\left[1 + B^{\sigma}_{\boldsymbol{S}}(\beta,0)\right] \ . \end{aligned} \tag{2.49}$$

The matrices in the last line of Eq. (2.49) are of size $N\times N$. We have the following determinant identity:

$$\det\left[1 + B^{\sigma}_{\boldsymbol{S}}(\beta,0)\right] = \det O^{\sigma}_{\boldsymbol{S}} \ , \tag{2.50}$$

where $O^{\sigma}_{\boldsymbol{S}}$ is a very sparse $Nm\times Nm$ matrix and its components are the $2m$ spatial matrices,

$$(O^{\sigma}_{\boldsymbol{S}})_{ab} = \delta_{a,b} + B^{\sigma}_{\boldsymbol{s}_a}(2\delta_{a,1} - 1)\delta_{a,b+1} \ . \tag{2.51}$$

The identity (2.50) can be shown for example by transforming $O^{\sigma}_{\boldsymbol{S}}$ to a triangular matrix using Gaussian elimination. The determinant is then given by the product of the diagonal entries, which is the left side of Eq. (2.50).

2.1.5.1 Calculation of Green functions

In the following, we show how the equal-time and imaginary-time displaced Green functions are calculated in the finite-temperature algorithms. The equal-time Green function is derived in a similar manner as the ground state Green function, using the generating functional $F[\eta]$ (2.35) with respect to a fermionic trace instead of $\langle\Psi_\mathrm{T}|\bullet|\Psi_\mathrm{T}\rangle$. This leads to

$$\begin{aligned} G_{\boldsymbol{S}}(\tau,\tau)_{x,y} &= \langle\hat{c}_x(\tau)\hat{c}_y^\dagger(\tau)\rangle_{\boldsymbol{S}} = \delta_{x,y} - \frac{\partial}{\partial\eta}\ln F[\eta]\Big|_{\eta=0} \\ &= \left[1 + B_{\boldsymbol{S}}(\tau,0)B_{\boldsymbol{S}}(\beta,\tau)\right]^{-1}_{x,y} \ . \end{aligned} \tag{2.52}$$

There are two ways to obtain the time displaced Green function (2.33), where now $\langle\bullet\rangle_{\boldsymbol{S}}$ is a thermal expectation value. On the one hand, $G_{\boldsymbol{S}}(\tau_1,\tau_2)$ is given by

$$\begin{aligned} G_{\boldsymbol{S}}(\tau_1,\tau_2)_{x,y} &\overset{\tau_1\geq\tau_2}{=} \frac{\mathrm{Tr}\left[U_{\boldsymbol{S}}(\beta,\tau_1)\;\hat{c}_x\;U_{\boldsymbol{S}}(\tau_1,\tau_2)\;\hat{c}_y^\dagger\;U_{\boldsymbol{S}}(\tau_2,0)\right]}{\mathrm{Tr}\left[U_{\boldsymbol{S}}(\beta,0)\right]} \\ &= \left[B_{\boldsymbol{S}}(\tau_1,\tau_2)G_{\boldsymbol{S}}(\tau_2,\tau_2)\right]_{x,y} \ , \\ G_{\boldsymbol{S}}(\tau_1,\tau_2)_{x,y} &\overset{\tau_1\leq\tau_2}{=} -\left[\left(1 - G_{\boldsymbol{S}}(\tau_1,\tau_1)\right)B_{\boldsymbol{S}}^{-1}(\tau_2,\tau_1)\right]_{x,y} \ , \end{aligned} \tag{2.53}$$

similar to zero-temperature expressions in Eq. (2.38). Additionally, we have the identity

$$G_{\boldsymbol{S}}(\tau_1,\tau_1) \overset{\tau_1\geq\tau_2}{=} B_{\boldsymbol{S}}(\tau_1,\tau_2)G_{\boldsymbol{S}}(\tau_2,\tau_2)B_{\boldsymbol{S}}^{-1}(\tau_1,\tau_2) \ , \tag{2.54}$$

see Ref. [62].

The n-particle Green functions can be also derived along the lines of Eq. (2.36) and (2.52), but using a generating functional $F[\eta_1,\cdots,\eta_n]$ which contains n source terms. The final result is a sum of products of single-particle Green functions which proves the validity of Wick's theorem for each field configuration $\boldsymbol{S}$. Since the calculation is quite lengthy, we refer the reader to Ref. [62] and Ref. [72] for the proof.

On the other hand, the space-time matrix $G_{\boldsymbol{S}}^\sigma$ of the imaginary time displaced Green functions is given by [71; 73]

$$(O_{\boldsymbol{S}}^\sigma)^{-1} = G_{\boldsymbol{S}}^\sigma \ , \tag{2.55}$$

where the entries are again the $N\times N$ matrices

$$(G_{\boldsymbol{S}}^\sigma)_{n_1,n_2} = G_{\boldsymbol{S}}^\sigma(n_1\Delta\tau, n_2\Delta\tau) = G_{\boldsymbol{S}}^\sigma(\tau_1,\tau_2) \ , \tag{2.56}$$

see Eq. (2.33).

The potential which describes the electronic interaction is diagonal in imaginary time,

$$V_\sigma(\boldsymbol{S}) = \mathrm{diag}\ \left[V_\sigma(\boldsymbol{s}_1), V_\sigma(\boldsymbol{s}_2), \cdots, V_\sigma(\boldsymbol{s}_m)\right] \tag{2.57}$$

We consider two configurations, labelled $\boldsymbol{S}$ and $\boldsymbol{S}'$. The associated Green function matrices are related by the following Dyson equation [74]

$$\begin{aligned} G^\sigma_{\boldsymbol{S}} &= \left[e^{-V_\sigma(\boldsymbol{S}')} O^\sigma_{\boldsymbol{S}'} + e^{-V_\sigma(\boldsymbol{S})} O^\sigma_{\boldsymbol{S}} - e^{-V_\sigma(\boldsymbol{S}')} O^\sigma_{\boldsymbol{S}'}\right]^{-1} e^{-V_\sigma(\boldsymbol{S})} \\ &= G^\sigma_{\boldsymbol{S}'} + G^\sigma_{\boldsymbol{S}'} \Delta^\sigma (1 - G^\sigma_{\boldsymbol{S}}) \; , \end{aligned} \tag{2.58}$$

where $\Delta^\sigma = e^{V_\sigma(\boldsymbol{S}')} e^{-V_\sigma(\boldsymbol{S})} - 1$. This is equivalent to

$$G^\sigma_{\boldsymbol{S}'} = G^\sigma_{\boldsymbol{S}} \left[1 + \Delta^\sigma \left(1 - G^\sigma_{\boldsymbol{S}}\right)\right]^{-1} \; . \tag{2.59}$$

One finds a similar Dyson equation for the equal-time Green functions, $G^\sigma_{\boldsymbol{S}}(\tau, \tau)$. To obtain this result, we assume that the configurations $\boldsymbol{S}$ and $\boldsymbol{S}'$ differ only at one point $\tau = n\Delta\tau$ in imaginary time. Then,

$$\Delta^\sigma = \text{diag}\;(0, \cdots, 0, \Delta^\sigma_n, 0, \cdots, 0) \; , \tag{2.60}$$

where $\Delta^\sigma_n = e^{V_\sigma(\boldsymbol{s}'_n)} e^{-V_\sigma(\boldsymbol{s}_n)} - 1$. Using Eq. (2.52), we can write

$$\begin{aligned} G^\sigma_{\boldsymbol{S}'}(\tau, \tau) &= \left[1 + B_{\boldsymbol{S}'}(\tau, 0) B_{\boldsymbol{S}'}(\beta, \tau)\right]^{-1} \\ &= \left[1 + (1 + \Delta^\sigma_n) B_{\boldsymbol{S}}(\tau, 0) B_{\boldsymbol{S}}(\beta, \tau)\right]^{-1} \\ &= G^\sigma_{\boldsymbol{S}}(\tau, \tau) \left[1 + \Delta^\sigma_n \left(1 - G^\sigma_{\boldsymbol{S}}(\tau, \tau)\right)\right]^{-1} \; . \end{aligned} \tag{2.61}$$

This identity is easily recovered by going backwards and substituting $1 = 1 + G^\sigma_{\boldsymbol{S}}(\tau, \tau) - G^\sigma_{\boldsymbol{S}}(\tau, \tau)$ in the last line as well as using the matrix identity $(A+B)^{-1} = A^{-1} - A^{-1} B (A+B)^{-1}$.

At this point, it is important to note one essential feature of the HF-QMC method, when the number of interacting sites N_c is smaller than the total number of lattice sites N. We denote the set of impurities by $\mathcal{M}$, such that there are N_c elements $\boldsymbol{r}_x \in \mathcal{M}$. In contrary to the assumption above, we now consider two arbitrary configurations $\boldsymbol{S}$ and $\boldsymbol{S}'$. We use the index $x = (\tau_x, \boldsymbol{i}_x)$ and $x^I = (\tau_x, \boldsymbol{r}_x)$ for the impurity entries only. Since

$$\left(\Delta^\sigma\right)_{x,y} = \left(\Delta^\sigma\right)_{x,x} \delta_{x,y} \delta_{\boldsymbol{i}_x, \boldsymbol{r}_x} \; , \tag{2.62}$$

we can pull out the impurity contribution in the Dyson equation (2.58) and effectively use the Dyson equation only for the impurity Green function,

$$(g^\sigma_{\boldsymbol{S}})_{x^I, y^I} = (G^\sigma_{\boldsymbol{S}})_{x,y} \, \delta_{\boldsymbol{i}_x, \boldsymbol{r}_x} \delta_{\boldsymbol{i}_y, \boldsymbol{r}_y} \; , \tag{2.63}$$

which is a $N_c m \times N_c m$ matrix. We obtain

$$\begin{aligned} g^\sigma_{\boldsymbol{S}} &= g^\sigma_{\boldsymbol{S}'} + g^\sigma_{\boldsymbol{S}'} \Delta^{I,\sigma} (1 - g^\sigma_{\boldsymbol{S}}) \; , \\ g^\sigma_{\boldsymbol{S}'} &= g^\sigma_{\boldsymbol{S}} \left[1 + \Delta^{I,\sigma} \left(1 - g^\sigma_{\boldsymbol{S}}\right)\right]^{-1} \; , \end{aligned} \tag{2.64}$$

with $\left(\Delta^{I,\sigma}\right)_{x^I, y^I} = \left(\Delta^\sigma\right)_{x,y} \delta_{\boldsymbol{i}_x, \boldsymbol{r}_x} \delta_{\boldsymbol{i}_y, \boldsymbol{r}_y}$.

2.1.6 Monte Carlo sampling

In this section, we discus the Monte Carlo sampling which is typically accomplished by a single spin-flip algorithm in the auxiliary field QMC methods. The acceptance probability, for example in the Metropolis algorithm (2.3), is based on the ratio

$$R = \frac{P_{\boldsymbol{S}'}}{P_{\boldsymbol{S}}} = \frac{w_{\boldsymbol{S}'}}{w_{\boldsymbol{S}}} \ , \tag{2.65}$$

where $R = \prod_\sigma R^\sigma$, see the expectation values (2.30) and (2.44). In the following, we consider two configurations $\boldsymbol{S}$ and $\boldsymbol{S}'$, that differ only at a single space-time point $(\boldsymbol{i}, \tau = n\Delta\tau$. The ratio is entirely based on the element $G^\sigma_{\boldsymbol{S}}(n\Delta\tau, n\Delta\tau)_{\boldsymbol{i},\boldsymbol{i}}$ of the equal-time Green function. At finite temperatures, we have

$$\begin{aligned} R^\sigma &= \frac{\det\left[1 + B^\sigma_{\boldsymbol{S}'}(\beta, 0)\right]}{\det\left[1 + B^\sigma_{\boldsymbol{S}}(\beta, 0)\right]} = \frac{\det O^\sigma_{\boldsymbol{S}'}}{\det O^\sigma_{\boldsymbol{S}}} = \frac{\det G^\sigma_{\boldsymbol{S}}}{\det G^\sigma_{\boldsymbol{S}'}} \\ &= \det\left[1 + \Delta^\sigma(1 - G^\sigma_{\boldsymbol{S}}\right] \\ &= \det\left[1 + \Delta^\sigma_n(1 - G^\sigma_{\boldsymbol{S}}(n\Delta\tau, n\Delta\tau)\right] \\ &= 1 + \Delta^\sigma_{n\boldsymbol{i}}\left[1 - G^\sigma_{\boldsymbol{S}}(n\Delta\tau, n\Delta\tau)_{\boldsymbol{i},\boldsymbol{i}}\right] \ . \end{aligned} \tag{2.66}$$

In going from the second line to the third line, we used the fact that the resulting matrix is so sparse in time that it can brought to triangular form with one row transformation. The same logic applies for the spatial components in lines three and four. $\Delta^\sigma_{n\boldsymbol{i}}$ is the local potential difference of the configurations. An identical result for R^σ holds for the PQMC, if the finite-temperature Green function is replaced by its zero-temperature analog.

The BSS and the HF algorithms differ in the set of equations from Sec. 2.1.5 they use. The HF method uses $G_{\boldsymbol{S}'}$ (2.59) to calculate and update the space-time Green function $G_{\boldsymbol{S}}$ (2.55).

The BSS and the PQMC method are based on calculating and updating the equal-time Green function, using $G_{\boldsymbol{S}}(\tau,\tau)$ (2.52) and $G_{\boldsymbol{S}'}(\tau,\tau)$ (2.61). Having updated one time-slice τ, the equal-time Green function on the adjacent time-slice $\tau + 1$ is calculated with Eq. (2.54).

Updating the Green functions requires a matrix inversion, see Eq. (2.59) and Eq. (2.61). Since the associated $N_{\text{dim}} \times N_{\text{dim}}$ matrix is the identity plus a rank-1 correction, the matrix inversion is efficiently done using the Sherman-Morrison-Woodbury formula (see Ref. [62] and Ref. [75]), which only requires $\mathcal{O}[(N_{\text{dim}})^2]$ instead of the $\mathcal{O}[(N_{\text{dim}})^3]$ operations if the inverse is computed from scratch. Taking $N_{\text{dim}} = mN_c$ in the HF-QMC, we therefore have $\mathcal{O}[(\beta N_c)^2]$ operation per update and $\mathcal{O}[(\beta N_c)^3]$ operations for the entire sweep through the space-time lattice. In the BSS-QMC and the PQMC, $N_{\text{dim}} = N$, and we have $\mathcal{O}(N^2)$ operation per update, $\mathcal{O}(N^3)$ operations per time-slice and $\mathcal{O}(\beta N^3)$ operations for one sweep through all time-slices.

The performance of the updating scheme can be enhanced by a cache optimization strategy known as delayed updates [76]. Multiple rank-1 updates may be delayed by k steps and be replaced by a rank-k update which can be performed efficiently by calling the general matrix multiplication subroutine `DGEMM` from the `BLAS` library.

Some comments are in order regarding the numerical stability of the algorithms. In general, the stability of an algorithm can be quantified by its condition number. The condition number is essentially the susceptibility of the algorithm to small variations of the input data, i.e. round-off errors in our case. The condition number κ of a matrix can be estimated by the ratio of the maximum to the minimum eigenvalue: $\kappa = |\max_i(\lambda_i)/\min_i(\lambda_i)|$. A well-conditioned matrix has $\kappa = \mathcal{O}(1)$ whereas for $\kappa \to \infty$ the matrix is ill-conditioned.

In particular, let us focus on the calculation of the equal-time Green function $G_{\boldsymbol{S}}(\tau, \tau)$, see Eq. (2.36) for the PQMC and Eq. (2.52) for the spatial formulation of the FTQMC. Both equations rely on the time-evolution matrix $B_{\boldsymbol{S}}$ which is the result of multiple matrix-matrix multiplications. For large projection parameters or for large inverse temperatures, the resulting matrix $B_{\boldsymbol{S}}$ has eigenvalues that are exponentially large and and at the same time eigenvalues that are of order one [62; 73]. Therefore, $B_{\boldsymbol{S}}$ becomes ill-conditioned and highly singular, i.e. non-invertible.

In the PQMC, the numerical stabilization is done by applying a singular-value decomposition on the matrices $B_{\boldsymbol{S}}(\tau, 0)P$ and $P^{\dagger}B_{\boldsymbol{S}}(\theta, \tau)$. One can show that the scales, i.e. the multiset of eigenvalues, then drops out of the calculation of the Green function (2.36) A detailed discussion of stabilization schemes for the spatial formulation of the finite-temperature QMC is given in Ref. [62]. Note that at finite-temperatures, the Green function matrix $G_{\boldsymbol{S}}$ can be calculated without stabilization. Due to the different eigenvalue structure of the matrix $O_{\boldsymbol{S}}$ compared to $B_{\boldsymbol{S}}$, its condition number grows only linearly with N at low temperatures [73].

Due to its discrete nature in imaginary time, one has a systematic error in the auxiliary field QMC method. The $\Delta\tau$–discretization corresponds to a high-energy cutoff which can be controlled by extrapolating to $\Delta\tau = 0$. The simulation presented in this thesis are based on the discretizations $\Delta\tau t = 0.1 - 0.25$ and for each project, we have checked that smaller values of $\Delta\tau$ leave the results invariant within the error bars.

2.1.7 The sign problem

The efficiency of a quantum Monte Carlo simulations for fermions rests on the assumption that the computing time scales only polynomially although the space of fermionic configurations grows exponentially with the particle number. This advantage is lost when the computing time also scales exponentially with increasing particle number. It is the case when the weights $w_{\boldsymbol{s}}$ in the sum over configurations (2.1) acquire negative values and therefore cannot be interpreted as a probability. In the language of complexity theory, the negative sign problem has been shown to be nondeterministic polynomial (NP) hard [77]. The classification of a problem as NP means that no polynomial time algorithm which runs on a deterministic classical computer is known to solve the problem, whereas problems in P can be solved in polynomial time. The subset of NP hard problems has the additional property that they are linked with polynomial complexity to any other problem in NP. Since the sign problem is NP hard and in case the conjecture NP $\neq$ P hold, the sign problem has no generic solution [77].

When negative weights $w_{\boldsymbol{s}}$ occur, one usually samples the configuration space according to the distribution $|w_{\boldsymbol{S}}|$ and assigns the sign $\mathrm{sgn}(w_{\boldsymbol{S}})$ to the quantity being sampled [55; 77]:

$$\langle A\rangle = \sum_{\boldsymbol{S}} P_{\boldsymbol{S}} A_{\boldsymbol{S}} = \frac{\sum_{\boldsymbol{S}} |w_{\boldsymbol{S}}|\,\mathrm{sgn}(w_{\boldsymbol{S}}) A_{\boldsymbol{S}}}{\sum_{\boldsymbol{S}} |w_{\boldsymbol{S}}|} \left[\frac{\sum_{\boldsymbol{S}} |w_{\boldsymbol{S}}|\,\mathrm{sgn}(w_{\boldsymbol{S}})}{\sum_{\boldsymbol{S}} |w_{\boldsymbol{S}}|}\right]^{-1} = \frac{\langle \mathrm{sgn}(w_{\boldsymbol{S}}) A_{\boldsymbol{S}}\rangle_{|w_{\boldsymbol{S}}|}}{\langle \mathrm{sgn}(w_{\boldsymbol{S}})\rangle_{|w_{\boldsymbol{S}}|}} \,. \tag{2.67}$$

The Monte Carlo estimator therefore is

$$\langle \widetilde{A}\rangle = \frac{\sum_{i=1}^{N_{\mathrm{meas}}} \mathrm{sgn}(w_{\boldsymbol{S}_i}) A_{\boldsymbol{S}_i}}{\sum_{i=1}^{N_{\mathrm{meas}}} \mathrm{sgn}(w_{\boldsymbol{S}_i})} \,. \tag{2.68}$$

The mean value of the sign, $\langle \mathrm{sgn}(w_{\boldsymbol{S}})\rangle$, becomes exponentially small with increasing system size and inverse temperature, whereas the relative error $\Delta[\mathrm{sgn}(w_{\boldsymbol{S}})]$ increases exponentially [77]. We have

$$\langle \mathrm{sgn}(w_{\boldsymbol{S}})\rangle = \frac{\sum_{\boldsymbol{S}} w_{\boldsymbol{S}}}{\sum_{\boldsymbol{S}} |w_{\boldsymbol{S}}|} = e^{-\beta N \Delta f} \,, \tag{2.69}$$

where Δf is the difference of the corresponding free energy densities, and

$$\Delta[\mathrm{sgn}(w_{\boldsymbol{S}})] = \frac{\sqrt{\langle [\mathrm{sgn}(w_{\boldsymbol{S}})]^2\rangle - \langle \mathrm{sgn}(w_{\boldsymbol{S}})\rangle^2}}{\sqrt{N_{\mathrm{meas}}}\langle \mathrm{sgn}(w_{\boldsymbol{S}})\rangle} \sim \frac{e^{\beta N \Delta f}}{\sqrt{N_{\mathrm{meas}}}} \,. \tag{2.70}$$

The (exponential) decay of the average sign (2.69) means that in a simulation most contributions from the Monte Carlo sampling cancel, i.e. the signal-to-noise-ratio decays exponentially with N and β [78]. An approximate way to get rid of the sign decay is the constrained path Monte Carlo, which has positive weights by construction but comes at the price of introducing a bias in terms of a trial wave function at zero temperature and a constraint on the fermionic determinant at finite temperatures [78; 79].

2.2 Interaction expansion continuous-time QMC

In the following, we give a very brief outline of the continuous-time QMC algorithm (CT-INT) which is a diagrammatic determinantal grand-canonical scheme based on a stochastic series expansion of the partition function in the interaction representation [80]. Since the method scales with $\mathcal{O}[(\beta N_c)^3]$ it is particular useful when the number N_c of correlated sites can be kept small (see Sec. 6.6). Recent overviews of the method can be found in Ref. [81] and Ref. [82].

We consider the partition function of the Hubbard model,

$$Z = \mathrm{Tr}\left[e^{-\beta(\mathcal{H}_0+\mathcal{H}_U)}\right] = \mathrm{Tr}\left[e^{-\beta\mathcal{H}_0} T e^{-\int\limits_0^\beta \mathrm{d}\tau\, \mathcal{H}_U(\tau)}\right] , \tag{2.71}$$

where the operator T denotes the time-ordering and we use an explicitly particle-hole symmetric formulation of the Hubbard interaction,

$$\begin{aligned} \mathcal{H}_U &= \frac{U}{2}\sum_{\boldsymbol{i}}\sum_{s=\pm}\prod_{\sigma}\left(\hat{n}_{\boldsymbol{i}\sigma}-\alpha_{\sigma s}\right) \\ &= U\sum_{\boldsymbol{i}}\left(\hat{n}_{\boldsymbol{i}\uparrow}-\frac{1}{2}\right)\left(\hat{n}_{\boldsymbol{i}\downarrow}-\frac{1}{2}\right) - 2U\delta^2 , \end{aligned} \tag{2.72}$$

with $\alpha_{\sigma s} = 1/2+\sigma s\delta$. Similar to the auxiliary field determinantal QMC method, the presence of particle-hole symmetry can be used to avoid the sign problem entirely, however only if the constant δ is chosen properly [83]. The evolution operator can be written as a series expansion,

$$\begin{aligned} & T e^{-\int\limits_0^\beta \mathrm{d}\tau\, \mathcal{H}_U(\tau)} \\ = \;& T\sum_k \frac{(-1)^k}{k!}\left[\int\limits_0^\beta \mathrm{d}\tau\, \mathcal{H}_U(\tau)\right]^k \\ = \;& T\sum_{k=0}^{\infty}\frac{1}{k!}\left(\frac{-U}{2}\right)^k\left[\int\limits_0^\beta \mathrm{d}\tau_1 \sum_{\boldsymbol{i}_1,s_1}\cdots\int\limits_0^\beta \mathrm{d}\tau_k\sum_{\boldsymbol{i}_k,s_k}\right]\prod_k\prod_\sigma\left[\hat{n}_{\boldsymbol{i}_k\sigma}(\tau_k)-\alpha_{\sigma s_k}\right] \\ = \;& \sum_{k=0}^{\infty}\left(\frac{-U}{2}\right)^k\left[\int\limits_0^\beta \mathrm{d}\tau_1 \sum_{\boldsymbol{i}_1,s_1}\cdots\int\limits_{\tau_{k-1}}^\beta \mathrm{d}\tau_k\sum_{\boldsymbol{i}_k,s_k}\right] T\prod_k\prod_\sigma\left[\hat{n}_{\boldsymbol{i}_k\sigma}(\tau_k)-\alpha_{\sigma s_k}\right] \\ = \;& \sum_{C_k}\left(\frac{-U}{2}\right)^k T\prod_k\prod_\sigma\left[\hat{n}_{\boldsymbol{i}_k\sigma}(\tau_k)-\alpha_{\sigma s_k}\right] . \end{aligned} \tag{2.73}$$

In the fourth line the time-ordering $\tau_1 \le \tau_2 \le \cdots \le \tau_k$ has been applied and in the fifth line, the sum $\sum_{C_k}$ denotes the combination of all sums and integrals. A configuration C_k is defined by k Hubbard vertices and the Ising spins s_a, i.e. $C_k = \{[\boldsymbol{i}_1,\tau_1,s_1],\cdots,[\boldsymbol{i}_k,\tau_k,s_k]\}$. The partition function (2.71) then is, using $Z_0 = \mathrm{Tr}[\exp(-\beta\mathcal{H}_0)]$,

$$\begin{aligned} Z &= \sum_{C_k}\left(\frac{-U}{2}\right)^k \mathrm{Tr}\left\{e^{-\beta\mathcal{H}_0}T\prod_k\prod_\sigma\left[\hat{n}_{\boldsymbol{i}_k\sigma}(\tau_k)-\alpha_{\sigma s_k}\right]\right\} \\ &= \sum_{C_k}\left(\frac{-U}{2}\right)^k \left\langle T\prod_k\prod_\sigma\left[\hat{n}_{\boldsymbol{i}_k\sigma}(\tau_k)-\alpha_{\sigma s_k}\right]\right\rangle_0 Z_0 \\ &= \sum_{C_k}\left(\frac{-U}{2}\right)^k \det M(C_k) Z_0 . \end{aligned} \tag{2.74}$$

Here, the Wick theorem [similar to Eq. (2.14)] has been employed to evaluate the expectation value $\langle \cdots \rangle_0$ of $4k$ fermionic operators. The matrix of free Green functions is defined here as

$$G^0_{\boldsymbol{i}_a,\boldsymbol{i}_b}(\tau_a,\tau_b) = \begin{pmatrix} \langle T\hat{c}^\dagger_{\boldsymbol{i}_a\uparrow}(\tau_a)\hat{c}_{\boldsymbol{i}_b\uparrow}(\tau_b)\rangle_0 & \langle T\hat{c}^\dagger_{\boldsymbol{i}_a\uparrow}(\tau_a)\hat{c}_{\boldsymbol{i}_b\downarrow}(\tau_b)\rangle_0 \\ \langle T\hat{c}^\dagger_{\boldsymbol{i}_a\downarrow}(\tau_a)\hat{c}_{\boldsymbol{i}_b\uparrow}(\tau_b)\rangle_0 & \langle T\hat{c}^\dagger_{\boldsymbol{i}_a\downarrow}(\tau_a)\hat{c}_{\boldsymbol{i}_b\downarrow}(\tau_b)\rangle_0 \end{pmatrix} , \tag{2.75}$$

with $a, b = 1, \cdots k$. Then, the $2k \times 2k$ matrix $M(C_k)$ has the following form

$$M(C_k) = \begin{pmatrix} G^0_{\boldsymbol{i}_1,\boldsymbol{i}_1}(\tau_1,\tau_1) - \alpha_1 & \cdots & G^0_{\boldsymbol{i}_1,\boldsymbol{i}_k}(\tau_1,\tau_k) \\ \cdots & \ddots & \cdots \\ G^0_{\boldsymbol{i}_k,\boldsymbol{i}_1}(\tau_k,\tau_1) & \cdots & G^0_{\boldsymbol{i}_k,\boldsymbol{i}_k}(\tau_k,\tau_k) - \alpha_k \end{pmatrix} . \tag{2.76}$$

We have introduced the matrix $\alpha_a = \mathrm{diag}(\alpha_{\uparrow s_a}, \alpha_{\downarrow s_a})$. In case that the model Hamiltonian has a $U(1)$ spin symmetry, the matrix $M(C_k)$ can be brought to block diagonal form and we have $\det M(C_k) = \det M_\uparrow(C_k) \det M_\downarrow(C_k)$. In summary, the partition function (2.74) can be rewritten as

$$\widetilde{Z} = Z/Z_0 = \sum_{C_k} \left(\frac{-U}{2}\right)^k \det M(C_k) = \sum_{C_k} w(C_k) , \tag{2.77}$$

and the configurations C_k can now be sampled according to the weight $w(C_k)$. Observables $\langle A(\tau)\rangle$ are computed as follows, using Eq. (2.74)

$$\begin{aligned}
\langle A(\tau)\rangle &= \frac{1}{Z}\mathrm{Tr}\left[e^{-\beta(\mathcal{H}_0+\mathcal{H}_U)}A(\tau)\right] \\
&= \frac{1}{Z}\sum_{C_k}\left(\frac{-U}{2}\right)^k \mathrm{Tr}\left\{e^{-\beta\mathcal{H}_0} T\prod_k\prod_\sigma \left[\hat{n}_{\boldsymbol{i}_k\sigma}(\tau_k) - \alpha_{\sigma s_k}\right] A(\tau)\right\} \\
&= \frac{1}{\widetilde{Z}}\sum_{C_k}\left(\frac{-U}{2}\right)^k \left\langle T\prod_k\prod_\sigma \left[\hat{n}_{\boldsymbol{i}_k\sigma}(\tau_k) - \alpha_{\sigma s_k}\right] A(\tau)\right\rangle_0 \\
&= \frac{1}{\widetilde{Z}}\sum_{C_k}\left(\frac{-U}{2}\right)^k \det M(C_k) \frac{\left\langle T\prod_k\prod_\sigma \left[\hat{n}_{\boldsymbol{i}_k\sigma}(\tau_k) - \alpha_{\sigma s_k}\right] A(\tau)\right\rangle_0}{\det M(C_k)} \\
&= \frac{1}{\widetilde{Z}}\sum_{C_k}\left(\frac{-U}{2}\right)^k \det M(C_k) \langle\langle A(\tau)\rangle\rangle_{C_k} ,
\end{aligned} \tag{2.78}$$

where the Monte Carlo estimator is given by

$$\langle\langle A(\tau)\rangle\rangle_{C_k} = \frac{\left\langle T\prod_k\prod_\sigma \left[\hat{n}_{\boldsymbol{i}_k\sigma}(\tau_k) - \alpha_{\sigma s_k}\right] A(\tau)\right\rangle_0}{\left\langle T\prod_k\prod_\sigma \left[\hat{n}_{\boldsymbol{i}_k\sigma}(\tau_k) - \alpha_{\sigma s_k}\right]\right\rangle_0} = \frac{\det \widetilde{M}(C_k)}{\det M(C_k)} . \tag{2.79}$$

In particular, one obtains the following estimate for the single-particle Green function

$$\begin{aligned}&\langle\langle T\hat{c}^{\dagger}_{\boldsymbol{i}\sigma}(\tau)\hat{c}_{\boldsymbol{j}\sigma'}(\tau')\rangle\rangle_{C_k} \qquad (2.80)\\ = \; &\left[G^0_{\boldsymbol{i},\boldsymbol{j}}(\tau,\tau')\right]_{\sigma,\sigma'} - \sum_a^k\sum_{\sigma_a}\sum_b^k\sum_{\sigma_b}\left[G^0_{\boldsymbol{i},\boldsymbol{i}_a}(\tau,\tau_a)\right]_{\sigma,\sigma_a}\left[M(C_k)^{-1}\right]_{a\sigma_a,b\sigma_b}\left[G^0_{\boldsymbol{i}_b,\boldsymbol{j}}(\tau_b,\tau')\right]_{\sigma_b,\sigma'} ,\end{aligned}$$

using elementary matrix and determinant identities [81]. Since for every configuration C_k of vertices and Ising spins the Wick theorem holds, an estimate for any observable can be calculated on the basis of the single particle Green functions (2.80). How observable are calculated efficiently in the CT-INT is discussed in Ref. [81].

The Monte Carlo sampling essentially consists of the addition and removal of Hubbard vertices $[\boldsymbol{i}_a, \tau_a, s_a]$. The acceptance ratio for a given move can be calculated with the Metropolis algorithm (2.3). For the complete description of the Monte Carlo sampling, we refer the reader to the original work [80] and to Ref. [83].

2.3 Dynamical mean field theory and dynamical cluster approximation

The DMFT is a theoretical concept which yields the exact solution of the Hubbard model for $d \to \infty$ [84; 85; 86; 87]. The DMFT can be motivated using the Baym-Kadanoff formalism as a thermodynamically consistent approximation to the Luttinger-Ward functional [88]. The corresponding algorithm is centered around the solution of a single-impurity model embedded in a lattice model of conduction electrons. The solution of this problem is obtained in a self-consistent manner, essentially by demanding that the Green function of the impurity model equals the local Green function of the lattice model. The DMFT has been especially successful in describing the Mott transition in strongly correlated electron systems [87].

Naturally, this procedure neglects dynamic long-wavelength fluctuations. Consequently, the DMFT can produce an ordered state at low-dimensions, thereby violating the Mermin-Wagner theorem which can be proven under very general assumptions [89]. Additionally, the method fails in the vicinity of critical points where long-wavelength fluctuations are dominant.

Although it is perfectly reasonable to question its applicability when the spatial dimension is as low as $d = 2$, there are parameter regimes where it can provide valuable insight when one keeps in mind the limitations of the method. An example is the paramagnetic phase of the Kondo lattice model (see Sec. 1.1.1). This phase is dominated by dynamic local correlations that build the correlated Kondo singlet state at low temperatures. The DMFT is expected to describe this phase correctly. However, it is always a good idea to check the quality of the results by re-introducing non-local spatial correlations on small length scales. This can be achieved by generalizing the DMFT from a single-impurity theory to a many-impurity, i.e. cluster, theory. For a review of cluster extension of the DMFT, see Ref. [88].

Apart from perturbative methods to solve the cluster (e.g. the non-crossing approximation), there are non-perturbative methods like the QMC method, the numerical renormalization group (NRG) or the method of exact diagonalization (ED) [88]. The advantage of an action-based QMC solver is that all information about the bath degrees of freedom are contained in the bath Green function $\mathcal{G}^0$, without the need to explicitly know the corresponding bath Hamiltonian. The bath is therefore implicit. In contrast, using other solvers (ED, NRG) requires to explicitly construct a bath Hamiltonian. The method we apply is the dynamical cluster approximations (DCA) [90] in combination with a QMC cluster solver [91; 92].

In real space, a cluster approximation means to divide the d-dimensional lattice in clusters of linear dimension L_c containing N_c sites each, where $N_\mathrm{c} = (L_\mathrm{c})^d$. The DMFT corresponds to the limit $N_c = 1$. Using scaling relations, it can be shown [88] that the exact self-energy is approximated by the DCA self-energy as

$$\Sigma(\boldsymbol{k}, i\omega_n) = \Sigma^{\mathrm{DCA}}(\boldsymbol{k}, i\omega_n) + \mathcal{O}(1/L_\mathrm{c}^2) \ . \tag{2.81}$$

Naturally, in the limit of infinite cluster size, the cluster method yields the exact solution of the model. However, in contrast to the finite-size lattice simulation, the cluster method is already non-trivial in the limit of $N_c = 1$ (DMFT) due to the inclusion of quantum fluctuations.

In the following, we briefly review the DCA which we apply to the two-dimensional Kondo lattice model (see Ch. 3). The DCA in constructed in momentum space and it introduces three different reciprocal lattices: (i) The reciprocal space of the non-interacting Hamiltonian, with N k-points, (ii) The reciprocal space consisting of N_c k-points, obtained by evenly tiling the Brillouin zone in N_c patches. (iii) The reciprocal space which corresponds to the real-space lattice of N_c interacting sites with periodic boundary conditions. The momenta in (i) are labelled by $\boldsymbol{k}$ and the momenta in (ii) and in (iii) are labelled by $\boldsymbol{K}$. These three reciprocal spaces are connected by the same self-consistency cycle as in the DMFT (see below). The DCA self-consistent scheme is therefore also centered around the single-particle self-energy. The cluster solver for the impurity problem is essentially needed to calculate the cluster self-energy $\Sigma^{\mathrm{DCA}}_{\mathrm{cluster}}(\boldsymbol{K}, i\omega_n)$.

The essential approximation of the DCA is to equate the irreducible quantities of the cluster, i.e. the self-energy or the irreducible vertices, with the irreducible quantities of the lattice. On the single particle level, we therefore have:

$$\Sigma^{\mathrm{DCA}}_{\mathrm{lattice}}(\boldsymbol{K}, i\omega_n) = \Sigma^{\mathrm{DCA}}_{\mathrm{cluster}}(\boldsymbol{K}, i\omega_n) \ . \tag{2.82}$$

The end of the self-consistency cycle is defined by the step where $\Sigma_{\mathrm{lattice}}(\boldsymbol{K}, i\omega_n)$ is converged to $\Sigma_{\mathrm{cluster}}(\boldsymbol{K}, i\omega_n)$ within a given accuracy. Then, we make use of Eq. (2.82) to compute the lattice reducible quantities that we are interested in, i.e. the lattice Green function [see Eq. (2.85)].

The reciprocal space (ii) is obtained from (i) by a coarse-graining procedure. From the perspective of a diagrammatic derivation of the DCA, this procedure amounts to a violation of momentum conservation at internal vertices of Green function legs in the diagrams that constitute the Baym-Kadanoff generating functional Φ (see Ref. [88] and references therein). We define a function $\boldsymbol{M}(\boldsymbol{k})$ which performs a unique mapping from a momentum $\boldsymbol{k}$ to the nearest coarse-grained momentum $\boldsymbol{K}$:

$$\boldsymbol{M} : \boldsymbol{k} \to \boldsymbol{K} \tag{2.83}$$

Momentum is only conserved between different $\boldsymbol{M}(\boldsymbol{k})$. Obviously, full momentum conservation is restored when each momentum patch contains only one $\boldsymbol{k}$-point. On the other hand, the DMFT corresponds to having only one momentum patch, i.e. the conservation of momentum at internal vertices is fully neglected. The lattice Green function $G_{\text{lattice}}(\boldsymbol{k}, i\omega_n)$ is replaced by its coarse-grained counterpart:

$$G^{\text{DCA}}_{\text{lattice, av.}}(\boldsymbol{K}, i\omega_n) = \frac{N_{\text{c}}}{N} \sum_{\widetilde{\boldsymbol{k}}} G^{\text{DCA}}_{\text{lattice}}(\boldsymbol{K} + \widetilde{\boldsymbol{k}}, i\omega_n) \; , \tag{2.84}$$

where

$$G^{\text{DCA}}_{\text{lattice}}(\boldsymbol{k}, i\omega_n) = \left\{ i\omega_n - \epsilon(\boldsymbol{k}) + \mu - \Sigma^{\text{DCA}}_{\text{lattice}}[\boldsymbol{M}(\boldsymbol{k}), i\omega_n] \right\}^{-1} \; . \tag{2.85}$$

In Eq. (2.84), $\sum_{\widetilde{\boldsymbol{k}}}$ denotes a sum over all momenta $\widetilde{\boldsymbol{k}}$ in the patch labelled by $\boldsymbol{K}$, and in Eq. (2.85), $\epsilon(\boldsymbol{k}) - \mu$ are the non-interacting energies. The coarse-graining has to be applied also to the generally k-dependent interaction. However, the Hubbard interaction is local and therefore not affected by the coarse-graining.

To make contact with the interacting cluster problem, defined in the reciprocal space (iii), we set up an appropriate "non-interacting" cluster Green function $\mathcal{G}^0_{\text{cluster}}(\boldsymbol{K}, i\omega_n)$ which however effectively inherits interaction effects due to the self-consistency cycle. Since we use a QMC cluster solver which in a diagrammatic picture sums all diagrams to all orders, the correct cluster-excluded Green function is

$$\left[\mathcal{G}^0_{\text{cluster}}(\boldsymbol{K}, i\omega_n)\right]^{-1} = \left[G^{\text{DCA}}_{\text{lattice, av.}}(\boldsymbol{K}, i\omega_n)\right]^{-1} + \Sigma^{\text{DCA}}_{\text{lattice}}(\boldsymbol{K}, i\omega_n) \; . \tag{2.86}$$

Using $\mathcal{G}^0_{\text{cluster}}(\boldsymbol{K}, i\omega_n)$ as input, the cluster solver computes $G^{\text{QMC}}_{\text{cluster}}(\boldsymbol{K}, i\omega_n)$. We then calculate

$$\Sigma^{\text{DCA}}_{\text{cluster}}(\boldsymbol{K}, i\omega) = \left[\mathcal{G}^0_{\text{cluster}}(\boldsymbol{K}, i\omega_n)\right]^{-1} - \left[G^{\text{QMC}}_{\text{cluster}}(\boldsymbol{K}, i\omega)\right]^{-1} \; . \tag{2.87}$$

This brings us back to the definition of the lattice self-energy $\Sigma^{\text{DCA}}_{\text{Lattice}}(\boldsymbol{K}, i\omega_n)$ [Eq. (2.82)] and completes the self-consistency cycle. To summarize, the self consistency cycle is:

$$\begin{aligned}
& \Sigma^{\text{DCA}}_{\text{cluster}}(\boldsymbol{K}, i\omega_n) = \Sigma_{\text{start}}(\boldsymbol{K}, i\omega_n) \\
\overset{(2.84)}{\longrightarrow} \; & G^{\text{DCA}}_{\text{lattice, av.}}(\boldsymbol{K}, i\omega_n) \overset{(2.86)}{\longrightarrow} \mathcal{G}^0_{\text{cluster}}(\boldsymbol{K}, i\omega_n) \\
\overset{\text{QMC}}{\longrightarrow} \; & G^{\text{QMC}}_{\text{cluster}}(\boldsymbol{K}, i\omega) \overset{(2.87),\,(2.82)}{\longrightarrow} \Sigma^{\text{DCA}}_{\text{lattice}}(\boldsymbol{K}, i\omega) \\
\overset{(2.84)}{\longrightarrow} \; & G^{\text{DCA}}_{\text{lattice, av.}}(\boldsymbol{K}, i\omega_n) \cdots
\end{aligned} \tag{2.88}$$

The end of the self-consistency loop is reached, when $G^{\text{DCA}}_{\text{lattice, av.}}(\boldsymbol{K}, i\omega_n) = G^{\text{QMC}}_{\text{cluster}}(\boldsymbol{K}, i\omega)$ and, accordingly, when the self-energy is converged.

One important issue in the theory of cluster extensions of the DMFT is causality. In a causal theory, the imaginary part of the retarded single-particle Green function $G^{\text{R}}(\boldsymbol{k}, \omega)$ and the imaginary part of the single-particle self energy $\Sigma(\boldsymbol{k}, \omega)$ are negative definite. This makes it for example possible to define a spectral function as $A(\boldsymbol{k}, \omega) = (-1/\pi)\text{Im}G^{\text{R}}(\boldsymbol{k}, \omega)$

which fulfills a sum rule. That every step in the DCA self-consistency cycle (2.88) preserves causality has been shown in Refs. [93; 88].

By choosing an enlarged unit cell, the DCA can be used to study symmetry breaking phases. In this case, the coarse-graining procedure has to be done based on the reduced Brillouin zone (see Ref. [17]).

The implementation of the HF-QMC in the self-consistency loop of the DMFT makes it necessary to Fourier transform the Green function twice per cycle, since the self-consistency equations are formulated in Matsubara frequencies whereas the QMC algorithms operates with the imaginary-time dependent Green function.

In computing $G(\tau)$ (suppressing the lattice momentum in the notation), we avoid the truncation of the frequency sum using the following trick [92], although we naturally have only a finite number $(2N_\omega + 1)$ of Matsubara frequencies,

$$\begin{aligned} G(\tau) &= \frac{1}{\beta} \sum_{n=-\infty}^{+\infty} e^{-i\omega_n\tau} \left[G(i\omega_n) - f(i\omega_n) + f(i\omega_n)\right] \\ &= \frac{1}{\beta} \sum_{n=-N_\omega}^{+N_\omega} e^{-i\omega_n\tau} \left[G(i\omega_n) - f(i\omega_n)\right] + \frac{1}{\beta} \sum_{n=-\infty}^{+\infty} e^{-i\omega_n\tau} f(i\omega_n) \\ &+ \frac{1}{\beta} \left[\sum_{n=-\infty}^{-N_\omega-1} + \sum_{n=N_\omega+1}^{+\infty} \right] e^{-i\omega_n\tau} \left[G(i\omega_n) - f(i\omega_n)\right] \\ &= \frac{1}{\beta} \sum_{n=-N_\omega}^{+N_\omega} e^{-i\omega_n\tau} \left[G(i\omega_n) - f(i\omega_n)\right] + \frac{1}{\beta} \sum_{n=-\infty}^{+\infty} e^{-i\omega_n\tau} f(i\omega_n) + \mathcal{O}[(\omega_{N_\omega+1})^{-3}] , \end{aligned} \tag{2.89}$$

where the function $f(i\omega_n)$ is defined by the high-frequency behavior of $G(i\omega_n)$,

$$G(i\omega_n) = \int_0^\beta \mathrm{d}\tau e^{i\omega_n\tau} G(i\omega_n) = \frac{a}{i\omega_n} + \frac{b}{(i\omega_n)^2} + \mathcal{O}[(\omega_n)^{-3}] = f(i\omega_n) + \mathcal{O}[(\omega_n)^{-3}] , \tag{2.90}$$

which is obtained after partial integration. Using the fermionic anti commutation relations, the coefficients are $a = G(\tau = 0^-) - G(\tau = 0^+) = 1$ and $b = -\frac{d}{d\tau}G(\tau = 0^-) + \frac{d}{d\tau}G(\tau = 0^+)$. Having evaluated the Matsubara sums (assuming $\tau > 0$), the Green function (2.89) finally reads

$$G(\tau) = \frac{1}{\beta} \sum_{n=-N_\omega}^{+N_\omega} e^{-i\omega_n\tau} \left[G(i\omega_n) - \frac{a}{i\omega_n} - \frac{b}{(i\omega_n)^2}\right] - \frac{a}{2} - \frac{(\beta - 2\tau)b}{4} + \mathcal{O}[(\omega_{N_\omega+1})^{-3}] . \tag{2.91}$$

After the QMC step, we need to compute $G(i\omega_n) = \int_0^\beta \mathrm{d}\tau \exp(i\omega_n\tau) G(\tau)$ which can be accomplished by using the maximum entropy method as a fitting routine (see Sec. 2.4).

2.4 Analytic continuation of imaginary-time data

Using the implementation of the QMC methods discussed in Sec. 2.1 and Sec. 2.2, we compute the thermal imaginary-time displaced Green function $\mathcal{G}(\tau)$:

$$\mathcal{G}(\tau) = -\langle T\hat{A}(\tau)\hat{A}^\dagger(0)\rangle \ , \tag{2.92}$$

where $\hat{A}$ denotes a fermionic or bosonic operator and we take $\tau \in [0, \beta)$. It fulfills $\mathcal{G}(\tau + \beta) = \mp\mathcal{G}(\tau)$ for fermions/bosons. To simplify the expressions, we have omitted quantum numbers like spin or momentum. However, $\mathcal{G}(\tau)$ is not a physical (accessible in an experiment) quantity. The method of analytic continuation [94] makes contact with the the retarded Green functions $G^R(t)$ and $G^R(\omega)$, that directly enter experimentally measurable quantities like the spectral function. We have the following Fourier transforms

$$\mathcal{G}(\tau) = \frac{1}{\beta}\sum_{\omega_n} e^{-i\omega_n\tau}\mathcal{G}(\omega_n) \ , \ \mathcal{G}(\omega_n) = \int\limits_0^\beta \mathrm{d}\tau e^{i\omega_n\tau}\mathcal{G}(\tau) \ , \tag{2.93}$$

where $\omega_n = (2n+1)\pi/\beta$ ($\omega_n = 2n\pi/\beta$) for fermions (bosons) and $n \in \mathbb{Z}$. The correlation functions defined in real and imaginary time $\tau = it$ can be expressed in terms of their Fourier components $G^R(\omega)$ and $\mathcal{G}(\omega_n)$. Both Fourier components can be obtained from the same complex valued function $\mathcal{C}(z)$:

$$\mathcal{C}(z) : \mathbb{C} \to \mathbb{C} \ , \tag{2.94}$$

which has the asymptotic form $\mathcal{C}(z) = (1/z)[1 + \mathcal{O}(1)/\mathrm{Im}z]$ [95]. Importantly, $\mathcal{C}(z)$ is analytic in the complex plane, except on the real axis. One obtains $\mathcal{C}(i\omega_n) = \mathcal{G}(\omega_n)$ and $\mathcal{C}(\omega + i0^+) = G^R(\omega)$. $\mathcal{C}(z)$ can be expressed as a Stieltjes transform of a density function $\widetilde{\rho}(\omega)/2\pi$:

$$\mathcal{C}(z) = \pm \int\limits_{-\infty}^{+\infty} \mathrm{d}\omega \frac{\widetilde{\rho}(\omega)/2\pi}{z-\omega} \ . \tag{2.95}$$

Since $\widetilde{\rho}(\omega)/2\pi$ is continuous, we can revert the transform and write

$$\widetilde{\rho}(\omega) = \pm i[\mathcal{C}(\omega + i0^+) - \mathcal{C}(\omega - i0^+)] = \mp 2 \ \mathrm{Im}G^R(\omega) \ , \tag{2.96}$$

where the second equation follows from $[\mathcal{C}(\omega + i0^+)]^\star = \mathcal{C}(\omega - i0^+)$ which can be seen directly from its Lehmann representation [59]. Using Eq. (2.95) at the argument $z = \omega_n$, one can apply the Fourier transform (2.93) and, after the calculating the sum over Matsubara frequencies, one obtains [94; 59]

$$\mathcal{G}(\tau) = \int\limits_{-\infty}^{+\infty} \mathrm{d}\omega K(\tau, \omega)\widetilde{A}(\omega) \ , \tag{2.97}$$

where the kernel function is $K(\tau, \omega) = e^{-\omega\tau}/(e^{-\beta\omega} \pm 1)$ and the general spectral function is $\widetilde{A}(\omega) = \widetilde{\rho}(\omega)/2\pi$. Equation (2.97) defines the problem of analytic continuation: we would like to extract the spectral function $A(\omega)$ given the input $\mathcal{G}(\tau)$, which is obtained, with statistical errors, from a QMC simulation. Therefore, a direct functional inversion of Eq. (2.97) is numerically ill-defined. However, it is possible to perform the analytic continuation using a stochastic maximum entropy method [94]. This method maps the problem of analytic continuation to a system of interacting classical fields at a fictitious temperature $1/\alpha$ which can be simulated by Monte Carlo methods. We refer the reader to the original work [94] for a complete description of the method.

2.5 Observables

In this section, we give a brief overview of the calculation of correlation functions in many-particle systems at finite temperature. For notational clarity, all quantum numbers different from position or momentum are suppressed. The quantity of interest for the study of spin (charge) excitations are the spin-spin (charge-charge) correlation function, defined as

$$S^{\alpha,\alpha}_{\boldsymbol{i},\boldsymbol{j}}(t-t') = C_1 \langle \hat{S}^{\alpha}_{\boldsymbol{i}}(t) \hat{S}^{\alpha}_{\boldsymbol{j}}(t') \rangle \ , \tag{2.98}$$

(C_1 denotes a constant reflecting different normalizations) and, in particular, its spectral representation, the dynamical spin (charge) structure factor

$$\begin{aligned} S^{\alpha,\alpha}(\boldsymbol{q},\omega) &= C_1 \frac{1}{N} \sum_{\boldsymbol{i},\boldsymbol{j}} e^{-i(\boldsymbol{i}-\boldsymbol{j})\boldsymbol{q}} \int_{-\infty}^{+\infty} \mathrm{d}t e^{i\omega t} \langle \hat{S}^{\alpha}_{\boldsymbol{i}}(t) \hat{S}^{\alpha}_{\boldsymbol{j}}(0) \rangle \\ &= C_1 \int_{-\infty}^{+\infty} \mathrm{d}t e^{i\omega t} \langle \hat{S}^{\alpha}_{\boldsymbol{q}}(t) \hat{S}^{\alpha}_{-\boldsymbol{q}}(0) \rangle \\ &= C_1 \frac{2\pi}{Z} \sum_{n,m} e^{-\beta E_n} |\langle n | \hat{S}^{\alpha}(\boldsymbol{q}) | m \rangle|^2 \delta(\omega + E_n - E_m) \ . \end{aligned} \tag{2.99}$$

The charge and spin operators are labelled by $\alpha = 0, x, y, z$. We have

$$\hat{S}^{\alpha}_{\boldsymbol{i}} = \frac{1}{2} \sum_{s,t} \hat{c}^{\dagger}_{\boldsymbol{i}s} \sigma^{\alpha}_{st} \hat{c}_{\boldsymbol{i}t} \ , \tag{2.100}$$

where $\sigma^0 = \mathrm{diag}(2,2)$ and the remaining σ^{α} are the Pauli matrices. In this notation, the charge operator is $\hat{S}^0_{\boldsymbol{i}} = \hat{n}_{\boldsymbol{i}}$. The expectation values are evaluated with respect to a Hamiltonian $\mathcal{H}$, with $\mathcal{H}|n\rangle = E_n|n\rangle$. The dynamical spin (charge) structure factor quantifies the fluctuations at a given frequency ω and is experimentally accessible through scattering experiments, for example neutron scattering. In the following, we review how $S^{\alpha,\alpha}(\boldsymbol{q},\omega)$ is related to the quantities we measure in the QMC method, namely imaginary-time dependent Green functions $\mathcal{G}(\tau)$ (2.92) and, after analytic continuation, spectral functions $A(\omega)$ (2.97).

The retarded spin-spin (charge-charge) correlation function is a response function (or a susceptibility) and it reads

$$C^{R}_{\boldsymbol{i},\boldsymbol{j}}(t-t') = -i\theta(t-t\prime) \langle [\hat{S}^{\alpha}_{\boldsymbol{i}}(t), \hat{S}^{\alpha}_{\boldsymbol{j}}(t')] \rangle \ . \tag{2.101}$$

When a many-particle system experiences a perturbation which couples to $\hat{S}^\alpha_{\boldsymbol{j}}$, the first order (linear) term of its response is a time-integral with $C^R_{\boldsymbol{i},\boldsymbol{j}}(t-t')$ being the kernel of the integral [59]. Its Fourier transform is

$$C^R(\boldsymbol{q},\omega) = -i\frac{1}{N}\sum_{\boldsymbol{i},\boldsymbol{j}} e^{-i(\boldsymbol{i}-\boldsymbol{j})\boldsymbol{q}} \int\limits_0^\infty \mathrm{d}t e^{i\omega t}\langle[\hat{S}^\alpha_{\boldsymbol{i}}(t), \hat{S}^\alpha_{\boldsymbol{j}}(0)]\rangle = -i\int\limits_0^\infty \mathrm{d}t e^{i\omega t}\langle[\hat{S}^\alpha_{\boldsymbol{q}}(t), \hat{S}^\alpha_{-\boldsymbol{q}}(0)]\rangle \ . \tag{2.102}$$

Additionally, we know that there exists a complex valued function $\mathcal{C}(\boldsymbol{q},z)$ (see 2.94) which has the property $\mathcal{C}(\boldsymbol{q},z\to\omega+i0^+) = C^R(\boldsymbol{q},\omega)$. Using the Lehmann representation of $\mathcal{C}(\boldsymbol{q},z)$ [59], one obtains

$$\begin{aligned} \mathrm{Im}\, C^R(\boldsymbol{q},\omega) &= \mathrm{Im}\, \mathcal{C}(\boldsymbol{q},z\to\omega+i0^+) \\ &= (e^{-\beta\omega}-1)\frac{\pi}{Z}\sum_{n,m} e^{-\beta E_n}|\langle n|\hat{S}^\alpha(\boldsymbol{q})|m\rangle|^2\delta(\omega+E_n-E_m) \ . \end{aligned} \tag{2.103}$$

Therefore, Im $C^R(\boldsymbol{q},\omega)$ is related to the quantity of interest, the dynamic spin structure factor $S^{\alpha,\alpha}(\boldsymbol{q},\omega)$ (2.99) as follows:

$$S^{\alpha,\alpha}(\boldsymbol{q},\omega) = \frac{2}{C_1}\frac{1}{e^{-\beta\omega}-1}\mathrm{Im}\, C^R(\boldsymbol{q},\omega) \ . \tag{2.104}$$

In order to finally see the connection to the numerically determined imaginary-time dependent Green function $\mathcal{G}(\tau) = \langle\hat{S}^\alpha_{\boldsymbol{q}}(\tau)\hat{S}^\alpha_{-\boldsymbol{q}}(0)\rangle$ we make use of Eq. (2.96) (for bosons) and Eq. (2.97). We have

$$\widetilde{A}(\boldsymbol{q},\omega) = \frac{1}{\pi}\mathrm{Im}\, C^R(\boldsymbol{q},\omega) \ , \tag{2.105}$$

and

$$\langle\hat{S}^\alpha_{\boldsymbol{q}}(\tau)\hat{S}^\alpha_{-\boldsymbol{q}}(0)\rangle = \frac{1}{\pi}\int\limits_{-\infty}^{+\infty}\mathrm{d}\omega\frac{e^{-\omega\tau}}{e^{-\beta\omega}-1}\mathrm{Im}\, C^R(\boldsymbol{q},\omega) \ . \tag{2.106}$$

To summarize, given $\mathcal{G}(\tau)$, we invert the expression (2.106) using the method of stochastic maximum entropy [94] to obtain Im $C^R(\boldsymbol{q},\omega)$. Via Eq. (2.104), we therefore can calculate the dynamic spin (charge) structure factor $S^{\alpha,\alpha}(\boldsymbol{q},\omega)$ (2.99). Note that Im $C^R(\boldsymbol{q},\omega)$ does not satisfy a sum rule, since Im $C^R(\boldsymbol{q},-\omega) = -$Im $C^R(\boldsymbol{q},\omega)$. Since the maximum entropy method needs a sum rule in order to define a probability distribution, the spectral function and the kernel of Eq. (2.97) have to be modified for bosonic Green functions [94].

In the case of fermionic particles, we mainly consider the electron-electron correlation function in a translation invariant many-particle system

$$A(\boldsymbol{k},t-t') = C_2\left(\langle\hat{c}_{\boldsymbol{k}}(t)\hat{c}^\dagger_{\boldsymbol{k}}(t')\rangle + \langle\hat{c}^\dagger_{\boldsymbol{k}}(t')\hat{c}_{\boldsymbol{k}}(t)\rangle\right) \ , \tag{2.107}$$

corresponding to the propagation of a particle and a hole, respectively (C_2 again denotes a normalization constant). Its spectral representation is the single-particle spectral function, similar to Eq. (2.99)

$$\begin{aligned} A(\boldsymbol{k},\omega) &= \int\limits_{-\infty}^{+\infty} \mathrm{d}t e^{i\omega t} A(\boldsymbol{k},t) \\ &= C_2 \frac{2\pi}{Z} \sum_{n,m} |\langle n|\hat{c}_{\boldsymbol{k}}|m\rangle|^2 \left(e^{-\beta E_n} + e^{-\beta E_m}\right) \delta(w + E_n - E_m) \; . \end{aligned} \tag{2.108}$$

The corresponding response function is the retarded single-particle Green function

$$G^R(\boldsymbol{k}, t-t') = -i\theta(t-t')\langle\{\hat{c}_{\boldsymbol{k}}(t), \hat{c}^\dagger_{\boldsymbol{k}}(t')\}\rangle \; , \tag{2.109}$$

and its Fourier components are obtained from $G^R(\boldsymbol{k},\omega) = \mathcal{C}(\boldsymbol{k}, z \to w + i0^+)$ (see 2.94). Using the Lehmann representation of $\mathcal{C}(\boldsymbol{k},z)$ [59], we have

$$\begin{aligned} \mathrm{Im}\, G^R(\boldsymbol{k},\omega) &= \mathrm{Im}\, \mathcal{C}(\boldsymbol{k}, z \to \omega + i0^+) \\ &= \frac{-\pi}{Z} \sum_{n,m} |\langle n|\hat{c}_{\boldsymbol{k}}|m\rangle|^2 \left(e^{-\beta E_n} + e^{-\beta E_m}\right) \delta(w + E_n - E_m) \; . \end{aligned} \tag{2.110}$$

Comparing with Eq. (2.108), we therefore obtain the spectral function

$$A(\boldsymbol{k},\omega) = -2C_2 \,\mathrm{Im}\, G^R(\boldsymbol{k},\omega) = -\frac{1}{\pi} \mathrm{Im}\, G^R(\boldsymbol{k},\omega) \; , \tag{2.111}$$

using $C_2 = 1/(2\pi)$. The prefactor C_2 can be obtained from the sum rule for Eq. (2.108),

$$1 = \int\limits_{-\infty}^{+\infty} \mathrm{d}\omega A(\boldsymbol{k},\omega) = 2\pi C_2 \langle\{\hat{c}_{\boldsymbol{k}}, \hat{c}^\dagger_{\boldsymbol{k}}\}\rangle = 2\pi C_2 \; . \tag{2.112}$$

3

Metamagnetism and Lifshitz Transitions in Models for Heavy Fermions

In this project, we have investigated metamagnetic transitions in the two-dimensional, doped Kondo lattice model which is the effective low-energy model of heavy-fermion systems. We show the existence of universal magnetization curves for different temperatures and Kondo coupling and take into account different Landé factors of the localized moments and the conduction electron spins. We show evidence for the interpretation of heavy-fermion metamagnetism in terms of a Lifshitz transition. By tracking the single-particle residue across the metamagnetic transition as a function of the external Zeeman field, we can rule out the breakdown of Kondo screening, even at magnetic fields that are comparable and larger than the heavy-fermion coherence scale. Numerically, we map the Kondo lattice model to a cluster approximation using the DMFT and the DCA (Sec. 2.3). This chapter is an extended reproduction of the associated publication [96].

3.1 The metamagnetic transition in heavy fermions

On general grounds, the metamagnetic transition corresponds to a non-linear increase of the magnetization at a well-defined value of the external magnetic field in certain fermion systems. Equally, distinct anomalies of thermodynamic quantities and in transport measurements have been observed at the same magnetic field [97; 98]. At the critical field, the heavy electron Fermi surface changes its topology [99; 97; 100; 101]. Metamagnetism has been known to occur in $\mathrm{CeRu_2Si_2}$ [102] and, amongst other fermionic systems, a pressure-tuned first order metamagnetic transition has been observed in bilayer ruthenates [103]. Recent experiments show a pronounced, first order metamagnetic transition in the heavy-fermion paramagnet CeTiGe [104]. Furthermore, the thermodynamic signatures of heavy-fermion compounds have been related to a metamagnetic quantum critical endpoint of the Ising universality class [105; 106].

The metamagnetic transition in heavy-fermion systems has been addressed previously by static mean-field approximations [107; 108]. By including temporal fluctuations, the DMFT results of Ref. [109] have shown the close relation of the magnetization profile to the quasiparticle coherence scale. In this project, we have extended the study in Ref. [109] by increasing the temperature range of the simulations, allowing for different Landé factors and by including non-local spatial fluctuations.

A Lifshitz transition is a quantum phase transition which occurs when the Fermi surface topology is deformed continuously [110; 111; 112]. It ows its name to I. M. Lifshitz who first classified the changes of the Fermi surface for the non-interacting electron gas and attributed anomalies of several several thermodynamic and kinetic observables to this transition [110]. Importantly, it is a topological transition which does not break a symmetry of the lattice. Lifshitz transitions play an important role in the study of the Fermi liquid phase of heavy-fermion systems, often as an alternative scenario to the breakdown of Kondo screening [113; 17; 114]. Zeeman-driven Lifshitz transitions were shown to explain many anomalies in thermodynamic and transport measurements of certain heavy-fermion metals [115].

This project is motivated by the interplay of two competing energy scales, the lattice coherence scale and the magnetic Zeeman scale. By varying the magnitude of the Landé factors we are able to show that the metamagnetic transition occurs when both scales are comparable. In principle, both the Kondo breakdown and the Lifshitz transitions are therefore valid scenarios. We measure the single-particle residue as a function of magnetic field throughout the metamagnetic transition and show that it is consistent with the picture of a coherent band dropping below the Fermi energy at the transition. Our results clearly point towards Lifshitz physics as the key player in the metamagnetic transition in models of heavy fermions.

3.2 Implementation of the Kondo lattice model

Our study of heavy-fermion metamagnetism is based on the solution of the following Kondo lattice model (see Eq. 1.1.1),

$$\mathcal{H} = -t \sum_{\langle \boldsymbol{i},\boldsymbol{j}\rangle,\sigma} (\hat{c}^{\dagger}_{\boldsymbol{i}\sigma}\hat{c}_{\boldsymbol{j}\sigma} + \text{H.c.}) - \mu \sum_{\boldsymbol{i},\sigma} \hat{c}^{\dagger}_{\boldsymbol{i}\sigma}\hat{c}_{\boldsymbol{i}\sigma} - \mu_B B \sum_{\boldsymbol{i}} (g_c \hat{S}^{c,z}_{\boldsymbol{i}} + g_f \hat{S}^{f,z}_{\boldsymbol{i}}) + J \sum_{\boldsymbol{i}} \hat{\boldsymbol{S}}^{c}_{\boldsymbol{i}} \cdot \hat{\boldsymbol{S}}^{f}_{\boldsymbol{i}} \;, \tag{3.1}$$

where a Zeeman magnetic field terms have been inclueded that couple to the c- and f-spins in the form of spin-dependent chemical potentials. The indices $\boldsymbol{i}, \boldsymbol{j}$ indicate sites on the two-dimensional square lattice. Throughout this chapter, we will adjust the chemical potential in order to realize a conduction electron band occupation of $n_c = 0.9$. Looking at the phase diagram (Fig. 1.3) of the KLM, the system is in the paramagnetic phase, as long as $J/t \gtrsim 1$.

Evidently, the KLM (3.1) has some limitations. For example, spin-orbit coupling is neglected which would cause the Landé g-factors to be tensor quantities. A realistic modeling of heavy-fermion materials would require more sophisticated approaches capturing these material specific features. Instead, the KLM (3.1) serves the purpose of describing the generic interplay between the magnetic Zeeman scale and the coherence scale of the Kondo system which can lead either to the Kondo breakdown or the Lifshitz transition scenario.

Following Ref. [18], the Heisenberg term can be rewritten as

$$\begin{aligned} J\sum_{\boldsymbol{i}} \hat{\boldsymbol{S}}^c_{\boldsymbol{i}} \cdot \hat{\boldsymbol{S}}^f_{\boldsymbol{i}} &= J\sum_{\boldsymbol{i}} \left[\frac{1}{2}\hat{n}^c_{\boldsymbol{i}} - \frac{1}{4}\hat{n}^c_{\boldsymbol{i}}\hat{n}^f_{\boldsymbol{i}} - \frac{1}{4}\left(\hat{c}^\dagger_{\boldsymbol{i},\alpha}\hat{f}_{\boldsymbol{i},\alpha}\hat{f}^\dagger_{\boldsymbol{i},\beta}\hat{c}_{\boldsymbol{i},\beta} + \text{H.c.}\right)\right] \\ &= -\frac{J}{4}\sum_{\boldsymbol{i}} \left(\hat{c}^\dagger_{\boldsymbol{i},\sigma}\hat{f}_{\boldsymbol{i},\sigma} + \hat{f}^\dagger_{\boldsymbol{i},\sigma}\hat{c}_{\boldsymbol{i},\sigma}\right)^2 \\ &\quad + \frac{J}{4}\sum_{\boldsymbol{i}} \left[\left(\hat{n}^c_{\boldsymbol{i}} + \hat{n}^f_{\boldsymbol{i}} - \hat{n}^c_{\boldsymbol{i}}\hat{n}^f_{\boldsymbol{i}}\right) - \left(\hat{c}^\dagger_{\boldsymbol{i},\alpha}\hat{f}_{\boldsymbol{i},\alpha}\hat{c}^\dagger_{\boldsymbol{i},\beta}\hat{f}_{\boldsymbol{i},\beta} + \text{H.c.}\right)\right] . \end{aligned} \tag{3.2}$$

We used the identities

$$\boldsymbol{\sigma}_{\alpha\beta} \cdot \boldsymbol{\sigma}_{\gamma\delta} = 2\delta_{\alpha\delta}\delta_{\beta\gamma} - \delta_{\alpha\beta}\delta_{\gamma\delta} \; , \tag{3.3}$$

and

$$\hat{c}^\dagger_{\boldsymbol{i},\alpha}\hat{f}_{\boldsymbol{i},\alpha}\hat{f}^\dagger_{\boldsymbol{i},\beta}\hat{c}_{\boldsymbol{i},\beta} + \text{H.c.} = \left(\hat{c}^\dagger_{\boldsymbol{i},\sigma}\hat{f}_{\boldsymbol{i},\sigma} + \hat{f}^\dagger_{\boldsymbol{i},\sigma}\hat{c}_{\boldsymbol{i},\sigma}\right)^2 - \left(\hat{c}^\dagger_{\boldsymbol{i},\sigma}\hat{f}_{\boldsymbol{i},\sigma}\right)^2 - \left(\hat{f}^\dagger_{\boldsymbol{i},\sigma}\hat{c}_{\boldsymbol{i},\sigma}\right)^2 - \hat{n}^f_{\boldsymbol{i}} + \hat{n}^c_{\boldsymbol{i}} \; , \tag{3.4}$$

in the first and in the second line, respectively. One immediately sees in the decomposition of the Heisenberg term [Eq. (3.2)] that the third line contains only constant terms and pair hopping terms. The former correspond to a uniform shift in the chemical potential and the latter have zero contribution in the subspace of single occupancy [18] of the f-orbital.

We therefore define the following auxiliary Hamiltonian,

$$\widetilde{\mathcal{H}} = \mathcal{H}_0 - \frac{J}{4}\sum_{\boldsymbol{i}} \left(\hat{c}^\dagger_{\boldsymbol{i},\sigma}\hat{f}_{\boldsymbol{i},\sigma} + \hat{f}^\dagger_{\boldsymbol{i},\sigma}\hat{c}_{\boldsymbol{i},\sigma}\right)^2 + \mathcal{H}_{\mathrm{U}_f} \; , \tag{3.5}$$

and use it for the numerical implementation of the Kondo lattice model [109; 18]. The Hubbard term reads $\mathcal{H}_{\mathrm{U}_f} = \frac{U_f}{2}\sum_{\boldsymbol{i}}\left[\sum_\sigma n^f_{i\sigma} - 1\right]^2$. Since single occupancy of the f-orbitals is guaranteed for $U_f \to \infty$, it is in this limit, that $\widetilde{\mathcal{H}}$ becomes equivalent to the original model (3.1).

3.3 Methods

The hallmark of Kondo physics is the crossover from weak to strong coupling of the ground state as the temperature is lowered. This has been first studied by K. Wilson with the numerical renormalization theory [2]. The crossover to the Kondo regime is mediated by temporal correlations, spatial correlations being secondary. Deep in the low temperature phase, even the static mean-field perspective can provide valuable insights [116].

We use the HF-QMC algorithm (see Sec. 2.1.5) to solve the KLM on small clusters, that contain one c- and one f-orbital (DMFT limit) and tow c- and two f-orbital orbitals, respectively. Cluster approximation schemes are particularly well designed to capture the Kondo physics since temporal correlations can be treated exactly. The approximation is on spatial correlations that are short ranged in the present situation. The DCA is a fully causal, non-perturbative method which is systematically improved by increasing the cluster sizes [93; 91]. The method is reviewed in Sec. 2.3. In the following, we outline the static mean field approach and the QMC-implementation for the KLM.

Mean-field theory

The static mean-field approximation is the approximation of the action of the model by its saddle-point. However, one can artificially increase the number of electron "flavors", from $N = 2$ [Eq. (3.1)] to an arbitrary integer N [117; 118]. In the absence of magnetic fields, this generalized Kondo lattice model has a $SU(N)$ symmetry, i.e. the Hamiltonian commutes with the $N^2 - 1$ operators, which generate the corresponding $su(N)$ Lie algebra. For $N \to \infty$, the saddle-point solution is the *exact* solution of the $SU(N)$ model. Therefore, instead of approximating the solution by throwing away fluctuations beyond first order in the $SU(2)$ model Hamiltonian (standard mean-field theory), we may approximate the Hamiltonian by its $SU(N)$ symmetric counterpart, which we can solve exactly. On the other hand, the magnetic field reduces the $SU(2)$ symmetry to a $U(1)$ symmetry [Eq. (3.1)], and therefore it cannot be readily included in the derivation of the saddle-point solution. Additionally, it is well-known that the saddle-point solution leads to an unphysical phase transition instead of the Kondo crossover. Interestingly, the magnetic matrix elements that couple the impurity f-orbitals to the external magnetic field can be chosen in such a way, that the magnetic field does not lift the degeneracy of the electron flavors completely. Then, one can recover the smooth Kondo crossover even in the large-N limit and in the presence of external magnetic fields [119].

The many-body partition function is

$$Z = \mathrm{Tr}\left[e^{-\beta\widetilde{\mathcal{H}}}\right] = Z_{\Delta\tau} + \mathcal{O}[(\Delta\tau)^2]\,, \tag{3.6}$$

where we introduced the imaginary time discretization $\beta = M\Delta\tau$ on the interval $[0, \beta]$. We have

$$\begin{aligned} Z_{\Delta\tau} &= \mathrm{Tr}\prod_{l=1}^{M}\Bigg\{\exp\big[-\Delta\tau\mathcal{H}_0\big]\int\mathrm{D}[\lambda]\,\exp\Big[-i\Delta\tau\sum_{\boldsymbol{i}}\lambda_{l\boldsymbol{i}}\big(\sum_{\sigma}n^f_{\boldsymbol{i}\sigma}-1\big)\Big] \\ &\quad\times\int\mathrm{D}[\phi]\,\exp\Big[-\Delta\tau J\sum_{\boldsymbol{i}}\Big(\phi^2_{l\boldsymbol{i}}-\phi_{l\boldsymbol{i}}\sum_{\sigma}\big(c^\dagger_{\boldsymbol{i},\sigma}f_{\boldsymbol{i},\sigma}+\mathrm{H.c.}\big)\Big)\Big]\Bigg\} \\ &= \int\mathrm{D}[\lambda,\phi]\,\exp\big[-S_{\mathrm{eff}}[\lambda,\phi]\big]\,. \end{aligned} \tag{3.7}$$

In Eq. (3.7), the two successive Hubbard-Stratonovich (HS) transformation reduce the quartic fermion terms to quadratic terms, introducing the fields $\lambda_{l\boldsymbol{i}}$ and $\phi_{l\boldsymbol{i}}$. In this notation, the integration measures $\mathrm{D}[\lambda, \phi]$ denote integration over spatial and time indices of the fields and contain normalization factors.

The saddle-point of the above defined action fulfills $\partial S_{\mathrm{eff}}/\partial\phi_{li} = \partial S_{\mathrm{eff}}/\partial\lambda_{li} = 0$. Static mean-field theory is obtained by dropping the τ-dependence in the HS fields, and one can furthermore request the homogeneous solution: $\phi_{li} \equiv \phi_0$, $\lambda_{li} \equiv \lambda_0$. The saddle-point equations,

$$\phi_0 = \frac{1}{2N}\langle\sum_{\boldsymbol{i}\sigma}c^\dagger_{\boldsymbol{i},\sigma}f_{\boldsymbol{i},\sigma} + \mathrm{H.c.}\rangle_{\mathrm{MF}},\;\; 1 = \frac{1}{N}\langle\sum_{\boldsymbol{i}\sigma}n^f_{\boldsymbol{i},\sigma}\rangle_{\mathrm{MF}}\,, \tag{3.8}$$

are then solved self-consistently. The respective mean field results for total magnetization and quasiparticle residues are discussed in Sec. 3.4. A detailed discussion of the hybridization mean-field calculation can be found in Ref. [109].

Sampling of the field configurations with HF-QMC

In order to go beyond the mean field saddle point, one may look at the Gaussian fluctuations around the saddle point. Furthermore, a systematic $1/N$ expansion around the mean field solution can be performed [120]. Instead, we integrate over all the field configurations through application of the HF-QMC algorithm which has been derived in Sec. 2.1.5. By carrying out the trace in Eq. (3.7), the partion function reads

$$Z_{\Delta\tau} = \int \mathrm{D}[\lambda, \phi] \prod_{\sigma} \det\left[G_{\sigma}^{-1}\right] , \tag{3.9}$$

where G_σ is the space-time dependent Green function. For the QMC implementation, the integral is replaced by a discrete sum which is sampled stochastically [see Eq. (2.49)]. The Heisenberg term and the Hubbard term of the Hamiltonian (3.5) are implemented using the discrete HS transforms Eq. (2.23) and Eq. (2.22), respectively [18]. During the simulation of Eq. (3.5), double occupancy of the f-orbitals can be suppressed to the desired accuracy.

The cluster approximation amounts to considering the interaction terms of the Hamiltonian only on sites $\boldsymbol{R} \in \mathcal{M}$ where $\mathcal{M}$ is a subset of N_c elements (sites) of the lattice. This subset naturally defines the extent to which spatial correlations are captured. We therefore solve the model

$$\mathcal{H} = \tilde{\mathcal{H}}_0 + J \sum_{\boldsymbol{R} \in \mathcal{M}} \hat{\boldsymbol{S}}^{c}_{\boldsymbol{R}} \cdot \hat{\boldsymbol{S}}^{f}_{\boldsymbol{R}} , \tag{3.10}$$

by using the auxiliary Hamiltonian (3.5). Here, $\tilde{\mathcal{H}}_0$ denotes the bath which has to be determined self-consistently. The DMFT/DCA method is reviewed in Sec. 2.3.

3.4 Field dependent magnetization curves

The magnetic field tunes the interacting Kondo model [Eq. (3.1)] from the strong coupling regime (i.e., *small* field) to the weak coupling regime (i.e., *large* field). The latter regime is defined as $B \gg T_{\mathrm{coh}}$. This limit is adiabatically connected to a phase, that is described by two copies of non-interacting c-electrons, which are spin split by the Zeeman energy, and fully polarized f-moments. On the other side of the transition, as long as the magnetic field is small, $B \ll T_{\mathrm{coh}}$, the hybridized bands can be expected to shift in a rigid manner. At an intermediate energy scale, which we define as $B \sim T_{\mathrm{coh}}$, we can think of two different scenarios: (i), the Kondo effect itself breaks down at the relevant energy scale or, (ii), a continuous transition occurs, which preserves the quasiparticles.

In scenario (i), the quasiparticle itself is destroyed by the external magnetic field. The spin resolved single-particle residue, labelled Z_σ, quantifies the overlap of the interacting wave function with the wave function of a bare conduction electron. It is an appropriate quantity to test this scenario, since the loss of quasiparticle coherence has to manifest itself as a sudden drop in the residue for both both spin projections.

In scenario (ii), the quasiparticles remain intact at the Fermi level. The spin dependent Fermi surfaces are then expected to undergo Lifshitz transitions which modify their topology.

By carefully tracking the single-particle residue and single-particle spectral function across the metamagnetic transition we collected evidence in favor of scenario (ii).

Below the coherence temperature, the Kondo lattice model is believed to form a heavy Fermi liquid which is characterized by Kondo screening of the local moments [11]. A fundamental result for Fermi liquids is the Luttinger theorem [121]. It states that the volume which is enclosed by the Fermi surface is invariant with respect to interactions and is essentially given by the total density of electrons. In the heavy Fermi liquid phase, the conduction electrons and the delocalized spins contribute both to the Fermi volume, which is therefore called "large". For the two-dimensional Kondo lattice, the Luttinger theorem is [122]

$$\mathcal{V}_{\mathrm{FL}} = \frac{K}{2}\left(n_{\mathrm{tot}} \bmod 2\right) = \frac{K}{2}\left[\left(n^c + n^f\right) \bmod 2\right] , \tag{3.11}$$

where $K = (2\pi)^2/V$ (V is the unit cell volume) and $n_f = 1$. The factor of 1/2 accounts for the spin degeneracy and the modulo operation is used to count only partially filled bands.

Following Ref. [109], we note that the magnetization profile (see Fig. 3.1) of a heavy-fermion model system can serve directly as a measure of coherence. For intermediate fields, the occupation number difference, $m = \sum_\sigma \sigma\left(n^c_\sigma + n^f_\sigma\right)$, reaches a plateau. In this phase, one band (the up-spin conduction band) is completely filled whereas the other band (the down-spin conduction band) is partially empty. In the case of half-filling, one can formally write $n_{\mathrm{tot}} = 2 = n_{\mathrm{tot}\uparrow} + n_{\mathrm{tot}\downarrow}$, with $n_{\mathrm{tot}\,\sigma} = 1$. Therefore, the up-spin conduction band has the density $n_{\mathrm{tot}\uparrow} = n^c_\uparrow + n^f_\uparrow = 1$. Since the combined electronic density is $n_{\mathrm{tot}} = n^c + 1$, which is true even in the presence of interaction, following the Luttinger theorem, the partially empty down-spin conduction band has the density $n_{\mathrm{tot}\downarrow} = n^c_\downarrow + n^f_\downarrow = n^c$. For the intermediate field values, we then have a magnetization plateau with the height

$$m = n^c_\uparrow + n^f_\uparrow - \left(n^c_\downarrow + n^f_\downarrow\right) = 1 - n^c . \tag{3.12}$$

This result is a consequence of coherence and Luttinger's theorem. Within the hybridization mean field theory, it has been shown that the corrections to the magnetization plateau are exponentially small [109].

The physical magnetization on the other hand, as derived from the free energy $\mathcal{F}$ of the system,

$$M(B) = -\frac{\partial \mathcal{F}}{\partial B} = \sum_\sigma \sigma\left(g_c n^c_\sigma + g_f n^f_\sigma\right) \tag{3.13}$$

does not generally display a plateau when the orbital couplings are unequal, $g_c \neq g_f$.

3.4.1 Data collapse $M(g_f/g_c, T/T_{\mathrm{coh}}, B/T_{\mathrm{coh}})$

For temperatures below the coherence scale T_{coh}, quasiparticle bands are formed via coherent superposition of the screening clouds of the local spins. To verify that the coherence scale is the unique underlying scale, a data collapse of DMFT and DCA data is carried out by scaling the magnetization with T_{coh}. Because the plateau width of the occupation number is a measure of the hybridization gap, a good estimate of T_{coh} is obtained from the position

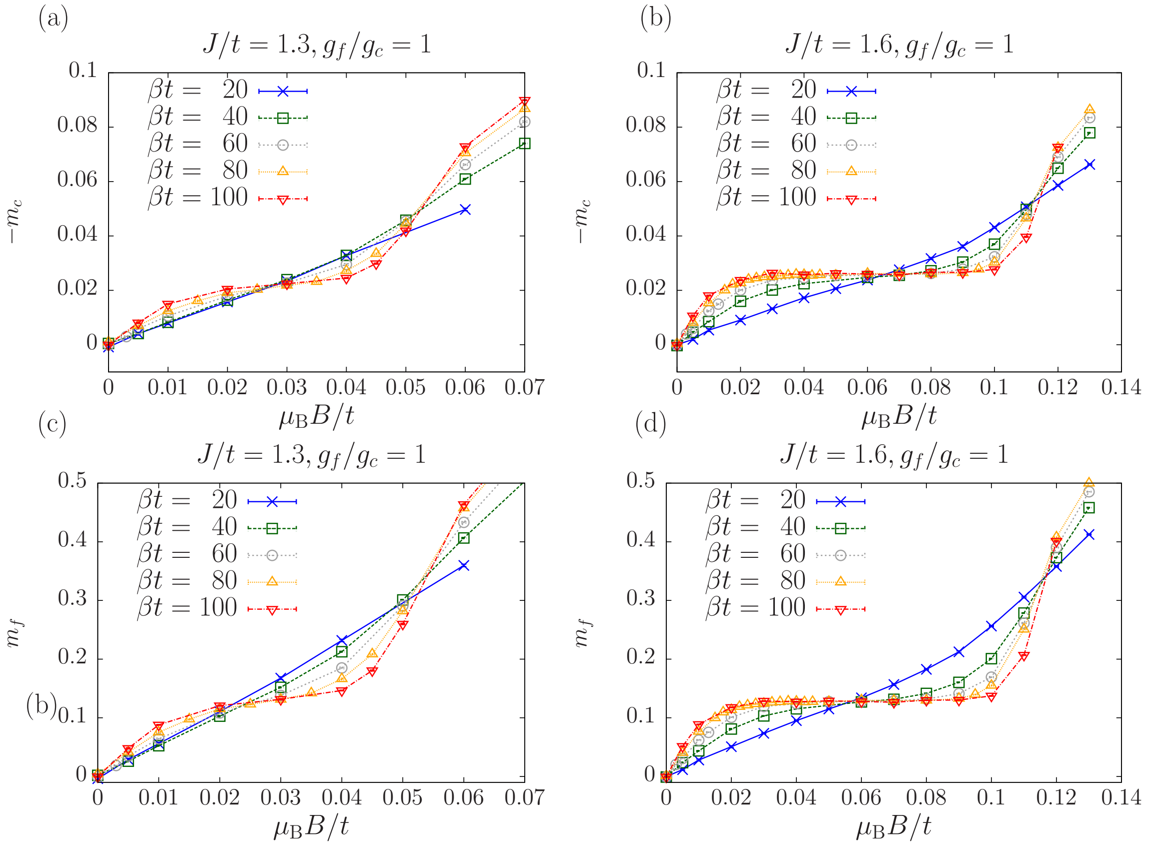

Figure 3.1: Temperature and magnetic field dependence of the magnetization m_c [(a),(b)] and m_f [(c),(d)]. As the temperature is lowered, the Kondo insulator is formed and in the Kondo regime, the width of the magnetization plateau is a measure for the single-particle band gap. Here, $J/t = 1.3$ (left) and $J/t = 1.6$ (right).

of the second kink at $B = B_{\mathrm{L2}}$, determined by the intersections of linear fits to the data on both sides of the transition at $\beta t = 100$ and $g_f/g_c = 1$. The scaling then becomes:

$$M(g_f/g_c, T, B, J) \to M(g_f/g_c, T/T_{\mathrm{coh}}, B/T_{\mathrm{coh}}) \; . \tag{3.14}$$

Effectively, the Kondo coupling J/t has disappeared as a parameter in the scaled magnetization. The data collapse, as shown in Fig. 3.2, is evident. For all values of g_f/g_c the magnetization shows two pronounced kinks at $B = B_{\mathrm{L1}}$ and $B = B_{\mathrm{L2}}$. The driving mechanism that shapes the magnetization roots in the competition of two energy scales: the dominant magnetic energy scale $g_f \mu_B B$ and the Kondo scale T_{coh}. At the second kink both scales become comparable, such that $B_{\mathrm{L2}} \propto g_f^{-1}$. The position of the second kink in dependence of the coupling ratio is shown in Fig. 3.3 and the data are in good agreement with the above argument. Increased Zeeman coupling to the local spins provokes the intermediate, plateau-like region to decrease and renders the increase at $B = B_{\mathrm{L2}}$ much steeper (Fig. 3.2).

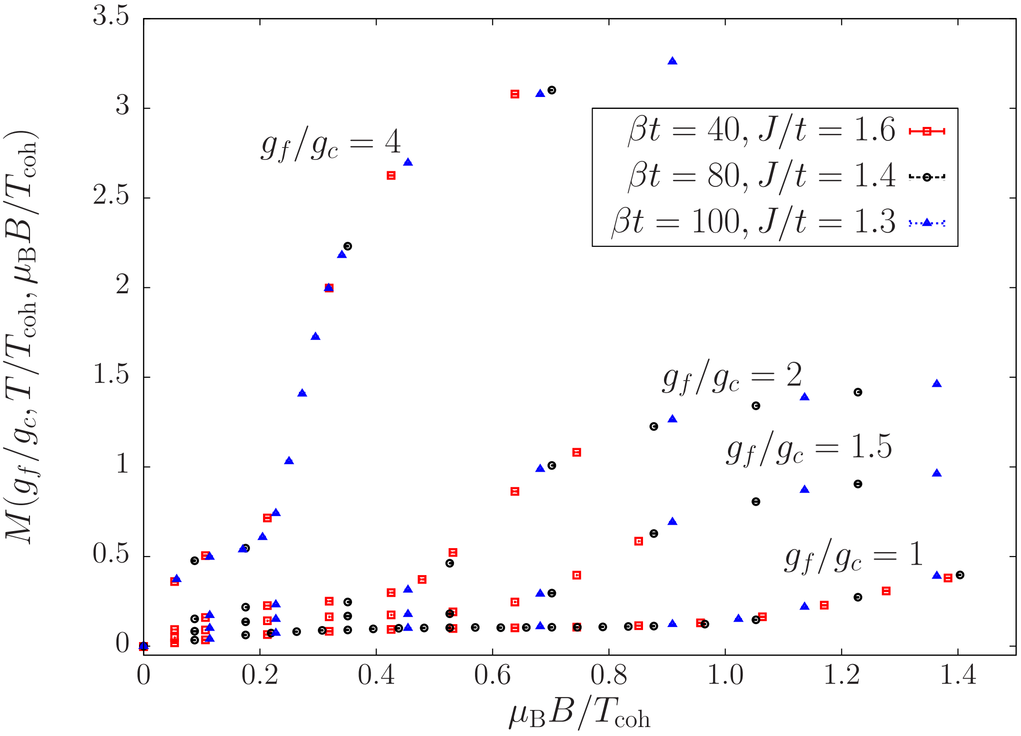

Figure 3.2: Magnetization $M(g_f/g_c, T/T_{\mathrm{coh}}, B/T_{\mathrm{coh}})$, scaled with the coherence temperature $T_{\mathrm{coh}}(J)$. The data collapse is observed for all ratios of Landé factors g_f/g_c, indicating that the coherence temperature is the unique energy scale for all measurements in this phase. Here, the results have been obtained from two-orbital DMFT calculations.

The mean-field solution, motivated by the paramagnetic saddle-point of the $SU(N)$ KLM, can be seen as the best approximation to the fully correlated model in terms of quadratic

J/t	1.3	1.4	1.6	2.0
DMFT	0.044	0.057	0.094	-
DCA	-	-	0.10	0.18

Table 3.1: Estimated values of the coherence temperatures T_{coh}/t, measured at $B = B_{\mathrm{L2}}$. Here, $g_f/g_c = 1$.

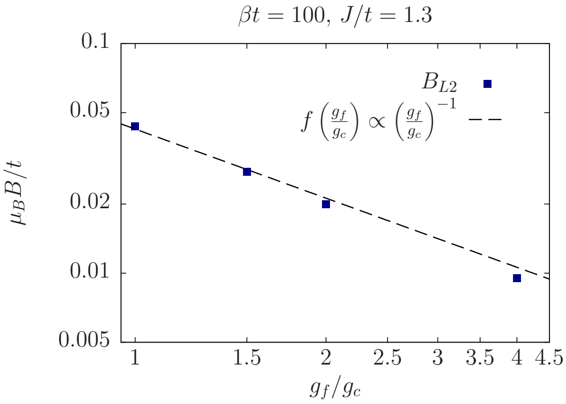

Figure 3.3: Dependence of the second Lifshitz transition, B_{L2}, on the ratio of Landé factors, g_f/g_c. We observe good agreement of the data with with $B_{\mathrm{L2}}(g_f/g_c) \propto \left(g_f/g_c\right)^{-1}$.

fermion contributions. Therefore, in the case that DMFT/DCA calculations support the notion of quasiparticles, the mean field perspective is legitimate. The mean field results are intended to complete the above described scenario of Lifshitz transitions. Static mean field calculations succeeds in reproducing the qualitative shape of M (Fig. 3.5). In the mean field picture, the two kinks in the magnetization correspond to two Lifshitz transitions.

At this point, the data collapse of the magnetization can be compared to a scaling approach of the resistivity in a recent cluster DMFT (CDMFT) study of the Anderson lattice model. Close to half-filling of the conduction band, this work equally reveals the lattice coherence temperature as the single underlying energy scale [123].

Our calculated metamagnetic curves, as shown in Fig. 3.2, bear notable similarity with recent experimental data of the paramagnetic heavy-fermion system CeTiGe [104]. This is discussed in Sec. 3.7.

3.5 Single-particle quantities

The analysis of the single-particle quantities is based on the observation, that the KLM has a Fermi liquid ground state for the chosen value of conduction band filling, $n_{\mathrm{c}} = 0.9$ [12], and for zero external magnetic field. The calculations were performed for $J/t = 1.3$, $g_f/g_c = 4$, $\beta t = 100$ and $\beta t = 200$. For these parameters, we identify two Lifshitz transitions that occur at $\mu_\mathrm{B}B_{\mathrm{L1}}/t \approx 0.002$ and at $\mu_\mathrm{B}B_{\mathrm{L2}}/t \approx 0.01075$. The latter corresponds to the metamagnetic transition.

A Fermi liquid signature is the analyticity of the retarded self energy $\Sigma(\boldsymbol{k},\omega)$ around the Fermi energy such that $\Sigma(\boldsymbol{k},\omega)$ allows for a polynomial expansion. We can characterize the Fermi liquid by the single-particle residue Z_σ and the effective quasiparticle mass $m^\star_\sigma/m_\sigma$. When the self energy is momentum independent, $\Sigma_\sigma(\boldsymbol{k},\omega) = \Sigma_\sigma(\omega)$, we have [60]

$$Z_\sigma = \lim_{\omega\to 0}\left[1 - \frac{\partial \mathrm{Re}\Sigma_\sigma(\omega)}{\partial\omega}\right]^{-1} , \tag{3.15}$$

and

$$Z_\sigma \frac{m^\star_\sigma}{m_\sigma} = 1 . \tag{3.16}$$

Alternatively, the single-particle residue may also be expressed with the Matsubara self-energy $\Sigma^{\mathrm{DMFT}}_\sigma(i\omega_n)$:

$$\left[Z^{\mathrm{DMFT}}_\sigma\right]^{-1} = \lim_{T\to 0}\left[1 - \frac{\mathrm{Im}\Sigma^{\mathrm{DMFT}}_\sigma(i\omega_n)}{\omega_n}\right]_{\omega_n=\pi T} . \tag{3.17}$$

In the following, we show that Eq. (3.15) and (3.17) are identical, i.e.

$$\lim_{\omega\to 0}\left[1 - \frac{\partial \mathrm{Re}\Sigma_\sigma(\omega)}{\partial\omega}\right]^{-1} = \lim_{T\to 0}\left[1 - \frac{\mathrm{Im}\Sigma^{\mathrm{DMFT}}_\sigma(i\omega_n)}{\omega_n}\right]_{\omega_n=\pi T} . \tag{3.18}$$

In general, the self-energy $\Sigma(\omega)$ can be decomposed as

$$\Sigma(\omega) = \Sigma_0 + \Sigma_1(\omega) , \tag{3.19}$$

where Σ_0 is a constant term. Following Ref. [124], we make use of the Kramers-Kronig relations which are applicable in case the self-energy decays at least like $|\omega|^{-1}$, i.e. $\lim\limits_{|\omega|\to 0} |\Sigma_1(\omega)\omega| \le 1$. We then have

$$\mathrm{Re}\Sigma_1(\omega) = \mathcal{P}\frac{1}{\pi}\int\limits_{-\infty}^{+\infty} \mathrm{d}\omega' \frac{\mathrm{Im}\Sigma_1(\omega')}{\omega' - \omega} . \tag{3.20}$$

On the other hand, one may write the self-energy $\Sigma_1(z)$, where $z \in \mathbb{C}$, as a Stieltjes transform [60]:

$$\Sigma_1(z) = \frac{1}{\pi}\int\limits_{-\infty}^{+\infty} \mathrm{d}\omega \frac{\mathrm{Im}\Sigma_1(\omega)}{\omega - z} , \tag{3.21}$$

where $-\mathrm{Im}\Sigma_1(\omega)/\pi$ is the spectral density. Evaluating $\Sigma_1(z)$ at the points $z = i\omega_n$, we have

$$\lim_{\omega_n\to 0}\left[\frac{\mathrm{Im}\Sigma_1(i\omega_n)}{\omega_n}\right] = \lim_{\omega_n\to 0}\left[\frac{1}{\pi}\int\limits_{-\infty}^{+\infty} \mathrm{d}\omega' \frac{\mathrm{Im}\Sigma_1(\omega')}{\omega'^2 + \omega_n^2}\right] = \lim_{\omega\to 0}\left[\frac{\partial \mathrm{Re}\Sigma_1(\omega)}{\partial\omega}\right] . \tag{3.22}$$

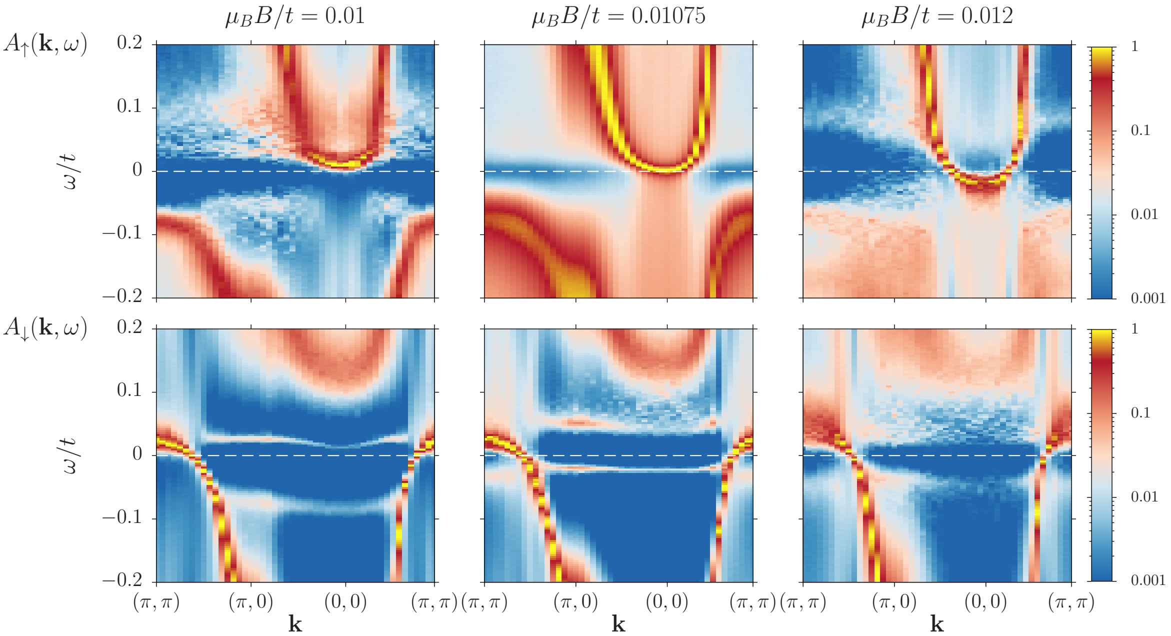

Figure 3.4: Single-particle spectral function $A_\sigma(\boldsymbol{k},\omega)$, measured across the metamagnetic transition at $\mu_\mathrm{B}B/t \approx 0.01$. Here, $\beta t = 200$. Note that the values of the magnetic field corresponds to the arrows in Fig. 3.5. The dashed line indicates the Fermi level. The narrow distribution of (quasiparticle) spectral weight close to the Fermi energy indicates that the Kondo coherence remains across the metamagnetic Lifshitz transition.

The last equation is obtained from Eq. (3.20). With the help of Eq. (3.22), we see that Eq. (3.18) is fulfilled.

The quantity $\mathrm{Im}\Sigma_\sigma^{\mathrm{DMFT}}(i\omega_n)$ across the metamagnetic transition at $B = B_{\mathrm{L2}}$ is displayed in Fig. 3.6. Evidently, the imaginary part of the Matsubara self energy is free of divergences for both spin projections at low frequencies ω_n . We take this as evidence for the continuous transition scenario.

The spectral function,

$$A_\sigma(\boldsymbol{k},\omega) = -\frac{1}{\pi}\,\mathrm{Im}\,G^\sigma_{\mathrm{Latt}}(\boldsymbol{k},\omega)\ , \tag{3.23}$$

measures the single-particle excitations (Fig. 3.4). Here, $G^\sigma_{\mathrm{Latt}}(\boldsymbol{k},\omega)$ is the retarded lattice Green function (see Sec. 2.3). The analytic continuation from imaginary time dependent QMC data has been performed with the stochastic maximum entropy method, outlined in Sec. 2.4.

The single-particle residues Z_σ [Eq. (3.17)] at $\beta t = 100$ and $\beta t = 200$ across the metamagnetic transition are shown in Fig. 3.5(b). $Z_\downarrow$ essentially follows the magnetization $M(B)$ (Fig. 3.5(a)). $A_\downarrow(\boldsymbol{k},\omega)$ displays well defined quasiparticle weight across the metamagnetic transition (Fig. 3.4) and hence accounts for a metallic state. $Z_\uparrow$ vanishes for an intermediate magnetic field range, close to $B_{L1} < B < B_{L2}$. In this locked phase, no up-spin Fermi surface

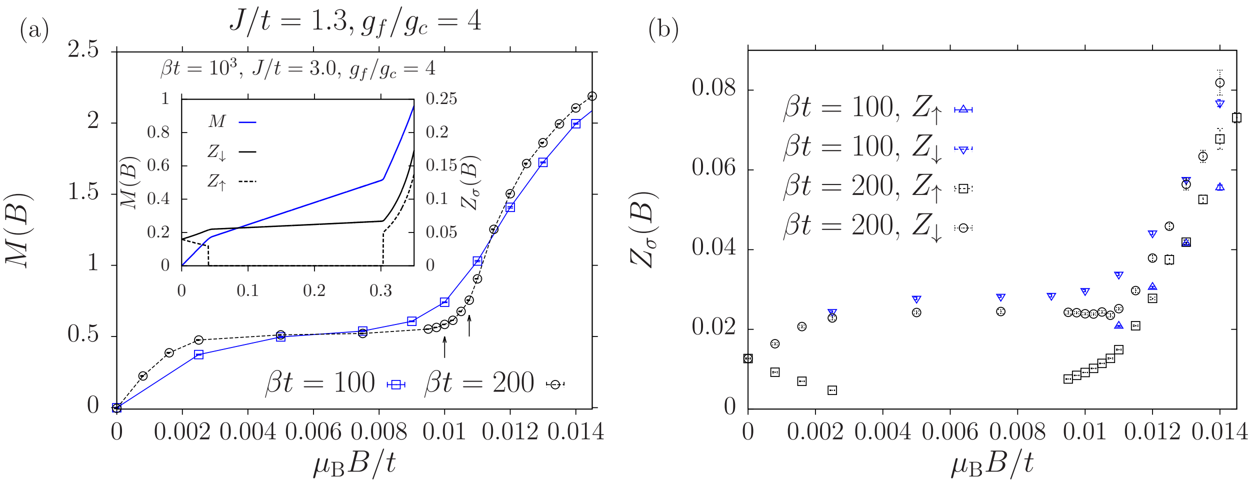

Figure 3.5: Low-temperature DMFT results for the magnetization $M(B)$ (a) and the single-particle residue $Z_\sigma(B)$ (b), traced across the metamagnetic transition at $\mu_B B/t \approx 0.01$. The arrows in (a) refer to the single-particle spectra of Fig. 3.4. Inset: static mean field results for $M(B)$ and $Z_\sigma(B)$.

is present. At $B = B_{L2}$, a topological change of the Fermi surface occurs since one up-spin band crosses the Fermi level at the gamma point, $(k_x, k_y) = (0, 0)$. $A_\uparrow(\boldsymbol{k}, \omega)$ shows a sharply defined quasiparticle band just below and at $B = B_{L2}$, see Fig. 3.4. The fact that the residue $Z_\uparrow$ does not vanish exactly at $B = B_{L2}$ can be related to the finite temperature. Also, we note that the single-particle residue is not fully converged in the intermediate field range, even at the lowest temperatures.

In the static mean field scenario, the two Lifshitz transitions are naturally present. As shown in the inset to Fig. 3.5, the single-particle residue $Z_\uparrow$, calculated from the mean field coherence factors at the Fermi energy, displays the expected step-like behavior.

Furthermore, the up-spin Fermi surface forms a closed loop centered at $\boldsymbol{k} = (\pi, \pi)$ enclosing unoccupied states, i.e. the up-spin Fermi surface is hole-like. Above B_{L2}, the down-spin Fermi surface is centered at $\boldsymbol{k} = (0, 0)$ and encloses occupied states, i.e. it is electron-like (see Fig. 3.4).

The Lifshitz transition at $B = B_{L2}$ equally marks the transition from heavy to light fermions which is reflected in the steep increase of Z_σ as the magnetic field is ramped up further, see Fig. 3.5(b). This is in accordance with the notion of adiabatic continuity to free fermions which is expected in the limit of high magnetic fields, i.e. weak coupling [125]. Based on the $\beta t = 200$ DMFT results, we conclude that a continuous transition from low to high magnetic fields occurs, at least at and above this temperature.

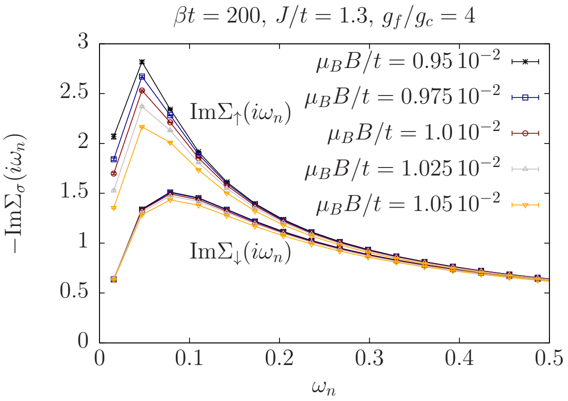

Figure 3.6: The imaginary part of the DMFT Matsubara self energies $\mathrm{Im}\Sigma_\sigma(i\omega_n)$, across the Lifshitz transition at $B_{\mathrm{L2}} \approx 0.01$. It is important to note that the data are compatible with a linear behavior, $\lim_{\omega_n\to 0} \mathrm{Im}\Sigma_\sigma(i\omega_n) \propto \omega_n$, and hence with a Fermi liquid.

3.6 First steps beyond DMFT

As it has been derived in Sec. 2.3, the DCA calculates the k-dependent self-energy $\Sigma_\sigma^{\mathrm{DCA}}(i\omega_n, \boldsymbol{K})$. This leads to the estimate for the residue

$$\left[Z_\sigma^{\mathrm{DCA}}(M(\boldsymbol{k}_f))\right]^{-1} = \lim_{T\to 0}\left[1 - \frac{\mathrm{Im}\Sigma_\sigma^{\mathrm{DCA}}(i\omega_n, M(\boldsymbol{k}_f))}{\omega_n}\right]_{\omega_n=\pi T},$$

The map function $M : \boldsymbol{k}_f \to \boldsymbol{K}$ maps the Fermi momentum to the matching reciprocal patch.

The 4-orbital DCA measurements agree with the 2-orbital DMFT results in the limits of strong coupling (*small* magnetic field) and weak coupling (*large* magnetic fields), see Fig. 3.8(a). In the intermediate regime, around $B = B_{\mathrm{L2}}$, deviations are detected in the magnetization as well as in the single-particle residues. The inclusion of spatial fluctuations softens the transition considerably. This can be understood from the notion of an effective Landé-factor g_f which becomes lower when spatial fluctuations are present, since, on the two-site cluster, the local moment can be quenched not only dynamically but also via local singlet formation. The single-particle residue in the down-spin projection displays no sign of vanishing across the metamagnetic transition (Fig. 3.8(b)).

3.7 Discussion and connection to experimental data

Lifshitz transitions are continuous quantum phase transition which do not change a symmetry of the ground state but the Fermi surface topology. [110]. Strictly speaking, they are defined for free fermion systems at zero temperature. Due to the unambiguous presence of quasiparticles, the notion of Lifshitz transition can be carried over to the KLM, also at finite temperatures. Driven by the external magnetic field, two consecutive Lifshitz transitions take

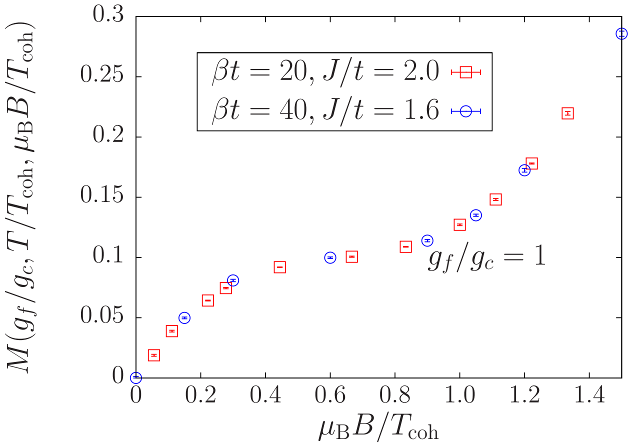

Figure 3.7: Magnetization $M(g_f/g_c, T/T_{\mathrm{coh}}, B/T_{\mathrm{coh}})$, scaled with the coherence temperature $T_{\mathrm{coh}}(J)$. Similar to the DMFT results (Fig. 3.2), the data follow an universal curve. Here, the results have been obtained from four-orbital DCA calculations.

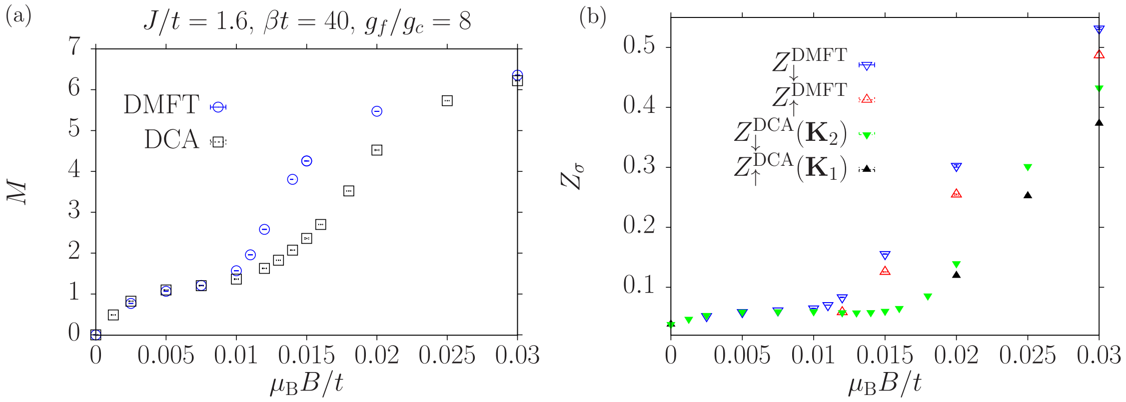

Figure 3.8: Comparison of the two-orbital DMFT to the four-orbital DCA calculations. Here, the k-vectors $\boldsymbol{K}_1 = (0, 0)$ and $\boldsymbol{K}_2 = (\pi, \pi)$ denote the relevant patches in reciprocal space in the DCA calculation.

place, at $B = B_{\mathrm{L1,2}}$, and the second one is identified with the metamagnetic transition. This scenario is maintained when the f-moments are allowed to couple more strongly to the field by altering the ratio g_f/g_c.
Collective effects challenging the quasiparticle coherence seem to be of minor importance during the metamagnetic transition, even when $B \sim T_{\mathrm{coh}}$. Naturally, our calculation scheme is limited to the dominantly paramagnetic regime of the KLM. The choice of parameters, $n_c = 0.9$ and $J/t \geq 1.3$ place our results unambiguously in the paramagnetic phase [16; 12; 17]. First steps (Fig. 3.8) in a systematic DCA study of larger clusters that can take into account the Ruderman-Kittel-Kasuya-Yosida (RKKY) interaction between local moments leave the Lifshitz scenario at the metamagnetic transition invariant. This is consistent with the fact that temporal fluctuations that generate the Kondo effect dominate the physics at the metamagnetic transition. Close to a critical point where the range of spatial fluctuations becomes large our approximation will fail and another modeling will be required.

Transport signatures of the Lifshitz transition can be calculated with the Boltzmann transport approximation. Topological changes of the bands that cross the Fermi energy can strongly influence transport measurements, in particular when these bands are shallow. This offers an explanation for the anomalies observed in Zeeman driven heavy-fermion systems [115].

Compared to our results for the magnetic field dependent single-particle spectrum (see Fig. 3.4), similar results have been obtained for the ferromagnetic phase of the Kondo lattice model without external field terms [126]. There, the spin-dependent shift of the quasiparticle weight is generated dynamically and leads to the notion of a spin-selective Kondo insulating phase.

Our results are applicable to heavy-fermion compounds that have a magnetic field-driven Lifshitz transition at the coherence scale.

The materials CeTiGe [104] and $\mathrm{CeRu_2Si_2}$ [97; 127] have a metamagnetic transition at magnetic energy scales that are consistent with their estimated coherence temperatures. In our model, the critical metamagnetic field corresponds to the second Lifshitz transition at B_{L2}. In this mechanism of competing energy scales we expect that the details of the band structure are of secondary importance. This is in contrast to Lifshitz transitions at magnetic fields much below the coherence scale where the details of the band structure are essential [115].

The metamagnetic signatures of our model (Fig. 3.2) are similar to recent experimental data of the paramagnetic 4f-based compound CeTiGe which exhibits a pronounced first-order metamagnetic transition [104]. In order to estimate the g-factor, we consider

$$T_{\mathrm{coh}} = g_f \mu_{\mathrm{B}} B \, . \tag{3.24}$$

The anticipated coherence scale, $T_{\mathrm{coh}} \approx 55$ K, is of the same order as the critical magnetic field of $\mu_0 B_{\mathrm{L2}} = 12.5$ T, assuming in our model a g-factor $g_f \approx 7$.

Equally, at lower fields, the magnetization is found to slightly change its slope, which might correspond to a first Lifshitz transition which in our model happens at B_{L1}. The experimentally observed distinct drop of the effective quasiparticle mass is in accordance with our findings for the KLM (see Sec. 3.4). Importantly, we find the metamagnetic transition to be continuous both in the two-orbital DMFT and in the four-orbital DCA calculations and on the temperature scales we can access.

$CeRu_2Si_2$ exhibits a continuous metamagnetic transition and simultaneously a Zeeman-driven topology change of the Fermi surface [97; 98]. The magnetization increases seemingly linear as the magnetic field is increased towards the metamagnetic field [127]. The critical field $\mu_0 B_{\mathrm{L2}} = 7.8$ T matches the coherence temperature of $T_{\mathrm{coh}} \approx 20$ K [97; 127] when the g-factor in our model is assumed to be $g_f \approx 4$. A Lifshitz transition at the coherence scale is therefore a plausible scenario for the metamagnetic transition in $CeRu_2Si_2$.

3.8 Conclusions

We have explored the Zeeman driven metamagnetic transition in the Kondo lattice model which is considered to be the paradigmatic low energy model for heavy-fermion systems. Results for the paramagnetic metallic phase of the KLM are obtained in the framework of DMFT/DCA which can exactly account for the Kondo effect.

Upon scaling the relevant energy scales with the lattice coherence scale the collapse of the magnetization data to a universal curve is observed, independent of the Kondo interaction (see Sec. 3.4) This data collapse has been confirmed for a range of Kondo couplings, temperatures and ratios of Landé factors. The pseudo spin nature of the f-orbitals, resulting from a Kramers doublet, can be taken in account with an effective Landé factor g_f and the competition of magnetic scale and coherence scale is invariant on the choice of g_f.

Using the DMFT (Sec. 3.5) and the DCA (Sec. 3.6), we have traced the single-particle residue from low to high magnetic fields and we report that it is continuous at the lowest temperatures our simulations can access. Two consecutive Lifshitz transitions occur as the field is ramped up and cause the change in topology of the spin-projected Fermi surfaces. This lead us to the finding that the metamagnetic transition in the KLM is coincident with a continuous Lifshitz transition. The absence of a singularity in the single-particle residue at the metamagnetic transition excludes the Kondo breakdown scenario.

At the temperature scale we can access, the sharp increase of magnetization at the metamagnetic transition can well be explained as a consequence of a continuous Lifshitz transition in heavy-fermion model systems where the Landé factor of the local spins is larger than the one for the itinerant electrons. In the course of this transition the excitations change their character from heavy fermions to light fermions.

The recently observed first order nature [104] of the metamagnetic phase transition at a temperature $T \ll T_{\mathrm{coh}}$ remains an open issue. Of particular importance is understanding if the KLM itself can account for the low temperature first order nature of the transition or if other competing energy scales such as coupling to the lattice [128] have to be taken into consideration.

4

π fluxes in correlated topological insulators

This chapter begins with a review of the concept of magnetic fluxes which are inserted into a quantum spin Hall insulator, followed by results for the Kane-Mele-Hubbard model on the honeycomb lattice augmented by two magnetic π fluxes. The quantum Hall state leaves a distinct fingerprint on a π flux, in the sense that a separation of spin and charge degrees of freedom occurs. This observation allows us to define a numerical measurement for the interacting many-electron system, which counts the number of (static) π fluxes in the system. Thereby, we obtain a topological observable which can diagnose the topological Z_2 index, even in a correlated system and without resorting to the boundary of the system [37; 38].

4.1 π flux insertion on a lattice

A flux ϕ which originates from an arbitrary external magnetic field $\boldsymbol{B}(\boldsymbol{r})$ is defined as $\phi = \int_S \boldsymbol{B}(\boldsymbol{r})\mathrm{d}\boldsymbol{S}$ and can be implemented in the lattice Hamiltonian in terms of a non-uniform vector potential. The vector potential occurs in the Peierls phase factors $\tau_{\boldsymbol{i},\boldsymbol{j}}$ that multiply the hopping amplitudes $t_{\boldsymbol{i},\boldsymbol{j}}$, i.e. $t_{\boldsymbol{i},\boldsymbol{j}} = t\ \tau_{\boldsymbol{i},\boldsymbol{j}} = t\ \exp[-i2\pi/\phi_0 \int_{\boldsymbol{i}}^{\boldsymbol{j}} \boldsymbol{A}(\boldsymbol{l})\mathrm{d}\boldsymbol{l}]$, where $\phi_0 = \frac{hc}{e}$. A π flux is defined as $\phi = \phi_0/2 = \pi$ in units of $\hbar = e = c = 1$. Inserting an external flux of π in a given unit cell amounts to distributing the phase factors $\tau_{\boldsymbol{i},\boldsymbol{j}}$ in such a way that their product along every closed contour around the plaquette is

$$\tau_{\boldsymbol{i},\boldsymbol{j}}\tau_{\boldsymbol{j},\boldsymbol{k}} \cdots \tau_{\boldsymbol{l},\boldsymbol{i}} = -1\,. \tag{4.1}$$

In general, choosing a gauge to represent a given magnetic field on a lattice geometry and determining the Peierls phase factors is not an easy task. However, for a localized π flux we may always choose a gauge where the Peierls phase factors are just $\tau_{\boldsymbol{i},\boldsymbol{j}} = \pm 1$. In a periodic system, fluxes can only be inserted in pairs (Fig. 4.1). Each hopping process from $\boldsymbol{i}$ to $\boldsymbol{j}$ that crosses the connecting line of a flux pair acquires a phase $\tau_{\boldsymbol{i},\boldsymbol{j}} = -1$, which fixes the position of both fluxes according to Eq. (4.1). In general, there is no one-to-one correspondence between the flux positions and the set of $\tau_{\boldsymbol{i},\boldsymbol{j}}$, i.e., one eventually has to make a gauge choice.

One realizes that the configuration $\{\tau_{\boldsymbol{i},\boldsymbol{j}}\}$ forms one state of the Hilbert space of a Z_2 lattice gauge theory [129]. If one considers only the $\tau_{\boldsymbol{i},\boldsymbol{j}}$ variables defined on the links of the lattice, the loop (4.1) defines the Z_2 flux $F_{\boldsymbol{i}}$ through the loop which encloses the plaquette

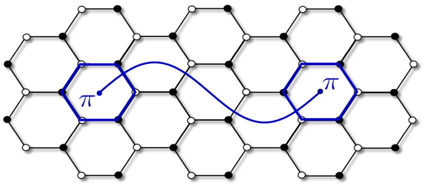

Figure 4.1: Definition of a π flux on a lattice. On a periodic lattice, π fluxes necessarily come in pairs. The location of the fluxes are determined by the ends of a string (blue line). The string (branch cut) is defined by demanding that each hopping process crossing it acquires a phase $e^{i\pi}$, i.e. reverses its sign. The overlap between these states is exponentially suppressed when they are inserted at the maximal distance of $L/2$ on a tours geometry.

$\boldsymbol{i}$ and can take the values ± 1. The fluxes $F_{\boldsymbol{i}}$ are not independent, and on a torus geometry, one has the constraint

$$\prod_{\boldsymbol{i}} F_{\boldsymbol{i}} = 1 \; . \tag{4.2}$$

Therefore, non-trivial Z_2 fluxes have to come in even numbers, i.e. in pairs [129]. The Hamiltonian for the Z_2 lattice gauge theory describes the dynamics of link variables, whereas we focus on a static configuration $\{\tau_{\boldsymbol{i},\boldsymbol{j}}\}$ which defines the number and the position of the π flux insertions.

Alternatively, a π flux can be thought of as originating from an external, time-reversal symmetry preserving magnetic field of the form

$$\boldsymbol{B}_{\pm}(\boldsymbol{r}) = \pi\delta(\boldsymbol{r} - \boldsymbol{r}_{\boldsymbol{i}})(\pm)\boldsymbol{e}_z \; . \tag{4.3}$$

$r_{\boldsymbol{i}}$ denotes the center of the lattice unit cell, for example a honeycomb plaquette. The flux is then given by

$$\phi_{\pm} = \int_{\hexagon} \boldsymbol{B}_{\pm}(\boldsymbol{r})\mathrm{d}\boldsymbol{S} = \pm\pi = \pm\frac{\phi_0}{2} \; , \tag{4.4}$$

where the last equality holds in units of $\hbar = e = c = 1$. When the flux takes the value $\phi = n\pi$, where $n \in \mathbb{Z}$, and when the flux is constrained to a single honeycomb plaquette it leaves the system time reversal invariant. The first condition follows from time reversal invariance which demands that the Aharonov-Bohm phase $e^{-i\phi}$ experienced by electrons encircling the flux insertion satisfies $e^{-i\phi} = e^{+i\phi}$. The constraint of localized fluxes furthermore guarantees that every possible path on the lattice leads to a Aharonov-Bohm phase of $e^{-in\pi} = \pm 1$.

4.1.1 Low-energy theory of π flux states

Once we have created a setup with two π fluxes as in Fig. 4.1, we have actually perturbed the lattice by two defects that occur at the endpoints of the string. The line itself is invisible in the eigenvalue spectrum since every closed contour on the lattice which excludes the endpoints intersects the defining line an even number of times. If we now consider a Hamiltonian of free electrons possessing a band structure with a non-trivial topological quantum number, for example the Kane-Mele model [22; 23] or the BHZ model [24] these defects will locally change the hopping integrals, according to Fig. 4.1, and they will become visible in the band gap of the insulator as Jackiw-Rebbi solitons [130; 37]. A point-defect in two spatial dimensions can be represented as a Jackiw-Rebbi soliton.

A very intuitive picture for the appearance of these in-gap modes has been given in Ref. [131] by considering the edge states on a boundary which is reconnected with a twist. Thereby, one can establish a connection between π flux insertions and topological defects. For the purpose of clarity, let us deform the string which defines the phase shift of π of the participating bonds in Fig. 4.1 to a rectilinear string. On a periodic lattice, we can interpret the string as being one segment of an imaginary line which cuts the lattice along one of its dimensions. Having this cut is equivalent to starting from the model on a cylinder geometry and reconnecting the two edge with bonds that have a phase shift along the string. The low-energy theory for the "edge" as defined above is given by a Dirac Hamiltonian with a mass term:

$$\mathcal{H}_{\text{edge}} = \int \mathrm{d}x \mathbf{\Psi}^{\dagger}(x) H_{\text{edge}}(-i\partial_x) \mathbf{\Psi}(x) \ , \tag{4.5}$$

where $\mathbf{\Psi}^{\dagger}(x) = (R^{\dagger}(x), L^{\dagger}(x))$ is the spinor of right and left moving chiral fields and

$$H_{\text{edge}}(-i\partial_x) = -iv\partial_x\sigma_z + m(x)\sigma_x \ . \tag{4.6}$$

Importantly, the mass $m(x)$ has acquired a spatial dependence and changes at the endpoints of the string, i.e. at the topological defects. This is in contrast to a situation where the edge is reconnected with uniform bonds, leading to a constant mass term in Eq. (4.6) as for bulk fermions. According to Refs. [131; 130; 132], each soliton contributes one localized, electronic zero mode per spin to the eigenvalue spectrum of the Hamiltonian. The occupation of one mode leads to an excess or a deficit of half a charge, and therefore the four possibilities to occupy both levels have the quantum numbers given in Fig. 4.2.

It is important to note, that these in-gap modes are fermionic and not Majorana fermion modes [37]. Their appearance at zero energy is a consequence of the particle-hole symmetry of the lattice Hamiltonian. In the Kane-Mele model (Sec. 1.2.1), the in-gap modes move to higher energies when a Rashba spin-orbit coupling is present. This term simultaneously breaks the particle-hole symmetry and the $U(1)$ spin symmetry.

4.1.2 Quantum numbers and spin-charge separation

The two in-gap modes that are induced by one π flux in a spinful model can either be singly or doubly occupied. In the former case, the two in-gap modes constitute a soliton with spin quantum number $S^z = \pm 1/2$ but no charge whereas in the latter case, the soliton has a fermion number of $q = \pm e$ but no spin (Fig. 4.2). The soliton state therefore is a realization of spin-charge separation in two spatial dimension. The concept of spin-charge separation as a fingerprint of the quantum spin Hall state on a π flux has been introduced in 2008, by Y. Ran, A. Vishwanath and D.-H. Lee [37] and by X.-L. Qi and S.-C. Zhang [38].

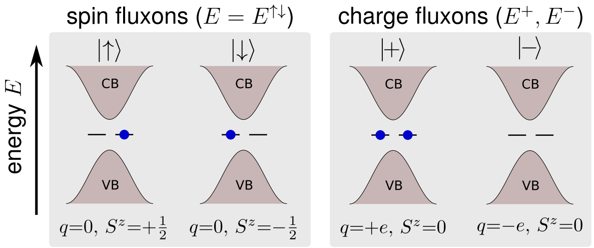

Figure 4.2: In a quantum spin Hall insulator, each flux represents a soliton leading to two localized modes (one per spin) in the band gap of the spectrum. The two modes can be occupied in four different ways which are labelled by the quantum numbers q and S^z. Two of the states form a Kramers pair of spin fluxons $|\uparrow\rangle$ and $|\downarrow\rangle$ with degenerate energies $E^{\uparrow\downarrow}$. The other two states are a doublet of charge fluxons $|+\rangle$ and $|-\rangle$ with energies E^+ and E^-.

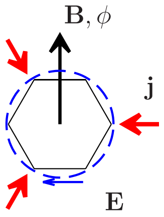

Figure 4.3: Sketch of a flux threading a hexagon. During the adiabatic increase of the flux $\phi_\sigma(t)$, charge or spin is pumped towards the hexagonal ring. Charge is pumped for $\phi_\uparrow(t) = -\phi_\downarrow(t)$ whereas spin is pumped for $\phi_\uparrow(t) = \phi_\downarrow(t)$. Naturally, this leads to a corresponding deficit of charge or spin which is either compensated by a second flux (periodic boundary conditions) or the lattice boundary (open boundary conditions).

The following gedankenexperiment [133; 38] of adiabatically switching on a time-dependent flux $\phi_\sigma(t)$ is closely related to the Laughlin argument for the transfer of charge from one edge of an integer quantum Hall sample to the other edge as a function of an external flux [134; 135].

Let us consider a time-reversal symmetric quantum spin Hall insulator which additionally has a $U(1)$ spin symmetry. Then, the conductivity tensor can be labelled by a spin index σ:

$$\sigma^\sigma = \begin{pmatrix} \sigma^\sigma_{xx} & \sigma^\sigma_{xy} \\ \sigma^\sigma_{yx} & \sigma^\sigma_{yy} \end{pmatrix} = \begin{pmatrix} 0 & \sigma\nu e^2/h \\ -\sigma\nu e^2/h & 0 \end{pmatrix}, \tag{4.7}$$

where $\nu \in \mathbb{Z}$. A magnetic field $\boldsymbol{B}_\sigma(\boldsymbol{x},t) = \boldsymbol{B}_\sigma(t)\delta(\boldsymbol{x}-\boldsymbol{x}_0)$ generates a magnetic flux $\phi_\sigma(t)$ piercing the plane (Fig. 4.3). Faraday's law induces a tangential electric field $\boldsymbol{E}_\sigma(\boldsymbol{x},t)$, via $\nabla \times \boldsymbol{E}_\sigma(\boldsymbol{x},t) = -1/c\,\partial\boldsymbol{B}_\sigma(\boldsymbol{x},t)/\partial t$. The electric field is proportional to a radial current in a quantum Hall system, since the longitudinal components vanish in Eq. (4.7):

$$\boldsymbol{j}_\sigma(\boldsymbol{x},t) = \sigma^\sigma_{xy}\left(\boldsymbol{E}_\sigma(\boldsymbol{x},t) \times \hat{\boldsymbol{z}}\right) . \tag{4.8}$$

The radial current $\boldsymbol{j}_\sigma(\boldsymbol{x},t)$ accumulates per spin sector a charge $Q_\sigma(\boldsymbol{x},t)$ in the center. We have

$$\begin{aligned}
\frac{\mathrm{d}}{\mathrm{d}t}Q_\sigma(\boldsymbol{x},t) &= \int \mathrm{d}^3\boldsymbol{x}\frac{\partial}{\partial t}\rho_\sigma(\boldsymbol{x},t) = -\int \mathrm{d}^3\boldsymbol{x}\nabla\cdot\boldsymbol{j}_\sigma(\boldsymbol{x},t) = -\int\limits_{\partial V}\mathrm{d}S\;\hat{n}_s\cdot\boldsymbol{j}_\sigma(\boldsymbol{x},t) \\
&= -\oint\limits_{C}\mathrm{d}l\;\hat{n}_c\cdot\boldsymbol{j}_\sigma\left(\boldsymbol{x}(l),t\right) = -\sigma^\sigma_{xy}\oint \boldsymbol{E}_\sigma(\boldsymbol{x},t)\cdot\mathrm{d}\boldsymbol{x} = \frac{\sigma^\sigma_{xy}}{c}\frac{\mathrm{d}}{\mathrm{d}t}\phi_\sigma(t)\;. \qquad (4.9)
\end{aligned}$$

Integration $\int_0^1 \mathrm{d}t$ on both sides gives

$$\Delta Q_\sigma = Q_\sigma(1) - Q_\sigma(0) = \frac{\sigma^\sigma_{xy}}{c}\left[\phi_\sigma(1)-\phi_\sigma(0)\right] = \sigma\nu e\frac{\phi_\sigma(1)}{\phi_0}\;, \qquad (4.10)$$

where we assumed that $\phi_\sigma(0)=0$.

In the following, we assume that both fluxes $\phi_\sigma(1)$ will take the values $\pm\pi$, independently of each other, i.e. $\phi_\uparrow(1)=\pm\phi_0/2$ ($\phi_\downarrow(1)=\pm\phi_0/2$). The accumulated charge is then $\Delta Q_\uparrow = \pm\nu\frac{e}{2}$ ($\Delta Q_\downarrow = \mp\nu\frac{e}{2}$). The charge quantum number ΔQ and the spin quantum number ΔS^z of the soliton, which is the composite object of the up- and the down-spin mode, are defined as

$$\begin{aligned}
\Delta Q &= \Delta Q_\uparrow + \Delta Q_\downarrow = \pm\nu e, 0\;, \\
\Delta S^z &= \frac{1}{2e}\left(\Delta Q_\uparrow - \Delta Q_\downarrow\right) = 0, \pm\nu\frac{1}{2}\;. \qquad (4.11)
\end{aligned}$$

The flux pumping process therefore leads to four different final states, labelled by their quantum numbers : the chargeon (+) and the holon (−) states, $\{\Delta Q = \pm\nu e,\ \Delta S^z = 0\}$, and the spinon states, $\{\Delta Q = 0,\ \Delta S^z = \pm\nu 1/2\}$. This line of reasoning still holds in the presence of interactions and disorder but relies on $U_s(1)$ symmetry. When this symmetry is not present, one can classify the final states by Kramers theorem for time-reversal invariant systems. One has a pair of generalized charge fluxons, that carry an odd number of electric charge, are even under time reversal and form a Kramers singlet. The generalized spin fluxons carry no charge and are odd under time reversal. They form a Kramers doublet. Accordingly, the authors of Ref. [38] defined the topological Z_2 index by the integer number of charges N_Γ pumped towards the flux insertion in the adiabatic process, where an even (odd) number N_Γ signifies a (non-) trivial state. We refer the reader to the discussion in Ref. [38].

4.2 Kane-Mele-Hubbard model with π flux insertions

The KM model (1.13) describes electrons on the honeycomb lattice with nearest-neighbor hopping and spin-orbit coupling [22] (see Sec. 1.2.1). Here we focus on the $U(1)$ spin symmetric case, i.e. set the Rashba term to zero. As discussed in the previous section, the π flux insertion amounts to impose a certain, gauge-dependent sign structure $\{\tau_{\boldsymbol{i},\boldsymbol{j}}\}$ on the hopping processes of the Hamiltonian. The flux-augmented KM model is given by

$$\mathcal{H}_0 = -\sum_{\langle\boldsymbol{i},\boldsymbol{j}\rangle} t(\boldsymbol{i},\boldsymbol{j})c^\dagger_{\boldsymbol{i}}c_{\boldsymbol{j}} + i\sum_{\langle\langle\boldsymbol{i},\boldsymbol{j}\rangle\rangle}\lambda(\boldsymbol{i},\boldsymbol{j})c^\dagger_{\boldsymbol{i}}\nu_{\boldsymbol{i}\boldsymbol{j}}\sigma_z c_{\boldsymbol{j}}\;, \qquad (4.12)$$

where $t(\boldsymbol{i},\boldsymbol{j}) = t\tau_{\boldsymbol{i},\boldsymbol{j}}$ and $\lambda(\boldsymbol{i},\boldsymbol{j}) = \lambda\tau_{\boldsymbol{i},\boldsymbol{j}}$. Accordingly, the KMH model with flux insertions is

$$\mathcal{H} = \mathcal{H}_0 + \mathcal{H}_{\mathrm{U}} \;, \tag{4.13}$$

using the definition (1.17) of the Hubbard term.

4.2.1 Observables

We proceed by considering the uniform ($\boldsymbol{q} = 0$) and static ($\omega = 0$) spin and charge susceptibilities. The imaginary-time susceptibility can be defined as the correlation function

$$\chi^{\alpha\alpha}_{\boldsymbol{ij}}(\tau) = \sum_{a,b=1}^{2} \left[\langle \hat{S}^{\alpha}_{\boldsymbol{i}a}(\tau)\hat{S}^{\alpha}_{\boldsymbol{j}b}(0)\rangle - \langle \hat{S}^{\alpha}_{\boldsymbol{i}a}\rangle\langle \hat{S}^{\alpha}_{\boldsymbol{j}b}\rangle \right] \;, \tag{4.14}$$

where $\alpha = \{0, z\}$ and in this notation, the total charge operator is $\hat{S}^0_{\boldsymbol{i}a} = \hat{n}_{\boldsymbol{i}a}$. The sum is over the orbital indices $a, b = \{1, 2\}$ and $\boldsymbol{i}$ indicates the unit cells. We have $\hat{S}^z_{\boldsymbol{i}a} = (1/2)\sum_\sigma \sigma \hat{c}^\dagger_{\boldsymbol{i}a\sigma}\hat{c}_{\boldsymbol{i}a\sigma}$ and $\hat{n}_{\boldsymbol{i}a} = \sum_\sigma \hat{c}^\dagger_{\boldsymbol{i}a\sigma}\hat{c}_{\boldsymbol{i}a\sigma}$. Note that in Eq. (4.14),

$$\begin{aligned} \langle \hat{S}^z_{\boldsymbol{i}a}\rangle &= 0 \;, & (4.15)\\ \sum_{\boldsymbol{i}a\boldsymbol{j}b}\langle \hat{S}^0_{\boldsymbol{i}a}\rangle\langle \hat{S}^0_{\boldsymbol{j}b}\rangle &= 4N^2 \;, & (4.16) \end{aligned}$$

due to the spin rotational symmetry and due to $\langle \hat{n}_{\boldsymbol{i}a}\rangle = 1$ at half-filling. $N = L^2$ is the number of unit cells. The Fourier transform is

$$\chi^{\alpha\alpha}_{\boldsymbol{q}}(i\omega_n) = \int_0^\beta \mathrm{d}\tau e^{i\omega_n\tau} \frac{1}{N}\sum_{\boldsymbol{i},\boldsymbol{j}} e^{-i(\boldsymbol{i}-\boldsymbol{j})\boldsymbol{q}} \chi^{\alpha\alpha}_{\boldsymbol{ij}}(\tau) \;, \tag{4.17}$$

where $\omega_n = 2\pi n/\beta$ are the bosonic Matsubara frequencies. To monitor the charge and spin degrees of freedom, induced by the π flux insertions, we use the *unnormalized* uniform static charge and magnetic susceptibilities defined as

$$\begin{aligned} \chi_c &= N \times \chi^{00}_{\boldsymbol{q}=\boldsymbol{0}}(i\omega_n = 0) \\ &= \int_0^\beta \mathrm{d}\tau \sum_{\boldsymbol{i},\boldsymbol{j}} \chi^{00}_{\boldsymbol{ij}}(\tau) = \int_0^\beta \mathrm{d}\tau \Big[\sum_{\boldsymbol{i},\boldsymbol{j}}\sum_{a,b=1}^{2} \langle \hat{S}^0_{\boldsymbol{i}a}(\tau)\hat{S}^0_{\boldsymbol{j}b}(0)\rangle - 4N^2 \Big] \\ &= \beta \Big[\sum_{\boldsymbol{i},\boldsymbol{j}}\sum_{a,b=1}^{2} \langle \hat{S}^0_{\boldsymbol{i}a}\hat{S}^0_{\boldsymbol{j}b}\rangle - 4N^2 \Big] \;, & (4.18)\\ \chi_s &= 4N \times \chi^{zz}_{\boldsymbol{q}=\boldsymbol{0}}(i\omega_n = 0) \\ &= 4N\beta \sum_{\boldsymbol{i},\boldsymbol{j}}\sum_{a,b=1}^{2} \langle \hat{S}^z_{\boldsymbol{i}a}\hat{S}^z_{\boldsymbol{j}b}\rangle \;. & (4.19) \end{aligned}$$

The factor of 4 in χ_s is a convention. To obtain the final result, we used $[\mathcal{H}, \sum_{\boldsymbol{i}} \hat{S}^0_{\boldsymbol{i}}] = 0$ and $[\mathcal{H}, \sum_{\boldsymbol{i}} \hat{S}^z_{\boldsymbol{i}}] = 0$. Therefore, the evaluation of the susceptibilities amounts to calculating the equal-time correlation functions, Eq. (4.18) and Eq. (4.19).

In the non-interacting case, we can readily evaluate the correlation functions. We have, for $\lambda_{\mathrm{R}} \neq 0$:

$$\begin{aligned} \chi_s^{zz} &= 4 \int_0^\beta \mathrm{d}\tau \sum_{\boldsymbol{i},\boldsymbol{j}} \langle \hat{S}^z_{\boldsymbol{i}}(\tau) \hat{S}^z_{\boldsymbol{j}}(0) \rangle \\ &= \sum_{n,m} \left| \sum_{x=(\boldsymbol{i},\sigma)} \sigma_{(x)} U^\dagger_{m,x} U_{x,n} \right|^2 \frac{e^{\beta(E_n - E_m)} - 1}{E_n - E_m} f(E_n) \left[1 - f(E_m)\right] , \end{aligned} \tag{4.20}$$

where $f(E_n)$ is the Fermi function and the unitary matrix U diagonalizes the Hamilton matrix H of Eq. (4.12), i.e. $H = UEU^\dagger$ and $E = \mathrm{diag}(E_1, \cdots, E_n)$ is the matrix of eigenvalues. In the absence of Rashba coupling, the model (4.12) is diagonal in the spin indices σ and one obtains the simplified expression

$$\chi_s^{zz} = \frac{\beta}{2} \sum_{n,\sigma} \left[1 + \cosh(\beta E_{n,\sigma})\right]^{-1} . \tag{4.21}$$

4.3 Thermodynamic signature of π fluxes

The low-energy Hilbert space of the KM model ($\omega \ll \Delta_{\mathrm{sp}}$) augmented by a pair of π fluxes contains the four states $|\uparrow\rangle$, $|\downarrow\rangle$, $|+\rangle$, $|-\rangle$ which are doubly degenerate (to exponential accuracy). Furthermore, they are exponentially localized and the localization length is set by the bulk energy gap Δ_{sp}. At least, this statement holds for the here considered values of λ/t. For a detailed discussion of the localization length of π fluxes in the Kane-Mele model, we refer the reader to Ref. [136]. The effective low-energy Hamiltonian of a single π flux insertion is

$$\mathcal{H} = \sum_{n=+,-,\uparrow,\downarrow} E|n\rangle\langle n| . \tag{4.22}$$

For this model, the spin (χ_s) and charge (χ_c) susceptibility,

$$\chi_s = 4\beta \left[\langle (\hat{S}^z)^2 \rangle - \langle \hat{S}^z \rangle^2 \right] , \; \chi_c = \beta \left[\langle \hat{n})^2 \rangle - \langle \hat{n} \rangle^2 \right] , \tag{4.23}$$

are

$$\chi_s = \chi_c = \beta/2 , \tag{4.24}$$

where $\beta = 1/k_{\mathrm{B}}T$. In the absence of Rashba coupling, the Curie law for χ_s directly follows from the quantized Hall conductivity (4.7) which leads to the definition of the spin quantum numbers (4.11), with $\nu = 1$ for the KM model. Repulsive electronic interactions are expected to gap out the charge states $|\pm\rangle$, thereby reducing the low-energy Hilbert space. At $U/t > 0$, we therefore expect, for a single π flux insertion:

$$\chi_s = \beta . \tag{4.25}$$

The spin susceptibility counts the number N_π of spin π fluxes in the lattice. This is similar to the prediction of a Curie law in polyacetylene which counts the number of topological excitations [132]. Figure 4.4 shows the non-interacting spin susceptibility, for the case of increased values of the flux density and for the case of additional Rashba coupling. In the latter case, S^z is non conserved but for small and intermediate values of the Rashba coupling ($\lambda_{\mathrm{R}} \sim \lambda$), the Curie law is approximately reproduced at low temperatures. The spin and charge susceptibilities, measured in the KMH model (4.13), are shown in Fig. 4.5. At $U/t = 4$, the low-temperature spin susceptibility follows a Curie law $\chi_s = 2\beta$, whereas the charge susceptibility vanishes exponentially. This is in accordance with the gapping out of the charge fluxons at low temperatures [see Eq. (4.25)]. The lowest temperature we have simulated is $T = 0.0125t$. When $T \to 0$, we expect the spin susceptibility to vanish exponentially due to the formation of a singlet state between the spin π fluxes.

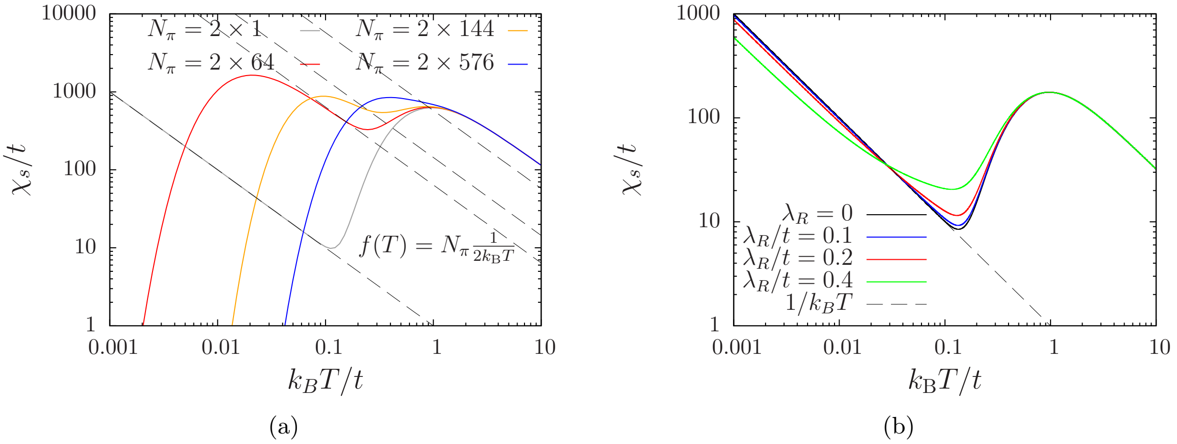

Figure 4.4: Non-interacting spin susceptibility measurements. (a) Spin susceptibilities the Kane-Mele model on a lattice of $N_{\mathrm{hc}} = 1152$ honeycomb plaquettes, augmented with N_π evenly spaced π fluxes. At low temperatures the susceptibility follows a Curie law $f(T) = N_\pi(1/2k_{\mathrm{B}}T)$ (dashed lines) in a given temperature range, except for the case of a dense fluxon lattice ($N_\pi = 2\times 576$) where $N_\pi = N_{\mathrm{hc}}$. The downward turn at lower temperatures defines the energy scale of the overlap integral between neighboring flux states. (b) Dependence of the spin susceptibility on the value of Rashba coupling on an 18×18 lattice, augmented with a pair of π fluxes at the maximal distance. Up to $\lambda_{\mathrm{R}}/t \sim 0.2$, the Curie law is reproduced to a good approximation. Note that the chemical potential has been adjusted to retain a half-filled band at finite values of λ_{R}. Here, $\lambda/t = 0.2$.

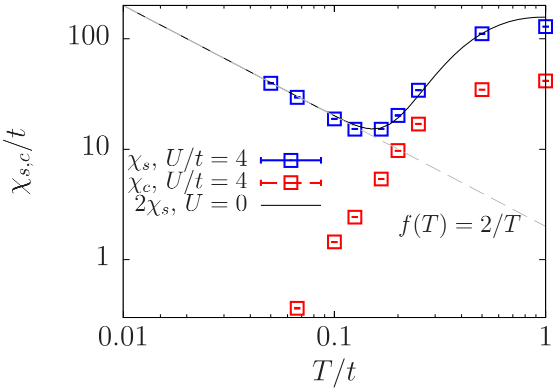

Figure 4.5: Spin and charge susceptibilities of the interacting Kane-Mele-Hubbard model, augmented with two maximally separated π fluxes. For the temperatures shown in the figure and below the temperature scale of $T/t \sim 0.1$, the two spin fluxons act as non-interacting, localized spin 1/2 moments. The charge susceptibility vanishes exponentially. Here, $L \times L = 12 \times 12$ and $\lambda/t = 0.2$ ($\lambda_{\mathrm{R}} = 0$).

4.4 Use of π fluxes as a topological observable in a correlated QSHI

We now turn to the Kane-Mele Hubbard model (4.13), augmented with a pair of π fluxes, to consider the effect of electronic interactions. Its phase diagram and the magnetic transition from a paramagnetic to an antiferromagnetic phase with transverse (XY) order is discussed in Sec. 1.2.1. As discussed earlier, the interacting phase is assumed to be adiabatically connected to the non-interacting QSHI phase, as long as time reversal symmetry is preserved. We use this model and its phase transition as a test case for the use of π fluxes to probe the topological non-trivial state. We expect that the spin susceptibility measured for increasing values of the Hubbard interaction reflects the phase transitions to the magnetic phase. The model (4.13) is solved using the PQMC method for $T = 0$ quantities (see Sec. 2.1.4) and the FTQMC method for measurements at finite temperatures (see Sec. 2.1.5).

We consider the dynamical spin structure factor for each lattice site. Analog to the finite temperature result of Sec. 2.5, we readily obtain the expression at $T = 0$:

$$S^{zz}(\boldsymbol{i},\omega) = 2\pi \sum_{n} \left|\langle n|\hat{S}^z_{\boldsymbol{i}}|0\rangle\right|^2 \delta(\omega - \Delta_n) \;, \tag{4.26}$$

where E_n and $|n\rangle$ are the eigenenergies and the eigenstates of the KMH model (4.13). To simplify the notation, $\boldsymbol{i}$ is used here as a combined index which included the orbitals of the unit cell. The energy $\Delta_n = E_n - E_0$ measures the energy above the ground state energy. This quantity measures the spectrum of spin excitations at site $\boldsymbol{i}$. To obtain a real-space map

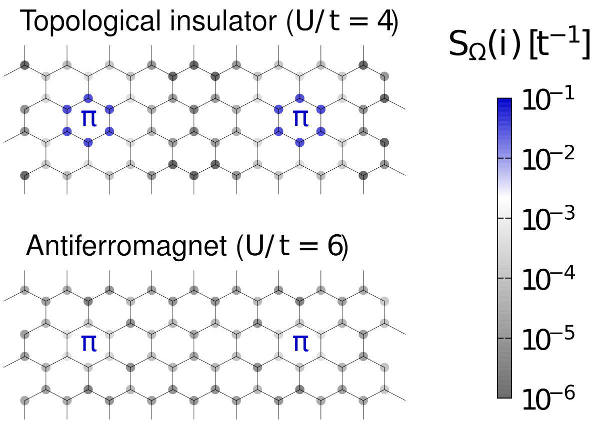

Figure 4.6: The zero-temperature energy-integrated dynamical spin structure factor $S_\Omega(i)$ of the Kane-Mele-Hubbard model, augmented with a pair of π fluxes on a 9×9 lattice. At $U/t = 4$, the presence of spin fluxons leads to the accumulation of spectral weight which is sharply localized on the flux-threaded plaquette. At $U/t = 6$, the flat distribution of spectral weight is consistent with the absence of spin fluxon states.

of the spin excitations, one may use the integrated quantity $S^{zz}_\Omega(\boldsymbol{i})$, where

$$S^{zz}_\Omega(\boldsymbol{i}) = \int\limits_0^\Omega \mathrm{d}\omega S^{zz}(\boldsymbol{i},\omega) \,, \tag{4.27}$$

and $0 < \Omega < \Delta_\mathrm{s}$. Naturally, the cutoff Ω is ill-defined, but as long as it takes a value smaller than the spin gap Δ_s, we observed that $S^{zz}_\Omega(\boldsymbol{i})$ showed only small quantitative differences for different values of Ω. We calculated this quantity within the correlated QSHI phase ($U/t = 4$) and well within the magnetic phase ($U/t = 6$) , see Fig. 4.6. In the former case, the integrated low-energy spectral weight at the flux-threaded hexagons is approximately three orders of magnitude larger than its average values on the sites that are further away from the fluxes. In the latter case, the very concept of flux states breaks down since time reversal symmetry is spontaneously broken and consequently we observe a rather flat distribution of spectral weight across the lattice.

The spin susceptibility detects the presence of flux insertions at $U/t > 0$ in form of a low-temperature Curie law. As explained in Sec. 4.3, each flux insertion now contributes a factor of $1/k_\mathrm{B}T$ to the susceptibility. Figure 4.7 shows the spin susceptibilities for increasing values of U/t and for lattice sizes of linear length $L = 9$ and $L = 12$. At $U/t = 4$, the low-temperature behavior of $\chi_s(T)$ follows a Curie law for both lattice sizes [Fig. 4.7(a)]. The Curie law sets in at $k_\mathrm{B}T/t \sim 0.2\Delta_s$, i.e. at a scale set by the spin gap. Charge excitations are exponentially suppressed on approximately the same scale [see $\chi_c(T)$ in Fig. 4.7(a)]. On the other hand, at $U/t = 6$, the low-energy excitations of the plain KMH model are spin waves. We interpret the almost temperature independent behavior of the low-temperature spin susceptibility of the flux-augmented model [Fig. 4.7(d)] to measure essentially the density

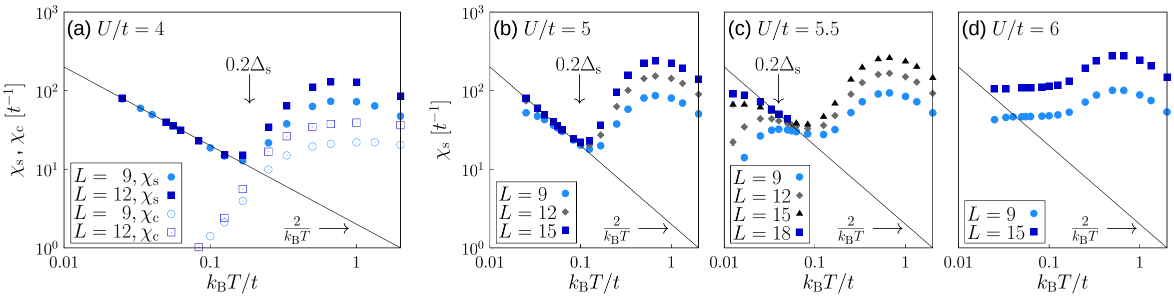

Figure 4.7: Spin (χ_s) and charge (χ_c) susceptibility of the Kane-Mele-Hubbard model, augmented with a pair of π fluxes placed at the maximal distance on $L \times L$ lattices. Within the QSHI phase ($U/t = 4, 5, 5.5$), we can identify an energy scale (indicated by arrows) below which the spin susceptibility follows a Curie law. This energy scale is set by the spin gap and we estimate it to be around $0.2\Delta_s$. On the largest lattices ($L = 15, 18$) a Curie law of the form $\chi_s = 2/(k_B T)$ is clearly present in the QSHI phase. In the AFMI phase ($U/t = 6$), the low-temperature behavior of the spin susceptibility is only weakly temperature dependent and its extrapolated value to $T = 0$ reflects the density of spin-wave excitations.

of these magnetic excitations, since spin fluxons are no longer defined in the magnetic phase. As the Hubbard interaction approaches the phase boundary, marked deviations of the Curie law occur in the form of a downward turn at low temperatures [Fig. 4.7(b),(c)]. This is an effect of the spin fluxon–spin fluxon interaction which is discussed in the following section.

4.5 Interaction between spin fluxons

Interaction effects between spin fluxons lead to deviations from the non-interacting low-temperature form of the spin susceptibility [see Fig. 4.7(b),(c) and Fig. 4.8]. The onset of the deviation from the Curie law determines the energy scale of the interaction. This energy scale gets larger with increasing U/t when the system is close to the magnetic phase transition [Fig. 4.8]. Therefore, the Hubbard interaction tunes the interaction strength between spin fluxons. Furthermore, this interaction has a finite range which also increases when the phase boundary is approached. The effect of the increasing interaction range is shown in Fig. 4.7 (b),(c). The phase transition in the KMH model is a condensation of magnetic excitons which are collective spin excitations. The magnetic excitons are initially gapped and lie in the transverse (XY) plane. They evolve into the gapless Goldstone modes of the magnetic state. We propose that, for Hubbard interactions below U_c/t, the spin fluxon–spin fluxon interaction is mediated by the exchange of magnetic excitons. We make a phenomenological ansatz and write down the part $S_{\pi-\pi}$ of the effective action which describes this interaction:

$$S_{\pi-\pi} = -g^2 \sum_{\boldsymbol{r}\neq\boldsymbol{r}'} \int_0^\beta \mathrm{d}\tau \int_0^\beta \mathrm{d}\tau' \left[S_\pi^+(\boldsymbol{r},\tau) D^0(\boldsymbol{r}-\boldsymbol{r}',\tau-\tau') S_\pi^-(\boldsymbol{r}',\tau') + \mathrm{H.c.} \right] , \tag{4.28}$$

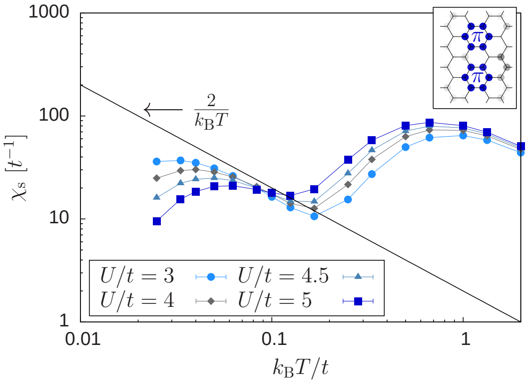

Figure 4.8: Spin susceptibility of the Kane-Mele-Hubbard model, augmented with a pair of π fluxes place at a distance of two lattice spacings (inset). An increase of the Hubbard interaction U/t leads to an increase in the spin fluxon–spin fluxon interaction. This is visible in the low-temperature deviations of the spin susceptibility from the Curie law which is based on non-interacting spin fluxons. Here, $\lambda/t = 0.2$, $\lambda_{\mathrm{R}} = 0$ and $L = 9$. The inset shows the local energy-integrated spin-structure factor $S_{\Omega}(i)$ at $U/t = 4$.

where the exciton propagator is approximated by its non-interacting form, the free bosonic Green function $D^0(\boldsymbol{r} - \boldsymbol{r}', \tau - \tau')$. $S^{\pm}_{\pi}$ are spin-flip operators that act on the spin fluxons.

In the following, we derive the low-energy limit of $D^0(\boldsymbol{r} - \boldsymbol{r}', \tau - \tau')$. The bosonic Matsubara Green function for free bosons is

$$D^0(\boldsymbol{q}, \tau) = -\langle T \hat{A}_{\boldsymbol{q}}(\tau) \hat{A}^{\dagger}_{\boldsymbol{q}}(0) \rangle \ , \tag{4.29}$$

where the expectation value is defined with respect to the bosonic Hamiltonian

$$\mathcal{H}_0 = \sum_{\boldsymbol{q}} \omega_{\boldsymbol{q}} \hat{b}^{\dagger}_{\boldsymbol{q}} \hat{b}_{\boldsymbol{q}} \ , \tag{4.30}$$

which describes the collective spin mode. The dispersion relation $\omega_{\boldsymbol{q}}$ is

$$\omega_{\boldsymbol{q}} = \sqrt{v_s^2 |\boldsymbol{q} - \boldsymbol{Q}|^2 + \Delta_s^2} = \Delta_s \left(1 + \frac{v_s^2}{2\Delta_s^2} |\boldsymbol{q} - \boldsymbol{Q}|^2 \right) + \mathcal{O}(|\boldsymbol{q} - \boldsymbol{Q}|^4) \ , \tag{4.31}$$

where v_s is the spin velocity and $\boldsymbol{Q}$ is the wave vector of magnetic order. Therefore, the minimal exciton energy is given by the spin gap, $\omega_{\boldsymbol{Q}} = \Delta_s$. The bosonic operator $\hat{A}_{\boldsymbol{q}}$ annihilates a bosonic mode at $\boldsymbol{q}$ either by the action of $\hat{b}_{\boldsymbol{q}}$ or by the action of $\hat{b}^{\dagger}_{-\boldsymbol{q}}$:

$$\hat{A}_{\boldsymbol{q}} = \hat{b}_{\boldsymbol{q}} + \hat{b}^{\dagger}_{-\boldsymbol{q}} \ . \tag{4.32}$$

Using the imaginary time dependence, $\hat{A}_{\boldsymbol{q}}(\tau) = e^{\tau \mathcal{H}_0} \hat{A}_{\boldsymbol{q}} e^{-\tau \mathcal{H}_0}$, and $\langle \hat{b}^{(\dagger)}_{\boldsymbol{q}} \hat{b}^{(\dagger)}_{-\boldsymbol{q}} \rangle = 0$ one obtains

$$\begin{aligned} D^0(\boldsymbol{q}, \tau) &\overset{\tau \geq 0}{=} -e^{-\omega_{\boldsymbol{q}} \tau} - 2 n_{\boldsymbol{q}} \cosh(\omega_{\boldsymbol{q}} \tau) \\ &= \frac{e^{-\omega_{\boldsymbol{q}} \tau}}{e^{-\beta \omega_{\boldsymbol{q}}} - 1} - \frac{e^{\omega_{\boldsymbol{q}} \tau}}{e^{\beta \omega_{\boldsymbol{q}}} - 1} \ , \end{aligned} \tag{4.33}$$

where $n_{\boldsymbol{q}} = (e^{\beta\omega_{\boldsymbol{q}}} - 1)^{-1}$. We consider $\lim_{\beta\to\infty} D^0(\boldsymbol{q},\tau) = -e^{-\omega_{\boldsymbol{q}}\tau}$, We define the real-space propagator $D^0(\boldsymbol{r},\tau)$,

$$\begin{aligned}
D^0(\boldsymbol{r},\tau) &= \int \mathrm{d}^2\boldsymbol{q}\; e^{i\boldsymbol{q}\boldsymbol{r}} D^0(\boldsymbol{q},\tau) \\
&\overset{\beta\to\infty}{=} -\int \mathrm{d}^2\boldsymbol{q}\; e^{i\boldsymbol{q}\boldsymbol{r}} e^{-\omega_{\boldsymbol{q}}\tau} \\
&\overset{|\boldsymbol{q}-\boldsymbol{Q}|\to 0}{=} -\int \mathrm{d}^2\boldsymbol{q}\; e^{i\boldsymbol{q}\boldsymbol{r}} e^{-\tau\left(\Delta_s+\frac{v_s^2}{2\Delta_s}|\boldsymbol{q}-\boldsymbol{Q}|^2\right)} \\
&\overset{\boldsymbol{q}\to\boldsymbol{q}'+\boldsymbol{Q}}{=} -e^{i\boldsymbol{Q}\boldsymbol{r}} \int \mathrm{d}^2\boldsymbol{q}'\; e^{i\boldsymbol{q}'\boldsymbol{r}} e^{-\tau\left(\Delta_s+\frac{v_s^2}{2\Delta_s}\boldsymbol{q}'^2\right)} \\
&= -\pi\sqrt{\frac{2}{v_s\tau}} e^{i\boldsymbol{Q}\boldsymbol{r}} e^{-\tau\Delta_s} e^{-\boldsymbol{r}^2\frac{\Delta_s}{2\tau v_s^2}}\ ,
\end{aligned} \tag{4.34}$$

where the last line follows after completing the square and evaluating the Gaussian integrals. In Eq. (4.34), the term $e^{i\boldsymbol{Q}\boldsymbol{r}}$ determines the sign of the interaction. The spin gap Δ_s determines the decay at large imaginary times. The absolute value of $D^0(\boldsymbol{r},\tau)$ increases as Δ_s decreases and at the same time, the interaction range of $D^0(\boldsymbol{r},\tau)$ increases. Since Δ_s is a monotonic decreasing function of U/t, the Hubbard interaction effectively tunes strength and range of the spin fluxon – spin fluxon interaction. At $U = U_c$, the spin gap is zero and the interaction range diverges. Using this phenomenological model, we can explain the spin susceptibility data [Fig. 4.7(b),(c) and Fig. 4.8]. when U/t approaches the critical value. The temperature where the data start to deviate from the Curie law is a tunable correlation-induced energy scale. The spin fluxon–spin fluxon interaction below this energy scale is mediated by the exchange of the collective spin excitations of the host systems, i.e. by the gapful magnetic excitations of the Kane-Mele-Hubbard model in the paramagnetic phase.

4.6 Conclusions

In quantum spin Hall insulators, π flux insertions represent topological defects (see Sec. 4.1). In this chapter, we have shown that they can be used as a universal probe for the topological Z_2 index in the presence of electronic correlations, following a proposal in Ref. [37]. The response to a π flux insertion is read out by a bulk measurement (Sec. 4.3). Therefore, this method does not suffer from severe finite size effects as it is the case for edge states of quantum spin Hall insulators. Furthermore, the method does not rely on adiabatic connection to a non-interacting QSHI. We observe a Curie behavior of the low-temperature spin-susceptibility which signals the presence of spin fluxon states in the bulk gap (Sec. 4.4) The presence of spin fluxons can in turn be uniquely attributed to a non-trivial topological bulk. In the $U_s(1)$ symmetric case, the observed Curie law directly follows from the quantized (spin) Hall conductivity σ_{xy}^s of the non-interacting model.

Additionally, in Sec. 4.5, we have presented results for the interaction between neighboring spin fluxons which one can understand, on a phenomenological level, as an exchange of magnetic excitons that are present in the host system. Interaction effects play a crucial role in the study of interacting spin fluxon system (see Ch. 5).

It is important to note that the π flux-augmented Kane-Mele-Hubbard model can be solved with quantum Monte Carlo methods without additional cost. The π flux insertions leave the relevant symmetries of the model invariant. For Monte Carlo calculations it is noteworthy that π flux insertions do not create a sign problem. In principle, π flux insertions can be used in any model for a QSHI.

Apart from its application as a numerical tool, π fluxes may also be experimentally realized. A strongly correlated topological insulator on the honeycomb lattice may emerge from Na_2IrO_3 [137] or with molecular graphene [138]. According to the proposal in Ref. [38], π fluxes can potentially be created in a QSHI by means of an adjacent superconductor and a magnetic field. This realization obviously breaks time reversal symmetry and it is therefore crucial to keep the flux states localized, in order to exponentially suppress the induced level splitting. Naturally, the fact that the diameter of the flux-threaded area is typically larger than the lattice constant, is an obstacle to the experimental realization. One can generalize this idea to arrays of fluxes using Abrikosov lattices. Alternatively, π fluxes may be realized using SQUIDSs.

Recent proposals that are relevant for the experimental realization of π fluxes as a probe of the topological index include artificial semiconductor honeycomb structures [139], cold atoms in optical lattices [140] and cold atoms on chips [141]. Furthermore, dislocations [142; 39] or wedge disclinations [40] in crystals can also give rise to π flux states.

Finally, the concept of π flux insertions in a two-dimensional lattice carries over to three-dimensional topological insulators [37; 143].

5

π flux based quantum spin models

The local moments which arise from π fluxes and the freedom to arrange them in arbitrary geometries which are only limited by the underlying lattice provide us with the possibility to build quantum spin-1/2 models. Furthermore, the magnetic excitations of the host quantum spin Hall insulator can be used to change the range of the spin fluxon–spin fluxon interactions. In this chapter, several realizations of spin models are discussed. The main focus is on the one-dimensional chain of spin fluxons which can be directly compared to the one-dimensional Heisenberg XXZ model.

5.1 Cluster of three spins

An interesting extension of the insertion of two π fluxes (Sec. 4.5) is the cluster of four π fluxes. Three of them are placed on the corners of an equidistant triangle and the fourth is placed at a larger distance away from the cluster (see inset in Fig. 5.1). Thereby, we have introduced two characteristic length scales in the systems. Since the range of the spin fluxon–spin fluxon interaction depends on temperature, we expect the spin susceptibility to reflect both length scales once the temperature is below the energy scale of the bulk system. Figure 5.1 shows the spin susceptibility [Eq. 4.19] which follows two Curie laws. The "high" temperature Curie law $\chi_s = 4/k_{\mathrm{B}}T$ is the response to the four non-interacting spin fluxons of the cluster. The "low" temperature Curie law $\chi_s = 2/k_{\mathrm{B}}T$ is generated by the far separated spin fluxon and by an effective spin-1/2 from the remaining triangle of three spin fluxons.

In the following, we explain the low temperature susceptibility results by deriving the ground state of a cluster of three spins. We make an ansatz in form of an anisotropic Heisenberg model:

$$\mathcal{H} = J_z \sum_{i=1}^{3} \hat{S}_i^z \hat{S}_{i+1}^z + \frac{1}{2} J_\perp \sum_{i=1}^{3} \left(\hat{S}_i^+ \hat{S}_{i+1}^- + \hat{S}_i^- \hat{S}_{i+1}^+ \right) . \tag{5.1}$$

This ansatz is motivated by the effective interaction between spin fluxons which we assume to be anisotropic and to be predominantly in the xy-plane [see Eq. (4.28)], i.e. $J_\perp \gg J_z$. The combined Hilbert space of the system is given by the tensor product of the three spin-1/2

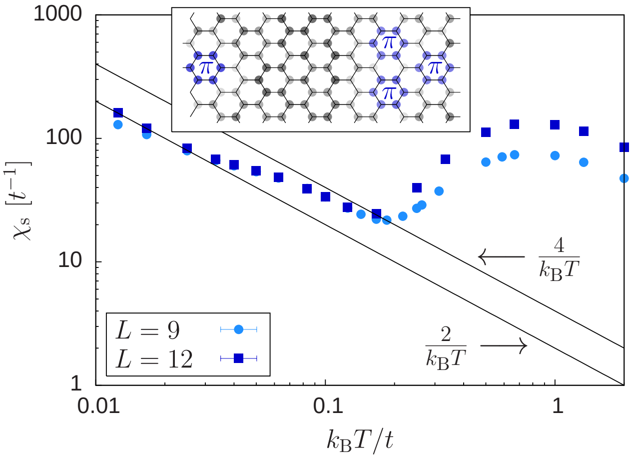

Figure 5.1: Spin susceptibility of the Kane-Mele Hubbard model, augmented with four π flux insertions. The parameters are $U/t = 4$ and $\lambda/t = 0.2$. At low temperature, the susceptibility follows a Curie law $\chi_s = 4/k_B T$, corresponding to the four independent spin fluxons localized at the flux insertions. At even lower temperatures, the susceptibility follows a Curie law $\chi_s = 2/k_B T$ corresponding to two effective spin-1/2 degrees of freedom. The inset shows the integrated local dynamic spin structure factor $S^{zz}_{\Omega}(\boldsymbol{i})$ for $L = 15$.

representations of $SU(2)$. Applying the rule for fusing two representations of spin operators,

$$(s_1) \otimes (s_2) = \sum_{s=|s_1-s_2|}^{|s_1+s_2|} (s) \,, \tag{5.2}$$

we have

$$(1/2) \otimes (1/2) \otimes (1/2) = [(0) \oplus (1)] \otimes (1/2) = (1/2) \oplus (1/2) \oplus (3/2) \,. \tag{5.3}$$

The spin systems can therefore be decomposed into two linear independent spin 1/2 representations and one spin 3/2 representation. The eight states are six $s = \pm 1/2$ states and two $s = \pm 3/2$ states. We proceed by setting up the Hamiltonian $\mathcal{H}'$ which describes the spin 1/2 subspace of the combined Hilbert space. The six states are

$$\begin{aligned} |i+\rangle &= |i\downarrow, i+1\uparrow, i+2\uparrow\rangle \\ |i-\rangle &= |i\uparrow, i+1\downarrow, i+2\downarrow\rangle \,, \end{aligned} \tag{5.4}$$

where $i = 1, 2, 3$ and periodic boundary conditions are assumed. Applying Hamiltonian (5.1) to the states (5.4), one obtains

$$\mathcal{H}' = -\frac{1}{4} J_z \sum_{i=1}^{3} |i\pm\rangle\langle i\pm| + \frac{1}{2} J_\perp \sum_{i=1}^{3} \Big[|i\pm\rangle\langle i+1\pm| + |i+1\pm\rangle\langle i\pm| \Big] \,. \tag{5.5}$$

By introducing the Fourier decomposition $|i\pm\rangle = (1/\sqrt{3})\sum_k e^{iki_\pm}|k\pm\rangle$ with $k = 2\pi n/L = 0, \pm 2\pi/3$, one has

$$\mathcal{H}' = \sum_{k,\alpha=\pm} |k\alpha\rangle\langle k\alpha| \left[-\frac{J_z}{4} + J_\perp \cos(ka) \right] , \tag{5.6}$$

and we set the lattice spacing $a = 1$ in the following. For $J_z = 0$, the ground state of Eq. (5.6) is:

$$\begin{aligned} J_\perp < 0 \quad &: \quad |\mathrm{gs}\rangle = |k = 0\pm\rangle \text{ , with } E_{\mathrm{gs}} = -|J_\perp| \text{ ,} \\ J_\perp > 0 \quad &: \quad |\mathrm{gs}\rangle = |k = \pm\frac{2\pi}{3}\pm\rangle \text{ , with } E_{\mathrm{gs}} = -\frac{J_\perp}{2} \text{ .} \end{aligned} \tag{5.7}$$

The uniform ground state $|k = 0\pm\rangle$ is two-fold degenerate and $|k = \pm\frac{2\pi}{3}\pm\rangle$ defines a chiral ground state which is four-fold degenerate. In principle, the ground state degeneracy can be obtained by measuring the entropy $S(T)$ of the flux-augmented Kane-Mele-Hubbard model. Using Eq. 5.7, one can then deduce the sign of the exchange coupling constant $J_\perp$. However, this is a demanding task in numerical simulations since it requires to measure extensive quantities, i.e. the temperature-dependent energy, to a high accuracy.

5.2 The one-dimensional π flux chain

The overlap of the well-localized wave functions attributed to the π fluxes can be quantified in terms of a hopping integral. Then, we expect a lattice arrangement of fluxes to have the eigenvalue spectrum of a tight-binding Hamiltonian, with dominant nearest-neighbor hopping terms. Naturally, one has to suppose that bulk lattice and flux lattice single-particle excitations are well separated in energy, or in other words, the bandwidth of the flux lattice has to fit in the band gap of the quantum spin Hall insulator.

We first test this idea by considering the Kane-Mele model on a periodic lattice with $L_x \times L_y = L_x \times 1$ unit cells, i.e. on a torus that is thin in the y (azimuthal)–direction. Each unit cell consists of $N_x \times N_y = 4 \times N_y$ honeycomb plaquettes. We observed that choosing $N_y \geq 12$ is sufficient to eliminate finite size effects. The lattice is augmented by the insertion of two π fluxes per unit cell (Fig. 5.2), leading to four eigenvalues in the band gap per k point.

We make the following ansatz for the non-interacting low-energy Hamiltonian:

$$\mathcal{H} = \sum_{i,\sigma} \left[t_1 \hat{a}^\dagger_{i\sigma}\hat{b}_{i\sigma} + t_2 \hat{b}^\dagger_{i\sigma}\hat{a}_{i+a\sigma} \right] + \text{H.c.} = \sum_k \left(\hat{a}^\dagger_{k\uparrow}, \hat{b}^\dagger_{k\uparrow}, \hat{a}^\dagger_{k\downarrow}, \hat{b}^\dagger_{k\downarrow} \right) \left[\mathbf{1} \otimes h(k) \right] \left(\hat{a}_{k\uparrow}, \hat{b}_{k\uparrow}, \hat{a}_{k\downarrow}, \hat{b}_{k\downarrow} \right)^T , \tag{5.8}$$

where $t_{1,2} \in \mathbb{C}$, a is the width of the unit cell, and

$$h(k) = \begin{bmatrix} 0 & t_1 + \bar{t}_2 e^{-ika} \\ \bar{t}_1 + t_2 e^{ika} & 0 \end{bmatrix} . \tag{5.9}$$

The spin index σ labels the Kramers doublet of spin fluxons. However, one has to keep in mind that the concept of spin fluxons vs. charge fluxons is only well-defined at finite repulsive electron-electron interactions.

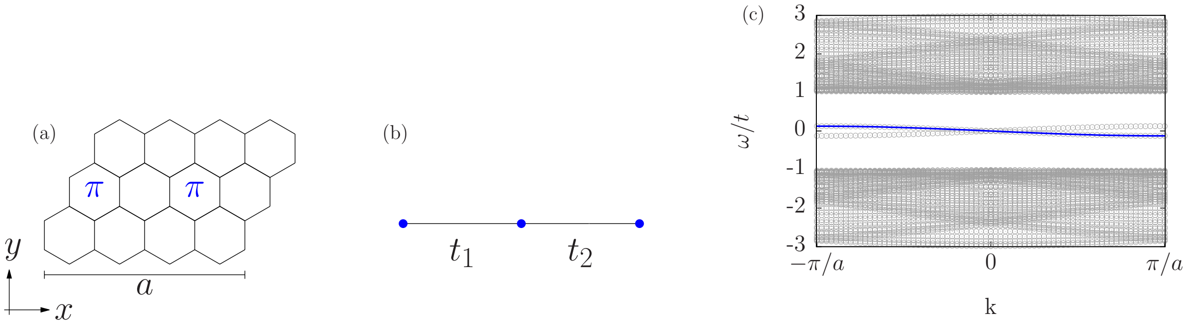

Figure 5.2: The one-dimensional π flux chain. (a) The unit cell carries two π fluxes and has a width of four honeycomb plaquettes. (b) Effective lattice and hopping parameters t_1 and t_2. (c) Non-interacting eigenvalue spectrum of the respective flux augmented Kane-Mele model. The line corresponds to the spectrum $\epsilon^{+}_{\sigma}(k)$ of the effective π flux Hamiltonian. Here, $\lambda/t = 0.2$.

The hopping coefficients $t_{1,2}$ are determined by the symmetry of the Hamiltonian (5.8) under time reversal and by exploiting that choosing a particular unit cell corresponds to choosing a particular gauge. The anti-unitary time reversal operator is given by $\theta = UK$, where K denotes complex conjugation and, here, $U = i\sigma_y \otimes \mathbf{1}$. Time-reversal symmetry demands $\theta\,[\mathbf{1}\otimes h(k)]\,\theta^{-1} = \overline{U\,[\mathbf{1}\otimes h(k)]\,U^{-1}} \overset{!}{=} [\mathbf{1}\otimes h(-k)]$, so

$$\bar{t}_1 + t_2 e^{ika} = t_1 + \bar{t}_2 e^{ika} \ . \tag{5.10}$$

On the other hand, we can define $U(1)$ gauge fields $\chi(i)$ and $\chi(i+a/2)$ that live on the orbitals a_i and b_i, respectively. The $\chi(i)$ shall be translation invariant and spin independent. Then, new operators $\tilde{a}_{i\sigma}$ and $\tilde{b}_{i\sigma}$ can be defined as

$$\begin{aligned} \tilde{a}_{i\sigma} &= e^{-i\chi(i)}\hat{a}_{i\sigma}, \\ \tilde{b}_{i\sigma} &= e^{-i\chi(i+a/2)}\hat{b}_{i\sigma} \ . \end{aligned} \tag{5.11}$$

In this gauge, the Hamiltonian (5.8) becomes

$$\begin{aligned} \widetilde{\mathcal{H}} &= \sum_{i,\sigma}\left[t_1\tilde{a}^{\dagger}_{i\sigma}\tilde{b}_{i\sigma} + t_2\tilde{b}^{\dagger}_{i\sigma}\tilde{a}_{i+a\sigma}\right] + \text{H.c.} \\ &= \sum_{i,\sigma}\left[t_1\hat{a}^{\dagger}_{i\sigma}\hat{b}_{i\sigma}e^{i[\chi(i)-\chi(i+a/2)]} + t_2\hat{b}^{\dagger}_{i\sigma}\hat{a}_{i+a\sigma}e^{-i[\chi(i)-\chi(i+a/2)]}\right] + \text{H.c.} \ . \end{aligned} \tag{5.12}$$

The chain with two orbitals gives us two possibilities to choose the unit cell, simply by shifting the unit cell by half its width a. This is accomplished by the action of a translation operator $T_{a/2}$, where $T^{-1}_{a/2}\hat{a}_i T_{a/2} = \hat{b}_i$ and $T^{-1}_{a/2}\hat{b}_i T_{a/2} = \hat{a}_{i+a}$. We equate the gauged Hamiltonian $\widetilde{\mathcal{H}}$ (5.12) with the Hamiltonian $\mathcal{H}$ (5.8), shifted by $a/2$:

$$\widetilde{\mathcal{H}} = T^{-1}_{a/2}\mathcal{H}T_{a/2} = \sum_{i,\sigma}\left[t_1\hat{b}^{\dagger}_{i\sigma}\hat{a}_{i+a\sigma} + t_2\hat{a}^{\dagger}_{i\sigma}\hat{b}_{i\sigma}\right] + \text{H.c.} \ . \tag{5.13}$$

One obtains

$$t_2 = t_1 e^{i[\chi(i)-\chi(i+a/2)]} = t_1 e^{i\phi} . \tag{5.14}$$

To progress, we assume that $t_1 \in \mathbb{R}$. Then the condition (5.10) of time-reversal is $e^{i\phi} = e^{-i\phi}$ and therefore $\phi \in \{0, \pi\}$. It immediately follows from Eq. (5.8) and (5.14) that the eigenvalue spectrum is $\epsilon_\sigma(k) = \pm 2t_1 \cos[(\phi + ka)/2]$. The observed low-energy spectrum of the π flux chain corresponds to the choice $\phi = \pi$ [Fig. 5.2(c)] and a least-square fit to the low-energy dispersion gives $t_1 = 0.126t$.

We observed that a finite Rashba interaction up to $\lambda_\mathrm{R} \sim \lambda$ does not change the low-energy spectrum qualitatively and the twofold degeneracy of the low-energy bands is retained. Increasing the distance between neighboring fluxes leads to the same spectrum but with a smaller band width.

5.2.1 Interaction effects

We now turn to the effect of interactions on the one-dimensional π flux chain, by considering the Kane-Mele-Hubbard model (see Sec. 1.2.1). This model has electronic interactions which can mediate an interaction between the spin fluxons by the exchange of collective magnetic excitations. As it has been demonstrated in Sec. 4.5, the interaction strength and range is inversely proportional to the spin gap. Therefore, we expect interaction effects on the one-dimensional π flux chain to be most prominent for values of the Hubbard interaction U/t close to the magnetic phase transition where the spin gap vanishes.

We consider the *normalized* uniform and static charge and magnetic susceptibilities, similar to Eq. (4.18) and Eq. (4.19),

$$\chi_c = \chi^{00}_{\boldsymbol{q}=\boldsymbol{0}}(i\omega_n = 0) , \tag{5.15}$$

$$\chi_s = 4 \times \chi^{zz}_{\boldsymbol{q}=\boldsymbol{0}}(i\omega_n = 0) , \tag{5.16}$$

and the zero-temperature dynamic spin structure factor (see Sec. 2.5)

$$S^{+-}(q,\omega) = \pi \sum_n \left| \langle 0 | \hat{S}^+_q | n \rangle \right|^2 \delta(\omega - \Delta_n) , \tag{5.17}$$

where $\Delta_n = E_n - E_0$ is the energy above the ground state energy. In the following, we show that the XXZ Heisenberg model is the effective spin model for the spin fluxon chain. By measuring the magnetic susceptibility χ_s and the dynamic spin structure factor $S^{+-}(q,\omega)$ as a function of the Hubbard interaction, we can trace the crossover from the interacting spin chain to the magnetic phase of the bulk.

5.2.1.1 Effective spin model at $U/t = 4$

The ground state of the one-dimensional Hubbard chain does not show a Mott transition in the sense of a transition at a finite value of the electron-electron interaction [144], but a $(U = 0)$–transition. Consequently, we expect the same to be true for the half-filled one-dimensional π flux chain, i.e. a nonzero charge gap and gapless spin excitation for any

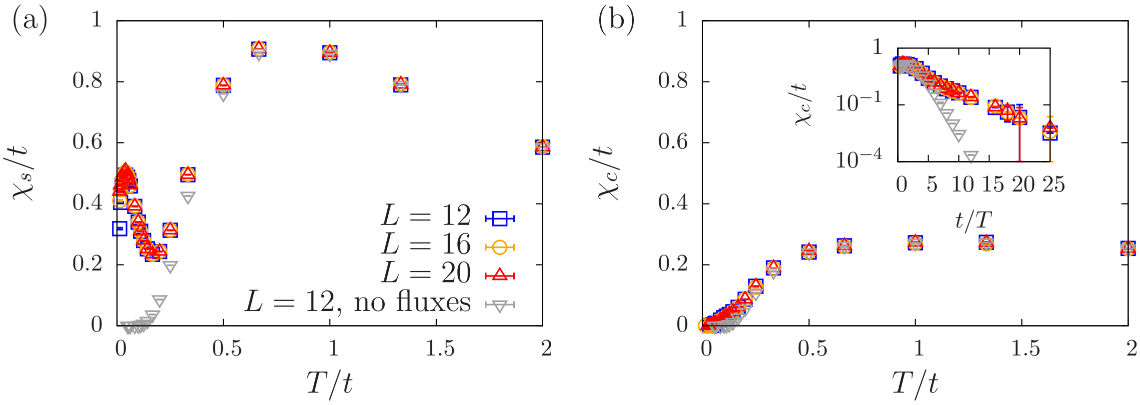

Figure 5.3: Uniform (site averaged) longitudinal spin susceptibility $\chi_s(T)$ (a) and uniform charge susceptibility $\chi_c(T)$ (b) of the flux augmented Kane-Mele Hubbard model at $U/t = 4$. Inset in (b): charge susceptibility as a function of inverse temperature on a logarithmic scale. Here, $\lambda/t = 0.2$.

$U/t > 0$. The spin and charge susceptibilities of the Kane-Mele-Hubbard model, augmented with the one-dimensional flux chain, are shown in Fig. 5.3. Calculations are done for a lattice geometry of $N_x L_x \times N_y L_y$ honeycomb plaquettes. Due to the flux insertions, we consider a ribbon geometry with periodic boundary conditions and take $L_y = 1$ and $N_y = 12$. We have $N_x = 4$ orbitals in the x-direction and $L_x = 3, 4, 5$ which corresponds to $6, 8$ and 10 flux insertions [see Fig. 5.2 (a)]. We use the notation $L = N_x L_x$. Our results are for $U/t = 4$. The spin susceptibility takes finite values at temperatures below $T/t \approx 0.2$ [Fig. 5.3(a)] suggesting that low-energy spin-fluxon excitations remain in the presence of the Hubbard interaction. On the other hand, the charge susceptibility is exponentially suppressed at low temperatures [Fig. 5.3(b)], i.e. $\chi_c \sim e^{-\Delta_c/T}$.

The remaining low-energy degrees of freedom at $U/t > 0$ are expected to be spin degrees of freedom, namely the Kramers doublets of well localized spin fluxon states. Due to the vicinity of the xy–ordered antiferromagnetic phase, the magnetic excitations of the bulk system, which mediate interactions between spin fluxons, are predominantly in the xy–plane. To obtain an effective spin model for the spin fluxon chain, we therefore make an ansatz in terms of an anisotropic Heisenberg Hamiltonian with nearest-neighbor interactions:

$$\mathcal{H}_{\text{eff}} = J \sum_i \left[\Delta \hat{S}_i^z \hat{S}_{i+1}^z + \frac{1}{2} \left(\hat{S}_i^+ \hat{S}_{i+1}^- + \hat{S}_i^- \hat{S}_{i+1}^+ \right) \right] . \tag{5.18}$$

This is the one-dimensional XXZ Heisenberg model. Note that the notation differs slightly from the notation in Ref. [145]. The anisotropy parameter Δ is expected to be $|\Delta| < 1$. In Fig. 5.4, we compare the spin susceptibility of the flux augmented Kane-Mele-Hubbard model with the susceptibility of the XXZ model at low temperatures. At elevated temperatures, $T/t \gtrsim 0.1$, bulk states of the quantum spin Hall insulator become visible. The results for the XXZ chain have been calculated with the stochastic-series-expansion (SSE) method with

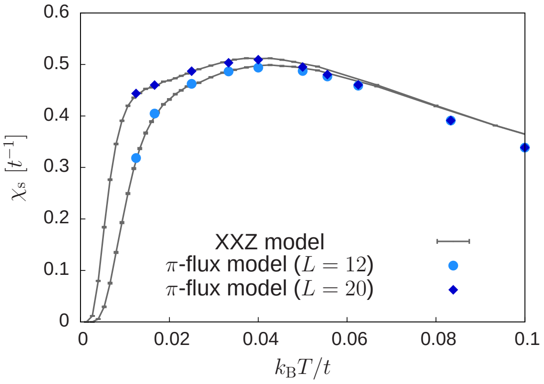

Figure 5.4: Comparison of the low-temperature spin susceptibility of the flux augmented Kane-Mele-Hubbard model (symbols) and of the one-dimensional XXZ Heisenberg model (lines). Here, the parameter L refers to the number of honeycomb plaquettes in the x-direction. Results for six π fluxes ($L = 12$) and for 10 π fluxes ($L = 20$) are shown.

operator-loop updates [146], using the implementation in the `ALPS 1.3` libraries [147]. The anisotropy parameter Δ has been used as a fit parameter. The value $\Delta = -0.05$ ($J^{zz}/|J^{xy}| = -0.1$ in the notation of Ref. [145]) reproduces well the results for a chain of six fluxes and of ten fluxes. The energy scale is set by J and, at this point, the sign of J is irrelevant. For $-1 < \Delta < 1$, the XXZ Heisenberg model is in the XY phase, which has a gapless excitation continuum and is symmetric about rotations in the XY plane [148]. Therefore, one expects the spin susceptibility $\chi_s(T = 0)$ to be finite and the vanishing of $\chi_s(T)$ as $T \to 0$ [Fig. 5.3(a)] may then be attributed to the finite size of the chains.

5.2.1.2 Crossover from the spin chain to the bulk magnetic phase

In Sec. 4.5, we have seen that the range and strength of the spin fluxon–spin fluxon interaction is tied to the magnitude of the Hubbard U/t. The important energy scale is the spin gap Δ_s which vanishes at the critical U_c/t. As $\Delta_s \to 0$, the correlation length of transverse correlations diverges. The location of the critical point U_c/t can be estimated from the scaling behavior of the real-space spin-spin correlation functions at large distances [49; 145], and we have $U_c/t = 5.7$ at $\lambda/t = 0.2$. Naturally, we assume here that the (intensive) number of inserted π fluxes does not perturb the magnetic phase boundary significantly. The charge degrees of freedom are suppressed below temperatures of $T/t = 0.05 - 0.1$, depending on the values of the Hubbard U/t [Fig. 5.5(b)]. Below this temperature and for $U/t < 5$, the magnetic susceptibility $\chi_s(T)$ is that of a spin chain. The magnitude of the exchange constant J can be estimated by the temperature $T_{\max}$ of the low-temperature maximum of $\chi_s(T)$ [(arrows in Fig. 5.5(a)]. The scaling plot of $\chi_s T(T/J)$ shows a satisfying data collapse at low temperatures [Fig. 5.5(c)]. We are therefore confident that up to $U/t \lesssim 5$, the spin chain can be described by the one dimensional XXZ Heisenberg model derived in the previous section.

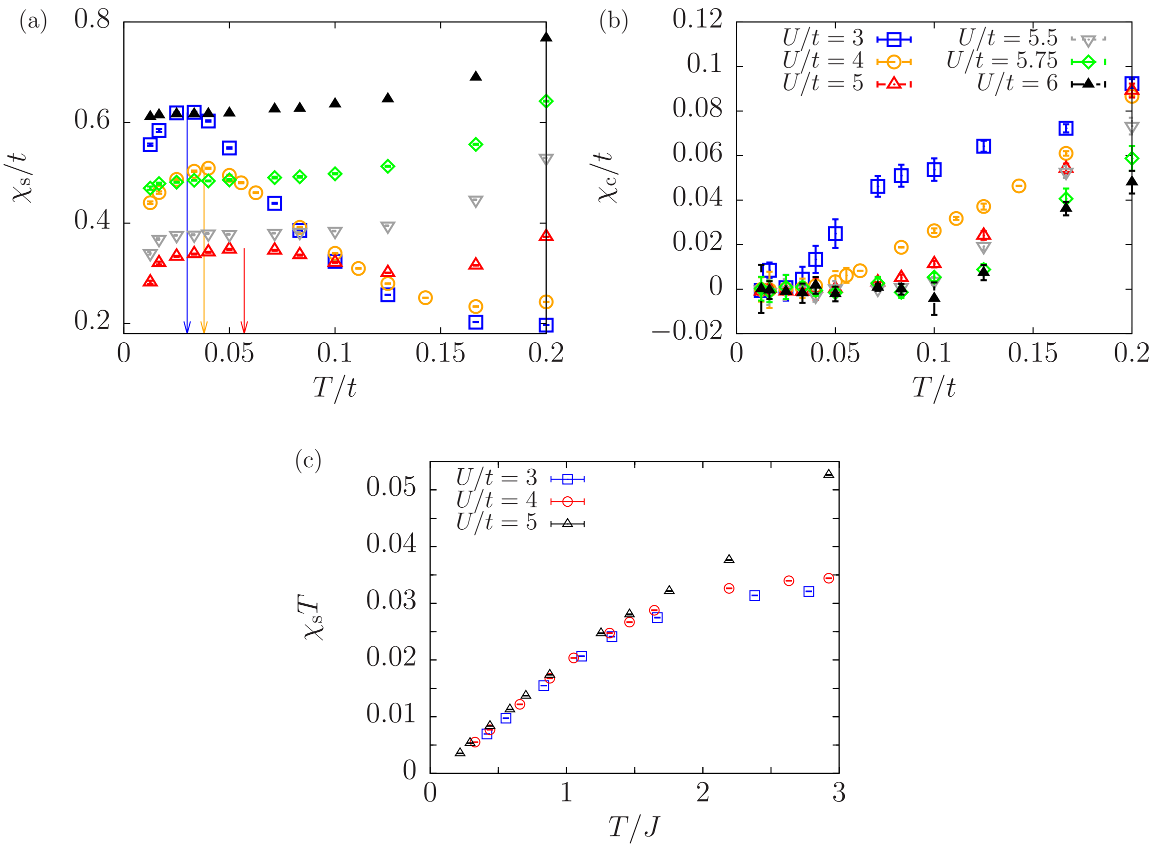

Figure 5.5: Uniform magnetic χ_s (a) and charge χ_c (b) susceptibilities of the Kane-Mele-Hubbard model, augmented with a π flux chain. The arrows in (a) indicate the temperature T_{max}. Scaling of the spin susceptibility χ_s, using the estimate $J = T_{\text{max}}$ (c). Here, $\lambda/t = 0.2$ and $L_x = 20$, $N_y = 12$.

Above U_c, the (longitudinal) magnetic susceptibility χ_s measures the spin wave excitations of the bulk magnetic phase. The spin waves are fluctuations transverse to the magnetic ordering vector. Since the magnetic order in the antiferromagnetic phase of the Kane-Mele-Hubbard model is predominantly in the XY-plane, the $\hat{S}^z$-$\hat{S}^z$ correlations pick up the spin wave signal. The transition to the bulk magnetic phase is shown in Fig. 5.6.

In order to understand the crossover from the spin chain to the magnetic phase, we look at the same susceptibility data, but now as a function of the Hubbard interaction U/t, see Fig. 5.7. In the plain lattice without external π fluxes, low-energy spin or charge degrees are absent. The magnetic order above U_c is reflected in an increase of χ_s which sharpens with temperature [Fig. 5.7(a),(b)]. The charge susceptibility χ_c of the flux-augmented Kane-Mele-Hubbard model reflects the shift in energy of the charge fluxon states from zero energy at $U = 0$ to higher (lower) energies for $U/t > 0$ [Fig. 5.7(d)]. The spin susceptibility χ_s has a minimum around $U/t \approx 5.25$ signifying the crossover from the spin chain to the bulk magnetic

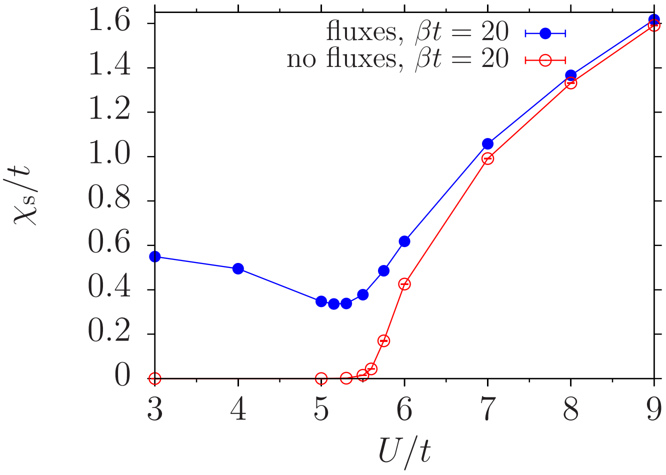

Figure 5.6: Comparison of the spin susceptibilities of the flux-augmented Kane-Mele-Hubbard model to the plain Kane-Mele-Hubbard model.

phase as the interaction range increases. The initial decrease of χ_s can be attributed to the increase of the effective coupling strength with increasing U/t (see Sec. 4.5).

The dynamic excitations of the spin fluxon chain are tracked by the dynamic spin structure factor. Since the effective XY spin model is symmetric about rotation in the XY-plane, we consider the transverse structure factor $S^{+-}(q, \omega)$ (5.17). The results for the flux-augmented Kane-Mele-Hubbard model on a ribbon with periodic boundary conditions are shown in Fig. 5.8. The key observations are (i) the presence of an excitation gap which decreases with increasing Hubbard interaction and (ii) spectral weight at low energies within the excitation gap. The excitation gap is the equivalent to the spin gap of the Kane-Mele-Hubbard model without flux insertions. The spectral weight in the spin gap stems from the spin fluxon chain. It is tempting to identify this spectral weight with the the spinon excitation continuum of a spin chain. The spinon excitation continuum is gapless at $q = 0$ and $q = \pi$. Due to the unit cell which carries two spin fluxons [Fig. 5.2(a)], we have to compare the excitation spectrum [Fig. 5.8] to a back-folded spinon excitation spectrum, which vanishes only at $q = 0$, like the observed spectrum. However, the present lattice sizes do not allow for an unbiased identification of the low-energy weight with the spinon excitation continuum.

5.3 Other π flux chain geometries

In the remainder of this chapter, we consider two other geometries of π flux insertions: the 2–leg π flux ladder and the π flux zigzag chain. Figure 5.9 shows the single-particle gap Δ_{sp} as a function of the number n of legs of a π flux ladder system, inserted in the (non-interacting) Kane-Mele model. A n leg ladder is an array of n parallel chains. The gap is zero for an odd number of legs and exponentially decaying with the number of legs for an even number of legs. For n even, the formation of pairs of bonding and anti-bonding orbitals lead to the finite

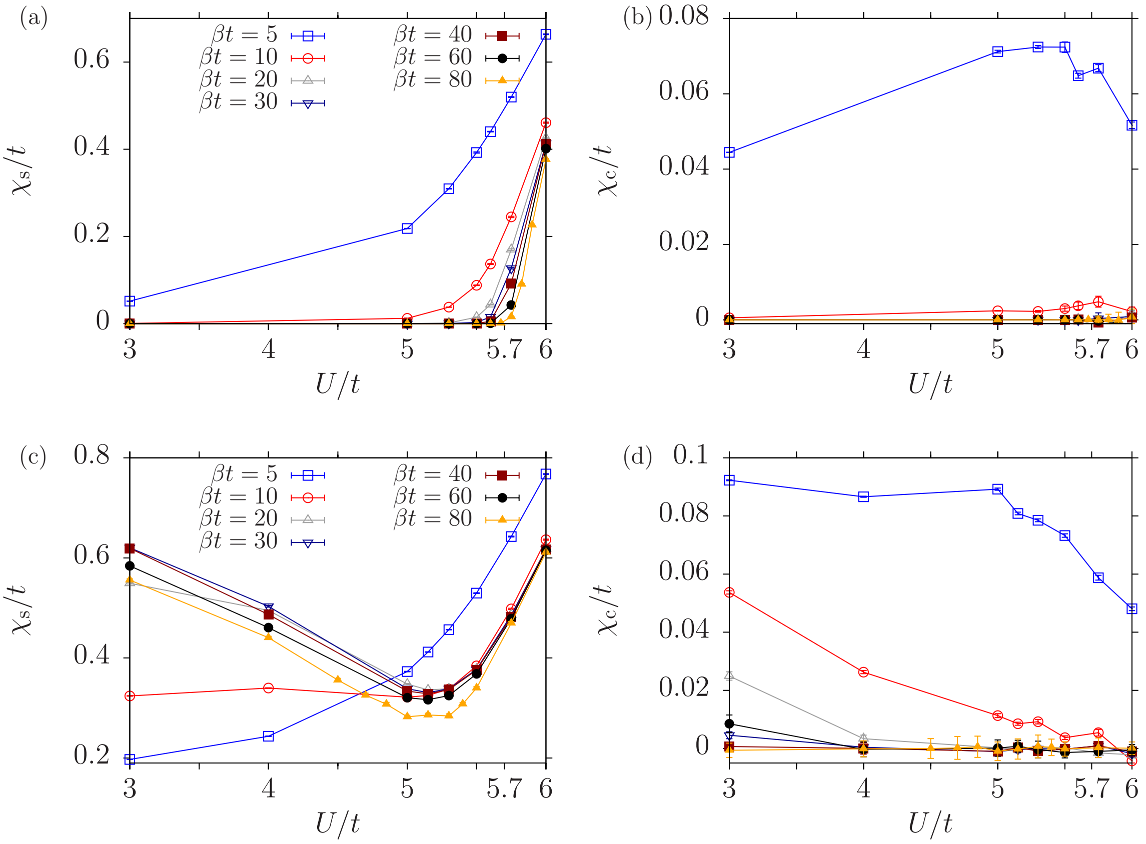

Figure 5.7: Uniform magnetic and charge susceptibilities, measured across the phase transition at $U_c/t = 5.7$. The results are for the Kane-Mele-Hubbard model, both without π fluxes [(a),(b)] and augmented with a π flux chain [(c), (d)]. Here, $\lambda/t = 0.2$ and $L_x = 20$, $N_y = 12$.

single-particle gap. For n odd, the excitations of the ladder system are essentially determined by the remaining chain, and can therefore be expected to be similar to the gapless π flux chain ($n = 1$). The behavior of the single-particle gap Δ_{sp} is reminiscent of the behavior of the spin gap in the crossover from the single antiferromagnetic Heisenberg spin-1/2 chain to the two-dimensional antiferromagnetic spin-1/2 square lattice. Ladders with an even number of legs have a finite spin gap and short range spin correlations while ladders with an odd number of legs have no spin gap and power-law spin correlations [149]. Naturally, in the π flux setup, a spin model is only obtained when the charge fluxons are gapped out by the Hubbard interaction. However, from the perspective of a mean-field theory, we can still expect that the even-odd effect observed for the π flux ladder in the non-interacting model persists when the π flux insertions are replaced by the spin-1/2 spin fluxons.

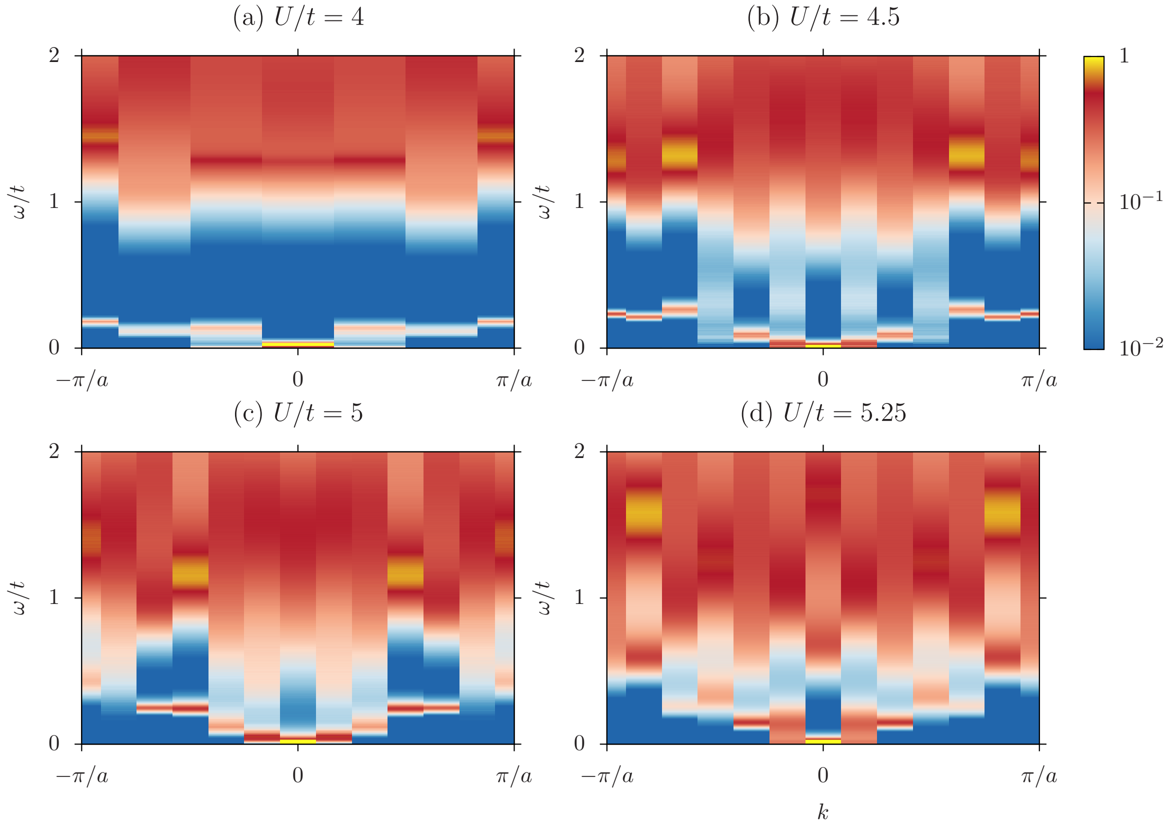

Figure 5.8: Zero-temperature transverse dynamic spin structure factor $S^{+-}(q,\omega)$ at $\lambda/t = 0.2$, for $L_x = 6$ ($U/t = 4$) and $L_x = 12$ ($U/t = 4.5, 5, 5.25$).

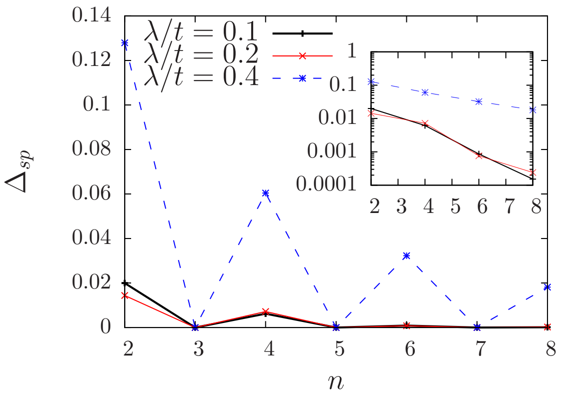

Figure 5.9: Single-particle gap Δ_{sp} of the Kane-Mele model, augmented by a n–leg π flux ladder. The inset shows the single-particle gap for even n on a logarithmic scale.

The 2-leg π flux ladder

We use the following ansatz for the Hamiltonian of the non-interacting 2-leg ladder:

$$\begin{aligned}\mathcal{H} \;=\; & \sum_{i,\sigma}\Big[t_{ab}\hat{a}^{\dagger}_{i\sigma}\hat{b}_{i\sigma} + t'_{ab}\hat{b}^{\dagger}_{i\sigma}\hat{a}_{i+a\sigma} + t_{bc}\hat{b}^{\dagger}_{i\sigma}\hat{c}_{i\sigma} + t_{cd}\hat{c}^{\dagger}_{i\sigma}\hat{d}_{i\sigma} + t'_{cd}\hat{d}^{\dagger}_{i\sigma}\hat{c}_{i+a\sigma} + t_{da}\hat{d}^{\dagger}_{i\sigma}\hat{a}_{i+a\sigma} + \mathrm{H.c.}\Big] + \\ & \sum_{i,\sigma}\Big[t_{ac}\hat{a}^{\dagger}_{i\sigma}\hat{c}_{i\sigma} + t'_{ac}\hat{a}^{\dagger}_{i\sigma}\hat{c}_{i-a\sigma} + t_{bd}\hat{b}^{\dagger}_{i\sigma}\hat{d}_{i\sigma} + t'_{bd}\hat{b}^{\dagger}_{i\sigma}\hat{d}_{i-a\sigma} + \mathrm{H.c.}\Big] \qquad (5.19)\end{aligned}$$

We assume the hopping parameters to be spin-independent. They are determined in the same manner as in Sec. 5.2. We obtain the Hamilton matrix

$$h_\sigma(k) = \begin{bmatrix} 0 & t_1(1-e^{-ika}) & t_3(1+e^{-ika}) & t_2e^{-ika} \\ t_1(1-e^{ika}) & 0 & -t_2 & -t_3(1+e^{-ika}) \\ t_3(1+e^{ika}) & -t_2 & 0 & t_1(-1+e^{-ika}) \\ t_2e^{ika} & -t_3(1+e^{ika}) & t_1(-1+e^{ika}) & 0 \end{bmatrix}. \qquad (5.20)$$

The eigenvalues are

$$\epsilon^{\pm\pm}_\sigma(k) = \pm t_1\left\{2 + t_2^2 + 2t_3^2 + 2(t_3^2-1)\cos(ka) \pm 4t_3\cos(ka/2)\left[2+t_2^2-2\cos(ka)\right]^{1/2}\right\}^{1/2} \qquad (5.21)$$

A least square fit of the low-energy orbitals of the flux-augmented Kane-Mele model at $\lambda/t = 0.6$ to $\epsilon^{\pm\pm}_\sigma(k)$ gives $t_1 = 0.234$, $t_2 = 0.781$ and $t_3 = 0.047$, see Fig. 5.10. We observe that the quality of the fit increases for increasing values of the spin-orbit coupling λ.

Interaction effects

The dependence of $\chi_{s,c}$ on temperature and Hubbard interaction is shown in Fig. 5.11. We estimate the critical value U_c of the Kane-Mele-Hubbard model without fluxes to be $U_c/t \approx 7$

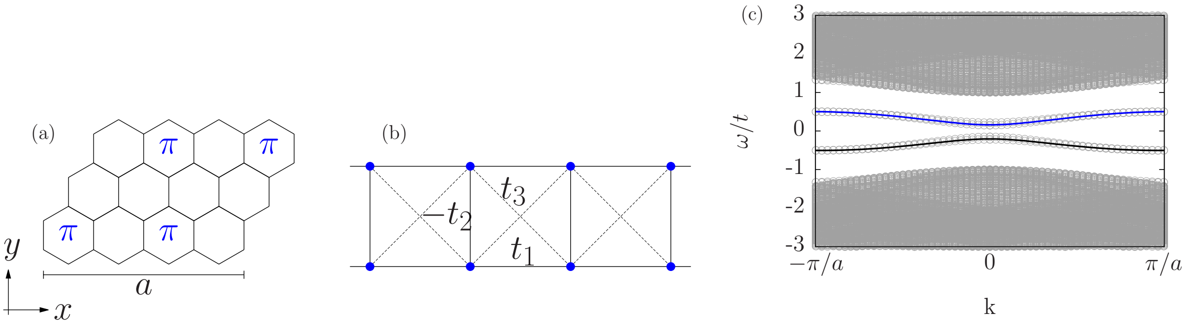

Figure 5.10: The 2-leg π flux ladder. (a) The unit cell carries four π fluxes and has a width of four honeycomb plaquettes. (b) Effective lattice and hopping parameters t_1, t_2 and t_3, where $t_i > 0$. (c) Non-interacting eigenvalue spectrum of the respective flux augmented Kane-Mele model. The lines correspond to the spectrum $\epsilon_\sigma^{\pm\pm}(k)$ (5.21) of the effective π flux Hamiltonian. Here, $\lambda/t = 0.6$.

at $\lambda/t = 0.4$ [49]. In contrast to Fig. 5.7, the susceptibility goes to zero in the limit of low-temperatures in the QSHI phase below U_c [Fig. 5.11 (c)]. This can be explained by the formation of singlet states between the spin fluxon along the rungs of the ladder. In this picture, the lowest excitation is the singlet-triplet excitation which leads to an exponential decreasing magnetic susceptibility as $T \to 0$. This interpretation is consistent with the temperature dependence of χ_s [Fig. 5.11 (a)].

The π flux zigzag chain

A π flux zig zag chain is shown in Fig. 5.12. It is equivalent to the linear π flux chain, but with additional next-nearest neighbor hopping terms $t_{a\sigma}$ and $t_{b\sigma}$. We again make an ansatz in terms of a simple tight-binding model, where the orbitals a and b denote the two π fluxes in the unit cell:

$$
\begin{aligned}
\mathcal{H} &= \sum_{i,\sigma} \left[t_{a\sigma}\hat{a}^\dagger_{i\sigma}\hat{a}_{i+a\sigma} + t_{b\sigma}\hat{b}^\dagger_{i\sigma}\hat{b}_{i+a\sigma} + t_{ab\sigma}\hat{a}^\dagger_{i\sigma}\hat{b}_{i\sigma} + t_{ba\sigma}\hat{a}^\dagger_{i\sigma}\hat{b}_{i-a\sigma} \right] + \text{H.c.} \\
&= \sum_{k} \left(\hat{a}^\dagger_{k\uparrow}, \hat{b}^\dagger_{k\uparrow}, \hat{a}^\dagger_{k\downarrow}, \hat{b}^\dagger_{k\downarrow} \right) \begin{bmatrix} h_\uparrow(k) & 0 \\ 0 & h_\downarrow(k) \end{bmatrix} \left(\hat{a}_{k\uparrow}, \hat{b}_{k\uparrow}, \hat{a}_{k\downarrow}, \hat{b}_{k\downarrow} \right)^T ,
\end{aligned} \tag{5.22}
$$

where

$$
h_\sigma(k) = \begin{bmatrix} t_{a\sigma}e^{ika} + \bar{t}_{a\sigma}e^{-ika} & t_{ab\sigma} + \bar{t}_{ba\sigma}e^{-ika} \\ \bar{t}_{ab\sigma} + t_{ba\sigma}e^{ika} & t_{b\sigma}e^{ika} + \bar{t}_{b\sigma}e^{-ika} \end{bmatrix} . \tag{5.23}
$$

Time-reversal symmetry demands that $\theta H(k)\theta^{-1} = H(-k)$ which leads to, using the same representation of θ as in Sec. 5.2:

$$
\begin{bmatrix} \bar{h}_\downarrow(k) & 0 \\ 0 & \bar{h}_\uparrow(k) \end{bmatrix} = \begin{bmatrix} h_\uparrow(-k) & 0 \\ 0 & h_\downarrow(-k) \end{bmatrix} . \tag{5.24}
$$

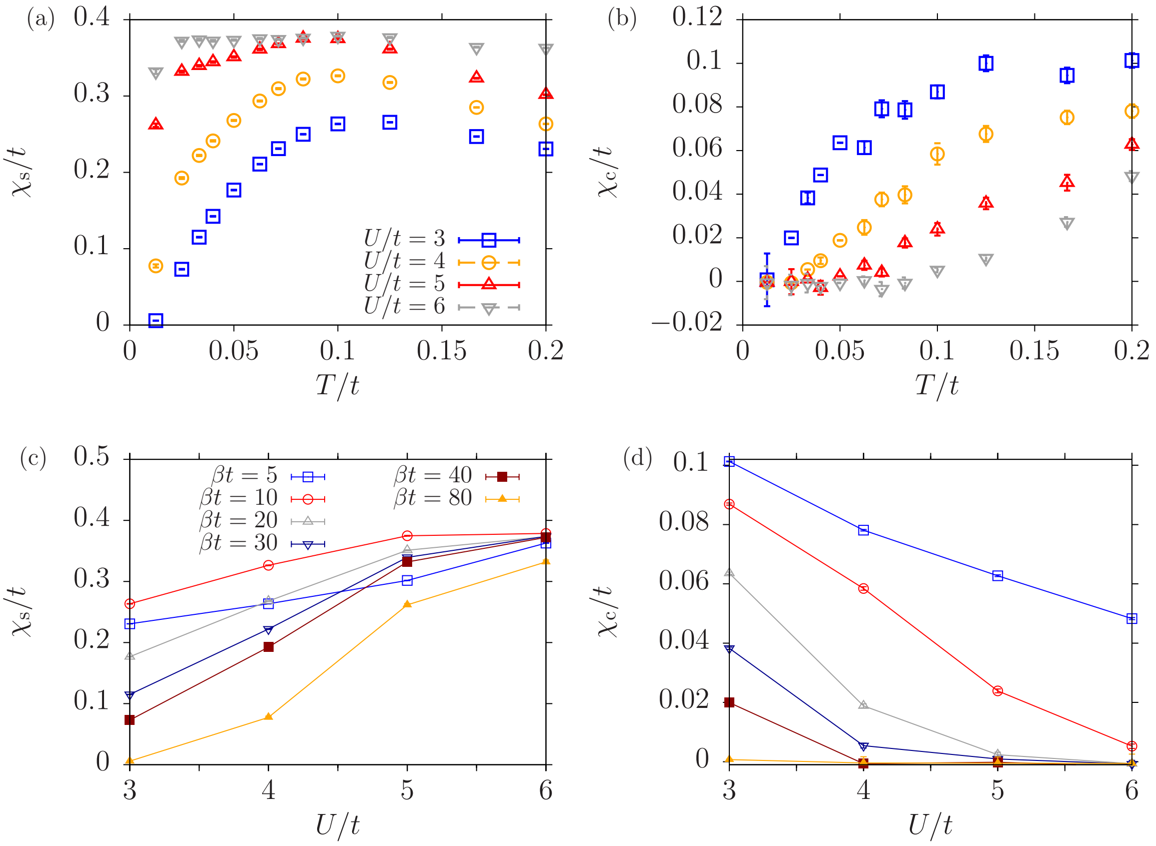

Figure 5.11: Uniform magnetic and charge susceptibilities of the Kane-Mele-Hubbard model, augmented with a 2–leg π flux ladder Here, $\lambda/t = 0.4$ and $L_x = 20$, $N_y = 12$.

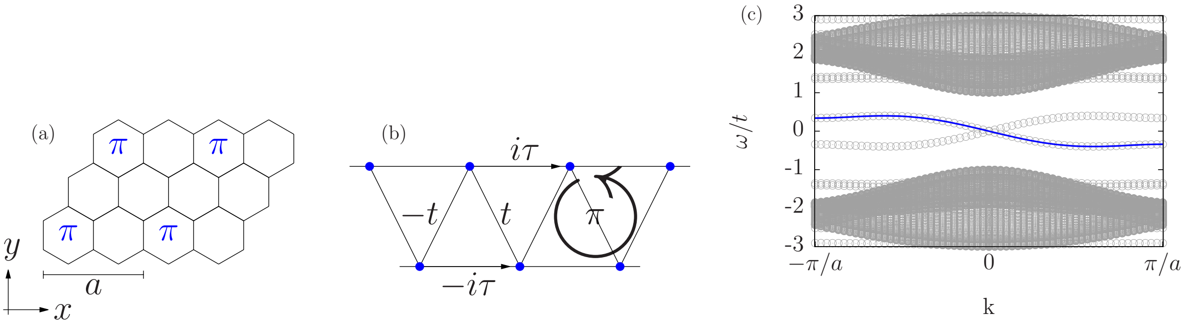

Figure 5.12: The π flux zigzag chain. (a) The unit cell carries two π fluxes and has a width of two honeycomb plaquettes. (b) Effective lattice and hopping parameters t_1 and t_2. Each unit cell of the effective model carries a flux of π. (c) Non-interacting eigenvalue spectrum of the respective flux augmented Kane-Mele model. The line corresponds to the spectrum $\epsilon^{\pm}_{\sigma}(k)$ (5.30) of the effective π flux Hamiltonian. Here, $\lambda/t = 0.4$.

We obtain the following conditions on the hopping parameters from time-reversal symmetry,

$$\begin{aligned}\mathrm{Re}\, t_{x\sigma} &= \mathrm{Re}\, t_{x-\sigma}\ ,\\ \mathrm{Im}\, t_{x\sigma} &= -\mathrm{Im}\, t_{x-\sigma}\ ,\\ t_{y\sigma} &= \bar{t}_{y-\sigma}\ ,\end{aligned} \tag{5.25}$$

where $x = a, b$ and $y = ab, ba$.

Along the lines of Sec. 5.2, we find further restrictions on the hopping parameters by introducing a $U(1)$ gauge field, leading to new operators $\tilde{a}_{i\sigma}$ and $\tilde{b}_{i\sigma}$ [Eq. (5.11)]. In this gauge, the Hamiltonian (5.22) is

$$\widetilde{\mathcal{H}} = \sum_{i,\sigma} \left[t_{a\sigma}\hat{a}^\dagger_{i\sigma}\hat{a}_{i+a\sigma} + t_{b\sigma}\hat{b}^\dagger_{i\sigma}\hat{b}_{i+a\sigma} + t_{ab\sigma}e^{i\phi}\hat{a}^\dagger_{i\sigma}\hat{b}_{i\sigma} + t_{ba\sigma}e^{-i\phi}\hat{b}^\dagger_{i\sigma}\hat{a}_{i+a\sigma}\right] + \mathrm{H.c.}\ . \tag{5.26}$$

Similar to Eq. (5.13), we consider $\widetilde{\mathcal{H}} \overset{!}{=} T^{\star-1}_{a/2}\mathcal{H}T^{\star}_{a/2}$. However, we define the operator $T^\star$ to combine the translation by half of a unit cell with a spin flip: where $T^{\star-1}_{a/2}\hat{a}_{i\sigma}T^{\star}_{a/2} = \hat{b}_{i-\sigma}$ and $T^{\star-1}_{a/2}\hat{b}_{i\sigma}T^{\star}_{a/2} = \hat{a}_{i+a-\sigma}$. We have

$$\begin{aligned} t_{a\sigma} &= t_{b-\sigma}\ ,\\ t_{ab\sigma} &= e^{-i\phi}t_{ba-\sigma}\ .\end{aligned} \tag{5.27}$$

We proceed by combining the conditions from time-reversal and gauge symmetry, Eq. (5.25) and Eq. (5.27). We assume that the nearest neighbor hopping parameters t_{ab}, t_{ba} are spin-independent. It immediately follows that $t_{ab}, t_{ba} \in \mathbb{R}$ and therefore $\phi = 0, \pi$. We set $t = t_{ab}$. Furthermore, we assume that the next-nearest neighbor hopping parameters $t_{a\sigma}, t_{b\sigma}$ are purely imaginary. The reason is that according to Eq. (5.25), their real part is spin-independent, which we set to zero at this point. Defining $\mathrm{Im}\, t_{x\sigma} = \tau_{x\sigma}$, we have $t_{x\sigma} = i\tau_{x\sigma}$ and

$$\tau_{a\sigma} = \tau_{b-\sigma} = -\tau_{b\sigma}\ . \tag{5.28}$$

The resulting Hamilton matrix (5.23) then reads

$$h_\sigma(k) = \begin{bmatrix} -2\sigma\tau\sin(ka) & t(e^{-ik}+e^{-i\phi}) \\ t(e^{ik}+e^{i\phi}) & 2\sigma\tau\sin(ka)\end{bmatrix}\ . \tag{5.29}$$

Its eigenvalues are

$$\epsilon^\pm_\sigma(k) = \pm 2\left[\tau^2\sin^2(ka) + t^2\cos^2\left(\frac{ka-\phi}{2}\right)\right]^{1/2}\ . \tag{5.30}$$

We find that, choosing $\phi = \pi$, a least-square fit to the low-energy bands of the flux augmented Kane-Mele model gives $\tau = 0.152$ and $t = 0.170$ for $\lambda/t = 0.4$ [see Fig. 5.12(c)].

Interaction effects

To study interaction effects, we have simulated the Kane-Mele-Hubbard model with the π flux zigzag chain. The spin and charge susceptibility data (Fig. 5.13) strongly resemble the corresponding measurements for the spin fluxon chain (Fig. 5.7). However, charge degrees of freedom are less easily suppressed as a function of increasing U/t and decreasing temperature, in comparison to the chain [Fig. 5.13 (f)]. χ_s shows a minimum [Fig. 5.13 (e)], similar to the spin fluxon chain. The minimum occurs however at $U/t \approx 4.5$ which is far below the critical interaction. Therefore, besides the the crossover from the spin chain to the magnetic bulk phase, this can possibly point to a phase transition within the zigzag spin fluxon chain. To investigate this issue, one would have to consider considerably large lattice sizes and to measure static as well as dynamic quantities.

5.4 Conclusions

In this chapter, we have presented various realizations of spin models that are built by π flux insertions in a QSHI. We have measured the crossover from a four spin fluxon system to an effective two spin fluxon system (Sec. 5.1). Using a Heisenberg spin model, we have been able to confirm that, apart from the distant spin fluxon, the cluster of three interacting spin fluxons delivers an effective spin 1/2 moment at low temperatures, thereby explaining the QMC spin susceptibility data.

We have explored aspects of the one-dimensional spin fluxon chain, see Sec. 5.2. Based on the favorable comparison of the spin susceptibilities, simulated with spin fluxons and calculated numerically using the SSE algorithm [147], we have established a connection to the one-dimensional XXZ Heisenberg model. One may speculate whether the interacting spin chains experience a phase transition *before* the spin gap Δ_s closes and bulk magnetic order sets in. However, observing this putative transition requires system sizes much larger than the ones we have studied.

In Sec. 5.3, we have looked at other chain geometries, built with spin fluxons. The corresponding susceptibility data of the 2-leg spin fluxon chain can be interpreted in terms of singlet states that form along the rungs of the ladder, in agreement with the well-known spin-1/2 ladder. The π flux zigzag chain represents a complex, and possibly frustrated, spin geometry with additional next-nearest neighbor interactions. The overall behavior of the susceptibilities seems to be similar to the one-dimensional π flux chain.

In summary, our results demonstrate a first step towards using the quantum spin Hall insulator, augmented with π fluxes, as a quantum simulator for spin systems. A lot of intriguing issues remain to be studied, especially the question of frustrated interactions, long-range spin interactions and possible interaction-driven phase transitions in the effective spin systems.

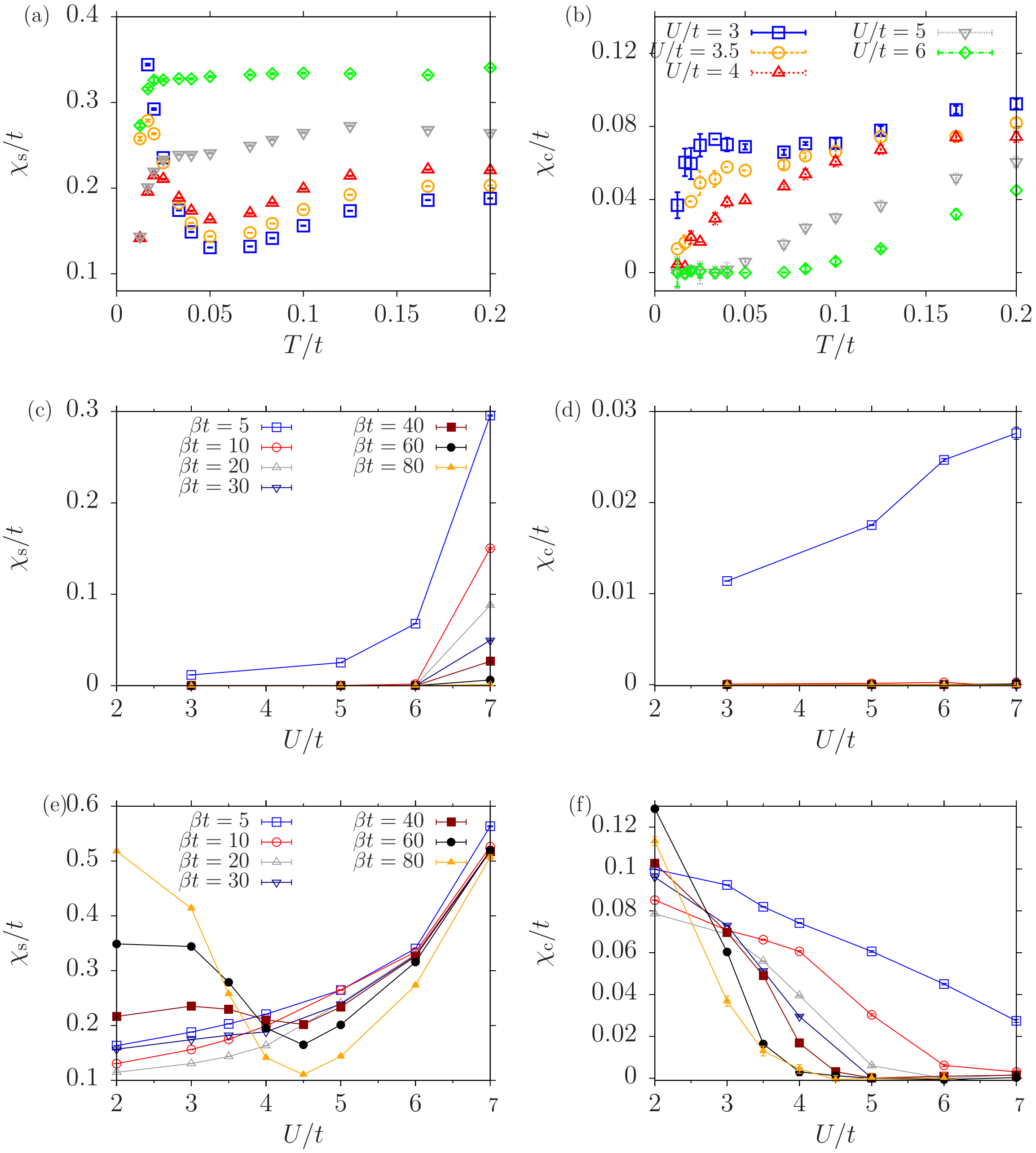

Figure 5.13: Uniform magnetic and charge susceptibilities, measured in the vicinity of the magnetic phase transition (at $U_c/t \approx 7.0$). The results are for the Kane-Mele-Hubbard model, augmented with a π flux zigzag chain [(a),(b) and (e),(f)] and for the plain Kane-Mele-Hubbard model [(c),(d)] Here, $\lambda/t = 0.4$ and $L_x = 20$, $N_y = 12$.

6

The Kane Mele model on the π flux honeycomb lattice

The preceeding chapter have been centered around the physics of the quantum spin Hall insulator perturbed by an intensive number of external π fluxes. In this chapter, we consider an externsive number of external π fluxes by augmenting the Kane-Mele model with one π flux per honeycomb plaquette. The physics of the resulting model the π-Kane-Mele model, is surprisingly reach. We begin the discussion with a detailed analysis of its non-interating properties which define the topological nature of the model. Similar to the Kane-Mele-Hubbard model, the onsite Coulomb repulsion can be modelled with a Hubbard term. We focus on the correlation along the edge of the model on a ribbon geometry and adress the effects of interactions by a bosonization analysis and by a quantum Monte Carlo study of the edge. This chapter partly reproduces results that have been published in Ref. [150].

6.1 π Kane-Mele-Hubbard model

Based on the KM model (1.13), we can construct a new model, referred to as the π *Kane-Mele model* (πKM model) by inserting a magnetic flux $\pm\pi$ into each hexagon of the underlying honeycomb lattice. As illustrated in Fig. 6.1, such an arrangement of fluxes of size $\pm\pi$ (in units of $\hbar = c = e = 1$) leads to a model with a unit cell consisting of two hexagons.

For each spin projection σ, the Hamiltonian takes the form of a modified Haldane model (1.10),

$$\mathcal{H}^{\sigma} = -\sum_{\langle \boldsymbol{i},\boldsymbol{j}\rangle} \left[t(\boldsymbol{i},\boldsymbol{j}) - \mu\delta_{\boldsymbol{i}\boldsymbol{j}}\right] \hat{c}^{\dagger}_{\boldsymbol{i},\sigma}\hat{c}_{\boldsymbol{j},\sigma} + i\sigma \sum_{\langle\langle \boldsymbol{i},\boldsymbol{j}\rangle\rangle} \lambda(\boldsymbol{i},\boldsymbol{j})\nu_{\boldsymbol{i},\boldsymbol{j}}\hat{c}^{\dagger}_{\boldsymbol{i},\sigma}\hat{c}_{\boldsymbol{j},\sigma} \,. \tag{6.1}$$

Here, $t(\boldsymbol{i},\boldsymbol{j}) = t\tau_{\boldsymbol{i},\boldsymbol{j}}$ and $\lambda(\boldsymbol{i},\boldsymbol{j}) = \lambda\tau_{\boldsymbol{i},\boldsymbol{j}}$ are the nearest-neighbor and next-nearest-neighbor hopping parameters, respectively; $\boldsymbol{i},\boldsymbol{j}$ index both lattice and orbital sites and μ is the chemical potential. The phase factor $\nu_{\boldsymbol{i},\boldsymbol{j}}$ has been defined in Sec. 1.2.1.

As discussed in Sec. 4.1, the additional, nonuniform hopping phase factors $\tau_{\boldsymbol{i},\boldsymbol{j}} = \pm 1$ account for the presence of the π fluxes. Due to the geometry of the four-orbital unit cell (Fig. 6.1), two gauges exist, i.e. distribution of phase factors, which have unitarily equivalent Hamiltonians. On a torus geometry, Hamiltonian (6.1) becomes

$$\mathcal{H}^{\sigma} = \sum_{\boldsymbol{k}} c^{\dagger}_{\boldsymbol{k},\sigma} H^{\sigma}(\boldsymbol{k}) c_{\boldsymbol{k},\sigma} \,, \tag{6.2}$$

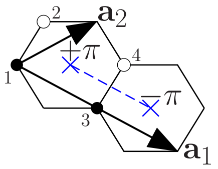

Figure 6.1: The unit cell of the π flux honeycomb lattice has four orbitals and is defined by the lattice vectors $\boldsymbol{a}_1 = (3, -\sqrt{3})$ and $\boldsymbol{a}_2 = (3/2, \sqrt{3}/2)$. Each honeycomb plaquette carries a magnetic flux $\pm\pi$. The flux positions are fixed by requiring that hopping terms crossing the dashed blue line (which is a gauge choice) acquire a phase of -1.

$d_1(\boldsymbol{k}) = -t\cos(\boldsymbol{k}\boldsymbol{a}_2)$	$d^{\sigma}_{12}(\boldsymbol{k}) = t\sin(\boldsymbol{k}\boldsymbol{a}_2)$
$d_3(\boldsymbol{k}) = -\frac{t}{2}\big[\sin(\boldsymbol{k}\boldsymbol{a}_2) - \sin(\boldsymbol{k}(\boldsymbol{a}_1 - \boldsymbol{a}_2))\big]$	$d^{\sigma}_{13}(\boldsymbol{k}) = -2\sigma\lambda\sin(\boldsymbol{k}\boldsymbol{a}_1/2)\cos(\boldsymbol{k}\boldsymbol{a}_1/2)$
$d_4(\boldsymbol{k}) = -\frac{t}{2}\big[\cos(\boldsymbol{k}(\boldsymbol{a}_1 - \boldsymbol{a}_2)) - \cos(\boldsymbol{k}\boldsymbol{a}_2)\big]$	$d^{\sigma}_{14}(\boldsymbol{k}) = -2\sigma\lambda\sin^2(\boldsymbol{k}\boldsymbol{a}_1/2)$
$d_{25}(\boldsymbol{k}) = t$	$d^{\sigma}_{15}(\boldsymbol{k}) = 2\sigma\lambda\sin(\boldsymbol{k}\boldsymbol{a}_2)$
$d^{\sigma}_{23}(\boldsymbol{k}) = t\cos(\boldsymbol{k}\boldsymbol{a}_1/2)\cos(\boldsymbol{k}(\boldsymbol{a}_1/2 - \boldsymbol{a}_2))$	$d^{\sigma}_{24}(\boldsymbol{k}) = \frac{t}{2}\big[\sin(\boldsymbol{k}(\boldsymbol{a}_1 - \boldsymbol{a}_2)) + \sin(\boldsymbol{k}\boldsymbol{a}_2)\big]$
$d^{\sigma}_{35}(\boldsymbol{k}) = 2\sigma\lambda\cos(\boldsymbol{k}\boldsymbol{a}_1/2)\cos(\boldsymbol{k}(\boldsymbol{a}_1/2 - \boldsymbol{a}_2))$	$d^{\sigma}_{45}(\boldsymbol{k}) = 2\sigma\lambda\cos(\boldsymbol{k}(\boldsymbol{a}_1/2 - \boldsymbol{a}_2))\sin(\boldsymbol{k}\boldsymbol{a}_1/2)$

Table 6.1: Nonzero coefficients $d_a(\boldsymbol{k})$ and $d^{\sigma}_{ab}(\boldsymbol{k})$ of Eq. (6.3).

where $c_{\boldsymbol{k},\sigma} = (\hat{c}_{1,\boldsymbol{k},\sigma}, \hat{c}_{3,\boldsymbol{k},\sigma}, \hat{c}_{2,\boldsymbol{k},\sigma}, \hat{c}_{4,\boldsymbol{k},\sigma})^T$ is the basis in which the nearest-neighbor (t) term is block off-diagonal. The Hamilton matrix $H^{\sigma}(\boldsymbol{k})$ can be expressed in terms of Dirac Γ matrices [22], $\Gamma^{(1,2,3,4,5)} = (\sigma_x \otimes \mathbf{1}, \sigma_z \otimes \mathbf{1}, \sigma_y \otimes \sigma_x, \sigma_y \otimes \sigma_y, \sigma_y \otimes \sigma_z)$ and their commutators $\Gamma^{ab} = [\Gamma^a, \Gamma^b]/(2i)$:

$$H^{\sigma}(\boldsymbol{k}) = \mu\mathbf{1} + \sum_{a=1}^{5} d_a(\boldsymbol{k})\Gamma^a + \sum_{a<b=1}^{5} d^{\sigma}_{ab}(\boldsymbol{k})\Gamma^{ab}\,. \tag{6.3}$$

The non-vanishing coefficients $d_a(\boldsymbol{k})$ and $d^{\sigma}_{ab}(\boldsymbol{k})$ are given in Table 6.1. As for the KM model, a spinful and time-reversal invariant Hamiltonian results by combining $\mathcal{H}^{\uparrow}$ and $\mathcal{H}^{\downarrow}$; λ then plays the role of an intrinsic spin-orbit coupling. Including the $U(1)$ spin symmetry breaking Rashba term (1.12), the πKM model is

$$\mathcal{H}_0 = -\sum_{\langle \boldsymbol{i},\boldsymbol{j}\rangle} t(\boldsymbol{i},\boldsymbol{j}) c^{\dagger}_{\boldsymbol{i}} c_{\boldsymbol{j}} + \mu\sum_{\boldsymbol{i}} c^{\dagger}_{\boldsymbol{i}} c_{\boldsymbol{i}} + i\sum_{\langle\langle \boldsymbol{i},\boldsymbol{j}\rangle\rangle} \lambda(\boldsymbol{i},\boldsymbol{j}) c^{\dagger}_{\boldsymbol{i}} \nu_{\boldsymbol{i}\boldsymbol{j}} \sigma_z c_{\boldsymbol{j}} + \frac{i}{2}\sum_{\langle \boldsymbol{i},\boldsymbol{j}\rangle} \lambda_{\mathrm{R}}(\boldsymbol{i},\boldsymbol{j}) c^{\dagger}_{\boldsymbol{i}} \left[\boldsymbol{e}_z(\boldsymbol{\sigma} \times \boldsymbol{d}_{\boldsymbol{i}\boldsymbol{j}})\right] c_{\boldsymbol{j}}\,, \tag{6.4}$$

where $c^{\dagger}_{\boldsymbol{i}} = (\hat{c}^{\dagger}_{\boldsymbol{i},\uparrow}, \hat{c}^{\dagger}_{\boldsymbol{i},\downarrow})$ and $\lambda_{\mathrm{R}}(\boldsymbol{i},\boldsymbol{j}) = \lambda_{\mathrm{R}}\tau_{\boldsymbol{i}\boldsymbol{j}}$. Similarly to Eq. (4.13), the Hamiltonian of the π *Kane-Mele-Hubbard* (π*KMH*) model is

$$\mathcal{H} = \mathcal{H}_0 + \mathcal{H}_{\mathrm{U}}\,. \tag{6.5}$$

6.2 Bulk properties of the πKM model

In this section, we discuss the band structure and the topological phases of the noninteracting model (6.2), corresponding to one spin sector of the πKM model. Subsequently, we show that the spinful πKM model (6.4) is Z_2 trivial at half filling.

6.2.1 Band structure

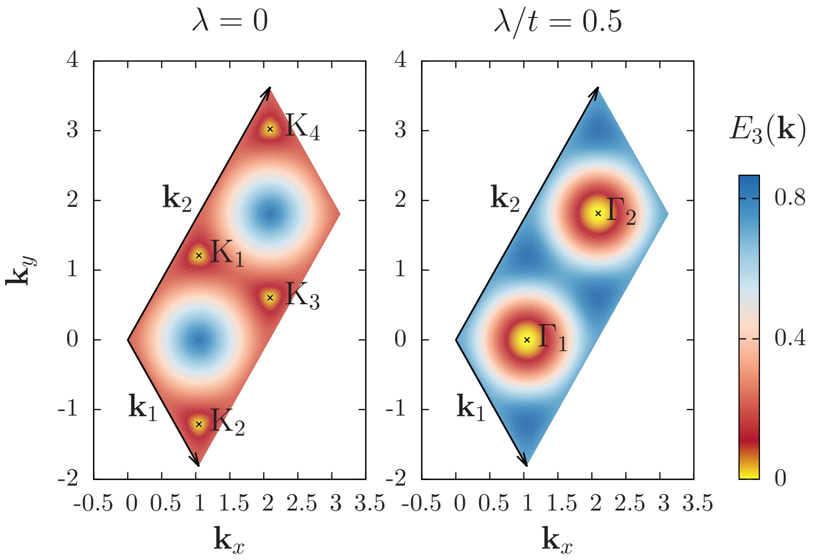

Figure 6.2: Contour plot of the lowest positive eigenvalue $E_3(\boldsymbol{k})$ in the Brillouin zone, which is spanned by the reciprocal vectors $\boldsymbol{k}_1 = 2\pi(1/6, -1/(2\sqrt{3}))$ and $\boldsymbol{k}_2 = 2\pi(1/3, 1/\sqrt{3})$. For $\lambda = 0$, $E_3(\boldsymbol{k})$ is zero at the Dirac points at $\boldsymbol{k} = \boldsymbol{K}_{1,2,3,4}$, whereas for $\lambda/t = 0.5$, $E_3(\boldsymbol{k})$ is zero at the quadratic band touching points, $\boldsymbol{k} = \boldsymbol{\Gamma}_{1,2}$. Here, $\lambda_{\mathrm{R}} = 0$.

The band structure is established by the eigenvalues of Eq. (6.2) which are, for $\mu = 0$, given by

$$E_m(\boldsymbol{k}) = \pm\Big\{3t^2 + 6\lambda^2 - 2\lambda^2 f(\boldsymbol{k}) \pm t\sqrt{2\big[3\big(t^2+8\lambda^2\big) + \big(t^2 - 16\lambda^2\big) f(\boldsymbol{k})\big]}\ \Big\}^{1/2}, \qquad (6.6)$$

where $f(\boldsymbol{k}) = \cos(\boldsymbol{k}\boldsymbol{a}_1) + \cos(2\boldsymbol{k}\boldsymbol{a}_2) - \cos[\boldsymbol{k}(2\boldsymbol{a}_2 - \boldsymbol{a}_1)]$. At $\lambda = 0$, $\mathcal{H}^\sigma$ has four distinct Dirac points $\boldsymbol{K}_i$ with linear dispersion at zero energy,

$$E(\boldsymbol{K}_i + \boldsymbol{k}) = \sqrt{\frac{3}{2}}\,t\,(k_x + k_y) + \mathcal{O}(k^2)\ , \qquad (6.7)$$

where $\boldsymbol{K}_{1,2} = (\pi/3)(1, \pm 2/\sqrt{3})$, $\boldsymbol{K}_3 = (\pi/3)(2, 5/\sqrt{3})$ and $\boldsymbol{K}_4 = (\pi/3)(2, 1/\sqrt{3})$. At $\lambda/t = 1/2$, the spectral gap closes quadratically at two points $\boldsymbol{\Gamma}_i$,

$$E(\boldsymbol{\Gamma}_i + \boldsymbol{k}) = \frac{3\sqrt{3}}{4}\,t\,\big(k_x^2 + k_y^2\big) + \mathcal{O}(k^4)\ , \qquad (6.8)$$

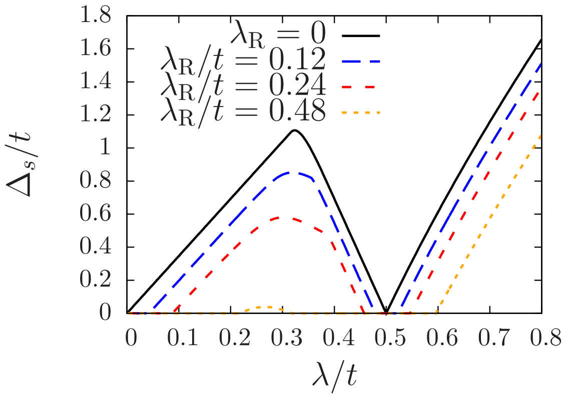

Figure 6.3: Single-particle gap $\Delta_s(\lambda)$ for different values of the Rashba interaction λ_{R}.

where $\mathbf{\Gamma}_1 = (\pi/3)(1,0)$ and $\mathbf{\Gamma}_2 = (\pi/3)(2,\sqrt{3})$ (Fig. 6.2). For the spinful model (6.4) with nonzero Rashba coupling, the point of quadratic band crossing is replaced by a finite region with zero band gap (Fig. 6.3).

6.2.2 Quantized Hall conductivity

In the following, we consider the Chern insulator which is defined by $H^\sigma(\boldsymbol{k})$, see Eq. (6.2). The response of the insulator to an external electromagnetic field will reveal the topological properties of its band structure. This response is the optical conductivity tensor. Here we state the result of the linear response calculation which is derived in Appendix A. In linear response to an external vector potential, we obtain the optical conductivity tensor of a general, n-band system which is described by the non-interacting Hamilton matrix $H^\sigma(\boldsymbol{k})$,

$$\sigma^\sigma_{\alpha,\beta}(\omega) = \frac{1}{N}\frac{(e/\hbar)^2}{i(\omega+i0^+)}\left[\langle K^\sigma_\alpha\rangle\delta_{\alpha,\beta} - \Lambda^\sigma_{\alpha,\beta}(\omega)\right] \ , \tag{6.9}$$

where

$$\begin{aligned}
\langle K^\sigma_\alpha\rangle &= \sum_{\boldsymbol{k},n} f[E^\sigma_n(\boldsymbol{k})]\mathrm{Tr}[K^\sigma_\alpha(\boldsymbol{k})P^\sigma_n(\boldsymbol{k})] \ , \\
\Lambda^\sigma_{\alpha,\beta}(\omega) &= \sum_{\boldsymbol{k},m,n} \lambda^\sigma_{mn}(\boldsymbol{k},\omega)\mathrm{Tr}[J^\sigma_\alpha(\boldsymbol{k})P^\sigma_n(\boldsymbol{k})J^\sigma_\beta(\boldsymbol{k})P^\sigma_m(\boldsymbol{k})] \ , \\
\lambda^\sigma_{mn}(\boldsymbol{k},\omega) &= \frac{f[E^\sigma_m(\boldsymbol{k})] - f[E^\sigma_n(\boldsymbol{k})]}{\omega + i0^+ + E^\sigma_m(\boldsymbol{k}) - E^\sigma_n(\boldsymbol{k})} \ .
\end{aligned} \tag{6.10}$$

The following matrix quantities have been introduced: the current $J^\sigma_\alpha(\boldsymbol{k}) = \partial H^\sigma(\boldsymbol{k})/\partial k_\alpha$, the kinetic energy $K^\sigma_\alpha(\boldsymbol{k}) = -\partial^2 H^\sigma(\boldsymbol{k})/\partial k^2_\alpha$ and the projector on the n-th band $P^\sigma_n(\boldsymbol{k})$. The Fermi function is $f[E^\sigma_n(\boldsymbol{k})]$.

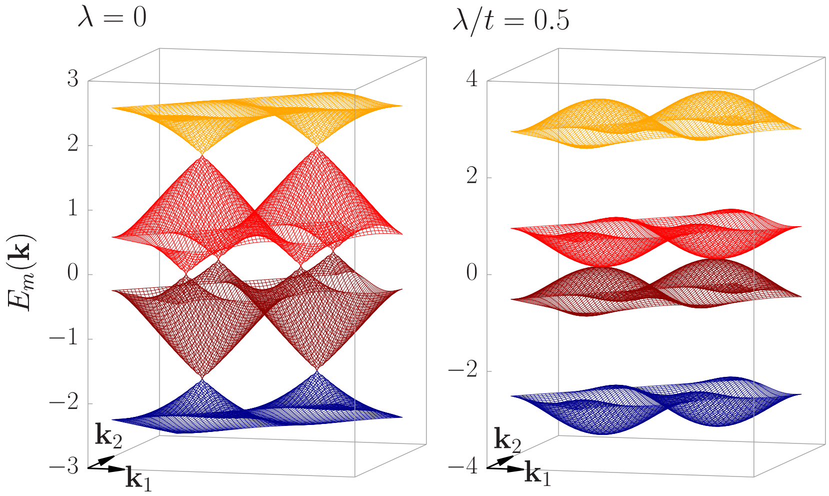

Figure 6.4: The eigenvalue spectrum $E_m(\boldsymbol{k})$ of $\mathcal{H}^\sigma$ [Eq. (6.1)] has four Dirac cones at $\lambda = 0$, and two points of quadratic band crossing at $\lambda/t = 0.5$.

The Hall conductivity is then computed by taking the zero-frequency limit of the optical conductivity,

$$\lim_{\omega \to 0} \mathrm{Re}\left[\sigma^\sigma_{xy}(\omega)\right] = \sigma^\sigma_{xy} = \left[\sum_{n=1}^{N_{\mathrm{occ}}} C^\sigma_n\right] \frac{e^2}{h} \,. \tag{6.11}$$

It directly measures the (first) Chern number C^σ of the gap, which is the sum of the Chern numbers C^σ_n of the N_{occ} occupied bands. Figure 6.5 shows the Chern number as a function of the chemical potential μ and the ratio t_2/t_1. Transitions between different Chern insulators are topological phase transitions and necessarily involve an intermediate metallic state where the Chern number can in principle take any value. Of particular interest for the understanding of correlation-induced instabilities is the transition at $\mu = 0$ as a function of t_2/t_1 between the states with $C^\sigma = \pm 2$. At $t_2/t_1 = 1/2$, we find a a quadratic band crossing point with a nonzero density of states.

For the spinful model (6.4) with $U = 0$ and a $U(1)$ spin symmetry ($\lambda_{\mathrm{R}} = 0$), one can define a quantized spin Hall conductivity σ^s_{xy} in terms of the Hall conductivity σ^σ_{xy} of $\mathcal{H}^\sigma$ (6.2). At $\mu = 0$, σ^σ_{xy} and σ^s_{xy} take the values

$$\sigma^\sigma_{xy} = \mp\sigma 2\frac{e^2}{h} \,, \quad \sigma^s_{xy} = \frac{\hbar}{2e}\left(\sigma^\uparrow_{xy} - \sigma^\downarrow_{xy}\right) = \mp 2\frac{e}{2\pi} \,. \tag{6.12}$$

The sign change occurs at the quadratic band crossing point at $\lambda/t = \lambda_0 = 1/2$.

6.2.3 Topological Z_2 invariant

In the general case where the $U(1)$ spin symmetry is broken, for example by the presence of a Rashba term, the topological properties of a system with time-reversal symmetry are determined by the Z_2 topological invariant [23]. However, the actual computation of the invariant

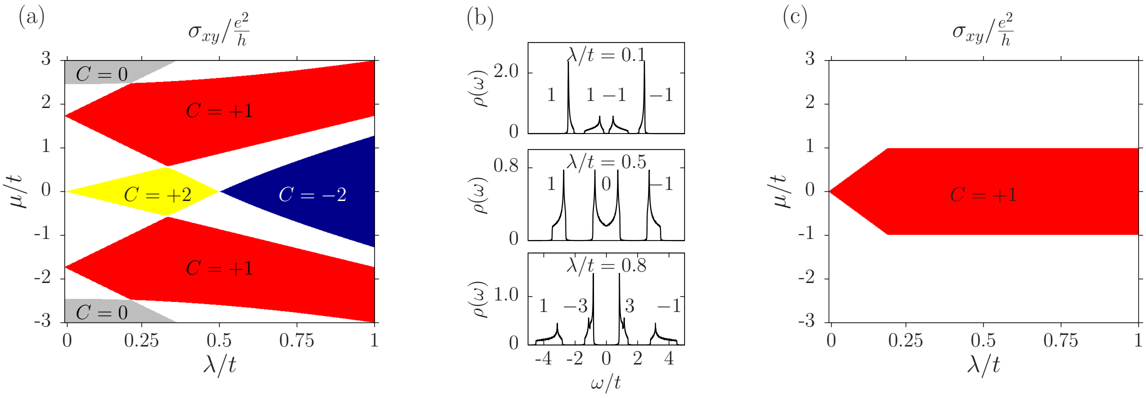

Figure 6.5: (a) Total Chern number $C^{\downarrow} = \sum_n C_n^{\downarrow}$ of the occupied bands of $\mathcal{H}^{\downarrow}$ [Eq. (6.1)], as obtained from the Hall conductivity $\sigma_{xy}^{\downarrow}$ in the insulating phases which are separated by metallic regions (white). (b) Density of states $\rho(\omega) = (1/4N)\sum_{\boldsymbol{k},n}\delta(\omega - E_n(\boldsymbol{k}))$ and Chern numbers C_n of the individual bands. (c) Same calculation as in (a), but for the model without external fluxes, i.e. the plain Kane-Mele model.

is a difficult task, already at the level of a tight-binding Hamiltonian. This difficulty can be traced back to the Bloch functions in the Brillouin zone which are only defined up to a k-dependent phase. Time-reversal symmetry guarantees that a globally smooth gauge of the Bloch functions exist but there is no general recipe to find this gauge. A finite Chern number is an obstruction to the existence of a globally smooth gauge but, due to time-reversal invariance, the Chern number is zero [31]. An comprehensive overview over the various methods is given in Ref [32]. Recently, it has been shown that the Z_2 index can be calculated in two and three dimensions with a manifestly gauge-independent method that only relies on time-reversal symmetry [32; 151]. In this section, we provide a brief review of the method.

We start with a general gapful, time-reversal symmetric Hamiltonian $\mathcal{H} = \sum_{\boldsymbol{k}} \boldsymbol{c}^{\dagger} H(\boldsymbol{k}) \boldsymbol{c}$,

$$\theta H(\boldsymbol{k}) \theta^{-1} = H(-\boldsymbol{k}) \, , \tag{6.13}$$

where θ is the time-reversal operator. For the implementation of the method it is necessary to set up the Hamiltonian matrix $H(\boldsymbol{k})$ on a rectangular unit cell, i.e. $\boldsymbol{k}_i = 2\pi/a_i \hat{\boldsymbol{e}}_i$ with $i = x, y$. The projector $P_{\boldsymbol{k}}$ on the occupied eigenstates $|u_i(\boldsymbol{k})\rangle$ of the Hamiltonian is

$$P_{\boldsymbol{k}} = \sum_i |u_i(\boldsymbol{k})\rangle\langle u_i(\boldsymbol{k})| \, , \tag{6.14}$$

which is a gauge invariant quantity.

The method relies on examining the full non-abelian adiabatic transport along time-reversal invariant lines in the Brillouin zone. The idea is to consider the adiabatic change of one component of the reciprocal lattice vector, say k_y, along high-symmetry paths $k_y \in (k, k')$ in a rectangular Brillouin zone, while keeping the other component (k_x) fixed. This process is determined by the unitary evolution operator (the monodromy) $U_{k,k'}$ and its differential equation

$$i\frac{\mathrm{d}}{\mathrm{d}k}U_{k,k'} = i\left[P_k, \partial_k P_k\right] U_{k,k'} \ . \tag{6.15}$$

The initial condition is $U_{k',k'} = P_{k'}$. Equation (6.15) is integrated by evenly discretizing the path (k, k'),

$$U_{k,k'} = \lim_{N\to\infty} \prod_{n=1}^{N} P_{k'+k\frac{n-1}{N-1}} \ . \tag{6.16}$$

We define two paths in the Brillouin zone. On path (1), $k_y \in [0, \pi]$, whereas on path (2), $k_y \in [-\pi, \pi]$. k_x takes the values $k_x = 0, \pi$. Since we vary the k_y component while keeping k_x fixed, we write

$$U_{k_x,k\,;\,k_x,k'} = U_{k,k'} \ , \tag{6.17}$$

and define the matrices $v^{(1)}(\boldsymbol{k})$ and $v^{(2)}(\boldsymbol{k})$ by

$$\begin{aligned} v^{(1)}_{ij}(k_x) &= \langle u_i(k_x,\pi)|U_{(k_x,\pi\,;\,k_x,0)}|u_j(k_x,0)\rangle \\ v^{(2)}_{ij}(k_x) &= \langle u_i(k_x,\pi)|U_{(k_x,\pi\,;\,k_x,-\pi)}|u_j(k_x,\pi)\rangle \ . \end{aligned} \tag{6.18}$$

Furthermore, we define the unitary matrix $w(\boldsymbol{k})$,

$$w_{ij}(\boldsymbol{k}) = \langle u_i(-\boldsymbol{k})|\theta|u_j(\boldsymbol{k})\rangle \ . \tag{6.19}$$

Importantly, $w(\boldsymbol{k})$ is antisymmetric [31] at the four time-reversal invariant momenta Γ_i. Therefore, one can define a Pfaffian at these momenta, which satisfies $\mathrm{Pf}[w(\Gamma_i)]^2 = \det[w(\Gamma_i)]$.

The main conclusion of Prodan's derivation (see Ref. [32]) is the one-dimensional pseudo-invariant

$$\frac{\mathrm{Pf}[w(k_x,0)]}{\mathrm{Pf}[w(k_x,\pi)]}\frac{\det[v^{(1)}(k_x)]}{\sqrt{\det[v^{(2)}(k_x)]}} = \pm 1 \ , \tag{6.20}$$

where $k_x = 0, \pi$. The sign depends on the branch of $\sqrt{\det[v^{(2)}(k_x)]}$. However, once we have made a choice, the sign of Eq. (6.20) cannot change under smooth perturbations of the Hamiltonian. The topological invariant Ξ_{2D} is then given as the product of both pseudo-invariants:

$$\Xi_{\mathrm{2D}} = \pm 1 = \prod_{k_x=0,\pi} \frac{\mathrm{Pf}[w(k_x,0)]}{\mathrm{Pf}[w(k_x,\pi)]}\frac{\det[v^{(1)}(k_x)]}{\sqrt{\det[v^{(2)}(k_x)]}} \ . \tag{6.21}$$

The invariant is computed numerically [152], by discretizing the paths with ~ 1000 steps. The complex function $f[z(k_x)] = \sqrt{z(k_x)}$ is multivalued for a given value of the argument $z(k_x) \in \mathbb{C}$. In our case, $z(k_x) = \det[v^{(2)}(k_x)]$. To resolve this ambiguity, we evaluate $f[z(k_x)]$ always on the top Riemann sheet and compute $z(k_x)$ along the (discretized) path $k_x = [0, \pi]$ to determine the number N_{cross} which counts the number of crossing of $z(k_x)$ with the branch cut at $(-\infty, 0]$. The invariant is then given by

$$\Xi_{\mathrm{2D}} = \Xi_{\mathrm{2D}}\Big|_{\sqrt{z(k_x)}\text{ on top Riemann sheet}} \times (-1)^{N_{\mathrm{cross}}} \ . \tag{6.22}$$

For the πKM model (6.4) at half filling ($\mu = 0$) we obtain, as expected, a trivial insulator ($\Xi_{2\mathrm{D}} = +1$). In contrast, if the chemical potential lies in the lower (upper) band gap, i.e., at quarter (three-quarter) filling, we obtain a quantum spin Hall insulator ($\Xi_{2\mathrm{D}} = -1$).

It is interesting to consider how other bulk probes for the Z_2 index lead to the conclusion of a trivial insulating state at half filling. For example, the Z_2 index can be probed by looking at the response to a magnetic π flux [38; 37; 145]. In the quantum spin Hall state, threading a δ-function π flux through the lattice amounts to generating a Kramers pair of states located at the middle of the gap. Provided that the particle number is kept constant during the adiabatic pumping of the π flux, these mid-gap states give rise to a Curie law in the uniform spin susceptibility. This signature of the quantum spin Hall state has been detected in Ref. [145] in the presence of correlations. For the half-filled πKM model, the insertion of a π flux leads to a pair of Kramers degenerate states which form bonding and anti-bonding combinations and thereby cut off the Curie law at energy scales below the bonding-anti-bonding gap.

6.3 Bulk correlation effects

We begin our analysis of the effect of electron-electron interactions by considering the πKMH model (6.5) on a torus geometry. In order to compare our mean-field predictions to quantum Monte Carlo results, we set the Rashba spin-orbit coupling and the chemical potential to zero. The πKMH model then is at the particle-hole symmetric point and takes the form

$$\mathcal{H} = \mathcal{H}_0 + U \sum_{\boldsymbol{i}} (\hat{n}_{\boldsymbol{i}\uparrow} - 1/2)(\hat{n}_{\boldsymbol{i}\downarrow} - 1/2)\ . \tag{6.23}$$

The KMH model without additional π fluxes is known to exhibit long-range, transverse antiferromagnetic order at large values of U/t [52; 153; 154; 155].

We therefore decouple the Hubbard term in Eq. (6.23) in the spin sector, allowing for an explicit breaking of time-reversal symmetry. The mean-field Hamiltonian reads

$$\mathcal{H}_{\mathrm{mf}} = \mathcal{H}_0 - \frac{2U}{3} \sum_{\boldsymbol{i}} \left(2\hat{S}_{\boldsymbol{i}} \langle \hat{S}_{\boldsymbol{i}} \rangle - \langle \hat{S}_{\boldsymbol{i}} \rangle^2 \right) + \frac{UN}{2}\ , \tag{6.24}$$

where $\mathcal{H}_0$ is given by Eq. (6.4) with $\lambda_{\mathrm{R}} = 0$, and $\hat{S}_{\boldsymbol{i}} = (\hat{S}^x_{\boldsymbol{i}}, \hat{S}^y_{\boldsymbol{i}}, \hat{S}^z_{\boldsymbol{i}})$. Assuming antiferromagnetic order, we make the ansatz $\langle \hat{S}_{\boldsymbol{i}} \rangle = S_{\mathrm{mf},\boldsymbol{i}}$ and

$$\begin{array}{rcl} S^x_{\mathrm{mf},\boldsymbol{i}} & = & \nu_{\boldsymbol{i}}\, m\ ,\ \ S^{y,z}_{\mathrm{mf},\boldsymbol{i}} = 0\ , \\ S^x_{\mathrm{mf},\boldsymbol{i}} & = & \dfrac{1}{Z}\dfrac{1}{2} \displaystyle\sum_{s,s'} \mathrm{Tr}\left[e^{-\beta \mathcal{H}_{\mathrm{mf}}\{S^x_{\mathrm{mf},\boldsymbol{i}}\}} \hat{c}^{\dagger}_{\boldsymbol{i},s} \sigma_x \hat{c}_{\boldsymbol{i},s'} \right]\ , \end{array} \tag{6.25}$$

where $\nu_{\boldsymbol{i}} = +1$ ($\nu_{\boldsymbol{i}} = -1$) if $\boldsymbol{i}$ indexes the orbitals $1, 3$ ($2, 4$). Equation (6.25) is solved self-consistently, resulting in the phase diagram shown in Fig. 6.6(a). We find a magnetic phase with transverse antiferromagnetic order above a critical value of U/t which depends on λ/t. In particular, at the quadratic band crossing point ($\lambda_0 = 0.5$), the magnetic transition occurs

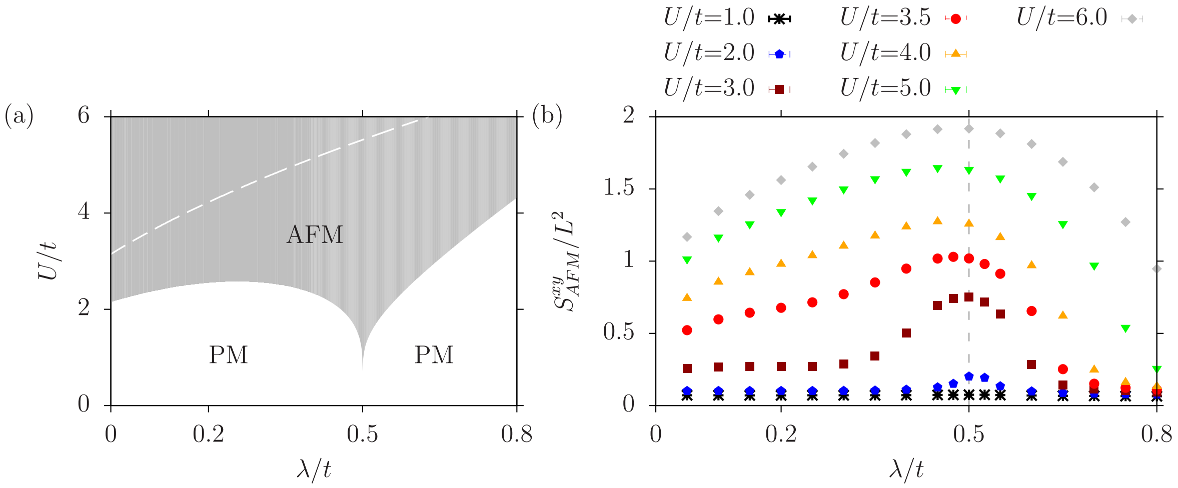

Figure 6.6: (a) Phase diagram of the mean-field Hamiltonian (6.24), showing the existence of a magnetically order phase with xy magnetic order above a critical value U_c that depends on the spin-orbit coupling λ. For $\lambda/t = 0.5$, where the model has a quadratic band crossing point, magnetic order exists for any nonzero value of U_c. The dashed line denotes the magnetic phase boundary for the plain KMH model. (b) Transverse magnetic structure factor S^{xy}_{AFM} of the model (6.5) for different values U/t, as obtained from quantum Monte Carlo simulations of the πKMH model on a 6×6 lattice with periodic boundary conditions and at inverse temperature $\beta t = 40$.

at infinitesimal values of U/t as a result of the Stoner instability associated with the nonvanishing density of states at the Fermi level. By tuning the system away from the quadratic band crossing point, the critical interaction increases.

The πKMH lattice model (6.23) can be studied efficiently using the auxiliary-field determinant quantum Monte Carlo method (see Sec. 2.1), since simulations are free of a sign problem given particle-hole, time-reversal and $U(1)$ spin symmetry [153; 154; 49]. This requirement excludes the $U(1)$ spin symmetry breaking Rashba term.

To study the magnetic phase diagram of the πKMH model (6.23), we apply an implementation of the BSS-QMC discussed in Sec. 2.1.5. The Trotter discretization has been chosen as $\Delta\tau t = 0.1$. An inverse temperature $\beta t = 40$ has been sufficient to obtain converged results.

The observable we are interested in is the transverse antiferromagnetic structure factor,

$$S^{xy}_{\mathrm{AFM}} = \frac{1}{L^2}\sum_{\boldsymbol{i},\boldsymbol{j}}(-1)^{\nu_i+\nu_j}\langle \hat{S}^+_{\boldsymbol{i}}\hat{S}^-_{\boldsymbol{j}} + \hat{S}^-_{\boldsymbol{i}}\hat{S}^+_{\boldsymbol{j}}\rangle \tag{6.26}$$

calculated as a function of the interaction U and the spin-orbit coupling λ. Simulations were done on a 6×6 π-flux honeycomb lattice (equivalent to 72 honeycomb plaquettes).

As shown in Fig 6.6(b), for small U/t, the structure factor has a clear maximum close to λ_0, where the weak-coupling magnetic instability is observed in mean-field theory. At larger values of U/t, the maximum becomes less pronounced, and the enhancement of S^{xy}_{AFM} for all values of λ/t is compatible with the existence of a magnetic phase for all λ/t at large U/t. These numerical results seem to confirm the overall features of the mean-field phase diagram. The numerical determination of the exact phase boundaries from a systematic finite-size scaling is left for future work.

6.4 Edge states of the πKM model

We now consider the edge states of the noninteracting πKM model (6.4) on a zigzag ribbon with open (periodic) boundary conditions in the $\boldsymbol{a}_1$ ($\boldsymbol{a}_2$) direction [Fig. 6.7(a)], and with momentum $k = \boldsymbol{k}\cdot\boldsymbol{a}_2$ along the edge. Since the model is Z_2 trivial, we expect an even number of edge modes to traverse the bulk gap. Furthermore, given the spin Chern number $\sigma^s_{xy}/(e/2\pi) = \pm 2$ [see Eq. (6.12)], we expect two helical edge modes at half filling. Figure 6.7(b) shows the eigenvalue spectrum with degenerate Kramers doublets at the time-reversal invariant momenta $k = 0$ and $k = \pi$. For $\lambda_0 < \lambda/t < \lambda_\pi$, where $\lambda_\pi = \sqrt{3}/2$, the eigenvalue spectrum of Eq. (6.1) has two additional cones at $k = \pi \pm \delta$. They are unstable in the sense that their existence relies on the $U(1)$ spin symmetry.

The edge modes at $k = 0$ ($k = \pi$) and $\sigma =\uparrow,\downarrow$ can be further characterized by their Fermi velocity v_0 (v_π) and—in the case of a $U(1)$ spin symmetry—by their chirality (the sign of the velocity). The chirality changes at λ_0 and λ_π. For $\lambda/t < \lambda_0$, the edge modes have the same chirality, so that the $(0,\sigma)$ modes propagates in the same direction as the (π,σ) modes. In contrast, for $\lambda_0 < \lambda/t < \lambda_\pi$, they have opposite chirality since the direction of propagation of the $(0,\sigma)$ modes is reversed after going through the point of quadratic band crossing. At

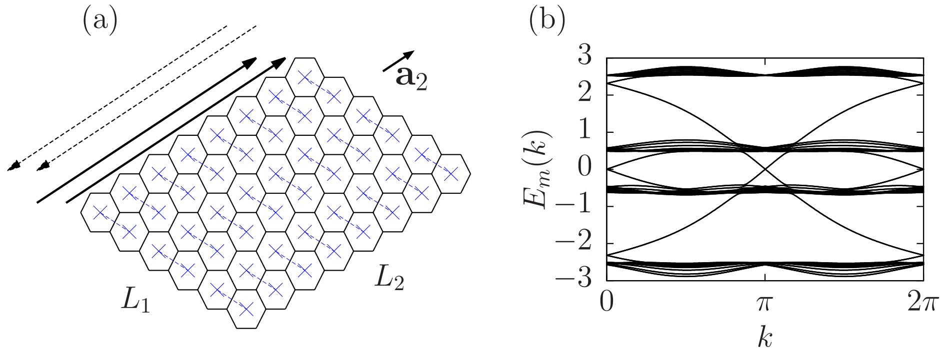

Figure 6.7: (a) Ribbon geometry of the π flux honeycomb lattice. In the spinful case, the edge states consist of two Kramers doublets with Fermi velocities v_0 and v_π. (b) Eigenvalue spectrum $E_m(k)$ of Eq. (6.4) for $\lambda/t = 0.3$ and $\lambda_\mathrm{R}/t = 0.1$ on a zigzag ribbon.

$\lambda/t = \lambda_\pi$, the additional cones at $k = \pi \pm \delta$ merge with the (π, σ) modes. Consequently, the direction of propagation of the (π, σ) modes is reversed and for $\lambda/t > \lambda_\pi$ both edge modes have the same chirality again. In the limit $\lambda/t \to \infty$, v_0 and v_π become equal. Furthermore, the velocities have equal magnitude but opposite sign at $\lambda/t = \lambda_s \approx 0.665$.

To study the edge states, we consider the local single-particle spectral function

$$A_i^\sigma(k,\omega) = -\frac{1}{\pi}\mathrm{Im}\, G_{ii}^\sigma(k,\omega + i0^+)\,, \tag{6.27}$$

where the local noninteracting Green function is

$$G_{ii}^\sigma(k,\omega + i0^+) = \left[\omega + i0^+ - H(k)\right]^{-1}_{i\sigma,i\sigma}\,. \tag{6.28}$$

The edge corresponds to the orbital index $i = 2$ [Fig. 6.4(a)] and for brevity we will omit the index i in the following. A discussion of the charge and the spin structure factor along the edge is included in the Appendix B.

The Fermi velocities v_0 and v_π and the local spectral function are shown in Fig. 6.8 [1]. A similar phase with two helical edge modes at $k = 0, \pi$ has been found in the KM model with additional third-neighbor hopping terms [156].

In the remainder of this section, we concentrate on the low-energy properties of the πKM model (6.4). Furthermore, we focus on the edge modes at the time-reversal invariant momenta $k = 0, \pi$, and neglect the two additional, unstable modes at $k = \pi \pm \delta$ occurring for $\lambda_0 < \lambda/t < \lambda_\pi$ which are gapped out by any finite Rashba coupling. Then, the effective Hamiltonian can be written in terms of right (left) moving fields $R_1(x)$ $[L_1(x)]$ at the Fermi wave vector $k_\mathrm{F}^{(1)} = 0$ and right (left) moving fields $R_2(x)$ $[L_2(x)]$ at $k_\mathrm{F}^{(2)} = \pi$:

$$\mathcal{H} = \int \mathrm{d}x \boldsymbol{\Psi}^\dagger(x) H_\mathrm{edge}(-i\partial_x)\boldsymbol{\Psi}(x)\,, \tag{6.29}$$

---

[1] The color schemes are based on gnuplot-colorbrewer; 10.5281/zenodo.10282.

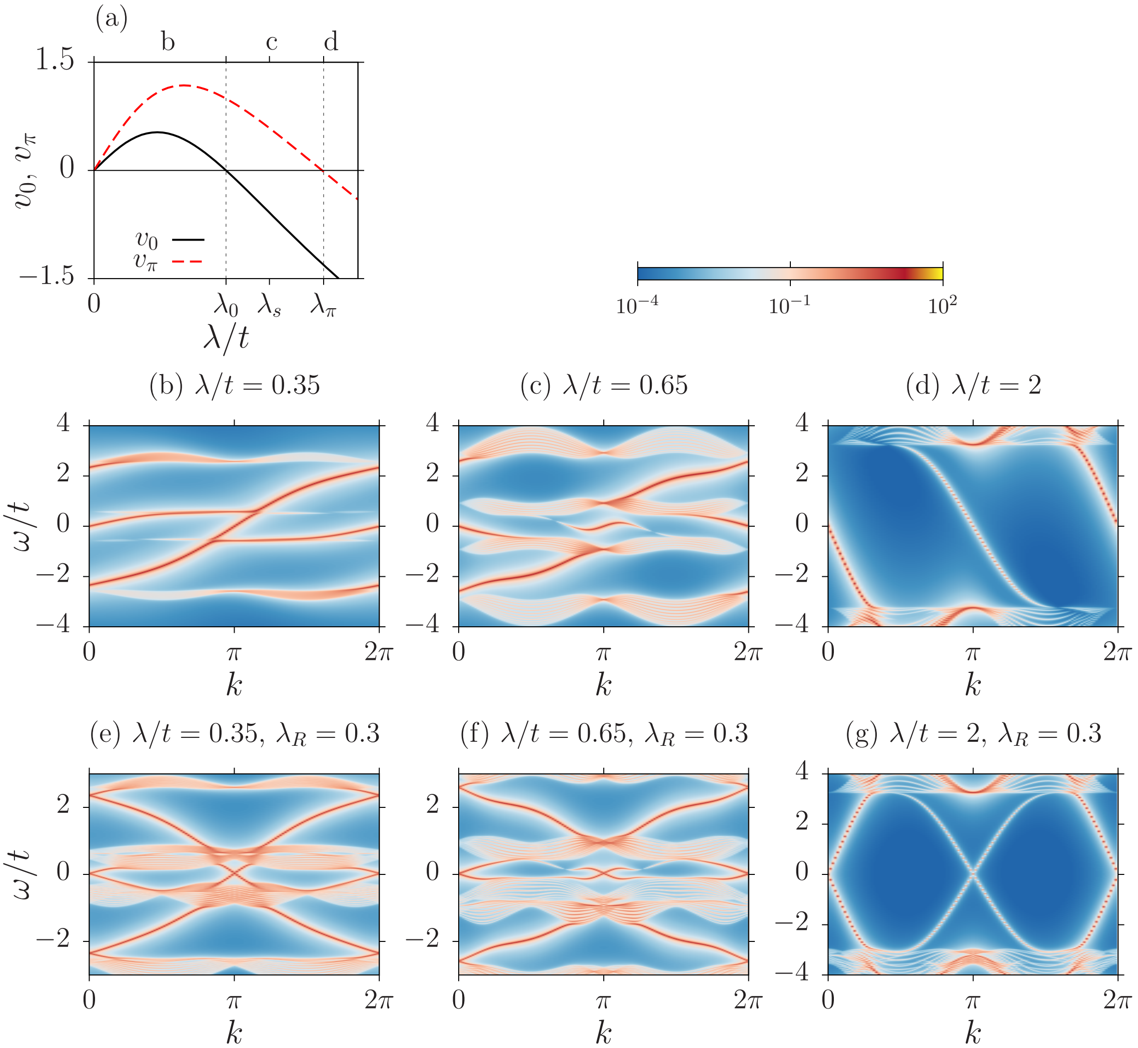

Figure 6.8: (a) The Fermi velocity v_0 (v_π) changes sign at λ_0 (λ_π) so that for $\lambda_0 < \lambda < \lambda_\pi$, the $(0, \sigma)$ and (π, σ) edge modes have opposite chirality. λ_s defines a symmetric point where $v_0 = -v_\pi$ holds. (b)–(d) Single-particle spectral function $A^{\uparrow}(k, \omega)$ along the edge. (e)–(g) Spin-averaged single-particle spectral function $A(k, \omega) = \sum_\sigma A^\sigma(k, \omega)/2$ along the edge. Here, $\lambda_{\mathrm{R}} = 0$ in (a)–(d), and $\lambda_{\mathrm{R}}/t = 0.3$ in (e)–(g).

where $\mathbf{\Psi}^\dagger(x) = (R_1^\dagger(x), L_1^\dagger(x), R_2^\dagger(x), L_2^\dagger(x))$. The chiral fields have the anti-commutation relations

$$\begin{aligned} \{R_i(x), R_j^\dagger(x')\} &= \{L_i(x), L_j^\dagger(x')\} = \delta_{ij}\delta(x-x') \, , \\ \{R_i(x), L_j^\dagger(x')\} &= \{L_i(x), R_j^\dagger(x')\} = 0 \, . \end{aligned} \tag{6.30}$$

In the $U(1)$ spin symmetric case, we have

$$H_{\mathrm{edge}}(-i\partial_x) = -i\partial_x \, \mathrm{diag}(v_1, v_2) \otimes \sigma_z \, . \tag{6.31}$$

Hamiltonian (6.29) will be the starting point for the bosonization analysis in Sec. 6.5.

6.4.1 Effective low-energy model

The edge of a two-dimensional bulk has two time-reversal invariant momenta, $k = 0$ and $k = \pi$, and therefore several possibilities exist to have two pairs of helical edge states: (i) both Kramers doublets cross at $k = 0$ (or $k = \pi$), (ii) one Kramers doublet crosses at $k = 0$ while the other crosses at $k = \pi$, and (iii) each Kramers doublet has one branch at $-k$ (or $\pi - k$) and its time-reversed branch at $+k$ (or $\pi + k$). In cases (i) and (iii), degenerate states which are not Kramers partners exist at the same momentum and can be mixed by single-particle backscattering. The edge states (i) and (iii) are therefore unstable at the single-particle level. In contrast, the edge states (ii) are stable at the single-particle level if translation symmetry is preserved at the edge, thereby forbidding scattering between states at $k = 0$ and $k = \pi$.

The metallic edge modes of Eq. (6.4) are an instance of case (ii). Given time-reversal symmetry and no interactions, the edge states remain gapless even in the generic case without $U(1)$ spin symmetry as long as translation symmetry and hence the momentum k along the edge is preserved. On the other hand, the states acquire a gap when time-reversal symmetry is broken. This is the case in the presence of, for example, a Zeeman term that also breaks the $U(1)$ spin symmetry.

To illustrate this point, we consider the most general time-reversal symmetric formulation of the model (6.29) in momentum space. Let $R_i^\dagger(p)$ $[L_i^\dagger(p)]$ create an electron with velocity v_i $[-v_i]$ (where $v_1 \equiv v_0$ and $v_2 \equiv v_\pi$) and momentum $k = p + (i-1)\pi$. Then, Eq. (6.29) reads

$$\mathcal{H} = \sum_p \mathbf{\Psi}^\dagger(p) H_{\mathrm{edge}}(p) \mathbf{\Psi}(p) \, , \tag{6.32}$$

where $\mathbf{\Psi}^\dagger(p) = (R_1^\dagger(p), L_1^\dagger(p), R_2^\dagger(p), L_2^\dagger(p))$ and

$$H_{\mathrm{edge}}(p) = H_{\mathrm{SO}}(p) + H_{\mathrm{S}} \, , \tag{6.33}$$

where $H_{\mathrm{SO}}(p)$ is a general spin-orbit term and H_{S} a single-particle scattering term. Time-reversal symmetry is preserved when $\Theta H_{\mathrm{edge}}(p)\Theta^{-1} = H_{\mathrm{edge}}(-p)$, where $\Theta = \Gamma^3\Gamma^5 K$. Here, K denotes complex conjugation and the Γ matrices were defined in Sec. 6.1.

The spin-orbit coupling

$$H_{\mathrm{SO}} = p \begin{pmatrix} v_1 \boldsymbol{\sigma}\cdot\boldsymbol{e}_1 & 0 \\ 0 & v_2 \boldsymbol{\sigma}\cdot\boldsymbol{e}_2 \end{pmatrix} = H_{U(1)}(p) + H_{\mathrm{R}}(p) \tag{6.34}$$

can be split into a $U(1)$ spin-symmetric term, $H_{U(1)}(p)$, and a Rashba term, $H_{\mathrm{R}}(p)$. The (not necessarily equal) spin quantization axes are labeled by real unit vectors $\boldsymbol{e}_i$. Choosing $\boldsymbol{e}_i$ to point along the z-axis one may write the $U(1)$ spin symmetric part as

$$H_{U(1)}(p) = p \begin{pmatrix} v_1 \sigma_z e_1^z & 0 \\ 0 & v_2 \sigma_z e_2^z \end{pmatrix} = p\left(v_+ \Gamma^{15} + v_- \Gamma^{34}\right) , \tag{6.35}$$

where $v_\pm = (v_1 e_1^z \pm v_2 e_2^z)/2$. Note that the generator of the $U(1)$ spin symmetry is $\Gamma^{34} = \mathbf{1} \otimes \sigma_z$.

One way to break the $U(1)$ spin symmetry is to include the Rashba term $H_{\mathrm{R}}(p)$ by setting $\boldsymbol{e}_1 \neq \boldsymbol{e}_2$. This can be accomplished by choosing, for example, $\boldsymbol{e}_1 = (0, 0, e_1^z)^T$ and $\boldsymbol{e}_2 = (e_2^x, e_2^y, e_2^z)^T$, leading to

$$H_{\mathrm{R}}(p) = p v_2 \begin{pmatrix} 0 & 0 \\ 0 & \sigma_x e_2^x + \sigma_y e_2^y \end{pmatrix} = \frac{p v_2}{2}\left[(\Gamma^{45} - \Gamma^{13}) e_2^x - (\Gamma^{35} + \Gamma^{14}) e_2^y\right] . \tag{6.36}$$

H_{S} breaks the translation symmetry of the bulk model in the sense that it allows single-particle scattering between the $i = 1$ and $i = 2$ branches of the low-energy model. Its general, time-reversal symmetric form is

$$H_{\mathrm{S}} = \begin{pmatrix} 0 & h_{\mathrm{S}} \\ h_{\mathrm{S}}^\star & 0 \end{pmatrix} = \alpha_1 \Gamma^1 + \alpha_3 \Gamma^3 + \alpha_4 \Gamma^4 + \alpha_5 \Gamma^5 = H_{\mathrm{S},U(1)} + H_{\mathrm{S}'} , \tag{6.37}$$

where h_{S} denotes the corresponding complex 2×2 matrix and $\alpha_i \in \mathbb{R}$. Note that H_{S} generally breaks the $U(1)$ spin symmetry since $[H_{\mathrm{S}}, \Gamma^{34}] = 2i(\alpha_4 \Gamma^3 - \alpha_3 \Gamma^4)$. Therefore, we write it as the sum of a symmetry-preserving term, $H_{\mathrm{S},U(1)} = \alpha_1 \Gamma^1 + \alpha_5 \Gamma^5$, and a symmetry-breaking term, $H_{\mathrm{S}'} = \alpha_3 \Gamma^3 + \alpha_4 \Gamma^4$.

We consider the following three cases: (a) unbroken translation symmetry and unbroken $U(1)$ spin symmetry, (b) broken translation symmetry but unbroken spin symmetry, and (c) broken translation symmetry and broken spin symmetry.

In case (a), we have $H_{\mathrm{S}} = 0$, and $U(1)$ spin symmetry amounts to $\boldsymbol{e}_1 = \boldsymbol{e}_2$. This implies $H_{\mathrm{R}}(p) = 0$, so that

$$H^{(a)}_{\mathrm{edge}}(p) = H_{U(1)}(p) . \tag{6.38}$$

The spectrum of $H^{(a)}_{\mathrm{edge}}(p)$ is gapless, as shown in Fig. 6.9(a).

In case (b), we have

$$H^{(b)}_{\mathrm{edge}}(p) = H_{U(1)}(p) + H_{\mathrm{S},U(1)} , \tag{6.39}$$

and the spectrum, shown in Fig. 6.9(b), has two cones centered at $p_0 = \pm\sqrt{(\alpha_1^2 + \alpha_5^2)/(v_+^2 - v_-^2)}$, with the linearized dispersion

$$E_\pm(p) = \pm \frac{v_+^2 - v_-^2}{v_+}(p \pm p_0) + \mathcal{O}(p^2) . \tag{6.40}$$

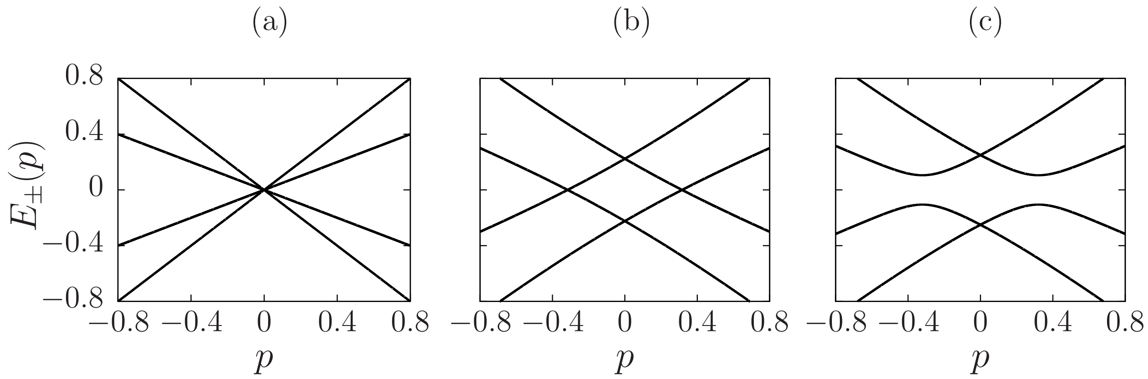

Figure 6.9: Spectrum $E_\pm(p)$ of the effective model (6.33), with $v_1 = 1$, $v_2 = 0.5$, and $\boldsymbol{e}_1 = \boldsymbol{e}_2 = \boldsymbol{e}_z$. (a) Both translation symmetry and $U(1)$ spin symmetry are preserved ($\alpha_i = 0$). (b) Translation symmetry is broken, but $U(1)$ spin symmetry is preserved ($\alpha_1 = 0.2$, $\alpha_5 = 0.1$, $\alpha_3 = \alpha_4 = 0$). (c) Both translation symmetry and $U(1)$ spin symmetry are broken ($\alpha_1 = 0.2$, $\alpha_5 = 0.1$, $\alpha_3 = 0.1$, $\alpha_4 = 0.05$).

This illustrates that, as long as spin is conserved, the breaking of translation symmetry does not gap out the edge states.

Finally, case (c) can be realized by adding the Rashba term (6.36) to Eq. (6.39) or, alternatively, by considering

$$H^{(c)}_{\text{edge}}(p) = H_{U(1)}(p) + H_{\text{S}} \, , \tag{6.41}$$

where $\alpha_i \neq 0$. The resulting spectrum is gapped, see Fig. 6.9(c).

6.4.2 Spin polarization carried by the edge states

Returning to the original πKM model (6.4), we expect the combination of disorder (which breaks translation symmetry) and Rashba spin-orbit coupling to open a gap in the edge states. We introduce on-site random disorder of strength λ_{W} and with a box distribution $-1 < w_{\mathbf{i}} < 1$, leading to the additional term $\lambda_{\text{W}} \sum_{\mathbf{i},\sigma} w_{\mathbf{i}} \hat{c}^\dagger_{\sigma,\mathbf{i}} \hat{c}_{\sigma,\mathbf{i}}$ in the Hamiltonian (6.4). We consider a cylindric geometry of the lattice, with open boundary conditions in the $\mathbf{a}_1$-direction and twisted boundary conditions in the $\mathbf{a}_2$-direction. The twisted boundary conditions are generated by a (spin-independent) boundary phase θ_2, with $0 \geq \theta_2 < 2\pi$. This setup corresponds to a cylinder threaded by a flux $\Phi = \theta_2/2\pi$ and is similar to the Laughlin gedankenexperiment [157; 134; 135]. By deforming the cylinder to a disk, we see that this setup is conceptually the same as the flux pumping gedankenexperiment considered in Sec. 4.1.2. The only difference is that the flux is time-dependent in the latter setup whereas now the flux depends on the twist phase. In a quantum spin Hall insulator, spin is pumped in processes where $\Phi_\uparrow = \Phi_\uparrow$ [38]. The absence of charge pumping, i.e. the absence of net transverse electric charge transport, becomes evident by computing the evolution of the edge states with increasing flux. As it is discussed in Ref. [157] for the plain Kane-Mele model,

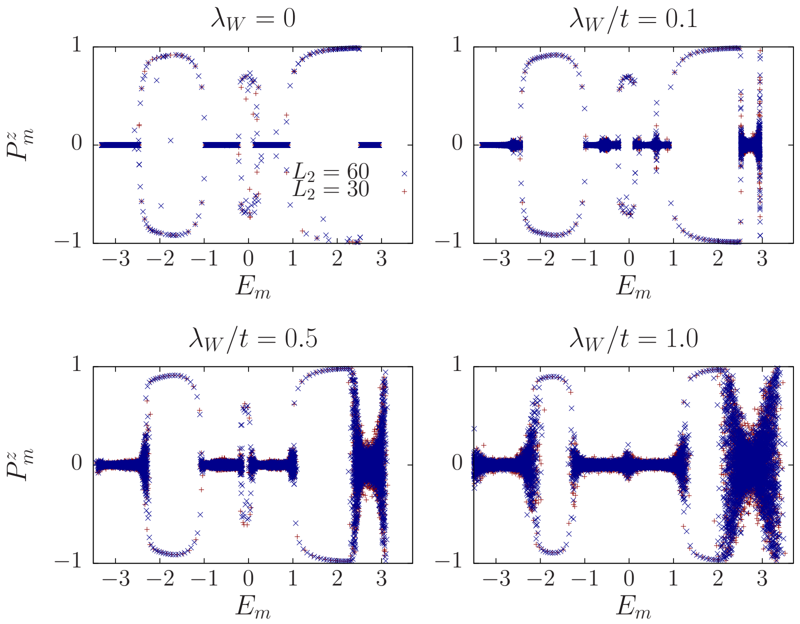

Figure 6.10: Spin polarization P_m^z of each single-particle eigenstate $|m\rangle$ as a function of the eigenenergy E_m. λ_{W} is the strength of the on-site disorder term. Here, $\lambda/t = 0.35$, $\lambda_{\mathrm{R}}/t = 0.3$, $L_1 = 121$ and $L_2 = 30, 60$.

upon completing a full cycle $\Phi = 0 \to 1$, two states evolve out of the Fermi sea. However, they correspond to states that move in opposite, transverse direction in real space and therefore do not lead to charge pumping.

The spin polarization on the lattice of N sites is defined as

$$P_m^z = \frac{\hbar}{2}\langle m|\vec{c}^\dagger\left(\sigma_z \otimes \mathbf{1}_{N\times N}\right)\vec{c}\;|m\rangle\;, \tag{6.42}$$

where $|m\rangle$ denotes a single-particle eigenstate of the πKM model plus the disorder term and $\vec{c} = (\hat{c}_{\uparrow,1}, \cdots \hat{c}_{\uparrow,N}, \hat{c}_{\downarrow,1}, \hat{c}_{\downarrow,N})^T$. When $\theta_2 = 0$, all eigenstates have a partner with the same energy (Kramers degeneracy). Because of time-reversal symmetry, the spin per Kramers pair is zero. A finite twist phase $0 < \theta_2 < 2\pi$ lifts the Kramers degeneracies by breaking time reversal symmetry. In the πKM model, similar to the KM model [157], the spin polarization then becomes non-zero (see Fig. 6.10, at $\theta_2/2\pi = 0.01$).

The spin polarization, in dependence of the eigenenergies E_m, is finite only within the spectral gaps of the Hamiltonian that are traversed by edge states. In the πKM model, there are three spectral gaps which have edge states. The two pairs of helical edge states corresponds to states in the central energy gap and a single pair of helical edge states corresponds to states each in the upper and the lower energy gap. On a lattice of finite dimensions, the spin polarization consequently has three contributions (Fig. 6.10). In general, a pair of

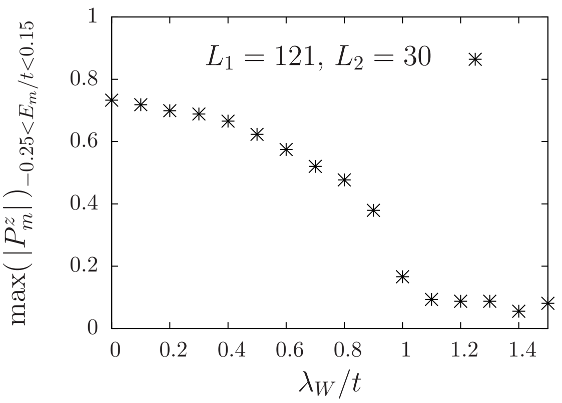

Figure 6.11: Absolute value of the spin polarization contributed by the two pairs of helical edge states which have energies $-0.25 \leq E_m/t \leq 0.15$, as a function of disorder strength λ_{W}. ($\lambda/t = 0.35$, $\lambda_{\mathrm{R}}/t = 0.3$).

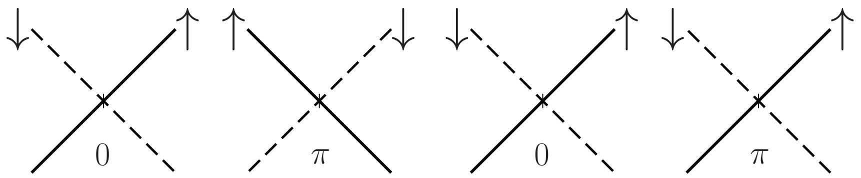

(a)

(b)

Figure 6.12: The $(0, \sigma)$ and (π, σ) edge modes at (a) $\lambda/t = \lambda_s$ where $v_{0,\sigma} = -v_{\pi,\sigma}$, (b) $\lambda/t \to \infty$ where $v_{0,\sigma} = v_{\pi,\sigma}$.

Kramers doublets is not protected from localization by disorder [28]. The observation of finite values of the part of the spin polarization which is contributed by the two pair of edge states, up to sizable disorder strengths of $\lambda_W \lesssim t$ (Fig. 6.11) can therefore only be attributed to strong finite size effects. The question of edge state destruction by disorder deserves further investigation.

6.4.3 Low-energy spin symmetries at $\lambda/t = \lambda_s$ and for $\lambda/t \to \infty$

In the following, we focus on two values of the intrinsic spin-orbit coupling, $\lambda/t = \lambda_s$ and $\lambda/t \to \infty$, where the velocities of the $(0, \sigma)$ and the (π, σ) modes obey $v_{0,\sigma} = -v_{\pi,\sigma}$ and $v_{0,\sigma} = v_{\pi,\sigma}$, respectively (see Fig. 6.12). The corresponding low-energy Hamiltonians are

$$H^s_{\mathrm{edge}}(-i\partial_x) = -i\partial_x v \begin{pmatrix} \sigma_z & 0 \\ 0 & -\sigma_z \end{pmatrix} = -i\partial_x v \Gamma^{15} \,, \tag{6.43}$$

where $\mathbf{\Psi}_s^\dagger(x) = (R_1^\dagger(x), L_1^\dagger(x), L_2^\dagger(x), R_2^\dagger(x))$, and

$$H_{\text{edge}}^{\infty}(-i\partial_x) = -i\partial_x v \begin{pmatrix} \sigma_z & 0 \\ 0 & \sigma_z \end{pmatrix} = -i\partial_x v \Gamma^{34} \, , \tag{6.44}$$

where $\mathbf{\Psi}_\infty^\dagger(x) = (R_1^\dagger(x), L_1^\dagger(x), R_2^\dagger(x), L_2^\dagger(x))$. While the $SU(2)$ spin symmetry is obviously broken, we show in the following that a chiral $SU(2)$ symmetry exists for $\lambda/t = \lambda_s$.

The electron annihilation operator $\hat{c}_\sigma(x)$ can be written in terms of the fields $R_i(x)$ and $L_i(x)$ [158],

$$\begin{aligned} \hat{c}_\uparrow(x) &= \left[R_1(x)e^{-ik_{\text{F}}^{(1)}x} + Y_2(x)e^{-ik_{\text{F}}^{(2)}x}\right]/\sqrt{2} \, , \\ \hat{c}_\downarrow(x) &= \left[L_1(x)e^{-ik_{\text{F}}^{(1)}x} + \bar{Y}_2(x)e^{-ik_{\text{F}}^{(2)}x}\right]/\sqrt{2} \, , \end{aligned} \tag{6.45}$$

where $k_{\text{F}}^{(1)} = 0$, $k_{\text{F}}^{(2)} = \pi$. For $\lambda/t = \lambda_s$, the $i = 1$ and $i = 2$ modes have opposite helicity, so $Y_2(x) = L_2(x)$ and $\bar{Y}_2(x) = R_2(x)$. For $\lambda/t \to \infty$, we have $Y_2(x) = R_2(x)$ and $\bar{Y}_2(x) = L_2(x)$. The fermionic anti-commutation relations follow from Eq. (6.30). The spin operators can be expressed for both cases as

$$\hat{S}^a(x) = \frac{1}{2}\sum_{\sigma,\sigma'} \hat{c}_\sigma^\dagger(x)\sigma_{\sigma,\sigma'}^a \hat{c}_{\sigma'}(x) = \frac{1}{4}\sum_{\sigma,\sigma'} \Psi_\sigma^\dagger(x) s_{\sigma,\sigma'}^a \Psi_{\sigma'}(x) \, , \tag{6.46}$$

with the constraint of single occupancy, $\hat{c}_\uparrow^\dagger(x)\hat{c}_\uparrow(x) + \hat{c}_\downarrow^\dagger(x)\hat{c}_\downarrow(x) = 1$. The matrices s^a are given by

$$\begin{aligned} s^x &= \mathbf{1}\otimes\sigma_x + (\sigma_x\otimes\sigma_x)\, e^{i\pi x} = \Gamma^{45} - \Gamma^{23}e^{i\pi x} \, , \\ s^y &= \mathbf{1}\otimes\sigma_y + (\sigma_x\otimes\sigma_y)\, e^{i\pi x} = -\Gamma^{35} - \Gamma^{24}e^{i\pi x} \, , \\ s^z &= \mathbf{1}\otimes\sigma_z + (\sigma_x\otimes\sigma_z)\, e^{i\pi x} = \Gamma^{34} - \Gamma^{25}e^{i\pi x} \, . \end{aligned} \tag{6.47}$$

They have the commutation relation $[s^a/4, s^b/4] = i\epsilon^{abc}(s^c/4)$.

Apart from the spin operators, Eq. (6.46), there are three additional operators which have the commutation relations of the $su(2)$ Lie algebra. These operators are represented by the matrices

$$\Sigma_x \equiv \Gamma^{23} \, , \ \ \Sigma_y \equiv \Gamma^{24} \, , \ \ \Sigma_z \equiv \Gamma^{34} \, , \tag{6.48}$$

which appear in Eq. (6.47) and satisfy $[\Sigma_a/2, \Sigma_b/2] = i\epsilon^{abc}(\Sigma_c/2)$. They are related to the additional chiral degree of freedom which is introduced by the edge mode 'orbitals' taking the values $i = 1, 2$. For $\lambda/t = \lambda_s$, all three generators Σ_a are symmetries of the low-energy Hamiltonian (6.43), i.e., $[H_{\text{edge}}^s, \Sigma_a] = 0$, whereas for $\lambda/t \to \infty$, this is only true for Σ_z. Therefore, and apart from the spin symmetry, a chiral $SU(2)$ symmetry is present for $\lambda/t = \lambda_s$ which turns into a chiral $U(1)$ symmetry for $\lambda/t \to \infty$.

We define a rotation by $\pi/2$, described by

$$U_a = \exp\left[-i(\pi/4)\Sigma_a\right] = (\mathbf{1} - i\Sigma_a)/\sqrt{2} \, . \tag{6.49}$$

Then, $U_a^\dagger \hat{S}^b(x) U_a = M_{ab}$ is the rotation by $\pi/2$ of the spin component $\hat{S}^b(x)$ around the $\boldsymbol{e}_a$ axis, where

$$M = \begin{pmatrix} \hat{S}^x(x) & e^{i\pi x}\hat{S}^z(x) & -e^{i\pi x}\hat{S}^y(x) \\ -e^{i\pi x}\hat{S}^z(x) & \hat{S}^y(x) & e^{i\pi x}\hat{S}^x(x) \\ -\hat{S}^y(x) & \hat{S}^x(x) & \hat{S}^z(x) \end{pmatrix} . \tag{6.50}$$

In particular, we obtain the relations

$$U_x^\dagger \hat{S}^z(x) U_x = -e^{i\pi x}\hat{S}^y(x) \ , \quad U_y^\dagger \hat{S}^z(x) U_y = e^{i\pi x}\hat{S}^x(x) \ , \quad U_z^\dagger \hat{S}^y(x) U_z = \hat{S}^x(x) \ . \tag{6.51}$$

We now consider the static spin structure factor

$$S^a(q) = \frac{1}{\sqrt{N}} \sum_x e^{-iqx} \langle \hat{S}^a(x) \hat{S}^a(0) \rangle \ , \tag{6.52}$$

where the expectation value is defined with respect to the effective Hamiltonian (6.29). Using the symmetry relations (6.51) we get

$$\begin{aligned} S^z(q) &= S^x(q+\pi) && \text{for}\, \lambda/t = \lambda_s \ , \\ S^x(q) &= S^y(q) && \text{for}\, \lambda/t = \lambda_s \,\text{and}\, \lambda/t \to \infty \ . \end{aligned} \tag{6.53}$$

Equation (6.53) relates the longitudinal and transverse components of the spin-spin correlation functions. In Sec. 6.6, we numerically show that this low-energy symmetry is preserved in the presence of interactions. It is therefore an emergent symmetry of the interacting πKMH model (6.5). However, because the chiral spins [Eq. (6.48)] do not commute with the Rashba term [e.g., Eq. (6.36)], this symmetry hinges on $U(1)$ spin symmetry.

6.5 Bosonization for the edge states

At low energies, the edge states of the πKMH model (6.5) can be described in terms of a two-component [159; 160; 161; 162] Tomonaga-Luttinger liquid [163; 158]. The Tomonaga-Luttinger liquid is the stable low-energy fixed point of gapless interacting systems in one dimension [164].

We consider the free Hamiltonian with two left and two right movers that are labelled by the index $i = 1$ and $i = 2$. As interaction terms, we consider intra-forward scattering of strength $g_f^{(i)}$ within the $i = 1$ and $i = 2$ branches, and inter-forward scattering of strength g'_f between the branches $i = 1$ and $i = 2$. Note that we focus on the case of two pairs of edge modes crossing at $k = 0$ and $k = \pi$, respectively, since only those are protected by time-reversal symmetry (see Sec. 6.4).

In the following, we show that at half filling, umklapp scattering between the edge modes is a relevant perturbation in the sense of the renormalization group (RG). In the framework of RG, a perturbation is relevant if it changes the low-energy behavior of the model and irrelevant if it does not. In our case, umklapp scattering can drive the model away from the Luttinger liquid fixed point and open gaps in the low-energy spectrum. The effect of a perturbation is best understood by considering the scaling behavior of the action which describes the Luttinger liquid fixed point, S_0, and a perturbative term, following Ref. [158]:

$$S = S_0 + g \int \mathrm{d}t\mathrm{d}x A(x,t) \underset{x\to\lambda x, t\to\lambda t}{\longrightarrow} S = S_0 + g\lambda^{2-\Delta} \int \mathrm{d}t\mathrm{d}x A(x,t) \ , \tag{6.54}$$

where $A(\lambda x, \lambda t) = \lambda^{-\Delta} A(x,t)$ is assumed. For $\Delta < 2$ ($\Delta > 2$) the perturbation is relevant (irrelevant) and for $\Delta = 2$ it is marginal [158; 144]. From the scaling behavior of the action, one can derive the mass gap m: $m \sim g_0^{1/(2-\Delta)}$, where g_0 is a measure for the bare coupling [158].

We begin our analysis by considering the following kinetic and interaction terms,

$$\begin{aligned} \mathcal{H} &= \sum_{i=1}^{2} \Big[v_i \int \mathrm{d}x \left(L_i^\dagger(x)(i\partial_x)L_i(x) + R_i^\dagger(x)(-i\partial_x)R_i(x) \right) \\ &\quad + g_f^{(i)} \int \mathrm{d}x\, \rho_i^2(x) \Big] + g_f' \int \mathrm{d}x\, \rho_1(x)\rho_2(x) \ , \end{aligned} \tag{6.55}$$

where $L_i(x)$ [$R_i(x)$] are the left (right) moving fields, and $\rho_i(x) = R_i^\dagger(x)R_i(x) + L_i^\dagger(x)L_i(x)$ is the electronic density.

To bosonize the above Hamiltonian (6.55), we introduce the bosonic fields $\phi_i(x)$ and $\Pi_i(x)$. We have

$$\partial_x \phi_i(x) = \pi \rho_i(x) \tag{6.56}$$

$$\Pi_i(x) = R_i(x)^\dagger R_i(x) - L_i^\dagger(x) L_i(x) \ , \tag{6.57}$$

and

$$\left[\phi_i(x), \Pi_{i'}(x')\right] = i\delta_{i,i'}\delta(x-x') \ . \tag{6.58}$$

In the following, we implicitly assume the dependency of the fields on the position x. Using the bosonic fields, the Hamiltonian (6.55) is

$$\begin{aligned} \mathcal{H} &= \frac{1}{2\pi} \int \mathrm{d}x \sum_{i=1}^{2} \left[v_i \left(\pi \Pi_i\right)^2 + v_i K_i^{-2} \left(\partial_x \phi_i\right)^2 \right] + \frac{g_f'}{\pi^2} \int \mathrm{d}x\, \partial_x\phi_1 \partial_x \phi_2 \\ &= \frac{1}{2\pi} \int \mathrm{d}x \left[\pi^2 \Pi^T M \Pi + \left(\partial_x\phi\right)^T N \partial_x \phi \right] \ , \end{aligned} \tag{6.59}$$

where $K_i = (1 + 2g_f^{(i)}/\pi v_i)^{-1/2}$ is a dimensionless parameter. In the last line, we defined $\Pi = (\Pi_1, \Pi_2)^T$, $\phi = (\phi_1, \phi_2)^T$, and

$$M = \begin{pmatrix} v_1 & 0 \\ 0 & v_2 \end{pmatrix} , \ N = \frac{1}{\pi} \begin{pmatrix} \pi v_1 + 2g_f^{(1)} & g_f' \\ g_f' & \pi v_2 + 2g_f^{(2)} \end{pmatrix} , \tag{6.60}$$

using the notation of Orignac *et al.* [165; 160]. The off-diagonal elements in M are zero, since there is no single-particle scattering from the $i = 1$ to the $i = 2$ cone. Hamiltonian (6.59) is decoupled by rescaling the fields:

$$\begin{aligned}
\mathcal{H} &= \frac{1}{2\pi}\int \mathrm{d}x \left[\pi^2 \Pi'^T \Pi' + \left(\partial_x \phi'\right)^T M^{1/2} N M^{1/2} \partial_x \phi'\right] \\
&= \frac{1}{2\pi}\int \mathrm{d}x \left[\pi^2 \Pi''^T \Pi'' + \left(\partial_x \phi''\right)^T \Delta \partial_x \phi''\right] \\
&= \frac{1}{2\pi}\int \mathrm{d}x \sum_{i=1}^{2} \Delta_{ii}^{1/2} \left[\pi^2 \widetilde{\Pi}_i^2 + \left(\partial_x \widetilde{\phi}_i\right)^2\right] , \qquad (6.61)
\end{aligned}$$

where

$$\begin{aligned}
\Pi' &= M^{1/2} \Pi , \\
\phi' &= M^{-1/2} \phi , \\
\Pi'' &= S^{-1} \Pi' , \\
\phi'' &= S^{-1} \phi' , \\
\widetilde{\Pi} &= \Delta^{-1/4} \Pi'' , \\
\widetilde{\phi} &= \Delta^{1/4} \phi'' . \qquad (6.62)
\end{aligned}$$

Δ is a diagonal matrix and S a rotation, defined via

$$\Delta = S^{-1} M^{1/2} N M^{1/2} S . \qquad (6.63)$$

Therefore, the linear transformation to the new bosonic fields $\widetilde{\Pi}$ and $\widetilde{\phi}$ is

$$\begin{aligned}
\Pi &= M^{-1/2} S \Delta^{1/4} \widetilde{\Pi} \equiv P \widetilde{\Pi} , \\
\phi &= M^{1/2} S \Delta^{-1/4} \widetilde{\phi} \equiv Q \widetilde{\phi} . \qquad (6.64)
\end{aligned}$$

The canonical commutation relations (6.58) are preserved, since

$$\left[\widetilde{\phi}_i(x), \widetilde{\Pi}_{i'}(x')\right] = \sum_{k,k'} Q^{-1}_{i,k} \left(P^{-1}\right)^T_{k',i'} \left[\phi_k(x), \Pi_{k'}(x')\right] = i\delta_{i,i'} \delta(x - x') . \qquad (6.65)$$

We have

$$Q = M^{1/2} S \Delta^{-1/4} = \begin{pmatrix} S_{11} v_1^{1/2} \Delta_{11}^{-1/4} & S_{12} v_1^{1/2} \Delta_{22}^{-1/4} \\ S_{21} v_2^{1/2} \Delta_{11}^{-1/4} & S_{22} v_2^{1/2} \Delta_{22}^{-1/4} \end{pmatrix} , \qquad (6.66)$$

$$\Delta_{ii} = \frac{v_1 N_{11} + v_2 N_{22}}{2} \pm \left[\left(\frac{v_1 N_{11} - v_2 N_{22}}{2}\right)^2 + v_1 v_2 N_{12}^2\right]^{1/2} , \qquad (6.67)$$

and, for $g'_f \neq 0$,

$$S = \begin{pmatrix} \frac{\mathrm{sgn}(g'_f)}{\sqrt{1+s_1}} & \frac{\mathrm{sgn}(g'_f)}{\sqrt{1+s_2}} \\ \frac{\mathrm{sgn}(\Delta_{11} - v_1 N_{11})}{\sqrt{1+s_1^{-1}}} & \frac{\mathrm{sgn}(\Delta_{22} - v_1 N_{11})}{\sqrt{1+s_2^{-1}}} \end{pmatrix} , \qquad (6.68)$$

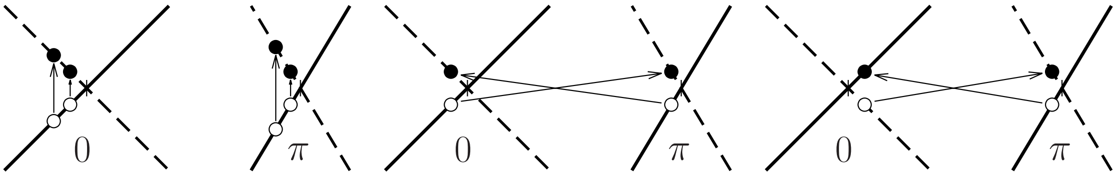

(a) g_u^1 and g_u^2 (b) $g'_{u,1}$ (c) $g'_{u,2}$

Figure 6.13: The edge modes cross at $k = 0$ and $k = \pi$ with in general nonequivalent Fermi velocities v_1 and v_2. We consider the intra-umklapp scattering process (a), and the inter-umklapp scattering processes (b) and (c).

where $s_i = (\Delta_{ii} - N_{11}v_1)^2/v_1v_2N_{12}^2$. Note that for $g'_f = 0$, $S = \mathbf{1}$.

We consider the following interactions as perturbations to Eq. (6.61):

$$\mathcal{H}' = h_u + h'_{u,1} + h'_{u,2} \ . \tag{6.69}$$

The *intra*-umklapp scattering of strength $g_u^{(i)}$ [Fig. 6.13(a)] is

$$h_u = \sum_{i=1}^{2} g_u^{(i)} \int \mathrm{d}x \ L_i^\dagger(x) L_i^\dagger(x+a) R_i(x) R_i(x+a) e^{i4k_\mathrm{F}^{(i)}x} + \mathrm{H.c.} \ , \tag{6.70}$$

the *inter*-umklapp scattering of strength $g'_{u,1}$ [Fig. 6.13(b)] is

$$h'_{u,1} = g'_{u,1} \int \mathrm{d}x \ L_1^\dagger(x) L_2^\dagger(x) R_1(x) R_2(x) \ e^{i2(k_\mathrm{F}^{(1)}+k_\mathrm{F}^{(2)})x} + \mathrm{H.c.} \ , \tag{6.71}$$

and the *inter*-umklapp scattering of strength $g'_{u,2}$ [Fig. 6.13(c)] is

$$h'_{u,2} = g'_{u,2} \int \mathrm{d}x \ L_1^\dagger(x) R_2^\dagger(x) L_2(x) R_1(x) \ e^{i2(k_\mathrm{F}^{(1)}-k_\mathrm{F}^{(2)})x} + \mathrm{H.c.} \ . \tag{6.72}$$

The fermionic operators are

$$R_i = \exp(-i\phi_{R,i})/\sqrt{2\pi} \ , \ L_i = \exp(i\phi_{L,i})/\sqrt{2\pi} \ , \tag{6.73}$$

omitting the Klein factors, and we have $\phi_i = (\phi_{R,i} + \phi_{L,i})/2$. Furthermore, we assume

$$4k_\mathrm{F}^{(i)}x = 2(k_\mathrm{F}^{(1)} + k_\mathrm{F}^{(2)})x = 2(k_\mathrm{F}^{(1)} - k_\mathrm{F}^{(2)})x = 2\pi n \ , \tag{6.74}$$

corresponding to half-filled bands. Then,

$$\mathcal{H}' = \sum_{i=1}^{2} \frac{g_u^{(i)}}{2\pi^2} \int \mathrm{d}x \cos(4\phi_i) + \frac{g'_{u,1}}{2\pi^2} \int \mathrm{d}x \cos[2(\phi_1 + \phi_2)] + \frac{g'_{u,2}}{2\pi^2} \int \mathrm{d}x \cos[2(\phi_1 - \phi_2)] \ . \tag{6.75}$$

6.5.1 Scaling analysis

Obviously, the interaction terms occurring in $\mathcal{H}'$ (6.75) can not be treated exactly by bosonization as the forward interaction terms in $\mathcal{H}$, see Eq. (6.55) and (6.61). If the interaction is weak, the cosine-terms in Eq. (6.75) may be replaced by their series expansion, for example. Instead, we study the impact of the cosine-terms using RG scaling arguments in the following. For a review of bosonization and the RG method, we refer the reader to Refs. [158] and [144]. The scaling dimension Δ of an operator $A(z,\bar{z})$, using $z=\tau+ix$ and $\bar{z}=\tau-ix$, is formally the sum of its right and left conformal dimensions, h and $\bar{h}$: $\Delta=h+\bar{h}$. It determines the asymptotic behavior (up to a constant factor) of the correlation function

$$\langle A(z,\bar{z})A^{\dagger}(0,0)\rangle \sim z^{-2h}\bar{z}^{-2\bar{h}} \;, \tag{6.76}$$

where $\langle\bullet\rangle$ denotes a thermal expectation value. In the present case, A stands for the cosine-terms in Eq. (6.75). The calculation of their scaling dimension boils down to the calculation of expectation values of vertex operators of the form $\exp(i\beta\phi(z,\bar{z}))$. A very useful relation is

$$\langle e^{i\beta_1\phi(z,\bar{z})}e^{i\beta_2\phi(0,0)}\rangle \sim z^{-\frac{\beta_1^2}{4}}\bar{z}^{-\frac{\beta_2^2}{4}}\delta_{\beta_1+\beta_2,0} \;, \tag{6.77}$$

see [72] and [163].

For the intra-umklapp terms in Eq. (6.75) we consider

$$\sum_{i,j}\langle\cos\left[4\phi_i(z,\bar{z})\right]\cos\left[4\phi_j(0,0)\right]\rangle = \frac{1}{4}\sum_{i,j}\langle e^{i4\phi_i(z,\bar{z})}e^{-i4\phi_j(0,0)}\rangle \;+\; \text{similar terms} \;. \tag{6.78}$$

For the calculation, it is sufficient to consider the first term in Eq. (6.78). We proceed by transforming to new fields, $\phi_i(z,\bar{z})=\sum_k Q_{ik}\widetilde{\phi}_k(z,\bar{z})$ [Eq. 6.64]. Then, the first term on the right side of Eq. 6.78 is

$$\begin{aligned}
\frac{1}{4}\sum_{i,j}\langle e^{i4\phi_i(z,\bar{z})}e^{-i4\phi_j(0,0)}\rangle &= \frac{1}{4}\sum_{i,j}\langle e^{i4Q_{i,1}\widetilde{\phi}_1(z,\bar{z})}e^{-i4Q_{j,1}\widetilde{\phi}_1(0,0)}\rangle\langle e^{i4Q_{i,2}\widetilde{\phi}_2(z,\bar{z})}e^{-i4Q_{j,2}\widetilde{\phi}_2(0,0)}\rangle \\
&= \frac{1}{4}\sum_{i,j} z^{-4Q_{i,1}Q_{j,1}}\bar{z}^{-4Q_{i,1}Q_{j,1}}\delta_{Q_{i,1}+Q_{j,1},0} \\
&\qquad \times z^{-4Q_{i,2}Q_{j,2}}\bar{z}^{-4Q_{i,2}Q_{j,2}}\delta_{Q_{i,2}+Q_{j,2},0} \\
&= \frac{1}{4}\sum_{i}|z|^{-8(Q_{i,1}^2+Q_{i,2}^2)} = \frac{1}{4}\sum_{i}|z|^{-2\Delta_u^{(i)}} \;.
\end{aligned} \tag{6.79}$$

In the first line, we assume that the fields $\widetilde{\phi}_1$ and $\widetilde{\phi}_2$ do not interact. The last line defines the scaling dimensions $\Delta_u^{(i)}$. In the same manner, we obtain the scaling dimension Δ'_{u1} and Δ'_{u2} of the vertex operators $\exp[i2(\phi_1+\phi_2)]$ and $\exp[i2(\phi_1-\phi_2)]$. To summarize, we have :

$$\begin{aligned}
\Delta_u^{(1)} &= 4\left(Q_{11}^2+Q_{12}^2\right) , \\
\Delta_u^{(2)} &= 4\left(Q_{21}^2+Q_{22}^2\right) , \\
\Delta'_{u1} &= \left(Q_{11}+Q_{21}\right)^2+\left(Q_{12}+Q_{22}\right)^2 , \\
\Delta'_{u2} &= \left(Q_{11}-Q_{21}\right)^2+\left(Q_{12}-Q_{22}\right)^2 \;.
\end{aligned} \tag{6.80}$$

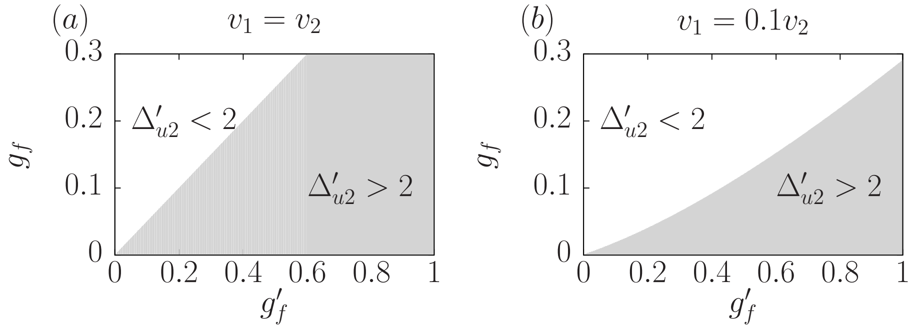

Figure 6.14: Phase diagram of the inter-umklapp process $g'_{u,2}$ in the (g'_f,g_f) plane for (a) equivalent and (b) nonequivalent velocities of the edge modes. The scattering process is relevant (irrelevant) in the region where $\Delta'_{u2} < 2$ ($\Delta'_{u2} > 2$).

The scaling dimension Δ determines whether the respective scattering process in $\mathcal{H}'$ [Eq. (6.75)] is a relevant ($\Delta < 2$) or irrelevant ($\Delta > 2$) perturbation to the free bosonic Hamiltonian $\mathcal{H}$ [Eq. (6.61)].

Let us start with $g'_f = 0$. Then, we have two separate Dirac cones and the scaling dimension for intra-umklapp scattering is

$$\Delta_u^{(i)} = 4v_i\Delta_{ii}^{-1/2} = 4K_i \ , \tag{6.81}$$

see Eq. (6.59). In other words, intra-umklapp scattering ($g_f^{(i)}$) becomes relevant when $K_i < 1/2$. As expected, this result reproduces the known scaling dimension of this process for the one-component helical liquid [28; 26].

In the case of weak coupling ($g_f^{1,2} \ll 1$ and $g'_f \ll 1$), we come to the following conclusions: (i) Intra-umklapp scattering is RG-irrelevant, with $\Delta_u^{(1,2)} > 2$. This is similar to the case of the one-component helical liquid [28; 26]. (ii) Inter-umklapp scattering $g'_{u,1}$ is RG-relevant, with $\Delta'_{u1} < 2$. (iii) The relevance of the inter-umklapp scattering $g'_{u,2}$ is determined by the phase diagram shown in Fig. 6.14.

If the $U(1)$ spin symmetry is preserved, only one of the two inter-umklapp scattering processes $g'_{u,1}$ or $g'_{u,2}$ is allowed by symmetry, depending on the chirality of the $(0,\sigma)$ and (π,σ) modes which is determined by the intrinsic spin-orbit coupling λ. As shown in Fig. 6.8(a), for $\lambda/t < \lambda_0$ and $\lambda/t > \lambda_\pi$, both edge movers have the same chirality so that inter-umklapp scattering corresponds to the $g'_{u,2}$ term. In contrast, for $\lambda_0 < \lambda/t < \lambda_\pi$, the edge movers have opposite chirality and inter-umklapp scattering is given by the $g'_{u,1}$ term.

The above distinction no longer holds when the $U(1)$ spin symmetry is broken. In this case, $g'_{u,1}$ is always RG-relevant, whereas the relevance of $g'_{u,2}$ depends on the forward scattering strengths g_f and g'_f and on the edge velocities, see Fig. 6.14.

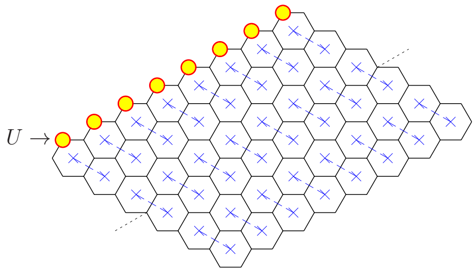

Figure 6.15: Sketch of the ribbon geometry where the on-site Hubbard interaction is only retained on the orbitals of a single zigzag edge.

For $\lambda/t = \lambda_\mathrm{s}$ ($\lambda/t \to \infty$), our low-energy theory is similar to the fusion of two anti-parallel (parallel) helical edge modes [159], see also Fig. 6.12. However, in the latter setup, the spatial overlap of the two edge wave functions can be neglected, whereas it is included in the interaction term of Eq. (6.55).

6.6 Quantum Monte Carlo results for edge correlation effects

Interaction effects on the helical edge states can be studied numerically by taking advantage of the exponential localization of the edge states and of the insulating nature of the bulk which has no low-energy excitations. Accordingly, the low-energy physics is captured by considering the Hubbard term only for the edge sites at the top edge of a zigzag ribbon. The bulk therefore is considered noninteracting and establishes the topological band structure; it plays the role of a fermionic bath (Fig. 6.15).

We arrive at this effective model by partitioning the πKMH Hamiltonian (6.5) formally in one part containing operators on the top edge and another part containing the bulk (including the opposite edge),

$$\mathcal{H} = \mathcal{H}_0^{(\mathrm{bulk})} + \mathcal{H}_0^{(\mathrm{hyb})} + \mathcal{H}_U^{(\mathrm{bulk})} + \mathcal{H}_0^{(\mathrm{edge})} + \mathcal{H}_U^{(\mathrm{edge})} \,, \tag{6.82}$$

where $\mathcal{H}_0^{(\mathrm{hyb})}$ describes the hopping processes between the top edge and the bulk. If we set $\mathcal{H}_U^{(\mathrm{bulk})} = 0$, the corresponding action $\mathcal{S} = \mathcal{S}^{(\mathrm{bulk+hyb})} + \mathcal{S}^{(\mathrm{edge})}$ is quadratic in the bulk fields, thus they can be integrated out leading to an effective action for the top edge:

$$\mathcal{S}^{(\mathrm{edge,\ eff})} = -\int\limits_0^\beta \mathrm{d}\tau \int\limits_0^\beta \mathrm{d}\tau' \sum_{i,\sigma} \sum_{j,\sigma'} c^\dagger_{i,\sigma}(\tau) \mathcal{G}^{-1}_{0\sigma\sigma'}(i-j, \tau-\tau') c_{j\sigma'}(\tau') + \mathcal{H}_U^{(\mathrm{edge})} \,, \tag{6.83}$$

where $\mathcal{G}_0$ is the free Green function of the πKM model $\mathcal{H}_0$ and i, j index edge sites.

The effective model (6.83) can be efficiently simulated using the CT-INT QMC method, presented in Sec. (2.2). Compared to the KMH model, where the same approach has previously been used to study edge correlation effects [153; 166], the additional Rashba term leads to a moderate sign problem.

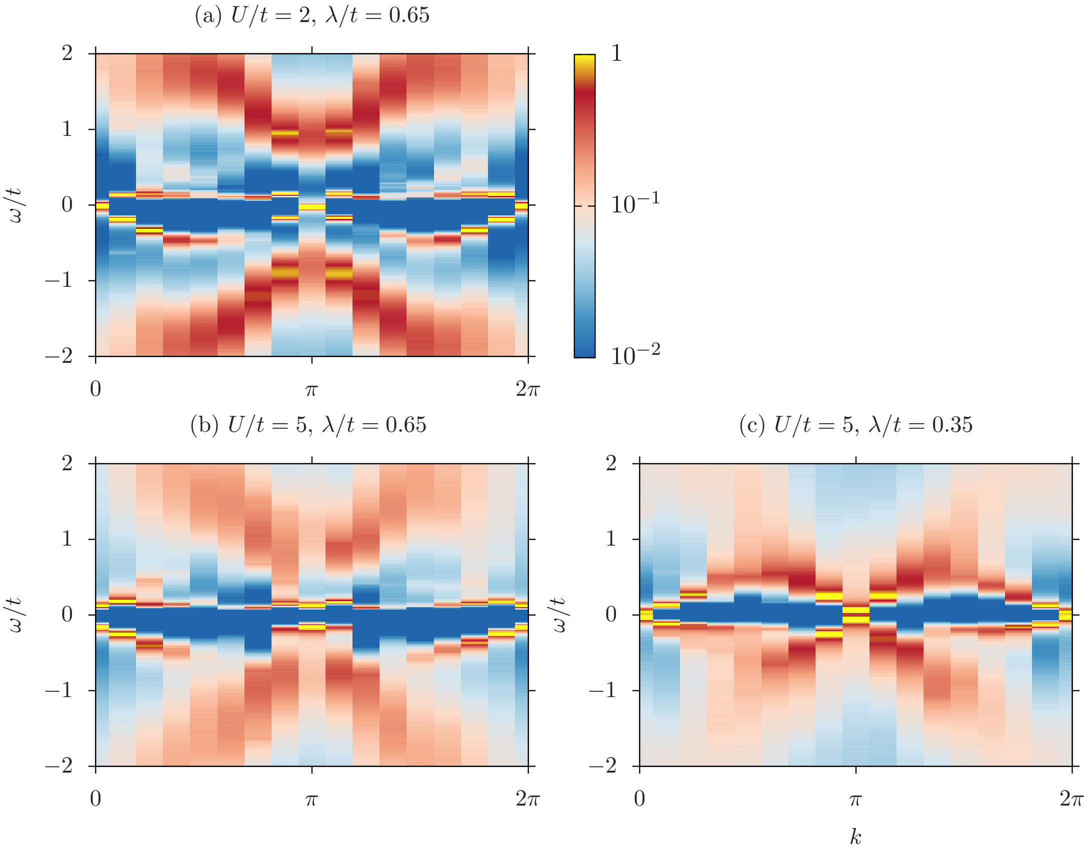

Figure 6.16: QMC results for the spin-averaged single-particle spectral function $A(k, \omega)$ [Eq. (6.84)]. (a) Weak coupling $U/t = 2$, (b),(c) strong coupling $U/t = 5$. Here, $\lambda_\mathrm{R}/t = 0.3$.

We focus on two values of the spin-orbit coupling λ/t and set the Rashba coupling to $\lambda_\mathrm{R}/t = 0.3$. For $\lambda/t = 0.35$, the edge modes at $k = 0$ and $k = \pi$ have different velocities ($v_0 < v_\pi$), whereas at $\lambda/t = 0.65$, we have $v_0 \approx v_\pi$. As in the KMH model [166], we observe that the velocities of the edge states remain almost unchanged with respect to the noninteracting case.

We have done simulations for a zigzag ribbon of dimensions $L_1 = 25$ (open boundary condition) and $L_2 = 16$ (periodic boundary condition), see also Fig. 6.7(a). For $\lambda_\mathrm{R} = 0$, $\mu = 0$ corresponds to half filling. Although the band filling in general changes as a function of λ_R (the Rashba term breaks the particle-hole symmetry), the Kramers degenerate edge states at $k = 0, \pi$ are pinned to $\omega = \mu$. The choice $\mu = 0$ then again corresponds to half-filled Dirac cones, and allows for umklapp scattering processes. The inverse temperature has been set to $\beta t = 60$ for all simulations.

6.6.1 Single-particle spectral function

Using the CT-INT QMC method in combination with the stochastic maximum entropy method (see Sec. 2.4), we calculate the spin-averaged spectral function (Sec. 2.5) at the edge,

$$\begin{aligned} A(k,\omega) &= \frac{1}{2}\sum_{\sigma} A^{\sigma}(k,\omega)\,, \\ A^{\sigma}(k,\omega) &= -\frac{1}{\pi}\mathrm{Im}\;G^{\sigma}(k,\omega)\;, \end{aligned} \tag{6.84}$$

where $G^{\sigma}(k,\omega)$ is the interacting single-particle Green function, and k is the momentum along the edge.

As shown in Fig. 6.16(a), for $U/t = 2$, the numerical results suggest the existence of gapless edge states. In contrast, for a stronger interaction $U/t = 5$, a gap is clearly visible both at $k = 0$ and $k = \pi$. While the bosonization analysis in Sec. 6.5 predicts a gap as a result of relevant umklapp scattering for any $U > 0$, the size of the gap depends exponentially on U/t. The apparent absence of a gap in Fig. 6.16(a) can therefore be attributed to the small system size used ($L_2 = 16$).

Figure 6.16(c) shows the spectral function (6.84) for $\lambda/t = 0.35$, where $v_0 < v_\pi$. Compared to the case of $\lambda/t = 0.65$ [Fig. 6.16(b)] where $v_0 \approx v_\pi$, the gap in the edge states is much smaller. We expect this dependence on the Fermi velocities to also emerge from the bosonization in the form of a velocity-dependent prefactor that determines the energy scale of the gap [144].

6.6.2 Charge and spin structure factors

We consider the charge structure factor

$$N(q) = \frac{1}{\sqrt{N}}\sum_{x} e^{-iqx}\left[\langle\hat{n}(x)\hat{n}(0)\rangle - \langle\hat{n}(x)\rangle\langle\hat{n}(0)\rangle\right]\;, \tag{6.85}$$

where x is the position along the edge. Figure 6.17(b) shows results for different values of U/t, $\lambda/t = 0.65$, and $\lambda_\mathrm{R}/t = 0.3$. For a weak interaction, $U/t = 1$, $N(q)$ exhibits cusps at $q = 0$ and $q = \pi$ that indicate a power-law decay of the real-space charge correlations. Upon increasing U/t, the cusps becomes less pronounced, which suggests a suppression of charge correlations by the interaction. This is in accordance with the existence of a gap in the single-particle spectral function [Fig. 6.16(b)]. A suppression of charge correlations is also observed for $\lambda = 0.35$, see Fig. 6.17(a).

The spin structure factors ($a = x, z$)

$$S^a(q) = \frac{1}{\sqrt{N}}\sum_{x} e^{-iqx}\langle\hat{S}^a(x)\hat{S}^a(0)\rangle \tag{6.86}$$

are shown in Fig. 6.18. For $\lambda/t = 0.65$ and $U/t = 2$, $S^x(q)$ has cusps at $q = 0$ and $q = \pi$ [Fig. 6.18(c)], and varies almost linearly in between. With increasing U/t [$U/t = 5$ in

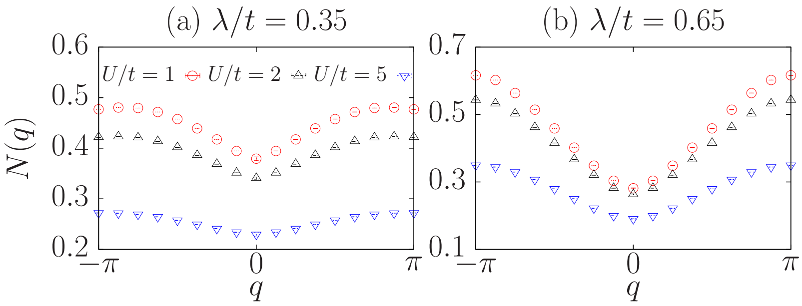

Figure 6.17: QMC results for the charge structure factor $N(q)$ [Eq. (6.85)], for (a) $\lambda/t = 0.35$ and (b) $\lambda/t = 0.65$. Here, $\lambda_\mathrm{R}/t = 0.3$.

Fig. 6.18(d)], correlations with $q = 0$ become much stronger. Whereas $q = 0$ spin correlations dominate the x component of spin, the structure factor $S^z(q)$ in Fig. 6.18(d) indicates equally strong correlations with $q = \pi$ for the z component. The resulting spin order resembles that of a canted anti-ferromagnet. Qualitatively similar results, although with a less pronounced increase of spin correlations between $U/t = 2$ and $U/t = 5$, are also observed for $\lambda/t = 0.35$, as shown in Figs. 6.18(a),(b).

Despite a small but nonzero Rashba coupling, the results in Figs. 6.18(c) and (d) reveal the expected symmetry relation $S^z(q) = S^x(q+\pi)$ which roots in the chiral $SU(2)$ symmetry of the corresponding low-energy Hamiltonian (see Sec. 6.4.3). Our quantum Monte Carlo results show that this symmetry survives even in the presence of strong correlations. The results in Fig. 6.18 are almost identical to the case with $\lambda_\mathrm{R} = 0$ (not shown), suggesting that the Rashba term breaks the chiral symmetry only weakly. On the other hand, the symmetry is clearly absent for $\lambda/t = 0.35$ [Figs. 6.18(a),(b)].

6.6.3 Effective spin model for $\lambda/t = \lambda_s$

For strong interactions U/t, there exist no low-energy charge fluctuations at the edge, allowing for a description in terms of a spin model. We consider the case of (nearly) equal velocities, $\lambda/t = 0.65$, and make an ansatz in the form of a Heisenberg model with nearest-neighbor interactions,

$$\begin{aligned} \mathcal{H}_\mathrm{spin} &= \sum_i \left(J_x S_i^x S_{i+1}^x + J_y S_i^y S_{i+1}^y + J_z S_i^z S_{i+1}^z \right) \\ &= J \sum_i \left(S_i^x S_{i+1}^x + S_i^y S_{i+1}^y - S_i^z S_{i+1}^z \right) . \end{aligned} \tag{6.87}$$

In the second line, the coupling constants J_a have been fixed by imposing the invariance under the rotations given in Eq. (6.49), $[H^s_\mathrm{spin}, U_a] = 0$, and using the relations $U_a^\dagger \hat{S}^b(x) U_a = M_{ab}$ [cf. Eq. (6.50)]. Hamiltonian (6.87) corresponds to the XXZ Heisenberg model, tuned to the ferromagnetic isotropic point that separates the Ising phase from the Luttinger liquid phase via a first order transition. In both cases, one expects strong spin correlations [167], as observed in Fig. 6.18(d).

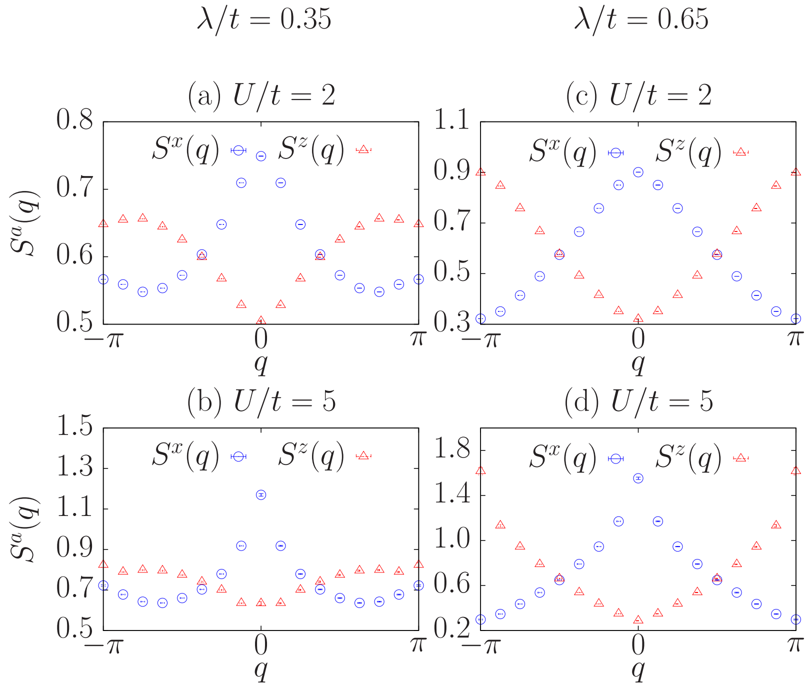

Figure 6.18: QMC results for the spin structure factors $S^x(q)$ and $S^z(q)$ [Eq. (6.86)], for $\lambda/t = 0.35$ [(a),(b)] and $\lambda/t = 0.65$ [(c),(d)]. Here, $\lambda_\mathrm{R}/t = 0.3$.

6.7 Conclusions

In this section, the πKM model has been introduced, corresponding to the Kane-Mele model on a honeycomb lattice with a magnetic flux of $\pm\pi$ through each hexagon. The flux insertion doubles the size of the unit cell, and leads to a four-band model for each spin sector. For one spin direction, the band structure has four Dirac points which acquire a gap for nonzero spin-orbit coupling λ (see Sec. 6.2). At half filling, the spinless model has a Chern insulating ground state with Chern number 2 or -2, depending on the spin-orbit coupling (6.2.2). The transition between these states occurs via a phase transition at $\lambda/t = 1/2$, and the band structure features a quadratic crossing at the critical point. The spinful πKM model is trivial in the Z_2 classification, with an even number of Kramers doublets (6.2.3). If translation symmetry at the edge is unbroken, the helical edge states are stable at the single-particle level even in the presence of a Rashba coupling that breaks the $U(1)$ spin symmetry (Sec. 6.4.1) The $U(1)$ spin symmetric low-energy model of the edge states has a chiral symmetry when the edge state velocities have equal magnitude and either the same or opposite sign (Sec. 6.4.3). Interestingly, this chiral symmetry has been shown to survive even in the presence of interactions, see Sec. 6.6.2.

Regarding the effect of electronic correlations in the bulk, the combination of mean-field calculations and quantum Monte Carlo simulations (Sec. 6.3) suggest the existence of a quantum phase transition to a state with long-range, antiferromagnetic order, similar to the Kane-Mele-Hubbard model. The critical value of the interaction depends on the spin-orbit coupling. At $\lambda/t = 1/2$, where the quadratic band crossing occurs, a weak-coupling Stoner instability exists.

In Secs. 6.5 and 6.6, we have presented a detailed study of correlation effects on the edge states in the paramagnetic bulk phase, using bosonization and quantum Monte Carlo simulations. At half filling, the bosonization analysis predicts the opening of a gap in the edge states as a result of umklapp scattering for any nonzero interaction . For strong coupling, we are able to confirm this prediction with QMC simulations. Umklapp processes are only effective at commensurate filling and therefore can be eliminated by doping away from half filling. In this case, we expect the interacting model to have stable edge modes, provided translation symmetry is not broken. At large U/t, the emergent chiral symmetry can be used to derive an effective spin model of the XXZ Heisenberg type (see Sec. 6.6.3).

Our model may be regarded as a two-dimensional counterpart of TCIs. Whereas the gapless edge states of the latter are protected by crystal symmetries of the two-dimensional surface, the edge states in the πKM model are protected (at the single-particle level, or away from half filling) by translation symmetry. TCIs have an even number of surface Dirac cones which are related by a crystal symmetry. The cones can be displaced in momentum space without breaking time-reversal symmetry by applying inhomogeneous strain [168]. This is in contrast to topological insulators with an odd number of Dirac points where at least one Kramers doublet is pinned at a time-reversal invariant momentum. In TCIs, umklapp scattering processes can be avoided either by doping away from half filling or by moving the Dirac points. In our model, the edge modes have in general unequal velocities and cannot be mapped onto each other by symmetry. The Dirac points are pinned at the time-reversal invariant momenta, and subject to umklapp scattering at half filling.

Similarly to the recent experimental realization of the topological Haldane model using ultracold fermions [169], the πKM model may be experimentally realizable in ultracold atomic gases, where optical flux lattices can be used to create periodic magnetic flux densities [141; 170; 171; 172].

7

Summary

At this point, we would like to summarize the individual projects and to highlight the common thread of the thesis. We have investigated correlations effects in many-electron systems using quantum Monte Carlo methods to simulate the interactions. In particular, we have studied heavy-fermion metamagnetism and interacting local moments resulting from π fluxes in correlated topological insulators.

The physics of heavy fermions roots in the Kondo effect which is a genuine example of correlation induced phenomena in condensed matter physics. The notion of metamagnetism describes the non-linear magnetic reponse of certain heavy-fermion compounds to an external magnetic field. We have considered the Kondo lattice model, being an appropriate low-energy model of heavy-fermion systems, and investigated the competition of the magnetic energy scale with the intrinsic scale of the model, namely the lattice coherence temperature. Our main finding is that a metamagnetic transition occurs when the magnetic field is comparable to the lattice coherence temperature. Interestingly, the Kondo effect does not break down and the simulations rather show a gradual crossover from heavy to light fermions as the field further increases. Therefore, we come to the conclusion that the metamagnetic transition in heavy-fermion systems can be understood as a Lifshitz transition of well-defined quasiparticle bands, even in the presence of sizeable magnetic fields.

In contrast to heavy fermions, that owe their sheer existence to electronic interactions, the notion of topological insulators has been first of all developped from a non-interacting perspective. A common and natural assumption is that weak electronic interactions generate a state of matter which is adiabatically connected to the non-interacting phase. Our focus has been primarly on interaction induced features of *correlated* topological insulators. We have studied the response of a correlated topological insulator to a perturbation in the form of external magnetic π fluxes. By measuring the magnetic susceptibility, one can determine the topological Z_2 index and thereby classify the topological nature of the insulating phase.

Besides measuring the topological index, we have shown how to exploit the properties of π fluxes in correlated topological insulators in a different way. Each π flux is accompanied by a spin degree of freedom and multiple π fluxes can be inserted almost arbitrarily on the lattice. We have studied the resulting quantum spin models in various geometries.

We have proposed the π Kane-Mele model and investigated its topological and magnetic phase diagram. The new model is obtained from the Kane-Mele model by inserting a π flux in each unit cell of the underlying hexagonal lattice. For spinless electrons, the model is a Chern insulator with two topologically distinct phases. We have focussed on the spinful case and studied the effect of correlations in the bulk and on the edge of the insulator. The model has two Kramers pairs when put on a ribbon geometry and therefore is a Z_2 trivial insulator. However, as long as translation symmetry is preserved, the edge states are protected from scattering processes on the single-particle level. We have studied the possible scattering mechanisms in the effective interacting low-energy model and have been able to partly confirm the predictions from the bosonization analysis using quantum Monte Carlo simulations. Since the π Kane-Mele model is protected by translation symmetry, it can be considered as a two-dimensional instance of a topological crystalline insulator.

A

Calculation of the optical conductivity

To derive the expression (6.9) for the optical conductivity, we consider the Chern insulator on a torus geometry. It is defined as [Eq. (6.2)]:

$$\mathcal{H}^\sigma = \sum_{\boldsymbol{i},\boldsymbol{j}} c^\dagger_{\boldsymbol{i},\sigma} T^\sigma_{\boldsymbol{i}-\boldsymbol{j}} c_{\boldsymbol{i},\sigma} = \sum_{\boldsymbol{k}} c^\dagger_{\boldsymbol{k},\sigma} H^\sigma(\boldsymbol{k}) c_{\boldsymbol{k},\sigma} = \sum_{\boldsymbol{k},n} E_n(\boldsymbol{k}) c^\dagger_{\boldsymbol{k},\sigma} P^\sigma_n(\boldsymbol{k}) c_{\boldsymbol{k},\sigma} \,, \tag{A.1}$$

where $U^\sigma(\boldsymbol{k}) H^\sigma(\boldsymbol{k}) U^{\sigma\dagger}(\boldsymbol{k}) = \mathrm{diag}[E^\sigma_1(\boldsymbol{k}), \cdots, E^\sigma_4(\boldsymbol{k})]$ and $[P^\sigma_n(\boldsymbol{k})]_{i,j} = U^\sigma_{i,n}(\boldsymbol{k}) U^{\sigma\dagger}_{n,j}(\boldsymbol{k})$ is the projector on the n-th band. For the simplicity of the notation, we drop the spin index and only reintroduce it in the final result (A.12). In the case of a Chern insulator, the electromagnetic response of the Hamiltonian reveals the topological properties of the band structure. In the following, we derive the optical conductivity by calculating the current $\langle \hat{\boldsymbol{j}}(t) \rangle$ to first order in time-dependent perturbation theory via the Kubo formula [59]. We couple the four-band Hamiltonian (A.1) to an electric field via a vector potential $\boldsymbol{A}(t)$. The vector potential is assumed to be homogeneous on the scale of $|\boldsymbol{i} - \boldsymbol{j}|$; therefore its spatial dependence can be dropped. We have

$$\begin{aligned}
\mathcal{H} &= \sum_{\boldsymbol{i},\boldsymbol{j}} c^\dagger_{\boldsymbol{i}} T_{\boldsymbol{i}-\boldsymbol{j}} c_{\boldsymbol{j}} e^{\frac{2\pi i}{\phi_0} \int_{\boldsymbol{i}}^{\boldsymbol{j}} \boldsymbol{A}(t) \mathrm{d}\boldsymbol{l}} \\
&= \sum_{\boldsymbol{i},\boldsymbol{j}} c^\dagger_{\boldsymbol{i}} T_{\boldsymbol{i}-\boldsymbol{j}} c_{\boldsymbol{i}} + \frac{2\pi i}{\phi_0} \sum_{\boldsymbol{i},\boldsymbol{j}} c^\dagger_{\boldsymbol{i}} T_{\boldsymbol{i}-\boldsymbol{j}} c_{\boldsymbol{j}} (\boldsymbol{j} - \boldsymbol{i}) \boldsymbol{A}(t) + \mathcal{O}[\boldsymbol{A}(t)^2] \\
&= \mathcal{H}_0 + \theta(t - t_0) \mathcal{H}_1(t) + \mathcal{O}[\boldsymbol{A}(t)^2] \,. \qquad (A.2)
\end{aligned}$$

The Kubo formula expresses the time-evolution of an observable only in terms of expectation values in equilibrium. For the current $\hat{\boldsymbol{j}}(t, t_0)$, it is

$$\begin{aligned}
\langle \hat{\boldsymbol{j}}(t, t_0) \rangle &= \langle \hat{\boldsymbol{j}}(t) \rangle_0 - \frac{i}{\hbar} \int_{t_0}^{\infty} \mathrm{d}t' \theta(t - t') \langle [\boldsymbol{j}^I(t), \mathcal{H}^I_1(t')] \rangle_0 e^{-0^+(t-t')} \\
&= \langle \hat{\boldsymbol{j}}(t) \rangle_0 + \int_0^\infty \mathrm{d}s \; C^{\mathrm{R}}_{\hat{\boldsymbol{j}},\mathcal{H}_1}(t, t - s) e^{-0^+ s} \,, \qquad (A.3)
\end{aligned}$$

where $C^{\mathrm{R}}_{\hat{\boldsymbol{j}},\mathcal{H}_1}(t,t-s) = -(i/\hbar)\theta(s)\langle[\hat{\boldsymbol{j}}^I(t),\mathcal{H}_1^I(t-s)]\rangle_0$ is a retarded Green function. The superscript I denotes the interaction picture for (possibly explicitly time-dependent) operators $X(t)$, i.e. $X^I(t) = \exp\left(i\mathcal{H}_0 t/\hbar\right)X(t)\exp\left(-i\mathcal{H}_0 t/\hbar\right)$. The factor $\exp[-0^+(t-t')]$ is included to enforce the response term to vanish for $t \gg t'$. In the second line, we shifted the integration variable and took $t_0 = -\infty$. In the following, we write $\langle\hat{\boldsymbol{j}}(t)\rangle = \langle\hat{\boldsymbol{j}}(t,-\infty)\rangle$.

To define the appropriate current on the lattice, one has to temporarily reintroduce the spatial dependence in the vector potential $\boldsymbol{A}(\boldsymbol{r},t)$. The current density $\hat{\boldsymbol{j}}(\boldsymbol{r},t)$ can then be defined as the functional derivative $\hat{\boldsymbol{j}}(\boldsymbol{r},t) = -c\delta\mathcal{H}/\delta\boldsymbol{A}(\boldsymbol{r},t)$. Accordingly, the total current $\hat{\boldsymbol{j}}(t)$ is

$$\begin{aligned}
\hat{\boldsymbol{j}}(t) &= \frac{1}{N}\sum_{\boldsymbol{r}}\hat{\boldsymbol{j}}(\boldsymbol{r},t) = -\frac{c}{N}\sum_{\boldsymbol{r}}\frac{\delta\mathcal{H}_1(t)}{\delta\boldsymbol{A}(\boldsymbol{r},t)} \\
&= -\frac{2\pi c i}{\phi_0 N}\sum_{\boldsymbol{i},\boldsymbol{j}}(\boldsymbol{j}-\boldsymbol{i})c^\dagger_{\boldsymbol{i}}T_{\boldsymbol{i}-\boldsymbol{j}}c_{\boldsymbol{j}}\left[1+\frac{2\pi i}{\phi_0}(\boldsymbol{j}-\boldsymbol{i})\boldsymbol{A}(t)\right] + \mathcal{O}[\boldsymbol{A}(t)^2] \\
&= \hat{\boldsymbol{j}}^{(1)} + \hat{\boldsymbol{j}}^{(2)}(t) + \mathcal{O}[\boldsymbol{A}(t)^2]\,,
\end{aligned} \tag{A.4}$$

where the $\boldsymbol{r}$-dependence of the vector potential is dropped again in the second line. $\hat{\boldsymbol{j}}^{(1)}$ $[\hat{\boldsymbol{j}}^{(2)}(t)]$ is the paramagnetic (diamagnetic) part of the current. Using Eq. A.4 and $\mathcal{H}_1(t) = (-c/N)^{-1}\hat{\boldsymbol{j}}^{(1)}\boldsymbol{A}(t)$, Eq. A.3 becomes

$$\begin{aligned}
\langle\hat{j}_\alpha(t)\rangle &= \langle\hat{j}^{(2)}_\alpha(t)\rangle_0 + \left(\frac{-c}{N}\right)^{-1}\int_0^\infty \mathrm{d}s\,\Pi^{\mathrm{R}}_{\alpha,\beta}(t,t-s)A_\beta(t-s)e^{-0^+s} \\
&= \frac{4\pi^2 c}{\phi_0^2 N}\langle K_\beta\rangle_0 A_\beta(t)\delta_{\alpha,\beta} + \left(\frac{-c}{N}\right)^{-1}\int_0^\infty \mathrm{d}s\,\Pi^{\mathrm{R}}_{\alpha,\beta}(t,t-s)e^{is(\omega+i0^+)}A_\beta(\omega)e^{-i\omega t} \\
&= \left[\frac{4\pi^2 c}{\phi_0^2 N}\langle K_\beta\rangle_0\delta_{\alpha,\beta} + \left(\frac{-c}{N}\right)^{-1}\int_0^\infty \mathrm{d}s\,\Pi^{\mathrm{R}}_{\alpha,\beta}(0,-s)e^{is(\omega+i0^+)}\right]\frac{c}{i\omega}E_\beta(\omega)e^{-i\omega t} \\
&= \langle\hat{j}_\alpha(\omega)\rangle e^{-i\omega t}\,.
\end{aligned} \tag{A.5}$$

In the first line, we set $\langle\hat{j}^{(1)}_\alpha(t)\rangle_0 = 0$ due to the absence of paramagnetic currents in the free model and we defined the current-current correlation function

$$\Pi^{\mathrm{R}}_{\alpha,\beta}(t,t-s) = -(i/\hbar)\theta(s)\langle[\hat{j}^{(1),I}_\alpha(t),\hat{j}^{(1),I}_\beta(t-s)]\rangle_0\,. \tag{A.6}$$

To obtain the second line, we assume that the system is perturbed by a single frequency only, i.e. $A_\alpha(t) = A_\alpha(\omega)\exp(-i\omega t)$. We define the kinetic energy term

$$K_\alpha = \sum_{\boldsymbol{i},\boldsymbol{j}}(j_\alpha - i_\alpha)^2 c^\dagger_{\boldsymbol{i}}T_{\boldsymbol{i}-\boldsymbol{j}}c_{\boldsymbol{j}} = \sum_{\boldsymbol{k}}c^\dagger_{\boldsymbol{k}}K_\alpha(\boldsymbol{k})c_{\boldsymbol{k}}\,, \tag{A.7}$$

where $K_\alpha(\boldsymbol{k}) = -\partial^2 H(\boldsymbol{k})/\partial k_\alpha^2$. In the third line, we chose a gauge where $E_\alpha(t) = (-1/c)\partial t A_\alpha(t)$, i.e. $E_\alpha(\omega) = (i\omega/c)A_\alpha(\omega)$, and we used $\Pi^{\mathrm{R}}_{\alpha,\beta}(t,t-s) = \Pi^{\mathrm{R}}_{\alpha,\beta}(0,-s)$.

We obtain, using Eq. (A.5)

$$\langle \hat{j}_\alpha(\omega) \rangle = \sigma(\omega)_{\alpha,\beta} E_\beta(\omega) \ , \tag{A.8}$$

where

$$\sigma(\omega)_{\alpha,\beta} = \frac{4\pi^2}{i\phi_0^2 N\omega} \left[\langle K_\beta \rangle_0 \delta_{\alpha,\beta} + \int_0^\infty \mathrm{d}s \ \widetilde{\Pi}^{\mathrm{R}}_{\alpha,\beta}(0,-s) e^{is(\omega+i0^+)} \right] \ , \tag{A.9}$$

with the definitions

$$\begin{aligned} \widetilde{\Pi}^{\mathrm{R}}_{\alpha,\beta}(0,-s) &= -(i/\hbar)\theta(s)\langle [\hat{j}^{(3)}_\alpha, \hat{j}^{(3),I}_\beta(-s)] \rangle_0 \ , & \text{(A.10)} \\ \hat{j}^{(3)}_\alpha &= \sum_{\boldsymbol{i},\boldsymbol{j}} (i_\alpha - j_\alpha) c^\dagger_{\boldsymbol{i}} T_{\boldsymbol{i}-\boldsymbol{j}} c_{\boldsymbol{j}} = \sum_{\boldsymbol{k}} c^\dagger_{\boldsymbol{k}} J_\alpha(\boldsymbol{k}) c_{\boldsymbol{k}} \ , & \text{(A.11)} \end{aligned}$$

where $J_\alpha(\boldsymbol{k}) = \partial H(\boldsymbol{k})/\partial k_\alpha$. Finally, we can evaluate the current-current correlation function by going to the diagonal basis and compute the integral in Eq. (A.9). We obtain the the optical conductivity tensor

$$\sigma^\sigma_{\alpha,\beta}(\omega) = \frac{1}{N} \frac{(e/\hbar)^2}{i(\omega + i0^+)} \left[\langle K^\sigma_\alpha \rangle \delta_{\alpha,\beta} - \Lambda^\sigma_{\alpha,\beta}(\omega) \right] \ , \tag{A.12}$$

where

$$\begin{aligned} \langle K^\sigma_\alpha \rangle &= \sum_{\boldsymbol{k},n} f[E^\sigma_n(\boldsymbol{k})] \mathrm{Tr}[K^\sigma_\alpha(\boldsymbol{k}) P^\sigma_n(\boldsymbol{k})] \ , \\ \Lambda^\sigma_{\alpha,\beta}(\omega) &= \sum_{\boldsymbol{k},m,n} \lambda^\sigma_{mn}(\boldsymbol{k},\omega) \mathrm{Tr}[J^\sigma_\alpha(\boldsymbol{k}) P^\sigma_n(\boldsymbol{k}) J^\sigma_\beta(\boldsymbol{k}) P^\sigma_m(\boldsymbol{k})] \ , \\ \lambda^\sigma_{mn}(\boldsymbol{k},\omega) &= \frac{f[E^\sigma_m(\boldsymbol{k})] - f[E^\sigma_n(\boldsymbol{k})]}{\omega + i0^+ + E^\sigma_m(\boldsymbol{k}) - E^\sigma_n(\boldsymbol{k})} \ , \end{aligned} \tag{A.13}$$

and $f[E^\sigma_n(\boldsymbol{k})]$ is the Fermi function. Note that we added an infinitesimal imaginary part to ω compared to Eq. (A.9). Furthermore, we reintroduced the spin indices.

$\mathcal{B}$

Charge and spin excitations of the πKM model

The analysis of the excitations along the edge of the πKM model on a cylinder geometry (see Sec. 6.4) is supplemented by the charge and spin excitations. We consider the local, spin-averaged single-particle spectral function $A(k,\omega)$ [see Eq. (2.108) and Eq. (6.27)], together with the local charge and spin structure factors, $N(q,\omega)$ and $S^{\alpha,\alpha}(q,\omega)$ (see Eq. 2.99). Here $k = \boldsymbol{k} \cdot \boldsymbol{a}_2$ is the momentum along the edge of the ribbon.

As already discussed in Sec. 6.4, due to the broken $U(1)$ spin symmetry, the only single-particle excitations on the edge are the modes that cross at the time-reversal invariant momenta $k = 0$ and $k = \pi$, respectively [see Fig. B.1(a), (e), (i), (m)].

The dynamical structure factors are governed by the support of the δ-functions in Eq. 2.99. Accordingly, the dynamical charge structure factor $N(q,\omega)$ generally has two linear ($q = 0$)-modes corresponding to the two edge excitations with the Fermi velocities v_0 and v_π [see Fig. B.1(b), (f), (j), (n)].

The dependency of the Fermi velocities $v_{0,\pi}$ on the spin-orbit coupling λ has been shown in Fig. 6.8. While the Fermi velocities are different in general ($\lambda/t = 0.35$ and $\lambda/t = 0.8$ in Fig. B.1), they are equal in magnitude at λ_s [$\lambda_s \approx 0.65$, see Fig. B.1 (e)-(h)] and for $\lambda/t \to \infty$ [represented by $\lambda/t = 2$, see Fig. B.1 (m)-(p)], as discussed in Sec. 6.4.3.

In Sec. 6.4.3, a symmetry which relates the spin-spin correlation functions $S^x(q)$ and $S^z(\omega)$ for $\lambda/t = \lambda_s$ has been derived [Eq. (6.53)], based on an effective low-energy model (6.43). While this derivation has been shown to hold only in the absence of Rashba spin-orbit coupling, the dynamic spin structure factors of the πKM model still show signs of this symmetry at moderate values of the Rashba coupling (here $\lambda_\mathrm{R}/t = 0.3$).

By comparing $S^{xx}(q,\omega)$ [Fig. B.1(g)] with $S^{zz}(q,\omega)$ [Fig. B.1(h)], one observes that $S^{xx}(q,\omega) \approx S^{zz}(q+\pi,\omega)$. This symmetry is clearly absent for the other values of the spin-orbit coupling λ/t.

The spin scattering processes within each Dirac cone (intra-orbital scattering) contribute to the dynamical spin structure factors at zero momentum transfer ($q = 0$) whereas the spin scattering processes between the Dirac cones (inter-orbital scattering) contribute at a momentum transfer $q = \pi$. At $\lambda/t = 0.65$ [Fig. B.1 (g)], the approximately linear mode of $S^{xx}(\pi,\omega)$ at low energies relates to a spin-flip scattering process which becomes particular effective since the edge modes have opposite chirality. This feature is absent at $\lambda/t = 2$ [Fig. B.1 (o)]. For this value of spin-orbit coupling, linear low-energy modes at both $S^{zz}(0,\omega)$

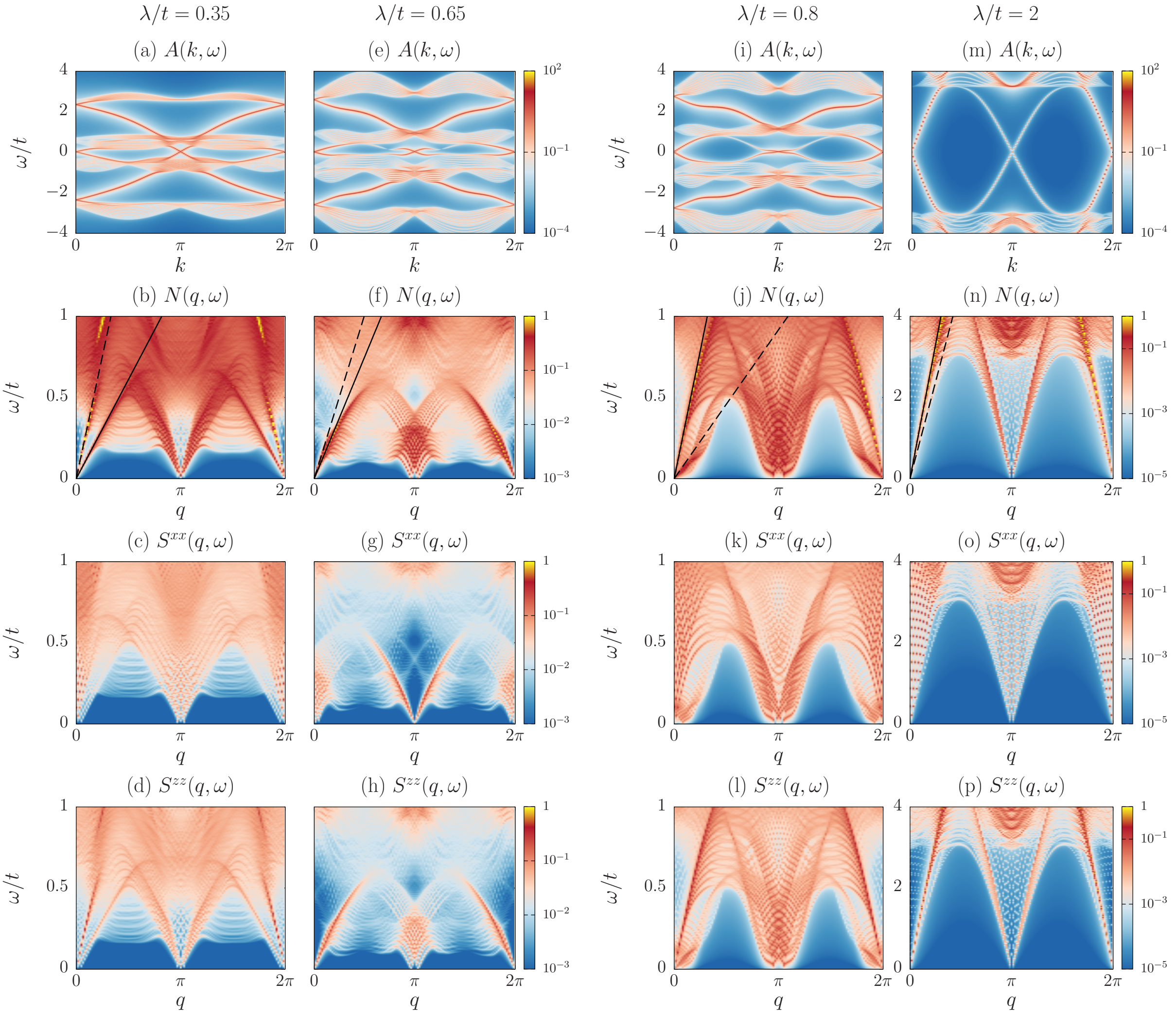

Figure B.1: Edge excitations at $\lambda_{\mathrm{R}}/t = 0.3$, including the spectral function $A_i(k,\omega)$ and the dynamical charge and spin structure factors $N(q,\omega)$ and $S^{xx(zz)}(q,\omega)$. The Fermi velocities v_0 and v_π are indicated by solid and dotted lines, respectively.

and $S^{zz}(\pi, \omega)$ are observed in agreement with the equal chiralities of the edge modes which makes possible low-energy scattering processes that (approximatively) preserve the spin.

Acknowledgments

During the last years, I have had the pleasure to be in a stimulating research environment. First of all, I would like to thank Fakher Assaad, the supervisor of my thesis. I have enjoyed working on interesting projects in your research group a lot.

I am also grateful to Martin Hohenadler for collaboration, and to Björn Trauzettel, François Crépin, Kai Fauth and Christian Praetorius for valuable discussions.

I would like to thank my office mates and PhD colleagues, both former and current, and friends in the department, Thomas Lang, Jutta Ortloff, Lee Martin, David Luitz, Florian Goth, Jan Werner, Kuang-Shing Chen, Francesco Parisen Toldin, Nico Parragh, Manuel Weber, Johannes Hofmann and Stefan Beyl, and also the department secretary Alexandra Lösch for the cheerful atmosphere and for many enlightening discussions.

Many thanks go to Manuel Weber, Thomas Lang and Jan Werner for proof-reading.

Thank you Janine for your support.

Bibliography

[1] J. Kondo, “Resistance Minimum in Dilute Magnetic Alloys”, *Progress of Theoretical Physics* **32** no. 1, (1964) 37–49. `http://ptp.ipap.jp/link?PTP/32/37/`.

[2] K. G. Wilson, “The renormalization group: Critical phenomena and the Kondo problem”, *Rev. Mod. Phys.* **47** (Oct, 1975) 773–840. `http://link.aps.org/doi/10.1103/RevModPhys.47.773`.

[3] A. C. Hewson, *The Kondo Problem To Heavy Fermions.* Cambridge University Press, Cambridge UK, 1997.

[4] H. Tsunetsugu, M. Sigrist, and K. Ueda, “The ground-state phase diagram of the one-dimensional Kondo lattice model”, *Rev. Mod. Phys.* **69** (Jul, 1997) 809–864. `http://link.aps.org/doi/10.1103/RevModPhys.69.809`.

[5] P. Gegenwart, Q. Si, and F. Steglich, “Quantum criticality in heavy-fermion metals”, *Nature Phys.* **4** (2008) 186.

[6] S. Yamamoto and Q. Si, “Global Phase Diagram of the Kondo Lattice: FromHeavy Fermion Metals to Kondo Insulators”, *Journal of Low Temperature Physics* **161** (2010) 233–262. `http://dx.doi.org/10.1007/s10909-010-0221-4`. 10.1007/s10909-010-0221-4.

[7] P. Coleman and A. Nevidomskyy, “Frustration and the Kondo Effect in Heavy Fermion Materials”, *Journal of Low Temperature Physics* **161** (2010) 182–202. `http://dx.doi.org/10.1007/s10909-010-0213-4`.

[8] E. Bauer and M. Rotter, *Magnetism of complex metallic alloys: crystalline electric field effects (Lecture Notes for the CMA Euroschool 2007, Ljubljana, Slovenia).* 2007.

[9] J. Flouquet, “On the Heavy Fermion Road”, *eprint arXiv:cond-mat/0501602* (Jan., 2005) , `cond-mat/0501602`.

[10] J. R. Schrieffer and P. A. Wolff, “Relation between the Anderson and Kondo Hamiltonians”, *Phys. Rev.* **149** (Sep, 1966) 491–492. `http://link.aps.org/doi/10.1103/PhysRev.149.491`.

[11] H. Tsunetsugu, "Rigorous results for half-filled Kondo lattices", *Phys. Rev. B* **55** (Feb, 1997) 3042–3045. `http://link.aps.org/doi/10.1103/PhysRevB.55.3042`.

[12] J. Otsuki, H. Kusunose, and Y. Kuramoto, "Evolution of a Large Fermi Surface in the Kondo Lattice", *Phys. Rev. Lett.* **102** (Jan, 2009) 017202. `http://link.aps.org/doi/10.1103/PhysRevLett.102.017202`.

[13] S. Doniach, "The Kondo lattice and weak antiferromagnetism", *Physica B+C* **91** no. 0, (1977) 231 – 234. `http://www.sciencedirect.com/science/article/pii/0378436377901905`.

[14] S. Burdin, A. Georges, and D. R. Grempel, "Coherence Scale of the Kondo Lattice", *Phys. Rev. Lett.* **85** (Jul, 2000) 1048–1051. `http://link.aps.org/doi/10.1103/PhysRevLett.85.1048`.

[15] F. F. Assaad, "Coherence scale of the two-dimensional Kondo lattice model", *Phys. Rev. B* **70** (Jul, 2004) 020402. `http://link.aps.org/doi/10.1103/PhysRevB.70.020402`.

[16] H. Watanabe and M. Ogata, "Fermi-Surface Reconstruction without Breakdown of Kondo Screening at the Quantum Critical Point", *Phys. Rev. Lett.* **99** (Sep, 2007) 136401. `http://link.aps.org/doi/10.1103/PhysRevLett.99.136401`.

[17] L. C. Martin, M. Bercx, and F. F. Assaad, "Fermi surface topology of the two-dimensional Kondo lattice model: Dynamical cluster approximation approach", *Phys. Rev. B* **82** (Dec, 2010) 245105. `http://link.aps.org/doi/10.1103/PhysRevB.82.245105`.

[18] S. Capponi and F. F. Assaad, "Spin and charge dynamics of the ferromagnetic and antiferromagnetic two-dimensional half-filled Kondo lattice model", *Phys. Rev. B* **63** (Mar, 2001) 155114. `http://link.aps.org/doi/10.1103/PhysRevB.63.155114`.

[19] F. Assaad, "Quantum Monte Carlo Simulations of the Half-Filled Two-Dimensional Kondo Lattice Model", *Phys. Rev. Lett.* **83** (Jul, 1999) 796–799. `http://link.aps.org/doi/10.1103/PhysRevLett.83.796`.

[20] M. Vojta, "From itinerant to local-moment antiferromagnetism in Kondo lattices: Adiabatic continuity versus quantum phase transitions", *Phys. Rev. B* **78** (Sep, 2008) 125109. `http://link.aps.org/doi/10.1103/PhysRevB.78.125109`.

[21] A. P. Schnyder, S. Ryu, A. Furusaki, and A. W. W. Ludwig, "Classification of Topological Insulators and Superconductors", in *American Institute of Physics Conference Series*, V. Lebedev and M. Feigel'Man, eds., vol. 1134 of *American Institute of Physics Conference Series*, pp. 10–21. May, 2009. `arXiv:0905.2029 [cond-mat.mes-hall]`.

[22] C. L. Kane and E. J. Mele, "Z_2 Topological Order and the Quantum Spin Hall Effect", *Phys. Rev. Lett.* **95** (Sep, 2005) 146802. `http://link.aps.org/doi/10.1103/PhysRevLett.95.146802`.

[23] C. L. Kane and E. J. Mele, "Quantum Spin Hall Effect in Graphene", *Phys. Rev. Lett.* **95** (Nov, 2005) 226801. `http://link.aps.org/doi/10.1103/PhysRevLett.95.226801`.

[24] B. A. Bernevig, T. L. Hughes, and S.-C. Zhang, "Quantum Spin Hall Effect and Topological Phase Transition in HgTe Quantum Wells", *Science* **314** no. 5806, (2006) 1757–1761. `http://www.sciencemag.org/content/314/5806/1757.abstract`.

[25] M. König, S. Wiedmann, C. Brüne, A. Roth, H. Buhmann, L. W. Molenkamp, X.-L. Qi, and S.-C. Zhang, "Quantum Spin Hall Insulator State in HgTe Quantum Wells", *Science* **318** no. 5851, (2007) 766–770. `http://www.sciencemag.org/content/318/5851/766.abstract`.

[26] C. Xu and J. E. Moore, "Stability of the quantum spin Hall effect: Effects of interactions, disorder, and Z2 topology", *Phys. Rev. B* **73** (Jan, 2006) 045322. `http://link.aps.org/doi/10.1103/PhysRevB.73.045322`.

[27] J. J. Sakurai, *Modern Quantum Mechanics.* Addison-Wesley, Reading, Massachusetts, 1994.

[28] C. Wu, B. A. Bernevig, and S.-C. Zhang, "Helical Liquid and the Edge of Quantum Spin Hall Systems", *Phys. Rev. Lett.* **96** (Mar, 2006) 106401. `http://link.aps.org/doi/10.1103/PhysRevLett.96.106401`.

[29] D. Thouless, M. Kohmoto, M. Nightingale, and M. den Nijs, "Quantized hall conductance in a two-dimensional periodic potential", *Phys. Rev. Lett.* **49** (Aug, 1982) 405–408. `http://link.aps.org/doi/10.1103/PhysRevLett.49.405`.

[30] M. Kohmoto, "Topological invariant and the quantization of the Hall conductance", *Annals of Physics* **160** no. 2, (1985) 343 – 354. `http://www.sciencedirect.com/science/article/pii/0003491685901484`.

[31] L. Fu and C. L. Kane, "Topological insulators with inversion symmetry", *Phys. Rev. B* **76** (Jul, 2007) 045302. `http://link.aps.org/doi/10.1103/PhysRevB.76.045302`.

[32] E. Prodan, "Manifestly gauge-independent formulations of the Z_2 invariants", *Phys. Rev. B* **83** (Jun, 2011) 235115. `http://link.aps.org/doi/10.1103/PhysRevB.83.235115`.

[33] Z. Wang and S.-C. Zhang, "Strongly correlated topological superconductors and topological phase transitions via Green's function", *Phys. Rev. B* **86** (Oct, 2012) 165116. `http://link.aps.org/doi/10.1103/PhysRevB.86.165116`.

[34] Z. Wang, X.-L. Qi, and S.-C. Zhang, "Topological invariants for interacting topological insulators with inversion symmetry", *Phys. Rev. B* **85** (Apr, 2012) 165126. `http://link.aps.org/doi/10.1103/PhysRevB.85.165126`.

[35] M. Hohenadler and F. F. Assaad, "Correlation effects in two-dimensional topological insulators", *Journal of Physics: Condensed Matter* **25** no. 14, (2013) 143201. `http://stacks.iop.org/0953-8984/25/i=14/a=143201`.

[36] Z. Y. Meng, H.-H. Hung, and T. C. Lang, "The characterization of topological properties in Quantum Monte Carlo simulations of the Kane-Mele-Hubbard model", *Modern Physics Letters B* (2013) 1430001. `http://dx.doi.org/10.1142/S0217984914300014`.

[37] Y. Ran, A. Vishwanath, and D.-H. Lee, "Spin-Charge Separated Solitons in a Topological Band Insulator", *Phys. Rev. Lett.* **101** (Aug, 2008) 086801. `http://link.aps.org/doi/10.1103/PhysRevLett.101.086801`.

[38] X.-L. Qi and S.-C. Zhang, "Spin-Charge Separation in the Quantum Spin Hall State", *Phys. Rev. Lett.* **101** (Aug, 2008) 086802. `http://link.aps.org/doi/10.1103/PhysRevLett.101.086802`.

[39] V. Juričić, A. Mesaros, R.-J. Slager, and J. Zaanen, "Universal Probes of Two-Dimensional Topological Insulators: Dislocation and π Flux", *Phys. Rev. Lett.* **108** (Mar, 2012) 106403. `http://link.aps.org/doi/10.1103/PhysRevLett.108.106403`.

[40] A. Rüegg and C. Lin, "Bound States of Conical Singularities in Graphene-Based Topological Insulators", *Phys. Rev. Lett.* **110** (Jan, 2013) 046401. `http://link.aps.org/doi/10.1103/PhysRevLett.110.046401`.

[41] L. Fu, "Topological Crystalline Insulators", *Phys. Rev. Lett.* **106** (Mar, 2011) 106802. `http://link.aps.org/doi/10.1103/PhysRevLett.106.106802`.

[42] T. H. Hsieh, H. Lin, J. Liu, W. Duan, A. Bansil, and L. Fu, "Topological crystalline insulators in the SnTe material class", *Nat. Commun.* **3** (2012) 982. `http://dx.doi.org/10.1038/ncomms1969`.

[43] R. Slager, A. Mesaros, V. Juricic, and J. Zaanen, "The space group classification of topological band-insulators", *Nat. Phys.* **9** no. 2, (2013) 98–102. `http://dx.doi.org/10.1038/nphys2513`.

[44] Y. Tanaka, Z. Ren, T. Sato, K. Nakayama, S. Souma, T. Takahashi, K. Segawa, and Y. Ando, "Experimental realization of a topological crystalline insulator in SnTe", *Nat. Phys.* **8** no. 11, (2012) 800–803. `http://dx.doi.org/10.1038/nphys2442`.

[45] P. Dziawa, B. Kowalski, K. Dybko, R. Buczko, A. Szczerbakow, M. Szot, E. Lusakowska, T. Balasubramanian, B. Wojek, M. Berntsen, O. Tjernberg, and

T. Story, “Topological crystalline insulator states inPb1xSnxSe”, *Nat. Mater.* **11** no. 12, (2012) 1023–1027. `http://dx.doi.org/10.1038/nmat3449`.

[46] S. Xu, C. Liu, N. Alidoust, M. Neupane, D. Qian, I. Belopolski, J. Denlinger, Y. Wang, H. Lin, L. Wray, G. Landolt, B. Slomski, J. Dil, A. Marcinkova, E. Morosan, Q. Gibson, R. Sankar, F. Chou, R. Cava, A. Bansil, and M. Hasan, “Observation of a topological crystalline insulator phase and topological phase transition in Pb1xSnxTe”, *Nat. Commun.* **3** (2012) 1192. `http://dx.doi.org/10.1038/ncomms2191`.

[47] F. D. M. Haldane, “Model for a Quantum Hall Effect without Landau Levels: Condensed-Matter Realization of the ”Parity Anomaly””, *Phys. Rev. Lett.* **61** (Oct, 1988) 2015–2018. `http://link.aps.org/doi/10.1103/PhysRevLett.61.2015`.

[48] A. Castro Neto, F. Guinea, N. Peres, K. Novoselov, and A. Geim, “The electronic properties of graphene”, *Rev. Mod. Phys.* **81** (Jan, 2009) 109–162. `http://link.aps.org/doi/10.1103/RevModPhys.81.109`.

[49] M. Hohenadler, Z. Y. Meng, T. C. Lang, S. Wessel, A. Muramatsu, and F. F. Assaad, “Quantum phase transitions in the Kane-Mele-Hubbard model”, *Phys. Rev. B* **85** (Mar, 2012) 115132. `http://link.aps.org/doi/10.1103/PhysRevB.85.115132`.

[50] F. F. Assaad and I. F. Herbut, “Pinning the Order: The Nature of Quantum Criticality in the Hubbard Model on Honeycomb Lattice”, *Phys. Rev. X* **3** (Aug, 2013) 031010. `http://link.aps.org/doi/10.1103/PhysRevX.3.031010`.

[51] C. Griset and C. Xu, “Phase diagram of the Kane-Mele-Hubbard model”, *Phys. Rev. B* **85** (Jan, 2012) 045123. `http://link.aps.org/doi/10.1103/PhysRevB.85.045123`.

[52] S. Rachel and K. Le Hur, “Topological insulators and Mott physics from the Hubbard interaction”, *Phys. Rev. B* **82** (Aug, 2010) 075106. `http://link.aps.org/doi/10.1103/PhysRevB.82.075106`.

[53] D.-H. Lee, “Effects of Interaction on Quantum Spin Hall Insulators”, *Phys. Rev. Lett.* **107** (Oct, 2011) 166806. `http://link.aps.org/doi/10.1103/PhysRevLett.107.166806`.

[54] A. Läuchli, “Exact Diagonalization”, in *Fall School on Advanced Algorithms for Correlated Quantum Matter (Würzburg, 30.09.2013-04.10.2013).*

[55] F. F. Assaad, “Quantum Simulations of Complex Many-Body Systems: From Theory to Algorithms - Lecture Notes”, in *Computational Many Particle Physics*, J. Grotendorst, D. Marx, and A. Muramatsu, eds., vol. 10 of *NIC Series*, p. 548. 2002.

[56] N. Metropolis, A. W. Rosenbluth, M. N. Rosenbluth, A. H. Teller, and E. Teller, “Equation of State Calculations by Fast Computing Machines”, *The Journal of*

Chemical Physics **21** no. 6, (1953) 1087–1092.
`http://scitation.aip.org/content/aip/journal/jcp/21/6/10.1063/1.1699114`.

[57] M. Troyer, *Classical and Quantum Monte Carlo Algorithms (Lecture Notes)*. ETH Zürich, 2003.

[58] B. Efron, *The Jackknife, the Bootstrap and other Resampling Plans*. SIAM, Philadelphia, 1982.

[59] H. Bruus and E. Flensberg, *Many-Body Quantum Theory in Condensed Matter Physics*. Oxford University Press, Oxford UK, 2004.

[60] J. W. Negele and H. Orland, *Quantum Many-Particle Systems*. Addison-Wesley, Boston US, 1988.

[61] R. Blankenbecler and R. L. Sugar, "Projector Monte Carlo method", *Phys. Rev. D* **27** (Mar, 1983) 1304–1311. `http://link.aps.org/doi/10.1103/PhysRevD.27.1304`.

[62] F. F. Assaad and H. G. Evertz, "World-line and Determinantal Quantum Monte Carlo Methods for Spins, Phonons and Electrons", in *Computational Many Particle Physics*, H. Fehske, R. Schneider, and A. Weiße, eds., vol. 739 of *Lecture Notes in Physics*, p. 277. Springer Verlag, Berlin, 2008.

[63] H. Shi, C. A. Jimenez-Hoyos, R. Rodriguez-Guzman, G. E. Scuseria, and S. Zhang, "Symmetry-projected wave functions in quantum Monte Carlo calculations", *Phys. Rev. B* **89** (Mar, 2014) 125129.
`http://link.aps.org/doi/10.1103/PhysRevB.89.125129`.

[64] J. Hubbard, "Calculation of Partition Functions", *Phys. Rev. Lett.* **3** (Jul, 1959) 77–78. `http://link.aps.org/doi/10.1103/PhysRevLett.3.77`.

[65] R. M. Fye, "New results on Trotter-like approximations", *Phys. Rev. B* **33** (May, 1986) 6271–6280. `http://link.aps.org/doi/10.1103/PhysRevB.33.6271`.

[66] H. Shi and S. Zhang, "Symmetry in auxiliary-field quantum Monte Carlo calculations", *Phys. Rev. B* **88** (Sep, 2013) 125132.
`http://link.aps.org/doi/10.1103/PhysRevB.88.125132`.

[67] J. E. Hirsch, "Discrete Hubbard-Stratonovich transformation for fermion lattice models", *Phys. Rev. B* **28** (Oct, 1983) 4059–4061.
`http://link.aps.org/doi/10.1103/PhysRevB.28.4059`.

[68] M. Feldbacher and F. F. Assaad, "Efficient calculation of imaginary-time-displaced correlation functions in the projector auxiliary-field quantum Monte Carlo algorithm", *Phys. Rev. B* **63** (Jan, 2001) 073105.
`http://link.aps.org/doi/10.1103/PhysRevB.63.073105`.

[69] R. Blankenbecler, D. J. Scalapino, and R. L. Sugar, “Monte Carlo calculations of coupled boson-fermion systems. I”, *Phys. Rev. D* **24** (Oct, 1981) 2278–2286. `http://link.aps.org/doi/10.1103/PhysRevD.24.2278`.

[70] J. E. Hirsch, “Two-dimensional Hubbard model: Numerical simulation study”, *Phys. Rev. B* **31** (Apr, 1985) 4403–4419. `http://link.aps.org/doi/10.1103/PhysRevB.31.4403`.

[71] J. E. Hirsch and R. M. Fye, “Monte Carlo Method for Magnetic Impurities in Metals”, *Phys. Rev. Lett.* **56** (Jun, 1986) 2521–2524. `http://link.aps.org/doi/10.1103/PhysRevLett.56.2521`.

[72] A. Tsvelik, *Quantum Field Theory in Condensed Matter Physics.* Cambridge University Press, Cambridge UK, 2003.

[73] J. E. Hirsch, “Stable Monte Carlo algorithm for Fermion lattice systems at low temperatures”, *Phys. Rev. B* **38** (Dec, 1988) 12023–12026. `http://link.aps.org/doi/10.1103/PhysRevB.38.12023`.

[74] R. M. Fye and J. E. Hirsch, “Monte Carlo study of the symmetric Anderson-impurity model”, *Phys. Rev. B* **38** (Jul, 1988) 433–441. `http://link.aps.org/doi/10.1103/PhysRevB.38.433`.

[75] W. Hager, “Updating the Inverse of a Matrix”, *SIAM Review* **31** no. 2, (1989) 221–239, `http://dx.doi.org/10.1137/1031049`. `http://dx.doi.org/10.1137/1031049`.

[76] G. Alvarez, M. S. Summers, D. E. Maxwell, M. Eisenbach, J. S. Meredith, J. M. Larkin, J. Levesque, T. A. Maier, P. R. C. Kent, and E. F. D. *et al.* in *SC 08: Proceedings of the 2008 ACM/IEEE Conference on Supercomputing*, p. 110. IEEE Press, Piscataway N.J., 2008.

[77] M. Troyer and U.-J. Wiese, “Computational Complexity and Fundamental Limitations to Fermionic Quantum Monte Carlo Simulations”, *Phys. Rev. Lett.* **94** (May, 2005) 170201. `http://link.aps.org/doi/10.1103/PhysRevLett.94.170201`.

[78] S. Zhang, “Constrained Path Monte Carlo For Fermions”, *eprint arXiv:cond-mat/9909090* (Sept., 1999) , `cond-mat/9909090`.

[79] S. Zhang, “Finite-Temperature Monte Carlo Calculations for Systems with Fermions”, *Phys. Rev. Lett.* **83** (Oct, 1999) 2777–2780. `http://link.aps.org/doi/10.1103/PhysRevLett.83.2777`.

[80] A. N. Rubtsov, V. V. Savkin, and A. I. Lichtenstein, “Continuous-time quantum Monte Carlo method for fermions”, *Phys. Rev. B* **72** (Jul, 2005) 035122. `http://link.aps.org/doi/10.1103/PhysRevB.72.035122`.

[81] D. J. Luitz, *Numerical methods and applications in many fermion systems.* PhD thesis, Universität Würzburg, 2012.

[82] E. Gull, A. J. Millis, A. I. Lichtenstein, A. N. Rubtsov, M. Troyer, and P. Werner, "Continuous-time Monte Carlo methods for quantum impurity models", *Rev. Mod. Phys.* **83** (May, 2011) 349–404. `http://link.aps.org/doi/10.1103/RevModPhys.83.349`.

[83] F. F. Assaad and T. C. Lang, "Diagrammatic determinantal quantum Monte Carlo methods: Projective schemes and applications to the Hubbard-Holstein model", *Phys. Rev. B* **76** (Jul, 2007) 035116. `http://link.aps.org/doi/10.1103/PhysRevB.76.035116`.

[84] W. Metzner and D. Vollhardt, "Correlated Lattice Fermions in $d = \infty$ Dimensions", *Phys. Rev. Lett.* **62** (Jan, 1989) 324–327. `http://link.aps.org/doi/10.1103/PhysRevLett.62.324`.

[85] E. Müller-Hartmann, "Correlated fermions on a lattice in high dimensions", *Zeitschrift für Physik B Condensed Matter* **74** no. 4, (1989) 507–512. `http://dx.doi.org/10.1007/BF01311397`.

[86] A. Georges and G. Kotliar, "Hubbard model in infinite dimensions", *Phys. Rev. B* **45** (Mar, 1992) 6479–6483. `http://link.aps.org/doi/10.1103/PhysRevB.45.6479`.

[87] A. Georges, G. Kotliar, W. Krauth, and M. J. Rozenberg, "Dynamical mean-field theory of strongly correlated fermion systems and the limit of infinite dimensions", *Rev. Mod. Phys.* **68** (Jan, 1996) 13–125. `http://link.aps.org/doi/10.1103/RevModPhys.68.13`.

[88] T. Maier, M. Jarrell, T. Pruschke, and M. H. Hettler, "Quantum cluster theories", *Rev. Mod. Phys.* **77** (Oct, 2005) 1027–1080. `http://link.aps.org/doi/10.1103/RevModPhys.77.1027`.

[89] N. D. Mermin and H. Wagner, "Absence of Ferromagnetism or Antiferromagnetism in One- or Two-Dimensional Isotropic Heisenberg Models", *Phys. Rev. Lett.* **17** (Nov, 1966) 1133–1136. `http://link.aps.org/doi/10.1103/PhysRevLett.17.1133`.

[90] M. H. Hettler, A. N. Tahvildar-Zadeh, M. Jarrell, T. Pruschke, and H. R. Krishnamurthy, "Nonlocal dynamical correlations of strongly interacting electron systems", *Phys. Rev. B* **58** (Sep, 1998) R7475–R7479. `http://link.aps.org/doi/10.1103/PhysRevB.58.R7475`.

[91] M. Jarrell, T. Maier, C. Huscroft, and S. Moukouri, "Quantum Monte Carlo algorithm for nonlocal corrections to the dynamical mean-field approximation", *Phys. Rev. B* **64** (Oct, 2001) 195130. `http://link.aps.org/doi/10.1103/PhysRevB.64.195130`.

[92] M. Jarrell, A. Macridin, K. Mikelsons, D. G. S. P. Doluweera, and J. E. Gubernatis, "The Dynamical Cluster Approximation with Quantum Monte Carlo Cluster Solvers", *AIP Conference Proceedings* **1014** no. 1, (2008) 34–106. `http://scitation.aip.org/content/aip/proceeding/aipcp/10.1063/1.2940445`.

[93] M. H. Hettler, M. Mukherjee, M. Jarrell, and H. R. Krishnamurthy, "Dynamical cluster approximation: Nonlocal dynamics of correlated electron systems", *Phys. Rev. B* **61** (May, 2000) 12739–12756. `http://link.aps.org/doi/10.1103/PhysRevB.61.12739`.

[94] K. S. D. Beach, "Identifying the maximum entropy method as a special limit of stochastic analytic continuation", *eprint arXiv:cond-mat/0403055* (Mar., 2004) .

[95] K. S. D. Beach, R. J. Gooding, and F. Marsiglio, "Reliable Padé analytical continuation method based on a high-accuracy symbolic computation algorithm", *Phys. Rev. B* **61** (Feb, 2000) 5147–5157. `http://link.aps.org/doi/10.1103/PhysRevB.61.5147`.

[96] M. Bercx and F. F. Assaad, "Metamagnetism and Lifshitz transitions in models for heavy fermions", *Phys. Rev. B* **86** (Aug, 2012) 075108. `http://link.aps.org/doi/10.1103/PhysRevB.86.075108`.

[97] R. Daou, C. Bergemann, and S. R. Julian, "Continuous Evolution of the Fermi Surface of $CeRu_2Si_2$ across the Metamagnetic Transition", *Phys. Rev. Lett.* **96** (Jan, 2006) 026401. `http://link.aps.org/doi/10.1103/PhysRevLett.96.026401`.

[98] H. Pfau, R. Daou, M. Brando, and F. Steglich, "Thermoelectric transport across the metamagnetic transition of $CeRu_2Si_2$", *Phys. Rev. B* **85** (Jan, 2012) 035127. `http://link.aps.org/doi/10.1103/PhysRevB.85.035127`.

[99] H. Aoki, S. Uji, A. K. Albessard, and Y. Onuki, "Transition of f electron nature from itinerant to localized: Metamagnetic transition in $CeRu_2Si_2$ studied via the de Haas˘van Alphen effect", *Phys. Rev. Lett.* **71** (Sep, 1993) 2110–2113. `http://link.aps.org/doi/10.1103/PhysRevLett.71.2110`.

[100] M. Sugi, Y. Matsumoto, N. Kimura, T. Komatsubara, H. Aoki, T. Terashima, and S. Uji, "Fermi Surface Properties of $CeRu_2(Si_{1-x}Ge_x)_2$ in Magnetic Fields above the Metamagnetic Transitions", *Phys. Rev. Lett.* **101** (Jul, 2008) 056401. `http://link.aps.org/doi/10.1103/PhysRevLett.101.056401`.

[101] S. Kitagawa, H. Ikeda, Y. Nakai, T. Hattori, K. Ishida, Y. Kamihara, M. Hirano, and H. Hosono, "Metamagnetic Behavior and Kondo Breakdown in Heavy-Fermion CeFePO", *Phys. Rev. Lett.* **107** (Dec, 2011) 277002. `http://link.aps.org/doi/10.1103/PhysRevLett.107.277002`.

[102] P. Haen, J. Flouquet, F. Lapierre, P. Lejay, and G. Remenyi, "Metamagnetic-like transition in CeRu2Si2", *Journal of Low Temperature Physics* **67** (1987) 391–419. `http://dx.doi.org/10.1007/BF00710351`. 10.1007/BF00710351.

[103] W. Wu, A. McCollam, S. A. Grigera, R. S. Perry, A. P. Mackenzie, and S. R. Julian, "Quantum critical metamagnetism of $Sr_3Ru_2O_7$ under hydrostatic pressure", *Phys. Rev. B* **83** (Jan, 2011) 045106. `http://link.aps.org/doi/10.1103/PhysRevB.83.045106`.

[104] M. Deppe, S. Lausberg, F. Weickert, M. Brando, Y. Skourski, N. Caroca-Canales, C. Geibel, and F. Steglich, "Pronounced first-order metamagnetic transition in the paramagnetic heavy-fermion system CeTiGe", *Phys. Rev. B* **85** (Feb, 2012) 060401. `http://link.aps.org/doi/10.1103/PhysRevB.85.060401`.

[105] F. Weickert, M. Brando, F. Steglich, P. Gegenwart, and M. Garst, "Universal signatures of the metamagnetic quantum critical endpoint: Application to $CeRu_2Si_2$", *Phys. Rev. B* **81** (Apr, 2010) 134438. `http://link.aps.org/doi/10.1103/PhysRevB.81.134438`.

[106] A. J. Millis, A. J. Schofield, G. G. Lonzarich, and S. A. Grigera, "Metamagnetic Quantum Criticality in Metals", *Phys. Rev. Lett.* **88** (May, 2002) 217204. `http://link.aps.org/doi/10.1103/PhysRevLett.88.217204`.

[107] S. Viola Kusminskiy, K. S. D. Beach, A. H. Castro Neto, and D. K. Campbell, "Mean-field study of the heavy-fermion metamagnetic transition", *Phys. Rev. B* **77** (Mar, 2008) 094419. `http://link.aps.org/doi/10.1103/PhysRevB.77.094419`.

[108] O. Howczak and J. Spałek, "Anderson lattice with explicit Kondo coupling revisited: metamagnetism and the field-induced suppression of the heavy fermion state", *Journal of Physics: Condensed Matter* **24** no. 20, (2012) 205602. `http://stacks.iop.org/0953-8984/24/i=20/a=205602`.

[109] K. S. D. Beach and F. F. Assaad, "Coherence and metamagnetism in the two-dimensional Kondo lattice model", *Phys. Rev. B* **77** (May, 2008) 205123. `http://link.aps.org/doi/10.1103/PhysRevB.77.205123`.

[110] I. M. Lifshitz *Sov. Phys. JETP* **11** (1960) 1130.

[111] Y. Blanter, M. Kaganov, A. Pantsulaya, and A. Varlamov, "The theory of electronic topological transitions", *Physics Reports* **245** no. 4, (1994) 159 – 257. `http://www.sciencedirect.com/science/article/pii/0370157394901031`.

[112] Y. Yamaji, T. Misawa, and M. Imada, "Quantum and Topological Criticalities of Lifshitz Transition in Two-Dimensional Correlated Electron Systems", *Journal of the Physical Society of Japan* **75** no. 9, (2006) 094719. `http://jpsj.ipap.jp/link?JPSJ/75/094719/`.

[113] A. Hackl and M. Vojta, "Kondo volume collapse, Kondo breakdown, and Fermi surface transitions in heavy-fermion metals", *Phys. Rev. B* **77** (Apr, 2008) 134439. `http://link.aps.org/doi/10.1103/PhysRevB.77.134439`.

[114] G.-M. Zhang, Y.-H. Su, and L. Yu, "Lifshitz transitions in a heavy Fermi liquid driven by short-range antiferromagnetic correlations in the two-dimensional Kondo lattice model", *Phys. Rev. B* **83** (Jan, 2011) 033102. `http://link.aps.org/doi/10.1103/PhysRevB.83.033102`.

[115] A. Hackl and M. Vojta, "Zeeman-Driven Lifshitz Transition: A Model for the Experimentally Observed Fermi-Surface Reconstruction in $\mathrm{YbRh_2Si_2}$", *Phys. Rev. Lett.* **106** (Mar, 2011) 137002. `http://link.aps.org/doi/10.1103/PhysRevLett.106.137002`.

[116] S. Burdin, "Low energy scales of kondo lattices: Mean-field perspective", in *Properties and Applications of Thermoelectric Materials*, V. Zlati and A. C. Hewson, eds., NATO Science for Peace and Security Series B: Physics and Biophysics, pp. 325–340. Springer Netherlands, 2009.

[117] N. Read and D. M. Newns, "On the solution of the Coqblin-Schreiffer Hamiltonian by the large-N expansion technique", *Journal of Physics C: Solid State Physics* **16** no. 17, (1983) 3273. `http://stacks.iop.org/0022-3719/16/i=17/a=014`.

[118] J. B. Marston and I. Affleck, "Large-n limit of the Hubbard-Heisenberg model", *Phys. Rev. B* **39** (Jun, 1989) 11538–11558. `http://link.aps.org/doi/10.1103/PhysRevB.39.11538`.

[119] D. Withoff and E. Fradkin, "Magnetization of the Coqblin-Schrieffer model in the large-N limit at nonzero field", *Phys. Rev. B* **34** (Dec, 1986) 8172–8175. `http://link.aps.org/doi/10.1103/PhysRevB.34.8172`.

[120] S. Saremi and P. A. Lee, "Quantum critical point in the Kondo-Heisenberg model on the honeycomb lattice", *Phys. Rev. B* **75** (Apr, 2007) 165110. `http://link.aps.org/doi/10.1103/PhysRevB.75.165110`.

[121] M. Oshikawa, "Topological Approach to Luttinger's Theorem and the Fermi Surface of a Kondo Lattice", *Phys. Rev. Lett.* **84** (Apr, 2000) 3370–3373. `http://link.aps.org/doi/10.1103/PhysRevLett.84.3370`.

[122] M. Vojta, "Orbital-Selective Mott Transitions: Heavy Fermions and Beyond", *Journal of Low Temperature Physics* **161** (2010) 203–232. `http://dx.doi.org/10.1007/s10909-010-0206-3`. 10.1007/s10909-010-0206-3.

[123] D. Tanasković, K. Haule, G. Kotliar, and V. Dobrosavljević, "Phase diagram, energy scales, and nonlocal correlations in the Anderson lattice model", *Phys. Rev. B* **84** (Sep, 2011) 115105. `http://link.aps.org/doi/10.1103/PhysRevB.84.115105`.

[124] L.-F. Arsenault, P. Sémon, and A.-M. S. Tremblay, "Benchmark of a modified iterated perturbation theory approach on the fcc lattice at strong coupling", *Phys. Rev. B* **86** (Aug, 2012) 085133. `http://link.aps.org/doi/10.1103/PhysRevB.86.085133`.

[125] A. Benlagra, T. Pruschke, and M. Vojta, "Finite-temperature spectra and quasiparticle interference in Kondo lattices: From light electrons to coherent heavy quasiparticles", *Phys. Rev. B* **84** (Nov, 2011) 195141. `http://link.aps.org/doi/10.1103/PhysRevB.84.195141`.

[126] R. Peters, N. Kawakami, and T. Pruschke, "Spin-Selective Kondo Insulator: Cooperation of Ferromagnetism and the Kondo Effect", *Phys. Rev. Lett.* **108** (Feb, 2012) 086402. `http://link.aps.org/doi/10.1103/PhysRevLett.108.086402`.

[127] J. Flouquet, P. Haen, S. Raymond, D. Aoki, and G. Knebel, "Itinerant metamagnetism of CeRu2Si2: bringing out the dead. Comparison with the new Sr3Ru2O7 case", *Physica B: Condensed Matter* **319** no. 14, (2002) 251 – 261.

[128] M. Raczkowski, P. Zhang, F. F. Assaad, T. Pruschke, and M. Jarrell, "Phonons and the coherence scale of models of heavy fermions", *Phys. Rev. B* **81** (Feb, 2010) 054444. `http://link.aps.org/doi/10.1103/PhysRevB.81.054444`.

[129] X.-G. Wen, *Quantum Field Theory of Many-Body Systems.* Oxford University Press, Oxford UK, 2004.

[130] R. Jackiw and C. Rebbi, "Solitons with fermion number 1/2", *Phys. Rev. D* **13** (Jun, 1976) 3398–3409. `http://link.aps.org/doi/10.1103/PhysRevD.13.3398`.

[131] D.-H. Lee, G.-M. Zhang, and T. Xiang, "Edge Solitons of Topological Insulators and Fractionalized Quasiparticles in Two Dimensions", *Phys. Rev. Lett.* **99** (Nov, 2007) 196805. `http://link.aps.org/doi/10.1103/PhysRevLett.99.196805`.

[132] W. P. Su, J. R. Schrieffer, and A. J. Heeger, "Soliton excitations in polyacetylene", *Phys. Rev. B* **22** (Aug, 1980) 2099–2111. `http://link.aps.org/doi/10.1103/PhysRevB.22.2099`.

[133] Weeks, C. and Rosenberg, G. and Seradjeh, B. and Franz, M., "Anyons in a weakly interacting system", *Nat Phys* **3** no. 11, (2007) 796–801. `http://dx.doi.org/10.1038/nphys730`.

[134] R. B. Laughlin, "Quantized Hall conductivity in two dimensions", *Phys. Rev. B* **23** (May, 1981) 5632–5633. `http://link.aps.org/doi/10.1103/PhysRevB.23.5632`.

[135] B. I. Halperin, "Quantized Hall conductance, current-carrying edge states, and the existence of extended states in a two-dimensional disordered potential", *Phys. Rev. B* **25** (Feb, 1982) 2185–2190. `http://link.aps.org/doi/10.1103/PhysRevB.25.2185`.

[136] M. Weber, M. Hohenadler, and F. F. Assaad, "Kondo screening of spin-charge separated fluxons by a helical liquid", *Phys. Rev. B* **89** (May, 2014) 205125. `http://link.aps.org/doi/10.1103/PhysRevB.89.205125`.

[137] A. Shitade, H. Katsura, J. Kuneš, X.-L. Qi, S.-C. Zhang, and N. Nagaosa, "Quantum Spin Hall Effect in a Transition Metal Oxide Na_2IrO_3", *Phys. Rev. Lett.* **102** (Jun, 2009) 256403. `http://link.aps.org/doi/10.1103/PhysRevLett.102.256403`.

[138] K. K. Gomes, W. Mar, W. Ko, F. Guinea, and H. C. Manoharan, "Designer Dirac fermions and topological phases in molecular graphene", *Nature* **483** no. 7389, (2012) 306–310. `http://dx.doi.org/10.1038/nature10941`.

[139] A. Singha, M. Gibertini, B. Karmakar, S. Yuan, M. Polini, G. Vignale, M. I. Katsnelson, A. Pinczuk, L. N. Pfeiffer, K. W. West, and V. Pellegrini, "Two-Dimensional Mott-Hubbard Electrons in an Artificial Honeycomb Lattice", *Science* **332** no. 6034, (2011) 1176–1179. `http://www.sciencemag.org/content/332/6034/1176.abstract`.

[140] B. Beri and N. R. Cooper, "$\mathbb{Z}_2$ Topological Insulators in Ultracold Atomic Gases", *Phys. Rev. Lett.* **107** (Sep, 2011) 145301. `http://link.aps.org/doi/10.1103/PhysRevLett.107.145301`.

[141] N. Goldman, I. Satija, P. Nikolic, A. Bermudez, M. A. Martin-Delgado, M. Lewenstein, and I. B. Spielman, "Realistic Time-Reversal Invariant Topological Insulators with Neutral Atoms", *Phys. Rev. Lett.* **105** (Dec, 2010) 255302. `http://link.aps.org/doi/10.1103/PhysRevLett.105.255302`.

[142] Y. Ran, Y. Zhang, and A. Vishwanath, "One-dimensional topologically protected modes in topological insulators with lattice dislocations", *Nat Phys* **5** no. 4, (2009) 298–303. `http://dx.doi.org/10.1038/nphys1220`.

[143] G. Rosenberg, H.-M. Guo, and M. Franz, "Wormhole effect in a strong topological insulator", *Phys. Rev. B* **82** (Jul, 2010) 041104. `http://link.aps.org/doi/10.1103/PhysRevB.82.041104`.

[144] T. Giamarchi, *Quantum Physics in One Dimension.* Oxford University Press, Oxford UK, 2004.

[145] F. F. Assaad, M. Bercx, and M. Hohenadler, "Topological Invariant and Quantum Spin Models from Magnetic π Fluxes in Correlated Topological Insulators", *Phys. Rev. X* **3** (Feb, 2013) 011015. `http://link.aps.org/doi/10.1103/PhysRevX.3.011015`.

[146] A. W. Sandvik, "Stochastic series expansion method with operator-loop update", *Phys. Rev. B* **59** (Jun, 1999) R14157–R14160. `http://link.aps.org/doi/10.1103/PhysRevB.59.R14157`.

[147] A. Albuquerque, F. Alet, P. Corboz, P. Dayal, A. Feiguin, S. Fuchs, L. Gamper, E. Gull, S. Gürtler, A. Honecker, R. Igarashi, M. Körner, A. Kozhevnikov, A. Läuchli, S. Manmana, M. Matsumoto, I. McCulloch, F. Michel, R. Noack, G. Pawlowski, L. Pollet, T. Pruschke, U. Schollwöck, S. Todo, S. Trebst, M. Troyer, P. Werner, and S. Wessel, "The alps project release 1.3: Open-source software for strongly correlated

systems", *Journal of Magnetism and Magnetic Materials* **310** no. 2, Part 2, (2007) 1187 – 1193.
`http://www.sciencedirect.com/science/article/pii/S0304885306014983`.
Proceedings of the 17th International Conference on Magnetism.

[148] H.-J. Mikeska and A. Kolezhuk, "One-dimensional magnetism", in *Quantum Magnetism*, U. Schollwöck, J. Richter, D. Farnell, and R. Bishop, eds., vol. 645 of *Lecture Notes in Physics*, pp. 1–83. Springer Berlin Heidelberg, 2004.
`http://dx.doi.org/10.1007/BFb0119591`.

[149] E. Dagotto and T. M. Rice, "Surprises on the Way from One- to Two-Dimensional Quantum Magnets: The Ladder Materials", *Science* **271** no. 5249, (1996) 618–623.
`http://www.sciencemag.org/content/271/5249/618.abstract`.

[150] M. Bercx, M. Hohenadler, and F. F. Assaad, "Kane-Mele-Hubbard model on the π-flux honeycomb lattice", *Phys. Rev. B* **90** (Aug, 2014) 075140.
`http://link.aps.org/doi/10.1103/PhysRevB.90.075140`.

[151] B. Leung and E. Prodan, "Effect of strong disorder in a three-dimensional topological insulator: Phase diagram and maps of the Z2 invariant", *Phys. Rev. B* **85** (May, 2012) 205136. `http://link.aps.org/doi/10.1103/PhysRevB.85.205136`.

[152] M. Wimmer, "Algorithm 923: Efficient Numerical Computation of the Pfaffian for Dense and Banded Skew-Symmetric Matrices", *ACM Trans. Math. Softw.* **38** no. 4, (Aug., 2012) 30:1–30:17. `http://doi.acm.org/10.1145/2331130.2331138`.

[153] M. Hohenadler, T. C. Lang, and F. F. Assaad, "Correlation Effects in Quantum Spin-Hall Insulators: A Quantum Monte Carlo Study", *Phys. Rev. Lett.* **106** (Mar, 2011) 100403. `http://link.aps.org/doi/10.1103/PhysRevLett.106.100403`.
erratum **109**, 229902(E) (2012).

[154] D. Zheng, G.-M. Zhang, and C. Wu, "Particle-hole symmetry and interaction effects in the Kane-Mele-Hubbard model", *Phys. Rev. B* **84** (Nov, 2011) 205121.
`http://link.aps.org/doi/10.1103/PhysRevB.84.205121`.

[155] M. Laubach, J. Reuther, R. Thomale, and S. Rachel, "Rashba spin orbit coupling in the Kane-Mele-Hubbard model", *arXiv:1312.2934* (2013) .

[156] H.-H. Hung, V. Chua, L. Wang, and G. A. Fiete, "Interaction effects on topological phase transitions via numerically exact quantum Monte Carlo calculations", *Phys. Rev. B* **89** (Jun, 2014) 235104.
`http://link.aps.org/doi/10.1103/PhysRevB.89.235104`.

[157] D. N. Sheng, Z. Y. Weng, L. Sheng, and F. D. M. Haldane, "Quantum Spin-Hall Effect and Topologically Invariant Chern Numbers", *Phys. Rev. Lett.* **97** (Jul, 2006) 036808. `http://link.aps.org/doi/10.1103/PhysRevLett.97.036808`.

[158] D. Sénéchal, “An introduction to bosonization”, *arXiv:cond-mat/9908262v1* (1999) .

[159] Y. Tanaka and N. Nagaosa, “Two Interacting Helical Edge Modes in Quantum Spin Hall Systems”, *Phys. Rev. Lett.* **103** (Oct, 2009) 166403. `http://link.aps.org/doi/10.1103/PhysRevLett.103.166403`.

[160] E. Orignac, M. Tsuchiizu, and Y. Suzumura, “Spectral functions of two-band spinless fermion and single-band spin-1/2 fermion models”, *Phys. Rev. B* **84** (Oct, 2011) 165128. `http://link.aps.org/doi/10.1103/PhysRevB.84.165128`.

[161] Y. Tada, R. Peters, M. Oshikawa, A. Koga, N. Kawakami, and S. Fujimoto, “Correlation effects in two-dimensional topological insulators”, *Phys. Rev. B* **85** (Apr, 2012) 165138. `http://link.aps.org/doi/10.1103/PhysRevB.85.165138`.

[162] C.-H. Chung, D.-H. Lee, and S.-P. Chao, “Kane-Mele Hubbard model on a zigzag ribbon: stability of the topological edge states and quantum phase transitions”, *arXiv:1401.4875* (2014) .

[163] J. von Delft and H. Schoeller, “Bosonization for beginners refermionization for experts”, *Annalen der Physik* **7** no. 4, (1998) 225–305. `http://dx.doi.org/10.1002/(SICI)1521-3889(199811)7:4<225::AID-ANDP225>3.0.CO;2-L`.

[164] F. D. M. Haldane, “'Luttinger liquid theory' of one-dimensional quantum fluids. I. Properties of the Luttinger model and their extension to the general 1D interacting spinless Fermi gas”, *Journal of Physics C: Solid State Physics* **14** no. 19, (1981) 2585. `http://stacks.iop.org/0022-3719/14/i=19/a=010`.

[165] E. Orignac, M. Tsuchiizu, and Y. Suzumura, “Competition of superfluidity and density waves in one-dimensional Bose-Fermi mixtures”, *Phys. Rev. A* **81** (May, 2010) 053626. `http://link.aps.org/doi/10.1103/PhysRevA.81.053626`.

[166] M. Hohenadler and F. F. Assaad, “Luttinger liquid physics and spin-flip scattering on helical edges”, *Phys. Rev. B* **85** (Feb, 2012) 081106. `http://link.aps.org/doi/10.1103/PhysRevB.85.081106`. erratum **86**, 199901(E) (2012).

[167] A. Luther and I. Peschel, “Calculation of critical exponents in two dimensions from quantum field theory in one dimension”, *Phys. Rev. B* **12** (Nov, 1975) 3908–3917. `http://link.aps.org/doi/10.1103/PhysRevB.12.3908`.

[168] E. Tang and L. Fu, “Strain-Induced Helical Flat Band and Interface Superconductivity in Topological Crystalline Insulators”, *arXiv:1403.7523v1* (2014) .

[169] G. Jotzu, M. Messer, R. Desbuquois, M. Lebrat, T. Uehlinger, D. Greif, and T. Esslinger, “Experimental realization of the topological Haldane model with ultracold fermions”, *Nature* **515** no. 7526, (2014) 237–240. `http://dx.doi.org/10.1038/nature13915`.

[170] N. R. Cooper, "Optical Flux Lattices for Ultracold Atomic Gases", *Phys. Rev. Lett.* **106** (Apr, 2011) 175301. `http://link.aps.org/doi/10.1103/PhysRevLett.106.175301`.

[171] M. Aidelsburger, M. Atala, S. Nascimbène, S. Trotzky, Y.-A. Chen, and I. Bloch, "Experimental Realization of Strong Effective Magnetic Fields in an Optical Lattice", *Phys. Rev. Lett.* **107** (Dec, 2011) 255301. `http://link.aps.org/doi/10.1103/PhysRevLett.107.255301`.

[172] A. Celi, P. Massignan, J. Ruseckas, N. Goldman, I. B. Spielman, G. Juzeliūnas, and M. Lewenstein, "Synthetic Gauge Fields in Synthetic Dimensions", *Phys. Rev. Lett.* **112** (Jan, 2014) 043001. `http://link.aps.org/doi/10.1103/PhysRevLett.112.043001`.